Dissipation in the Earth-Moon system

Mohammad Farhat

Sorbonne Université

Ecole doctorale d'astronomie et d'astrophysique
d'Ile-de-France

Institut de mécanique céleste et de calcul des éphémérides

Dissipation in the Earth-Moon System

---

par

Mohammad Ali Farhat

Thèse de doctorat de Astronomie et Astrophysique

Dirigée par

Jacques Laskar
et
Gwenaël Boué

Présentée et soutenue publiquement le

05 / 01 / 2023

Devant un jury compose de:

Dr. Alessandro Forte, University of Florida	Rapporteur
Dr. Robert Tyler, NASA Goddard Spaceflight Center	Rapporteur
Dr. François Forget, Sorbonne Université	Président du jury
Dr. Jihad Touma, American University of Beirut	Examinateur
Dr. Marianne Greff, Institut de Physique du Globe de Paris	Examinatrice
Dr. Frits Hilgen, Utrecht University	Examinateur
Dr. Jacques Laskar, Observatoire de Paris	Directeur de thèse
Dr. Gwenaël Boué, Observatoire de Paris	Invité
Dr. Pierre Auclair-Desrotour, Observatoire de Paris	Invité

To Mohammad Jouni (1989-2015)

Abstract

The long-term dynamical evolution of the Earth-Moon system is revisited. We address three distinct geophysical mechanisms pertaining to solid and fluid planetary mass redistributions affecting the system's history.

First, the effect of Cenozoic glacial cycles on the Earth's figure is constrained. In the framework of glacial isostatic adjustment, and using a recently compiled proxy of global ice volume, we self-consistently solve the sea level equation. We then present a time series of the evolution of the Earth's dynamical ellipticity over the Cenozoic ice age. We map out the problem in full generality, identifying major sensitivities to possible variations in surface loading, and to uncertainties in rheological modeling and internal viscosity profiles. We match our parametric exploration with present observations of the rate of change of J_2 and true polar wander measurements. We consequently provide well-constrained intervals for the relative perturbation in the dynamical ellipticity due to the Cenozoic ice age.

Next, we revisit the evolution history of the Earth-Moon distance. Available geological data provide snapshots of the lunar orbital history, the earliest registered to date at ~ 3.2 Ga. However, a complete theoretical reconstruction of the lunar orbit, which traces its evolution from the present state to a post-impact nosy neighbor at ~ 4.5 Ga is yet to be established. Namely, previous models of this reconstruction are often empirical, or numerically costly, and are always incompatible with the well-constrained lunar age. We undertake a systematic exploration of the time-varying tidal dissipation in the Earth's oceans and solid interior to provide, for the first time, a history of the lunar orbit that fits the present measurement of its recession and the estimated lunar age. Our work extends a lineage of earlier works on the analytical treatment of fluid tides on varying bounded surfaces, further coupled with bodily solid tidal deformations. We obtain a history of the lunar orbit that is predominantly shepherded by robust resonant excitations in the Earth's paleo-oceans. These resonances caused significant and, relatively, rapid variations in the lunar semi-major axis, the Earth's length of the day, and the Earth's obliquity. Consequently, these astronomical features should have driven major paleo-climatic variations through tidal heating and the changing insolation. Our solution demonstrates the robustness of the cyclostratigraphic method in unraveling astronomical quantities from sedimentary sequences.

Finally, we examine the effect of thermal tides on the evolution of planetary rotational motion. We revisit the hypothesis of a fixed Precambrian length of day for the Earth, which is contingent upon encountering a Lamb resonance in the atmosphere. We

construct an ab initio model of thermal tides describing a neutrally stratified atmosphere. The model takes into account dissipative processes with Newtonian cooling and the delayed thermal response of the ground. We retrieve from this model a closed form solution for the frequency-dependent thermal tidal torque. Our solution captures the main spectral features computed numerically in earlier studies using 3D general circulation models. In particular, the delayed response of the ground proves to be responsible for an asymmetry in the Lamb resonance, thus positing serious question marks on the rotational equilibrium hypothesis. Finally, though the study was motivated by the tidal history on Earth, the solution can be straightforwardly applied in exoplanetary settings.

Key Words: Earth – Moon – Oceanic tides – Atmospheric tides – Glacial isostatic adjustment – Terrestrial planets.

Resumé

L'évolution dynamique à long terme du système Terre-Lune est revisitée à travers trois mécanismes géophysiques distincts qui impliquent des redistributions de masse planétaire solide et fluide affectant l'histoire du système.

Tout d'abord, nous estimons l'effet des cycles glaciaires du Cénozoïque sur la figure de la Terre. Dans le cadre de la théorie de l'ajustement isostatique, et en utilisant une compilation récente des proxys du volume global de glace, nous résolvons l'équation du niveau de la mer, et nous présentons une série temporelle de l'évolution de l'ellipticité dynamique pendant les périodes glaciaires du Cénozoïque. Nous identifions les principales sensibilités de cette évolution aux variations potentielles de la charge de glace, et aux incertitudes de la modélisation rhéologique et des profils de viscosité interne. Nous ajustons notre modèle paramétrique aux observations récentes du taux de variation du J_2 et aux mesures de la dérive des pôles. Nous fournissons ainsi des estimations de la perturbation relative de l'ellipticité dynamique durant l'âge glaciaire du Cénozoïque.

Ensuite, nous revisitons l'histoire de l'évolution de la distance Terre-Lune. Les données géologiques disponibles fournissent des instantanés de l'histoire de l'orbite lunaire, le plus ancien enregistré à ce jour datant de $\sim$ 3.2 Ga. Cependant, une reconstruction théorique complète de l'orbite lunaire, qui retrace son évolution depuis l'état actuel jusqu'à sa formation il y a $\sim$ 4.5 Ga, restait à établir. En effet, les modèles précédents de cette reconstruction sont souvent empiriques ou numériquement coûteux, et sont tous incompatibles avec l'âge de la Lune. Nous entreprenons une caractérisation systématique de la dissipation de marée à la fois dans les océans et dans l'intérieur solide de la Terre. Nous fournissons ainsi, pour la première fois, une histoire de l'orbite lunaire en accord avec la mesure actuelle de sa récession et avec l'âge estimé de la Lune. Notre travail s'inscrit dans une lignée de travaux antérieurs sur le traitement analytique des marées fluides, couplées en outre aux déformations des marées solides. Nous obtenons une histoire de l'orbite lunaire qui est contrôlée par des excitations résonantes dans les paléo-océans de la Terre. Ces résonances ont provoqué des variations importantes et relativement rapides du demi-grand axe lunaire, de la durée du jour et de l'obliquité de la Terre. Ces variations astronomiques ont pu entraîner d'importantes variations paléoclimatiques dues au chauffage de marée et aux modifications de l'insolation à la surface de la Terre. Notre solution démontre aussi la robustesse de la méthode cyclostratigraphique pour extraire les données astronomiques des séquences sédimentaires.

Enfin, nous étudions l'effet des marées thermiques atmosphériques sur l'évolution du mouvement de rotation planétaire. Nous réexaminons, pour la Terre, l'hypothèse d'une

stagnation de la durée du jour pendant le Précambrien, qui résulterait de la rencontre d'une résonance d'un mode de Lamb dans l'atmosphère. Nous construisons un modèle ab initio de marées thermiques décrivant le cas d'une atmosphère à stratification neutre. Le modèle prend en compte les processus dissipatifs à travers le refroidissement radiatif de l'atmosphère et la réponse thermique retardée du sol. Nous extrayons de ce modèle une solution exacte du couple de marée thermique dépendant de la fréquence de marée. Notre solution rend compte des principales caractéristiques spectrales obtenues numériquement dans des études antérieures utilisant des modèles de circulation générale 3D. En particulier, la réponse retardée du sol s'avère être responsable d'une asymétrie dans la résonance du mode de Lamb, remettant ainsi sérieusement en doute l'hypothèse d'une stagnation de la durée du jour. Enfin, bien que l'étude ait été motivée par l'histoire des marées sur Terre, les solutions développées peuvent être directement appliquées à l'étude des exoplanètes.

Mots Clés: Terre – Lune – Marées océanique – Marées atmosphériques – Rebond post-glaciaire – Planètes telluriques.

Acknowledgements

Three years ago, I set foot in Paris for the first time. A stranger in a strange land, surrounded by a turbulent flow of people - soon enough to be muted by covid - with whom I basically had the minimum of shared concerns. Now that I wrap up my thesis work, in hindsight, I would never have imagined how things would turn out; and for the better part of it, it is my pleasure to express my sincere gratitude to many people who made my stay, thousands of kilometers away from home, bearable, and this thesis work possible.

Foremost, I was privileged to work with a team of three advisors, true descendants of the French school of scientific rigour: my thesis director, *Jacques Laskar*, a genuine scientific visionary, who really envisaged my thesis work since day one. Though Jacques pushed me out of my scientific comfort zone into a chaotic crossroads of interdisciplinary problems, he anchored me to his foothold in the scientific community, providing generous academic and non-academic support, along with the adequate pressure when pressure is due, to make this journey quite fruitful and, dare I say, enjoyable. Jacques' creativity, eye for detail, and ability to formulate fairly complicated processes in simple forms have always presented a model to learn from. Second, I couldn't have asked for a better thesis co-director and office mate than *Gwenaël Boué*. Gwenaël's readiness at all times to engage, discuss, and go through intricate calculations was absolutely essential for my thesis progress. His ability to resourcefully address any problem I share with him, formulating it in the proper mathematical or numerical framework, was outstanding. He always understood my limitations and carefully helped me push forward. Third, for the major part of this thesis, I am indebted to *Pierre Auclair-Desrotour*, whose signature can be readily seen in the details of the ideas and calculations made throughout this work. Pierre's clarity of thought when mapping problems, and rigorousness in addressing them have taught me a lot. I thank him, not only because I enjoyed our scientific collaboration, but because he proved to be a genuine friend. I can only look forward to continue working with this scientific family.

Jihad Touma, my life-time sincere mentor and friend, who taught me how to find pleasure in science, passionately and humbly. I remember attending, as a biology student, one of his lectures on classical mechanics back in 2014 and deciding to switch my studies to whatever this brilliant man works on. I frankly feared, at the end of my MS studies under his supervision in Beirut, that I would lose touch with him. Little did I know that once you're his apprentice, you're forever one; and for that I am extremely grateful. I am sure we will continue to think, dream, and build together.

I thank *Robert Tyler, Alessandro Forte, Marianne Greff, François Forget, Frits Hilgen, and Jihad Touma* for serving on my thesis jury, and for putting a lot of time and effort into reading my interdisciplinary thesis manuscript. I appreciated our vibrant (and long) exchange and discussion during the defense.

I am grateful to have had the opportunity of working on my thesis in the absolutely perfect working environment of IMCCE. One cannot really describe how wholesome it is to work there, interacting with all the kind-hearted lab members on a daily basis, all

the while pressuring them to speak in English. In particular, I thank *Hervé Manche* for his scientific help (which is often accompanied with some dark jokes); *Alain Chenciner* and *Alain Albouy* for three years of sharing their rich insights on science and history, and providing me with my only human interactions over months of quarantine during the covid pandemic; *Mickaël Gastineau* and *Stéphane Vaillant* for their technical help, which often required patience. . . I extremely thank *Rachida Amhidez, Lusiné Amirkhanyan, Amélie Muslewski*, and *Névada Mendes* as the administrative dream-team of the lab. Their sincere help on maneuvering the convoluted details of French bureaucracies was essential at every step of my PhD. On the side of the early-career folks of the lab, I thank *Federico Mogavero, Nam Hoang, Léo Bernus, Daniel Baguet, Ariane Courtot, Julie Vermersch*, and *Anne-Charlotte Perlbarg* for continuous discussions and outings, and I wish them all the best in their future endeavours. Finally, I thank *Philipe Robutel*, and I wish him the best of luck in captaining this precious team.

I am happy to have addressed in my research, though tangentially, certain geological problems, allowing me to meet few fellow geologists who became really good friends. *Matthias Sinnesael* and *Margriet Lantink*, I hope the scientific community in every field has more early career scientists who share their passion, integrity, and world concerns. I am lucky to have them as colleagues and friends, and I can only wish that this goes on.

My gratitude extends to *Giorgio Spada, Stéphane Labrosse, Yanick Ricard, Barbara Romanowicz*, and *Maëlis Arnould* for helpful exchanges on various geophysical aspects that entered in my thesis work, and to *Nicolas Rambaux* and *Marianne Greff* for serving on my thesis followup committee.

To my father and mother, my eternal source of support, even when it made no sense that I had to leave, I owe them my whole career, and certainly this diploma included. My brother and sister have provided my continuous reminder of home away from home. I can only hope this work blends with success stories they are authoring amidst very adverse conditions.

To *Mariam*, I attribute the person I have become, let alone this work that I have produced. The only person who actually lives behind every detail of my days, the success that I portray here, but more importantly, the failures that I have hidden. As she currently prepares her doctoral work, I hope I can at least mirror the stability (with quasi-periodic disruptions) that she has provided me with.

Above all, praise be to God, who laid down the faith of all scientists:

“Thou seest not in the creation of the All-merciful any imperfection. Return thy gaze; seest thou any fissure? Then return thy gaze again, and again, and thy gaze comes back to thee dazzled, aweary” ;

an exquisite positive feedback loop of seeking knowledge and excitement, or as Mohammad Abdus Salam puts it: “the deeper we seek, the more is our wonder excited, the more is the dazzlement for our gaze.”

CONTENTS

SYNOPSIS

In the era of exoplanetary exploration and wide astronomical surveys, much is left to fathom in the solar system. While it is compelling to seek answers to some of the most profound questions on the habitability of Earth analogs, the history of our own planetary neighborhood is still fraught with uncertainties. The collective amnesia of the inner solar system due to its chaotic nature, and of the Earth due to its bombardment history and the intense geomorphological evolution, left us with little archival traces. For us Earthlings, this historical blurriness hinders our complete understanding of abiogenesis and the consequent evolution of the ecosystem, up until we came into sight.

The Milankovitch theory of the variability in the Earth's insolation provides an exquisite tool for probing the complex interplay between astronomical and climatic variations. Ever since Milutin Milankovitch himself, there has been a growing appreciation of the importance of the theory among solar system dynamicists, geophysicists, geologists, paleontologists, climatologists, and the list goes on. In particular, our retrieval of the past dynamical evolution of the solar system has been used to tune the depths of ancient strata. Conversely, and more recently, with limitations on this retrieval arising, rhythmic strata are being used as an indirect astronomical observatory. The Milankovitch machinery has thus opened a very rich interdisciplinary scientific avenue, and this work is a mere telltale of the theory's beauty.

In this thesis, I pay the Earth's geophysical and dynamical history a humble visit, patching gaps in certain problems and addressing others that are more serious, perhaps perplexing. While all the studied problems are concerned with the Earth's history of deformation and mass redistribution, they are of different physical nature. Namely, the thesis addresses solid Earth viscoelastic deformation, oceanic gravitational tides over geological timescales, and atmospheric mass redistribution due to thermal forcing. I thus ask the reader to turn a blind eye to the possible discontinuities between the chapters. Concerning the thesis outline, I opted for a separate introduction to each chapter, rather than the common tradition of a single introductory chapter. Therein, I provide a historical overview of the problem, its state-of-the-art, and my motivation in

addressing it. Moreover, the reader will soon enough notice the interdisciplinary nature of the work. I thus “tried" to avoid surmising the reader’s familiarity with the theoretical background and provided, for each chapter, a conspectus on the matter. This might trigger the reader’s patience at some point, but it will certainly save me a lot of trouble when visiting back similar problems in the future. It is noteworthy that when writing the manuscript, the chapters were ordered chronologically, abiding by the progress of my thesis work in time. Finally, I hereafter let go of the singular first-person pronoun, in favor of the plural, as this work was in its entirety a team endeavour.

In Chapter 1 we describe the work of Farhat, Laskar, and Boué (2022b) on a limitation we have in computing the past rotational motion of the Earth. Namely, the Earth’s dynamical ellipticity, or equivalently the Earth’s oblateness enters as a parameter in computing the Earth’s rotational evolution. However, this parameter features an unconstrained history. Its variation is driven by all sorts of surface and internal mass redistributions. We focus in this chapter on the effect of surface loading and internal re-adjustment during glacial cycles. We utilize the theory of viscoelastic relaxation, the glacial isostatic adjustment formalism, and the theory of sea level variation to recover the Earth’s geopotential evolution during the Cenozoic.

Chapter 2 is devoted to the work of Farhat, Auclair-Desrotour, Boué, and Laskar (2022a) on the time-scale problem of the lunar origin. The latter corresponds to the incompatibility between the tidal modelling of the Earth-Moon system and the geologically constrained age of the Moon. We revisit this classical “conundrum" armed with a rich history of advancement in the linear theory of fluid tides. Our aim is to evade the time-scale problem by constructing a model that fits the present state of the lunar orbit and the lunar formation age.

In Chapter 3 we escape the Earth’s interior and surface into its atmosphere. Motivated by the hypothesis of a fixed Precambrian length-of-day on Earth, we revisit the theory of thermal tidal resonances. Our goal is to construct an ab initio model of thermal tides that can be satisfactorily and consistently accommodated into the Earth-Moon evolution history.

We conclude in Chapter 4 on these problems, and we provide an outlook of future problems that shall keep us busy in the near future.

CHAPTER 1

THE CENOZOIC DYNAMICAL ELLIPTICITY

1.1 Introduction

1.1.1 Glacial theory: a historical anecdote

Some twenty-thousand years ago, the Earth, as we know it today, was utterly dissimilar. Our planet was held in thrall by tightly gripping ice sheets that initiated at the poles, the capital of the glacial empire, and extended to lower latitudes, inattentive of the thriving ecosystem at the time. Quite reflective of any imperial expansion, the slow glacial spread mercilessly distorted the quasi-stable climate system, plummeting temperatures, burying mountains, drying oceans, and depressing land surfaces by its accumulating weight. Such relentless violations were destined to create scars when the ice sheets retreated, leaving behind a vengeful landscape that has been patiently, ever since, trying to re-establish its forsaken equilibrium.

Though this sketch might resonate negatively, it is exactly these scars that led the human mind to initially postulate, argue, and eventually accept the glacial theory[1]. The ice sheets' expansion and retreat grinding away the underlying surface, leaving deep grooves in bedrock, pulverizing existing material, and transporting eroded materials onto a chaotic clutter around their furthest extent, have left various clues for (mis-)interpretation. For example, countless versions exist of the sagas and folktales explaining the existence of unfamiliar rough boulders around the Alps and central Europe, up to Scandinavia. Was it the failed plan of the devil, who intended to drop these boulders upon a crowded church on a Sunday, but was, fortunately, intercepted and instead, furiously dropped them at random? Or were these huge boulders the homes of angry trolls, who communicated by throwing rocks on each other (a more plausible

[1] A neat and authoritative summary of the theory's development can be found in Imbrie and Imbrie (1986). A more historical archive on the matter can be found in Krüger (2013). We used these references to develop most of this section.

theory than the former as it explains the existence of scattered *Findlinge* - smaller pieces of rocks around their parent beds)? These "unnatural" erratic blocks around the Alps and European lowlands were indeed extremely attractive for locals and foreigners alike, and were turned into worship places and used as megalithic tombs.

From the devil's devious plans to homes of trolls, clashing theories of the existence of these weird piles of rock continued to emerge. The possibility of them having been flung away by volcanic eruptions was the major postulate in the 18th and early 19th centuries. Though met with strict objections, the eruption theory continued to attract adherents up till the 20th century (even after the theory of ice ages was widely accepted). In early 1940s, Dutch geologist Christoph Sandberg, clearly anachronistically, published a multi-volume work against the theory of ice ages and argued that these erratics are solidified mudflow that are the consequence of catastrophic volcanic eruptions. This theory was accompanied by another widely spread postulate that attempted to explain the non-local origin and migration of these rocks. Mainly depending on the analysis of fossil samples, it was suggested that these rocks were transported by monstrous, horrific floods. This claim was widely applauded in European communities as it was equated with the biblical major flood. Catastrophism was vastly dominant in the geological philosophy at the time; certainly because it provided, ironically, a pristine account of fossil records without opposing the word of God. And it is mostly because of this that the theory of ice ages was met with fierce resistance when introduced onto the scientific community. Namely, it was as early as 1787 that the existence of the erratic boulders was attributed to ancient glaciation. The early work of the Swiss minister Friedrich Kuhn, followed by the studies of James Hutton in the Swiss Jura, Jens Esmark in Norway, and Reinhard Bernhardi in central Germany, over the period of 40 years, were all independent observations and deductions on the existence of a vastly spreading ice sheet. But the postulate of the erratics being the deposits of the great flood was so deeply entrenched such that none of the pioneers of the glacial theory at the time were able to defend their revolutionary ideas.

It took another 25 years and another chain of scientists, accompanied with some happy coincidences, leading up to the famous meeting in Neuchâtel (1837), to overthrow the established theory of the major flood. The new chain of the glacial Swiss apostles started with Jean Pierre Perraudin, who put a lot of effort into finding a sympathetic ear for his observations of the Alpine glaciers. He eventually succeeded in doing so, and onward started the fundamental association between the ice-age research pioneers: Ignaz Venetz, Jean de Charpentier, and above all, Louis Agassiz. Venetz was the first to

FIGURE 1.1: The beginning of La Mer de Glace: one of the largest persisting glaciers in the Alps, extending nearly 5.6 km to the north of Mont Blanc near Chamonix, France. Lateral and medial moraines have clearly developed as the glacier retreats, and it does so by 30 ~ 40 meters per year, losing 4 to 5 meters in thickness. Photograph from personal library, taken in July, 2021.

bring up the topic of glaciers at the Swiss Society of Natural Sciences at Bern (1816), though he did so only to present new ideas on glacial movement and to describe the accumulation of moraines (Figure 1.1). His reluctance and patience to accept the theory at first led de Charpentier with his remarkable scientific reasoning to delve deeper into the theory and establish its proper foothold in the Swiss scientific community. But both were humble scientists lacking the aggressiveness required for the theory's triumph. And it was exactly those elements that Agassiz offered with his extravagant lectures, well established network, and frequent travels across the globe. His assertions about the extent of the ice sheets grew more and more strong, forcing a heated debate among the geological community. For instance, the great English geologist Charles Lyell, an advocate of the great flood theory at the time, and later an influential convert wrote: "Agassiz...has gone wild about glaciers. The whole of the great [Amazon] valley, down to its mouth was filled by ice...[though] he does not pretend to have met with a single glaciated pebble or polished rock." While a scientific clash was raging in Europe, Agassiz moved to the United States, where the theory was welcomed with less aggression. By the late 1860s, the theory of ice-ages had established a firm stronghold in both Europe and America, with scattered voices of opposition arising every now and then, but none being able to stand against the growing evidence of Agassiz' theory. A new scientific world has indeed emerged.

1.1.2 The rotational history of the Earth and some of its vexing problems

It is currently well established that the Earth's rotation has forever been in a continuously evolving state, with variability occurring on timescales that extend over the whole span from days to millions of years. Such variations are mainly quantified in terms of changes in the rate of rotation about the instantaneous spin axis (variations in the length of day - LOD hereafter), changes in the orientation of the spin axis relative to an outer reference frame (obliquity, axial precession, and nutation variations), and changes in the orientation of the spin axis relative to the surface geography (henceforth true polar wander, TPW).

A whole myriad of interconnected mechanisms and processes contribute to this multivariate evolution (Peltier, 2015). On relatively short daily to annual timescales, LOD variations arise primarily due to angular momentum exchange between the Earth's solid, oceanic, and atmospheric counterparts (Hide et al., 1980). On longer interannual timescales, El Niño–Southern Oscillation events that occur upon the atmosphere-ocean coupling across the equatorial Pacific region are associated with significant LOD variability excitations (Cox and Chao, 2002; Dickey et al., 2002). These signals are now confirmed with Very-Long Baseline Interferometry (VLBI) observations, and are accompanied with measurements from the global positioning system (GPS). The aforementioned signals can be explained by angular momentum exchange computations in global circulation models in the atmosphere and the ocean. However, a residual interdecadal signal requires additional angular momentum exchange that is attributed to core-mantle coupling (Holme, 2007; Duan and Huang, 2020).

On comparable timescales, various wobbles of annual and decadal (quasi-)periodicities were also identified. For example, the Chandler wobble, occurring with a period of about 14 months, involves angular displacement of the pole ranging between 100 and 200 milliarcseconds (mas) (Dahlen and Smith, 1975; Gross, 2000). However, identifying the exact excitation mechanism behind this wobble has been the subject of several studies as it turned out to be greatly elusive (Wahr, 1983; Jault and Le Mouël, 1993; Gross, 2000). The Markowitz wobble, with decadal periodicity, is associated with polar displacements of amplitude around 30 mas (Dickman, 1981). Over millennial timescales, both the Earth's spin rate and orientation exhibit apparent secular variations that are induced primarily by the last ice age, namely the late Pleistocene cycle of glaciation and deglaciation (Peltier, 1983). Consequently, a secular drift in the polar

position of $\sim 0.98°\text{Myr}^{-1}$ with a rate of ~ 3.5 mas yr^{-1} is measured (Argus and Gross, 2004). These variations are brought about through the process of glacial isostatic adjustment (GIA), which we expand on in the following sections of this chapter.

Quantitatively, these variations satisfy the classical Euler equation for the conservation of angular momentum of a body subject to external torques $\mathcal{T}_i$:

$$\frac{d}{dt}(I_{ij}\,\omega_j) + \varepsilon_{ijk}\,\omega_j\,I_{kl}\,\omega_l = \mathcal{T}_i, \tag{1.1}$$

where I_{ij} are elements of the the inertia tensor, ε_{ijk} is the Levi-Civita alternating tensor, and ω_j are the Cartesian components of the angular velocity vector. This equation is often linearized and solved for small perturbations in the inertia components ΔI_{ij} and velocity components m_i such that:

$$\begin{aligned}
I_{11} &= A + \Delta I_{11} \\
I_{22} &= B + \Delta I_{22} \\
I_{33} &= C + \Delta I_{33} \\
I_{ij} &= \Delta I_{ij}, \quad i \neq j \\
\omega_i &= \Omega(\delta_{i3} + m_i), \quad m_i = \omega_i/\Omega,
\end{aligned} \tag{1.2}$$

where the angular velocity Ω is that of the steady unperturbed rotation, while A, B, and C are the principal moments of inertia. Substitution of these perturbations into the angular momentum conservation gives the so-called linearized Liouville equations (e.g., Munk and MacDonald, 1960; Peltier, 2015):

$$\frac{dm_1}{dt} + \frac{C-A}{A}\Omega\, m_2 = \Psi_1\,, \tag{1.3}$$

$$\frac{dm_2}{dt} + \frac{C-A}{B}\Omega\, m_1 = \Psi_2\,, \tag{1.4}$$

$$\frac{dm_3}{dt} = \Psi_3\,, \tag{1.5}$$

where Ψ_i are the so-called 'excitation functions', which are functions of the external torques $\mathcal{T}_i$ and the quantities ΔI_{ij}, and are thus a combination of both external and internal perturbations. Eqs. (1.3) and (1.4) are used to trace the polar wander, while Eq. (1.5) is used to trace the evolution of the LOD. Ignoring any external torque, the variability of the LOD is driven by the changing axial component of the moment of inertia of the solid Earth, an influence that is generally observed on Earth in terms of the parameter $\dot{J}_2$. The latter is the time derivative of J_2, the non-dimensional degree 2,

order 0 coefficient in the spherical harmonic expansion of the gravitational potential of the Earth, or as often called the second zonal harmonic given by

$$J_2 = \frac{C - (A+B)/2}{R_E^2 M_E}. \tag{1.6}$$

Here R_E and M_E are the radius and the mass of the Earth. The relation between $\dot{J}_2$ and variations in the rotational velocity of the Earth, and consequently the LOD, is expressed as:

$$\dot{J}_2 = \frac{3}{2}\frac{C}{R_E^2 M_E}\frac{dm_3}{dt}. \tag{1.7}$$

Of specific interest to us in this context is computing the variation of the Earth's dynamical ellipticity, or ellipsoidal flattening, H, over the long timescales associated with glacial cycles. For the Earth, H is estimated to be around $1/299.8$ (Chambat et al., 2010), and is primarily a property of the mass distribution resulting from the hydrostatic competition between the dominant gravitational force and the weaker centrifugal force. It is related to the second zonal harmonic by

$$H = \frac{R_E^2 M_E}{C} J_2 = \frac{C - (A+B)/2}{C}. \tag{1.8}$$

Modern observational inferences of this quantity report an excess in the flattening of 0.5%, which corresponds to a difference between the equatorial and polar radii that is 110 m larger than equilibrium (Stacey and Davis, 2008; Chambat et al., 2010). This excess is also observed to be decreasing in an attempt of recovering the equilibrium figure (Cox and Chao, 2002). Mechanisms driving this excess vary in nature, magnitude, and time-scales as we described above. They range from astronomical forcing leading to a variation in the gravitational potential between the equator and the poles and tidal friction, to geophysical mechanisms pertaining to surface and internal adjustment in response to the mantle heterogeneity or to surface loading. The net outcome is altering the Earth's rotational motion and consequently the Milankovitch band cyclicity in proxy records (Peltier, 1983; Laskar et al., 1993a; Levrard and Laskar, 2003; Stephenson, 2008).

As a measure of the difference between the polar and equatorial moments of inertia, the dynamical ellipticity is a very significant parameter in astronomical and geophysical studies, and the difficulty in computing its present value or tracing its history over geological timescales poses several problems and enigmas on which we expand further in what follows.

- *The role played by H in TPW determination*

The Earth's background dynamical ellipticity, which was traditionally equated with the hydrostatic equilibrium ellipticity, is a key element in computing polar motion in response to glacial surface loading. When an ice sheet accumulates and loads the Earth at the pole, two competing forces directly arise and alter the rotational motion of the Earth: a force tipping the Earth to break the alignment between the glacial load and the pole, and consequently between the equatorial plane and the elliptical bulge; and another opposing force that acts on the bulge and tries to restore the Earth to its initial configuration. This opposing force is completely dependent on how the ellipticity of the Earth is modelled.

Namely, the background dynamical ellipticity H^{b} is often expressed in terms of the fluid tidal Love number $k_2^{\mathrm{T,f}}$ defined as (see Section 1.2.7 for a detailed definition of the Love numbers):

$$H^{\mathrm{b}} = k_2^{\mathrm{T,f}} \frac{R_{\mathrm{E}}^5}{3GC} \Omega^2, \tag{1.9}$$

where G is the gravitational constant. In the traditional rotational stability theory (Wu and Peltier, 1982), the fluid tidal Love number is the value the tidal Love number k_2^{T} takes in the limit of very long time, or identically, in the limit of the frequency s going to zero in the Laplace domain:

$$k_2^{\mathrm{T,f}} = k_2^{\mathrm{T}}(t = \infty) = k_2^{\mathrm{T}}(s = 0). \tag{1.10}$$

The background ellipticity implied by this approximation deviates from the observed value on the order of 1%. When the traditional rotation theory of an ice age Earth was developed (Wu and Peltier, 1982), it was well known that Eq. (1.10) is an approximation, but it was thought at the time that the induced inaccuracy is insignificant when dealing with 1D Earth models. However, the insightful work of Nakada (2002) presented perplexing results on predictions of present day TPW using the traditional theory. The author showed that results generated using an Earth model with an elastic lithosphere (the most common choice in Earth interior modelling), diverge significantly from those obtained with a viscoelastic lithosphere with extremely high viscosity. The rotational theory was later revised (Mitrovica et al., 2005), and it was shown that the underlying sensitivity to minor variations in the background ellipticity is due to an inherent instability introduced in the traditional theory (Matsuyama et al., 2010; Mitrovica and Wahr, 2011). Specifically, in the traditional theory, the Earth adjusts perfectly to changes in the orientation of the pole, losing memory of the initial

state. The updated theory developed in Mitrovica et al. (2005) ties the background ellipticity in the rotational stability computations to the observed value. Consequently, this 1% inaccuracy in the background ellipticity induces a difference for present TPW estimates between the traditional and revised theories by up to a factor of 4.

- *The role played by geological constraints on H in entangling viscosity inference*

Astronomical calibration is now a well established method of tuning a wide variety of climate proxy records such as isotopoic and elemental records, magnetic susceptibility, and organic records to astronomical solutions (Laskar et al., 1993a, 2004, 2011a; Gradstein et al., 2020). This method often allows the conversion of such depth-dependent records to time-dependent series, and it has been applied extensively to Cenozoic records (see e.g., Hilgen et al., 2012, 2015; Hinnov, 2018). The accuracy of this procedure is dependent on several factors, including the stability of the astronomical frequencies (especially the precession and obliquity bands), and the availability of some well dated points such as magnetic reversals. As we will discuss in the next section, the Milankovitch frequencies are functions of the dynamical ellipticity and the Earth-Moon tidal dissipation. As such, given our inability to directly measure the evolution of these two quantities in the past, palaeoclimatic records have been used to constrain their possible variation. For example, Lourens et al. (2001) obtained a depth-dependent series of titanium-aluminum ratios using core drilling in the Mediterranean (ODP Site 967). Upon calibration with the astronomical solutions, and by varying the dynamical ellipticity and tidal dissipation, they concluded that the relative perturbation - in the non-hydrostatic component - of the dynamical ellipticity over the last 3 Myr falls inside [-0.03%,+0.03%]. Similarly, Pälike and Shackleton (2000) constructed a magnetic susceptibility record from the Ceara Rise (ODP Leg 154), and concluded that the perturbation is bounded within [-0.01%,0.04%] over the last 25 Myr.

The obvious consistency between these independently imposed bounds is misleading, simply because the constrains are imposed over different time scales. In particular, the variation of H over the last 3 Myr is dominated by GIA, while over longer time intervals in the past it was dominated by mantle convection (Forte and Mitrovica, 1997; Ghelichkhan et al., 2021; Farhat et al., 2022b). These two geophysical processes are highly dependent on the internal viscosity profile of the Earth. By a suite of numerical experiments of GIA and mantle convection, Morrow et al. (2012) investigated the following question: what depth-dependent viscosity profile(s) of the Earth's interior would predict ellipticity variations that simultaneously match the two geologically

suggested bounds? Their results defined an enigma, in which no mantle viscosity profile can reconcile the two bounds over the two separate time intervals. Namely, GIA requires a relatively weak lower-mantle viscosity to satisfy the bound of Lourens et al. (2001), while a highly viscous lower mantle is required to match the bounds of Pälike and Shackleton (2000). As such, if taken for granted, geological constraints on H revive the possibility of the mantle viscosity being transient, i.e., the viscoelastic response of the Earth being dependent on the forcing timescale; a possibility explored for example in Sabadini et al. (1985), and abandoned later after overwhelming evidence in the literature of matching GIA byproduct observables with simpler viscosity models (e.g., Mitrovica and Forte, 2004; Roy and Peltier, 2017). However, as we shall see next, the effects of the dynamical ellipticity and tidal dissipation variations on Milankovitch cyclicities are interchangeable. Thus, tidal dissipation could have varied over 25 Ma in such a way to reconcile the two bounds, given, again, that the two bounds are taken at face value.

- *The role played by the unconstrained history of H in limiting our astronomical solutions*

The extended triumph of the Milankovitch theory of paleoclimates relies on the possibility of obtaining accurate solutions for the motion of the Earth over several millions of years. At present, reliable orbital solutions have been obtained for the solar system over about 50 Myr (Laskar et al., 2004, 2011a), and we know that extending the validity of the solution beyond this limit is hindered by the chaotic behaviour of the solar system (Laskar, 1989; Laskar et al., 2011b; Hoang et al., 2021). In contrast, the validity of the precession and obliquity solutions of the Earth is much more limited, to about 10 – 20 Myr (Laskar et al., 2004). This is due to several uncertainties that arise in the computation of the past rotational evolution of the Earth; the unconstrained history of the dynamical ellipticity being one of them, and here we expand on this in greater detail.

The independent canonical variables well suited to describe the rotational motion of the Earth are the Andoyer action-angle variables, with (L, X) being the action variables, and $(\ell, -\psi)$ their conjugate angles (Kinoshita, 1977). Using these variables and applying the gyroscopic approximation removes two of the six degrees of freedom necessary for the complete determination of the Earth's rotational dynamics, greatly simplifying the problem. This leaves us with: $L = C\Omega$, the magnitude of the rotational angular momentum of the Earth; $X = L\cos\varepsilon$, the projection of the angular momentum on the normal to the ecliptic, ε being the Earth's obliquity; ℓ, the hour angle between the equinox of a reference ecliptic and a fixed point of the equator; whereas $-\psi$ is the opposite of the general precession angle. We refer the interested reader to the works of Kinoshita (1977), Laskar (1986, 1996), and Neron de Surgy and Laskar (1997) for a full development of the Hamiltonian dynamical formulation in these variables, and we brief here on what is necessary for the purpose of our work. The Hamiltonian $\mathcal{H}$ describing the rotational motion of the Earth, which combines the rotational kinetic energy of the Earth, the potential energy of the torque exerted by the Sun and the Moon on the equatorial bulge of the Earth, and the gravitational perturbations of the other planets reads

$$\mathcal{H} = \frac{L^2}{2C} - \frac{\alpha}{2}\frac{X^2}{L} + 2C(t)X - L\sqrt{1-(X/L)^2}\left[\mathcal{A}(t)\sin\psi + \mathcal{B}(t)\cos\psi\right]. \quad (1.11)$$

Here we use the time dependent functions (Laskar, 1986)

$$\mathcal{A}(t) = \frac{2}{\sqrt{1-p^2-q^2}}\left[\dot{q} + p(q\dot{p} - p\dot{q})\right], \tag{1.12}$$

$$\mathcal{B}(t) = \frac{2}{\sqrt{1-p^2-q^2}}\left[\dot{p} + q(q\dot{p} - p\dot{q})\right], \tag{1.13}$$

$$C(t) = q\dot{p} - p\dot{q}, \tag{1.14}$$

with $q = \sin(i_{\rm E}/2)\cos\Omega_{\rm E}$ and $p = \sin(i_{\rm E}/2)\sin\Omega_{\rm E}$; $i_{\rm E}$ and $\Omega_{\rm E}$ being the orbital inclination and longitude of the ascending node of the Earth respectively. With these definitions, the functions $\mathcal{A}, \mathcal{B}$, and C describe the secular evolution of the orbit of the Earth driven by the gravitational perturbations of the other planets. Lastly, the precession "constant"[2] α is defined as

$$\alpha = \frac{3H}{2\Omega}\left(\frac{n_{\rm M}^2 m_{\rm M}}{(1-e_{\rm M}^2)^{3/2}}\left(1 - \frac{3}{2}\sin^2 i_{\rm M}\right) + \frac{n_\odot^2 m_\odot}{(1-e_\odot^2)^{3/2}}\right), \tag{1.15}$$

where $m_{\rm M}$ and $m_\odot$ are the masses of the Moon and the Sun respectively, $n_{\rm M}$ and $n_\odot$ are their mean motions, $e_{\rm M}$ and $e_\odot$ are their orbital eccentricities, while $i_{\rm M}$ is the orbital inclination of the Moon. The Hamiltonian canonical equations $dX/dt = \partial\mathcal{H}/\partial\psi$ and $d\psi/dt = -\partial\mathcal{H}/\partial X$ would then give the precession equations in the form (Laskar, 1986; Laskar et al., 1993a,b)

$$\frac{dX}{dt} = -L\sqrt{1-(X/L)^2}\left[\mathcal{A}(t)\cos\psi - \mathcal{B}(t)\sin\psi\right], \tag{1.16}$$

$$\frac{d\psi}{dt} = \alpha\frac{X}{L} - \frac{X}{L\sqrt{1-(X/L)^2}}\left[\mathcal{A}(t)\cos\psi + \mathcal{B}(t)\sin\psi\right] - 2C(t). \tag{1.17}$$

Evidently, it is exactly within α where uncertainties in the dynamical ellipticity and the tidal history of the Earth-Moon system propagate to limit our astronomical solutions laid down by $\mathcal{H}$, specifically through the parameters H, Ω, and $n_{\rm M}$, and to a lesser degree $e_{\rm M}$ and $i_{\rm M}$ (see for e.g. Section 9.2 in Laskar et al., 2004). Moreover, the fact that the signature of the past variation of the dynamical ellipticity and the orbital parameters of the Earth-Moon system are interchangeable makes it difficult to decipher their histories in geological records. Namely, as we mentioned in the previous section, variations in the LOD can compensate for variations in H, and vice versa. This degeneracy leads to questioning the geological constraints of Pälike and

[2] as this quantity is certainly not a constant, we added the quotations to emphasize that this traditionally used description is misleading.

Shackleton (2000) and Lourens et al. (2001) described earlier, and calls for more accurate modelling of the Earth-Moon geophysical and astronomical history.

Besides the uncertainty that H imposes on the rotational solution, variations in H can force the Earth into rotational resonances. A quasi-periodic decomposition of the perturbation function $\mathcal{A}(t) + i\mathcal{B}(t)$ into N modes of amplitudes, frequencies, and phases α_k, ν_k, and ϕ_k respectively, allows us to write $\mathcal{H}$ as (Laskar and Robutel, 1993):

$$\mathcal{H} = \frac{L^2}{2C} - \frac{\alpha}{2}\frac{X^2}{L} + 2C(t)X - L\sqrt{1-(X/L)^2}\sum_{k=1}^{N}\alpha_k \sin[\nu_k t + \phi_k + \psi]. \qquad (1.18)$$

This expression is identical to the Hamiltonian of an oscillator with frequency $\alpha\cos\varepsilon_0$, perturbed by a small amplitude quasi-periodic external forcing term. A resonance is thus encountered when the Earth's precession frequency $\dot{\psi} \approx \alpha\cos\varepsilon_0 = 50.47$ arcsec/yr is equal in magnitude and opposite in sign to one of the frequencies ν_k. In fact, the quasi-periodic decomposition of $\mathcal{A}(t) + i\mathcal{B}(t)$ reveals that a periodic term of small amplitude, related to the contributions of Jupiter and Saturn and labeled $s_6 - g_6 + g_5$, is characterized by a frequency $\nu_{23} = -50.33$ arcsec/yr (Laskar et al., 1993a, 2004). This suggests that variations in the precession frequency $\dot{\psi}$, propagating from variations in the dynamical ellipticity H through the precession "constant" α, can impose a rotational resonance. This scenario was examined parametrically by Laskar et al. (1993a) who found that a perturbation in H of -0.223% relative to the present value suffices to encounter such a resonance, forcing a significant obliquity increase of about 0.5 degrees (see Figure 9 of Laskar et al. 1993a).

In the rest of this chapter, we focus on computing the variation of the dynamical ellipticity during an ice age, where cycles of glaciation and deglaciation exert a varying surface load upon the Earth's lithosphere due to the movement of water between the ice caps and the oceans. This load forces the Earth to deform by subsiding under the growing load and rebounding upon its decay. However, this deformation is constrained by re-establishing an equilibrium between the deformation of the lithosphere and the underlying mantle; a state that is classically coined as isostatic equilibrium. Thus GIA describes the process of isostatic deformation due to ice and water surface loading variation. As a result of glaciation, surface mass is transferred into the poles and the dynamical ellipticity is reduced. This direct effect of glaciation is partially compensated by the delayed effect of GIA attempting to re-balance the inertia budget. The opposite occurs during deglaciation periods.

The influence of recent glacial cycles on the dynamical ellipticity have been first addressed outside the scope of GIA using simplified models of surface loading on a rigid Earth (Berger, 1988; Thomson, 1990; Dehant et al., 1990). The results are upper bound limits that cannot be attained in the context of a realistic Earth model, but were sufficient to the community at that time. More elaborate and meticulous approaches to the problem were motivated by the analysis of Laskar et al. (1993a) suggesting the resonance crossing with Jupiter and Saturn described above. This called for a sequence of works that used climatic proxy records over the past million years to constrain the glacial surface loading and the developed theory of the viscoelastic response of the Earth (Peltier and Jiang, 1994; Mitrovica and Forte, 1995; Mitrovica et al., 1997). All studies concluded with the unlikelihood of occurrence of the resonance. The problem was recently addressed again covering the past three million years corresponding to the interval of maximum glacial volumetric loading and continental spread over the surface of the Earth (Ghelichkhan et al., 2021). We attempt in what follows to trace H over an extended period of the Cenozoic.

1.2 Viscoelastic relaxation theory

In this section, we present the theoretical and numerical recipes upon which we construct the viscoelastic structure and behavior of the Earth, along with its response to surface loading, quantified by the famous Love numbers, and leading to our computation of the dynamical ellipticity. This section can be considered as a manifestation of our evolving understanding of the problem as we undertook the first foray, a rather vigilant one, into the realm of geophysics. Thus this formulation extends a lineage of studies on the topic, and an impatient reader who is familiar with the theory can refer directly to Section 1.2.7. We based the following conspectus on the works of Peltier (1974), Peltier and Andrews (1976), Sabadini and Peltier (1981), Wu and Peltier (1982), Peltier (1985), Wu and Ni (1996), Vermeersen and Sabadini (1997a), and heavily on the carefully laid out monograph of Sabadini et al. (2016).

1.2.1 Momentum and Poisson equations

We start by describing the response of a self-gravitating planetary model to external forces. Aiming at the long time-scale processes, we can neglect inertial forces and

establish linear momentum conservation by balancing out the force per unit volume $\vec{F}$ acting on an infinitesimal element in a continuum body and the stress σ acting at the surface of the element, namely

$$\boldsymbol{\nabla} \cdot \boldsymbol{\sigma} + \vec{F} = 0, \tag{1.19}$$

where the force $\vec{F}$ can account for gravitation due to the Earth, internal loads, surface loads, tidal forces of external bodies, centrifugal effect, seismic forcing, etc... We decompose this combination of effects into a family of non-conservative forces $\vec{F}_{\mathrm{nc}}$ and a family of conservative forces $\vec{F}_{\mathrm{c}}$. The non-conservative part mostly accounts for seismic forcing, internal loads, or the effect of discontinuities in the displacement across fault planes upon earthquakes (Smylie and Mansinha, 1971). The conservative part is expressed as a gradient of the total potential ϕ:

$$\vec{F}_{\mathrm{c}} = -(\rho^{\mathrm{E}} + \rho^{\mathrm{L}})\boldsymbol{\nabla}\phi, \tag{1.20}$$

where the densities are those of the Earth, ρ^{E}, and an external load at the surface of the Earth, ρ^{L}, and the potential ϕ is the sum of all the possibly felt potentials, thus

$$\phi = \phi^{\mathrm{E}} + \phi^{\mathrm{L}} + \phi^{\mathrm{T}} + \phi^{\mathrm{C}}, \tag{1.21}$$

where ϕ^{E} is the gravitational potential of the Earth, ϕ^{L} is that of the load, ϕ^{T} is the tidal potential, and ϕ^{C} is the centrifugal potential. Each of these potentials satisfies its own Poisson equation,

$$\begin{aligned}
\boldsymbol{\nabla}^2\phi^{\mathrm{E}} &= 4\pi G\rho^{\mathrm{E}}, \\
\boldsymbol{\nabla}^2\phi^{\mathrm{L}} &= 4\pi G\rho^{\mathrm{L}}, \\
\boldsymbol{\nabla}^2\phi^{\mathrm{T}} &= 4\pi G\rho^{\mathrm{T}}, \\
\boldsymbol{\nabla}^2\phi^{\mathrm{C}} &= -2\Omega^2.
\end{aligned} \tag{1.22}$$

Here ρ^{T} is the density of the tidally forcing external object, while the centrifugal potential at a position vector $\vec{r}$ due to the Earth's rotation with angular velocity $\boldsymbol{\Omega}$ is

$$\phi^{C} = \frac{1}{2}\left[(\boldsymbol{\Omega} \cdot \vec{r})^2 - (\Omega r)^2\right]. \tag{1.23}$$

With these definitions we can construct our initial system that needs to be solved. It describes the response of the Earth, as a continuum body, to external forces using both

the momentum conservation equation Eq. (1.19) and the total Poisson equation given by

$$\nabla^2\phi = 4\pi G(\rho^{\mathrm{E}} + \rho^{\mathrm{L}} + \rho^{\mathrm{T}}) - 2\Omega^2. \tag{1.24}$$

The momentum equation should be solved over the volume of the Earth, while the Poisson equation is to be solved over full space. Adopting the Lagrangian specification of the deformation, each particle in the continuum body will be tracked by a position vector

$$\vec{r} = \vec{r}_0 + \vec{r}_1(\vec{r}_0, t). \tag{1.25}$$

Following the work of Wolf (1991), any field f under study can be decomposed into local and material incremental parts such that

$$\begin{aligned} f(\vec{r}, t) &= f_0(\vec{r}) + f^{\Delta}(\vec{r}, t), \\ f(\vec{r}, t) &= f_0(\vec{x}) + f^{\delta}(\vec{r}, t), \end{aligned} \tag{1.26}$$

where the local field f^{Δ} is the increment of the field at a certain position $\vec{r}$ with respect to the initial field f_0 at the same position. In contrast, the material field f^{δ} is the increment of the field at $\vec{r}$ with respect to the initial field at the position $\vec{x}$, the initial position of the particle before moving to $\vec{r}$. Clearly, the only difference between the two incremental fields is the difference between the initial fields evaluated at the initial and current positions of the tested particle, a difference that results in the so-called advective field

$$f^{\delta} = f^{\Delta} + \vec{r}_1 \cdot \nabla f_0. \tag{1.27}$$

To model deformation, we assume that the body is initially in a non-rotating hydrostatic equilibrium, thus the initial hydrostatic stress is expressed as

$$\boldsymbol{\sigma_0} = -p_0 \boldsymbol{I}, \tag{1.28}$$

with $\boldsymbol{I}$ being the identity tensor, and p_0 the initial hydrostatic pressure. In this state, the Poisson equation is simply

$$\nabla^2\phi_0 = 4\pi G\rho_0. \tag{1.29}$$

Enforcing momentum conservation, we get the condition for the non-rotating hydrostatic equilibrium state as

$$-\nabla p_0 - \rho_0 \nabla \phi_0 = \vec{0}. \tag{1.30}$$

Now that the initial state is fully described, we are fully geared to perturb the system by introducing stress as a material increment such that

$$\boldsymbol{\sigma}(\vec{r},t) = -p_0(\vec{x})\vec{I} + \boldsymbol{\sigma}^{\delta}(\vec{x},t). \tag{1.31}$$

On the other hand, the natural choice for the description of the potential perturbations is that of local increments; we then have:

$$\begin{aligned}\phi(\vec{r},t) &= \phi_0(\vec{t}) + \phi^{\Delta}(\vec{r},t),\\ \rho(\vec{r},t) &= \rho_0(\vec{t}) + \rho^{\Delta}(\vec{r},t).\end{aligned} \tag{1.32}$$

Substituting the perturbed quantities in the momentum and Poisson equations, then cancelling equilibrium terms while keeping first-order perturbations, we obtain the incremental momentum and Poisson equations in the form:

$$\begin{aligned}\boldsymbol{\nabla}\cdot\boldsymbol{\sigma}^{\delta} + \boldsymbol{\nabla}(\vec{r}_1\cdot\boldsymbol{\nabla}p_0) - \rho^{\Delta}\boldsymbol{\nabla}\phi_0 - \rho_0\boldsymbol{\nabla}\phi^{\Delta} - \rho^{\mathrm{L}}\boldsymbol{\nabla}\phi_0 + \vec{F}_{\mathrm{nc}} &= \vec{0},\\ \boldsymbol{\nabla}^2\phi^{\Delta} = 4\pi G(\rho^{\Delta} + \rho^{\mathrm{L}} + \rho^{\mathrm{T}}) - 2\Omega^2.\end{aligned} \tag{1.33}$$

This system describes the quasi-static limit of the perturbed momentum conservation equation in which stresses are applied over long timescales such that the system evolves in an inertia-free fashion. Each of the terms in the momentum equation is physically understood as follows:

i) The first term, $\boldsymbol{\nabla}\cdot\boldsymbol{\sigma}^{\delta}$, describes the material incremental stress as established earlier.

ii) The second term, $\boldsymbol{\nabla}(\vec{r}_1\cdot\boldsymbol{\nabla}p_0)$, accounts for the advection of the initial hydrostatic pressure (the difference between incremental and material fields (Eq. 1.27) after the initial hydrostatic equilibrium condition of Eq. (1.30) is applied at the position $\vec{r}$. It is an essential term shown by Love (1911) to be absolutely critical for the description of processes of the free elastic gravitational oscillations of the planet. As shown in Peltier and Andrews (1976), it plays a significant role in the viscoelastic field theory by ensuring that the boundary conditions on the surface of the planet are met.

iii) The third term, $\rho^{\Delta}\boldsymbol{\nabla}\phi_0$, describes buoyancy forces as a result of density changes.

iv) The fourth term, $\rho_0\boldsymbol{\nabla}\phi^{\Delta}$, describes the gravitational perturbations.

v) The fifth term, $\rho^{\mathrm{L}}\boldsymbol{\nabla}\phi_0$, accounts for the weight of the surface load.

vi) The sixth term, $\vec{F}_{\mathrm{nc}}$, accounts for the non-conservative forces.

The coupling of the momentum and Poisson equations is controlled, at first, by the self-consistency of the incremental potential ϕ^{Δ} and the incremental density ρ^{Δ}. This coupling is imposed by the continuity equation of mass

$$\rho^{\Delta} = -\boldsymbol{\nabla}\cdot(\rho_0\vec{r}_1) = -\rho_0\Delta - \vec{r}_1\cdot\boldsymbol{\nabla}\rho_0, \tag{1.34}$$

where we denote by Δ the volume changes of the particle, namely:

$$\Delta = \boldsymbol{\nabla}\cdot\vec{r}_1. \tag{1.35}$$

The first term on the right hand side of the mass continuity equation (1.34) refers to density perturbation due to volume variations of the particle, while the second term represents the advection of the initial density field. Compared to the advection effect equation, this equation ensures that

$$\rho^{\delta} = -\rho_0\Delta. \tag{1.36}$$

1.2.2 Expanding the governing system in spherical harmonics

Considering that the Earth is composed of multiple concentric layers with a central core, a single or multiple layers representing the mantle, and a lithosphere just below the surface, each layer is to be characterized by a constant value of density ρ, rigidity μ, elasticity λ, and consequently a bulk modulus κ. At the boundaries between the layers, the parameters will have a step-function like variation. We consider no lateral variations in the parameters, so all the parameters are only depth-dependent. We use a spherical reference frame with an origin at the center of the Earth and with the coordinates (r,θ,ψ) measuring respectively the radial separation form the center, the co-latitude, and the longitude, with $(\hat{\boldsymbol{r}},\hat{\boldsymbol{\theta}},\hat{\boldsymbol{\psi}})$ denoting the respective unit vectors. The three–dimensional gradient operator is defined as:

$$\boldsymbol{\nabla} = \hat{\boldsymbol{r}}\partial_r + \frac{1}{r}\boldsymbol{\nabla}_{\mathrm{s}}, \tag{1.37}$$

where the surface gradient operator $\boldsymbol{\nabla}_{\mathrm{s}}$ is expressed as:

$$\boldsymbol{\nabla}_{\mathrm{s}} = \hat{\boldsymbol{\theta}}\partial_\theta + \hat{\boldsymbol{\psi}}\frac{1}{\sin\theta}\partial_\psi. \tag{1.38}$$

The divergence of a vector $\vec{u}$ then becomes

$$\boldsymbol{\nabla}\cdot\vec{u} = \partial_r u_r + \frac{2}{r}u_r + \frac{1}{r}\partial_\theta u_\theta + \frac{\cot\theta}{r}u_\theta + \frac{1}{r\sin\theta}\partial_\psi u_\psi, \tag{1.39}$$

and the Laplacian is written as:

$$\boldsymbol{\nabla}^2 = \partial_r^2 + \frac{2}{r}\partial_r + \frac{1}{r^2}\Big(\partial_\theta^2 + \cot\theta\partial_\theta + \frac{1}{\sin^2\theta}\partial_\psi^2\Big). \tag{1.40}$$

Considering only the radial dependence of the initial density, potential, pressure, and their gradients, the incremental Poisson and momentum equations become

$$\boldsymbol{\nabla}\cdot\boldsymbol{\sigma}^\delta - \rho_0\boldsymbol{\nabla}(g\vec{r}_1\cdot\hat{\boldsymbol{r}}) + \rho_0 g\Delta\hat{\boldsymbol{r}} - \rho_0\boldsymbol{\nabla}\phi^\Delta - \rho^{\mathrm{L}}g\hat{\boldsymbol{r}} + \vec{F}_{\mathrm{nc}} = \vec{0}, \tag{1.41}$$

$$\boldsymbol{\nabla}^2\phi^\Delta = -4\pi G(\rho_0\Delta + \partial_r\rho_0\vec{r}_1\cdot\hat{\boldsymbol{r}}) + 4\pi G(\rho^{\mathrm{L}} + \rho^{\mathrm{T}}) - 2\omega^2. \tag{1.42}$$

We expand all the variables in spherical harmonics, starting with the incremental potential,

$$\phi^\Delta(r,\theta,\psi) = \sum_{lm}\Phi_{lm}(r)Y_{lm}(\theta,\psi). \tag{1.43}$$

Hereafter, we reduce the double summation $\sum_{l=0}^{\infty}\sum_{m=-l}^{l}$ to the notation $\sum_{lm}$. The displacement on the other hand is first decomposed into a sum of spheroidal displacements, $\vec{r}_{\mathrm{S}}$, and toroidal displacements, $\vec{r}_{\mathrm{T}}$, such that

$$\vec{r}_{\mathrm{S}}(\vec{r}) = \sum_{lm}U_{lm}(r)\vec{R}_{lm}(\theta,\psi) + V_{lm}(r)\vec{S}_{lm}(\theta,\psi), \tag{1.44}$$

$$\vec{r}_{\mathrm{T}}(\vec{r}) = \sum_{lm}W_{lm}(r)\vec{T}_{lm}(\theta,\psi). \tag{1.45}$$

The spherical harmonic vectors are defined as:

$$\vec{R}_{lm} = Y_{lm}\hat{\boldsymbol{r}}, \tag{1.46}$$

$$\vec{S}_{lm} = r\boldsymbol{\nabla}Y_{lm} = \partial_\theta Y_{lm}\hat{\boldsymbol{\theta}} + \frac{1}{\sin\theta}\partial_\psi Y_{lm}\hat{\boldsymbol{\psi}}, \tag{1.47}$$

$$\vec{T}_{lm} = \boldsymbol{\nabla}\times(\vec{r}Y_{lm}) = \frac{1}{\sin\theta}\partial_\psi Y_{lm}\hat{\boldsymbol{\theta}} - \partial_\theta Y_{lm}\hat{\boldsymbol{\psi}}, \tag{1.48}$$

where their coefficients $\Phi_{lm}, U_{lm}, V_{lm}$ are referred to as the potential, radial, and tangential spheroidal displacements.

1.2.3 Linear rheology and the correspondence principle

The momentum (1.41) and Poisson (1.42) equations are to be supplemented by a third constraint that relates how incremental stress and strain affect each other. We restrict our study to the linear behavior as is the common tradition (e.g., Yuen and Peltier, 1982), and we start with Hook's law,

$$\sigma_{ij} = \lambda \Delta \delta_{ij} + 2\mu \epsilon_{ij}. \tag{1.49}$$

Here we recall that σ_{ij} is the stress tensor, Δ represents the volume changes of the particle (Eq. 1.35), δ_{ij} is the Kronecker delta function, and the shear modulus μ with the elasticity λ are the two Lamé parameters. To describe the rheological behavior, it's sufficient to consider one of the Lamé parameters since the other will have similar properties. Starting with

$$\sigma_{ij} = 2\mu \epsilon_{ij}, \tag{1.50}$$

the strain tensor is defined as

$$\boldsymbol{\epsilon} = \frac{1}{2}\left[\boldsymbol{\nabla} \otimes \vec{r}_1 + (\boldsymbol{\nabla} \otimes \vec{r}_1)^T\right], \tag{1.51}$$

where $\otimes$ stands for the algebraic product. This representation in dyadic formulation is equivalent to the usual definition in terms of Cartesian components x_i expressed as

$$\epsilon_{ij} = \frac{1}{2}\left(\frac{\partial r_{1i}}{\partial x_j} + \frac{\partial r_{1j}}{\partial x_i}\right), \tag{1.52}$$

Linear rheology defines the proportionality relation between tensors and their time derivatives. For example, the rheological behavior of a particle in a continuous medium is defined by

$$\ldots + a_2 \ddot{\sigma}_{ij} + a_1 \dot{\sigma}_{ij} + a_0 \sigma_{ij} = 2\mu(b_0 \epsilon_{ij} + b_1 \dot{\epsilon}_{ij} + b_2 \ddot{\epsilon}_{ij} + \ldots), \tag{1.53}$$

where a, b are constants. We can obtain the spectral form of such equations easily by moving into the frequency domain via a Fourier or a Laplace transformation, thus we

have

$$\big(\ldots + (i\omega)^2 a_2 + (i\omega)a_1 + a_0\big)\sigma_{ij}(\omega) = 2\mu\big(\ldots + (i\omega)^2 b_2 + (i\omega)b_1 + b_0\big)\epsilon_{ij}(\omega), \quad (1.54)$$

which can be also written as:

$$\sigma_{ij}(\omega) = 2\mu(\omega)\epsilon_{ij}(\omega), \quad (1.55)$$

where

$$\mu(\omega) = \mu\frac{\ldots + (i\omega)^2 b_2 + (i\omega)b_1 + b_0}{\ldots + (i\omega)^2 a_2 + (i\omega)a_1 + a_0}\,. \quad (1.56)$$

The latter equation has the form of Hooke's law, except that the components are now functions of the frequency. If we decompose the latter equation into partial fractions as in Legros et al. (2005), we obtain

$$\mu(\omega) = \mu\left(\ldots + i\omega\alpha_1 + \alpha_2 + \sum_{n\geq 3}\frac{\alpha_n}{i\omega + \frac{1}{\tau_n}}\right), \quad (1.57)$$

where α_n is a function of τ_n. The denominator has real roots $1/\tau_n$ with reciprocals being the relaxation times of $\mu(\omega)$. As a particular case, the dependence with $\mu(\omega) = \mu$ and $\alpha_2 = 1$ gives an elastic medium obeying Hooke's law. However, if we consider the dependence

$$\mu(\omega) = \mu\alpha_1 i\omega, \quad (1.58)$$

and noting that $\mu\alpha_1$ is the viscosity η, we obtain

$$\sigma_{ij}(\omega) = 2i\eta\omega\epsilon_{ij}(\omega), \quad (1.59)$$

or in the time domain

$$\sigma_{ij}(t) = 2\eta\dot{\epsilon}_{ij}(t). \quad (1.60)$$

This equation describes the law of diffusion of velocity defining a Newtonian viscous medium. Thus we have the two elementary components for rheological behaviours that are traditionally depicted in the literature as a spring and a piston. In particular, the Maxwell body has a stress-strain relation of the form:

$$\sigma_{ij} = 2\mu\left[\frac{i\omega}{i\omega + \frac{\mu}{\eta}}\right]. \quad (1.61)$$

Evidently, a Maxwell body reduces to an inviscid fluid for infinitely small frequencies, and it becomes elastic at very large frequencies. Moreover, if the strain is described by a Heaviside step function, i.e. $\epsilon_{ij} = H(t)$, then the relaxation process of the stress takes the form:

$$\sigma_{ij}(t) = 2\mu e^{-\frac{t}{\tau}} H(t), \tag{1.62}$$

where

$$\tau = \eta/\mu \tag{1.63}$$

is the so-called Maxwell time. Thus we can describe the transition from the elastic to the Newtonian fluid limit behavior of the Earth by the timescale τ. To explore further the viscoelastic behavior of a Maxwell body, we now employ the Laplace transform between the time and frequency domains. The Laplace transform of a function of time $f(t)$ is defined by

$$\mathcal{L}[f(t)] = \int_0^\infty f(t)e^{-st}dt, \tag{1.64}$$

where s denotes the variable frequency. We denote by tilde above any function ($\tilde{f}$) its Laplace transform for brevity. Applying the Laplace transform to Eq. (1.62) and making use of the definition of the stress tensor we get

$$\boldsymbol{\sigma}^\delta(s) = \lambda\tilde{\Delta}(s)\vec{I} + 2\tilde{\mu}(s)\tilde{\boldsymbol{\epsilon}}(s), \tag{1.65}$$

where the frequency dependent rigidity is the classical Maxwellian rigidity function defined as:

$$\tilde{\mu}(s) = \frac{\mu s}{s + 1/\tau}. \tag{1.66}$$

This sums up the beauty of the correspondence principle, which was first demonstrated by Biot (1956). Comparing the stress-strain relation in the frequency domain with that in the time domain, it is evident that they both have the same form. Thus to solve for the viscoelastic response of the Earth, it suffices to solve the for elastic response in the Laplace domain and then use the inverse Laplace transform to have the time-dependent solutions.

That said, given the viscoelastic stress-strain relation of Eq. (1.65), we develop the divergence of the stress using the definition of the strain in Eq. (1.51) to obtain

$$\boldsymbol{\nabla}\cdot\boldsymbol{\sigma}^\delta = (\lambda+\mu)\boldsymbol{\nabla}\Delta + \partial_r\lambda\Delta\hat{\boldsymbol{r}} + \mu\boldsymbol{\nabla}^2\vec{r}_1 + \partial_r\mu\big(2\partial_r\vec{r}_1 + \hat{\boldsymbol{r}}\times(\boldsymbol{\nabla}\times\vec{r}_1)\big), \tag{1.67}$$

where we have used $\boldsymbol{\nabla}\mu = \partial_r\mu\hat{\boldsymbol{r}}$ and $\boldsymbol{\nabla}\lambda = \partial_r\lambda\hat{\boldsymbol{r}}$.

1.2.4 Spheroidal deformations

Now we are equipped with all the tools needed to complete describing the viscoelastic response. The volume change in this framework is decomposed into spherical harmonics, namely:

$$\Delta = \boldsymbol{\nabla} \cdot \vec{r}_1 = \sum_{lm} \chi_{lm} Y_{lm}, \tag{1.68}$$

where

$$\chi_{lm} = \partial_r U_{lm} + \frac{2}{r} U_{lm} - \frac{l(l+1)}{r} V_{lm}. \tag{1.69}$$

The components U, V are the previously defined radial and tangential spheroidal displacements. We note that the toroidal displacement does not contribute to volume changes, and it has no component along $\hat{\boldsymbol{r}}$. This means that the local incremental density is only affected by spheroidal deformations such that

$$\rho^{\Delta} = -\rho_0 \boldsymbol{\nabla} \cdot \vec{r}_S - \partial_r \rho_0 \vec{r}_S \cdot \hat{\boldsymbol{r}}. \tag{1.70}$$

Next we consider the spherical harmonic expansion of the material incremental stress acting radially on the surface, and we use the Maxwell body in the Laplace domain equation to obtain

$$\boldsymbol{\sigma}^{\delta} \cdot \hat{\boldsymbol{r}} = \lambda \Delta \hat{\boldsymbol{r}} + \mu [\boldsymbol{\nabla}(\vec{r}_1 . \hat{\boldsymbol{r}}) - (\boldsymbol{\nabla} \hat{\boldsymbol{r}}) \cdot \vec{r}_1 + (\hat{\boldsymbol{r}} \cdot \boldsymbol{\nabla}) \vec{r}_1]. \tag{1.71}$$

Substituting the spherical harmonic expansions of displacements and volume changes, we have

$$\boldsymbol{\sigma}^{\delta} \cdot \hat{\boldsymbol{r}} = \sum_{lm} \left[R_{lm} \vec{R}_{lm} + S_{lm} \vec{S}_{lm} + T_{lm} \vec{T}_{lm} \right], \tag{1.72}$$

where the spherical harmonic coefficients are defined by:

$$R_{lm} = \lambda \chi_{lm} + 2\mu \partial_r U_{lm}, \tag{1.73}$$

$$S_{lm} = \mu \left(\partial_r V_{lm} + \frac{U_{lm} - V_{lm}}{r} \right), \tag{1.74}$$

$$T_{lm} = \mu \left(\partial_r W_{lm} - \frac{W_{lm}}{r} \right), \tag{1.75}$$

and we refer to these coefficients as the radial (R_{lm}), tangential spheroidal (S_{lm}), and toroidal stresses (T_{lm}). Using the expression of the divergence of the stress in Eq. (1.67), along with the incremental material Poisson equation (Eq. 1.42), we get the following

set of equations:

$$
\begin{aligned}
&-\rho_0\partial_r\Phi_{lm} - \rho_0\partial_r(gU_{lm}) + \rho_0 g\chi_{lm} + \partial_r(\lambda\chi_{lm} + 2\mu\partial_r U_{lm}) - \rho^L_{lm} g \\
&+ \frac{\mu}{r^2}[4r\partial_r U_{lm} - 4U_{lm} + l(l+1)(3V_{lm} - U_{lm} - r\partial_r V_{lm})] + f^R_{lm} = 0,
\end{aligned} \tag{1.76}
$$

$$
\begin{aligned}
&-\frac{\rho_0}{r}gU_{lm} - \frac{\rho_0}{r}\Phi_{lm} + \frac{\lambda}{r}\chi_{lm} + \partial_r\left[\mu\left(\partial_r V_{lm} + \frac{1}{r}U_{lm} - \frac{1}{r}V_{lm}\right)\right] \\
&+ \frac{\mu}{r^2}[5U_{lm} + 3r\partial_r V_{lm} - V_{lm} - 2l(l+1)V_{lm}] + f^S_{lm} = 0,
\end{aligned} \tag{1.77}
$$

$$
\partial_r\left[\mu\left(\partial_r W_{lm} - \frac{W_{lm}}{r}\right)\right] + \mu\left(\frac{3}{r}\partial_r W_{lm} - \frac{1 + l(l+1)}{r^2}W_{lm}\right) + f^T_{lm} = 0, \tag{1.78}
$$

$$
\boldsymbol{\nabla}^2_r\Phi_{lm} = -4\pi G(\rho_0\chi_{lm} + U_{lm}\partial_r\rho_0) + 4\pi G(\rho^L_{lm} + \rho^T_{lm}). \tag{1.79}
$$

Here we have also decomposed the densities of the loads, ρ^L, and the tidal forcing body, ρ^T, along with the non-conservative forces, $\vec{F}_{\rm nc}$, into spherical harmonics. Namely,

$$
\begin{aligned}
\rho^L &= \sum_{lm}\rho^L_{lm}Y_{lm}, \\
\rho^T &= \sum_{lm}\rho^T_{lm}Y_{lm}, \\
\vec{F}_{nc} &= \sum_{lm}(f^R_{lm}\vec{R}_{lm} + f^S_{lm}\vec{S}_{lm} + f^T_{lm}\vec{T}_{lm}).
\end{aligned} \tag{1.80}
$$

From the set of decomposed equations, we can clearly notice that the radial equation (1.76), the tangential spheroidal equation (1.77), and the Poisson equation (1.79) are decoupled from the toroidal equation (1.78), and thus they can be solved separately. We also note that toroidal deformations are only driven by seismic forces, meaning that surface loading, tidal forcing, and centrifugal effects only drive spheroidal deformations. Furthermore, the $l = 0, 1$ cases would require specific treatments, and they also do not contribute to the surface loading problem at hand (Farrell, 1972; Greff-Lefftz, 2011). We exploit this decoupling of the equations to focus only on spheroidal deformations. The remaining equations (1.76,1.77, and 1.79) are re-casted into six first-order differential equations that are well suitable for numerical integration given a specific model of the Earth with certain constraints. The spheroidal 6-vector solution $\vec{y}_{lm}$ is defined as

$$
\vec{y}_{lm} = (U_{lm}, V_{lm}, R_{lm}, S_{lm}, \Phi_{lm}, Q_{lm})^T, \tag{1.81}
$$

where the first two components, U_{lm} and V_{lm} are the radial and tangential displacements, the third (R_{lm}) and the fourth (S_{lm}) are the radial and tangential stresses, the fifth (Φ_{lm}) is the potential, while the sixth (Q_{lm}) is referred to as the "potential stress" defined by

$$Q_{lm} = \partial_r \Phi_{lm} + \frac{l+1}{r}\Phi_{lm} + 4\pi G\rho_0 U_{lm}. \tag{1.82}$$

With this formulation, the system of differential equations is written in the form:

$$\frac{d\vec{y}_{lm}(r)}{dr} = \vec{A}_l(r)\vec{y}_{lm}(r) - \vec{f}_{lm}(r), \tag{1.83}$$

where $\vec{A}_l(r)$ is a 6×6 matrix given by (for $\beta = \lambda + 2\mu$):

$$\begin{bmatrix}
-\frac{2}{r}\frac{\lambda}{\beta} & \frac{l(l+1)\lambda}{r\beta} & \frac{1}{\beta} & 0 & 0 & 0 \\
-\frac{1}{r} & \frac{1}{r} & 0 & \frac{1}{\mu} & 0 & 0 \\
\frac{4}{r}\left(\frac{3\kappa\mu}{r\beta} - \rho g\right) & \frac{l(l+1)}{r}\left(\rho_0 g - \frac{6\kappa\mu}{r\beta}\right) & -\frac{4\mu}{r\beta} & \frac{l(l+1)}{r} & -\rho_0\frac{l+1}{r} & \rho_0 \\
\frac{1}{r}\left(\rho_0 g - \frac{6\kappa\mu}{r\beta}\right) & \frac{2\mu}{r^2}\left[l(l+1)(1+\frac{\lambda}{\beta}) - 1\right] & -\frac{\lambda}{r\beta} & -\frac{3}{r} & \frac{\rho_0}{r} & 0 \\
-4\pi G\rho_0 & 0 & 0 & 0 & -\frac{l+1}{r} & 1 \\
\frac{-4\pi G\rho_0(l+1)}{r} & \frac{-4\pi G\rho_0 l(l+1)}{r} & 0 & 0 & 0 & \frac{l-1}{r}
\end{bmatrix}. \tag{1.84}$$

1.2.5 Boundary conditions

Solving the above system requires radial discretization depending on the used layered model, and supplemented with proper boundary conditions at the bottom interface, between intermediate interfaces, and at the surface. Suppose we have N layers in the used model, and r_j ($j = 1..N$), moving from core to surface, are the radii at the interfaces, with r_1 being the core-mantle boundary, and r_N being the radius of the Earth. We can impose different types of boundary conditions on our system depending on the level of complexity we want to employ, and on whether we have chemical compositional differences, a compressible model, or a homogeneous incompressible model. Here

we discuss boundary conditions on the surface, on the core-mantle boundary (CMB hereafter), and on interfaces between the layers.

1.2.5.1 Core-Mantle boundary condition

We model the core as an inviscid fluid. As such, in the absence of m-dependent forcing terms, the material incremental stress reads

$$\boldsymbol{\sigma}^{\delta}(\vec{r},t) = -p^{\delta}\vec{I} = \kappa\Delta\vec{I}, \tag{1.85}$$

and the radial and tangential stresses are

$$\begin{aligned} R_l &= \kappa\chi_l, \\ S_l &= 0. \end{aligned} \tag{1.86}$$

The CMB is a free-slip boundary where the solid mantle can slip over the fluid core without tangential stresses, hence the tangential displacement is set as a constant, and the 6-vector solution (Eq. 1.81) at the boundary is written as:

$$\vec{y}(r_C^+) = \begin{pmatrix} U_l(r_C^-) \\ 0 \\ R_l(r_C^-) \\ 0 \\ \Phi_l(r_C^-) \\ Q_l(r_C^-) \end{pmatrix} + C_1 \begin{pmatrix} 0 \\ 1 \\ 0 \\ 0 \\ 0 \\ 0 \end{pmatrix}. \tag{1.87}$$

Following Wu and Peltier (1982), the fluid core can be regarded as a viscoelastic body in the Laplace domain with frequency set to zero. We thus obtain the equations for the momentum components,

$$\frac{\partial_r R_l}{\rho_0} - \partial_r(gU_l) + g\chi_l - \partial_r\Phi_l = 0, \tag{1.88}$$

$$\frac{R_l}{\rho_0} - gU_l - \Phi_l = 0, \tag{1.89}$$

where forcing terms are omitted as they do not contribute at the core. Subtracting the radial derivative of the second equation from the first equation we get

$$\frac{\kappa}{\rho^2}\left(\partial_r\rho_0 + \frac{\rho_0 g}{\kappa}\right)\chi_l. \tag{1.90}$$

Eliminating the radial displacement and the volume changes from the Poisson equation, we obtain

$$\boldsymbol{\nabla}_r^2\Phi_l = 4\pi G\partial_r\rho_0\frac{\Phi_l}{g}. \tag{1.91}$$

The solution of this second order equation ψ_l should satisfy a regularity condition at the center, namely

$$\lim_{r\longrightarrow 0} r^{-l}\psi_l(r) = 1. \tag{1.92}$$

Thus the solution should be in the form

$$\Phi_l(r) = C_2\psi_l(r), \tag{1.93}$$

with ψ_l satisfying the regularity condition around the center. Regarding the other components of the solution, the above equations for the momentum components are not linearly independent, so we restrict our attention to the radial stress such that

$$R_l = \rho_0 g\left[U_l + \left(\frac{\Phi_l}{g}\right)\right] = \rho_0 g C_3. \tag{1.94}$$

This allows us to obtain the radial displacement, U_l, and the potential stress, Q_l, in terms of the constants of integration C_2, C_3, giving us:

$$U_l = -C_2\frac{\psi_l}{g} + C_3, \tag{1.95}$$

$$Q_l = C_2 q_l + 4\pi G\rho_0 C_2, \tag{1.96}$$

with q_l defined as

$$q_l = \partial_r\psi_l + \frac{l+1}{r}\psi_l - \frac{4\pi G\rho_0}{g}\psi_l. \tag{1.97}$$

With these solutions, the spheroidal vector solution at the CMB is written as $\vec{y}_l(r_1) = \vec{I}_C\vec{C}$, where the CMB matrix I_C is defined by

$$\vec{I}_C = \begin{bmatrix} -\psi_l(r_1)/g(r_1) & 0 & 1 \\ 0 & 1 & 0 \\ 0 & 0 & g(r_1)\rho_0(r_1^-) \\ 0 & 0 & 0 \\ \psi_l(r_1) & 0 & 0 \\ q_l(r_1) & 0 & 4\pi G\rho_0(r_1^-) \end{bmatrix}. \tag{1.98}$$

1.2.5.2 Surface boundary conditions

A complete analysis of the surface boundary conditions can be found in Sabadini et al. (2016) and Vermeersen and Sabadini (1997a), and we shall only brief here the final conditions for completeness. For the forcing of interest, the tangential stress S_{lm} is zero at the Earth's surface $a = r_{\rm N} = R_{\rm E}$, while the radial and potential stresses, R_l and Q_l respectively, are constrained. The full constraints are summarized in the form

$$\vec{P}_1\vec{y}(a^-) = \vec{b}, \tag{1.99}$$

where $\vec{P}_1$ is the projector of the stresses from the 6-vector solution $\vec{y}(r)$, and $\vec{b}$ is a 3-vector defined as:

$$\vec{b} = \sigma^{\rm L}_{lm}\vec{b}^{\rm L} + \left[\Phi^{\rm T}_{lm}(a) + \Phi^{\rm C}_{lm}(a)\right]\vec{b}^{\rm T}, \tag{1.100}$$

where

$$\vec{b}^{\rm L} = \begin{pmatrix} -\dfrac{(2l+1)g(a)}{4\pi a^2} \\ 0 \\ -\dfrac{(2l+1)G}{a^2} \end{pmatrix}, \tag{1.101}$$

$$\vec{b}^{\rm T} = \begin{pmatrix} 0 \\ 0 \\ \dfrac{2l+1}{a} \end{pmatrix}. \tag{1.102}$$

1.2.6 The viscoelastic solution

The differential system of Eq. (1.83) is to be solved for each harmonic degree, except for $l = 0, 1$ as mentioned earlier, from the center of the Earth with proper boundary conditions reaching the surface. Analytical solutions are found in the literature for the component equations, mostly for a homogeneous Earth, while numerical solutions via algorithms of numerical integration are more widely applicable for layered models. The general solution of the differential system of Eq. (1.83) can be written as (e.g., Sabadini et al., 2016)

$$\vec{y}_{lm} = \vec{\Pi}_l(r, r_0)\vec{y}_0 - \int_{r_0}^{r} \vec{\Pi}_l(r, r')f_{lm}(r')dr', \tag{1.103}$$

where $\vec{y}_{lm}(r_0) = \vec{y}_0$, and $\vec{\Pi}_l$ is the so-called propagator matrix, a 6×6 matrix used for solving the spheroidal deformation system. The propagator matrix satisfies the following system:

$$\frac{d\vec{\Pi}_l(r, r')}{dr} = \vec{A}_l(r)\vec{\Pi}_l(r, r'). \tag{1.104}$$

It is noteworthy that the propagator matrix follows a continuity constraint when crossing an internal interface inside the Earth, thus allowing the continuation of integration among layers. Namely:

$$\vec{\Pi}_l(r_j^+, r') = \vec{\Pi}_l(r_j^-, r'). \tag{1.105}$$

Moreover, imposing the CMB conditions discussed earlier on the general solution, we choose to start the integration at the top of the core, thus setting $r_0 = r_C^+$ to obtain

$$\vec{y}_{lm}(r_C^+) = \vec{y}_0 = \vec{I}_C\vec{C}. \tag{1.106}$$

As such, the fill solution is re-written as

$$\vec{y}_{lm}(r) = \vec{\Pi}_l(r, r_C^+)\vec{I}_C\vec{C} - \vec{w}(r), \tag{1.107}$$

where the component $\vec{w}(r)$ is defined as

$$\vec{w}(r) = \int_{r_C^+}^{r} \vec{\Pi}_l(r, r')\vec{f}_{lm}(r')dr'. \tag{1.108}$$

The three constants of integration in the vector $\vec{C}$ are to be estimated by imposing the boundary conditions. At the surface we have

$$\vec{P}_1\vec{y}_{lm}(a) = \vec{P}_1\left[\Pi_l(a, r_C)\vec{I}_C\vec{C} - \vec{w}(a)\right] = \vec{b}. \tag{1.109}$$

Noting that only the internal loads and seismic forces contribute to the vector $\vec{w}$, we ignore this element to find our spheroidal solution, though we keep it for now to establish a general solution. Using the latter equation we write the vector of constants of integration as

$$\vec{C} = (\vec{P}_1\vec{\Pi}_l(a, r_C)\vec{I}_C)^{-1}(\vec{P}_1\vec{w}(a) + \vec{b}). \tag{1.110}$$

Hence in full generality, we write the solution of the elastic problem which determines the spheroidal deformations and the perturbations of the potential within the Earth, as well as stresses, all in response to internal loading, surface loading, tidal, centrifugal, or seismic forcing, in the form given by

$$\vec{y}_{lm}(r) = \vec{\Pi}_l(r, r_C)\vec{I}_C \left[\vec{P}_1\vec{\Pi}_l(a, r_C)\vec{I}_C\right]^{-1} \left[\vec{P}_1\vec{w}(a) + \vec{b}\right] - \vec{w}(r). \tag{1.111}$$

This general solution can be expressed analytically once we determine the CMB matrix, $\vec{I}_C$, and the propagator matrix, $\vec{\Pi}_l$. The matrix $\vec{I}_C$ is by definition required to satisfy the regularity condition for the viscoelastic solution as we approach the center of the Earth. Assuming a uniform density core, the Poisson equation inside the core (Eq. 1.91) becomes

$$\boldsymbol{\nabla}^2\psi_l = 0, \tag{1.112}$$

admitting two independent solutions such that

$$\psi_l(r) = c_1 r^l + c_2 r^{-l+1}. \tag{1.113}$$

The regularity condition eliminates the first term leaving us with the second. As such, that the quantity q_l defined in Eq. (1.97) becomes

$$q_l(r) = 2(l-1)r^{l-1}. \tag{1.114}$$

Hence in the case of a homogeneous core, the general form of the CMB matrix in Eq. (1.98) is rewritten as

$$\vec{I}_C = \begin{bmatrix} -r^l/g(r_C) & 0 & 1 \\ 0 & 1 & 0 \\ 0 & 0 & g(r_C)\rho_0(r_C) \\ 0 & 0 & 0 \\ r^l & 0 & 0 \\ 2(l-1)r^{l-1} & 0 & 4\pi G\rho_0(r_C) \end{bmatrix}. \tag{1.115}$$

To find the propagator matrices, we discretize the governing differential equation (1.83) over the radially separated layers. It thus becomes

$$\frac{d\vec{y}_l(r)}{dr} = \vec{A}_l(r)\vec{y}_l(r) \qquad \text{for} \qquad r_{j-1} < r < r_j, \tag{1.116}$$

with the proposed solution

$$\vec{y}_l(r) = \vec{Y}_l(r)\vec{C} \qquad \text{for} \qquad r_{j-1} < r < r_j. \tag{1.117}$$

Here we denote by $\vec{Y}_l$ the fundamental 6×6 matrix whose columns are independent solutions of the spheroidal homogeneous differential system in the j^{th} layer, and by $\vec{C}$ the vector of integration constants. We also note that we have dropped the toroidal effects associated with internal forcing terms, and we focused on the spheroidal system. This allows us to re-write the propagator matrix of the j^{th} layer in the form

$$\vec{\Pi}_l(r, r') = \vec{Y}_l(r)\vec{Y}_l^{-1}(r') \qquad \text{for} \qquad r_{j-1} < r, r' < r_j, \tag{1.118}$$

where r, r' are in the same layer. Otherwise, when r, r' belong to different layers, the propagator matrix is to be obtained by the continuity equation of the solution across interfaces expressed as $\vec{y}_l(r_j^+) = \vec{y}_l(r_j^-)$. This gives us

$$\vec{\Pi}_l(r, r') = \vec{\Pi}_l(r, r_j)\left[\prod_{k=i+1}^{j} \Pi_l(r_k, r_{k-1})\right]\Pi_l(r_i, r'), \tag{1.119}$$

moving across the k^{th} layer between the i^{th} and j^{th} layers with $j > i$. To complete this analytical endeavour, we still need the matrix of linearly independent solutions $\vec{Y}_l(r)$. The analytical expression of this matrix was first obtained by Sabadini et al. (1982) and Wu and Peltier (1982), and it included three regular and three singular solutions at the

Earth's center. Both parts are given by

$$\vec{Y}_l(r) = \begin{pmatrix} \frac{lr^{l+1}}{2(2l+3)} & r^{l-1} & 0 \\ \frac{(l+3)r^{l+1}}{2(2l+3)(l+1)} & \frac{r^{l-1}}{l} & 0 \\ \frac{(l\rho_0 gr + 2(l^2-l-3)\mu)r^l}{2(2l+3)} & (\rho_0 gr + 2(l-1)\mu)r^{l-2} & \rho_0 r^l \\ \frac{l(l+2)\mu r^l}{(2l+3)(l+1)} & \frac{2(l-1)\mu r^{l-2}}{l} & 0 \\ 0 & 0 & r^l \\ \frac{2\pi G\rho_0 l r^{l+1}}{2l+3} & 4\pi G\rho_0 r^{l-1} & (2l+1)r^{l-1} \end{pmatrix}$$

$$\begin{pmatrix} \frac{(l+1)r^{-l}}{2(2l-1)} & r^{-l-2} & 0 \\ \frac{(2-l)r^{-l}}{2l(2l-1)} & -\frac{r^{-l-2}}{l+1} & 0 \\ \frac{(l+1)\rho_0 gr - 2(l^2+3l-l)\mu}{2(2l-1)r^{l+1}} & \frac{(\rho_0 gr - 2(l+2)\mu)}{r^{l+3}} & \frac{\rho_0}{r^{l+1}} \\ \frac{(l^2-1)\mu}{l(2l-1)r^{l+1}} & \frac{2(l+2)\mu}{(l+1)r^{l+3}} & 0 \\ 0 & 0 & \frac{1}{r^{l+1}} \\ \frac{2\pi G\rho_0(l+1)}{(2l-1)r^l} & \frac{4\pi G\rho_0}{r^{l+2}} & 0 \end{pmatrix}. \quad (1.120)$$

We recall that this fundamental matrix represents solutions for the incompressible case, i.e. solutions of the differential system of Eq. (1.83) where in the limit of $\kappa \to \infty$. The construction of the propagator matrix requires also the inverse of the fundamental matrix $\vec{Y}_l(r)$. The analytical expression was obtained by Spada et al. (1991, 1992), and we denote it by $\vec{\bar{Y}}_l(r)$. The latter satisfies:

$$\vec{Y}_l(r) = \vec{D}_l(r)\vec{\bar{Y}}_l(r), \quad (1.121)$$

where $\vec{D}_l(r)$ is a diagonal matrix defined as:

$$\mathrm{Diag}[\vec{D}_l(r)] = \frac{1}{(2l+1)}\left(\frac{l+1}{r^{l+1}}, \frac{l(l+1)}{2(2l-1)r^{l-1}}, -\frac{1}{r^{l-1}}, lr^l, \frac{l(l+1)}{2(2l+3)}r^{l+2}, r^{l+1}\right). \tag{1.122}$$

After tedious, but straightforward manipulation, the matrix $\bar{\bar{Y}}_l(r)$ is expressed as

$$\bar{\bar{Y}}_l(r) = \begin{pmatrix} \frac{\rho g r}{\mu} - 2(l+2) & 2l(l+2) & -\frac{r}{\mu} & \frac{lr}{\mu} & \frac{\rho r}{\mu} & 0 \\ -\frac{\rho g r}{\mu} + \frac{2(l^2+3l-1)}{l+1} & -2(l^2-1) & \frac{r}{\mu} & \frac{(2-l)r}{\mu} & -\frac{\rho r}{\mu} & 0 \\ 4\pi G\rho & 0 & 0 & 0 & 0 & -1 \\ \frac{r}{\mu} + 2(l-1) & 2(l^2-1) & -\frac{r}{\mu} & -\frac{(l+1)r}{\mu} & \frac{\rho r}{\mu} & 0 \\ -\frac{\rho g r}{\mu} - \frac{2(l^2-l-3)}{l} & -2l(l+2) & \frac{r}{\mu} & \frac{(l+3)r}{\mu} & -\frac{\rho r}{\mu} & 0 \\ 4\pi G\rho r & 0 & 0 & 0 & 2l+1 & -r \end{pmatrix}. \tag{1.123}$$

1.2.7 Loading Love numbers and model stratification

Considering the general solution of Eq. (1.81), we denote by $\vec{K}_{lm}$ the 3-vector containing only the displacements and local incremental potential defined as

$$\vec{K}_{lm}(a) = \vec{P}_2\vec{y}_{lm}(a) = \vec{B}_l(a)\left[\vec{P}_1\vec{w}(a) + \vec{b}\right] - \vec{P}_2\vec{w}(a), \tag{1.124}$$

where the second projection matrix $\vec{P}_2$ projects the displacement components, and we have defined:

$$\vec{B}_l(a) = \vec{P}_2\vec{\Pi}(r, r_C)\vec{I}_C\left[\vec{P}_1\vec{\Pi}_l(a, r_C)\vec{I}_C\right]^{-1}. \tag{1.125}$$

We recall that $\vec{w}(a)$ vanishes if we neglect internal loading and only consider surface, tidal, or centrifugal effects, as is the focus of our study here. The Love numbers are defined via non-dimensional Green functions (Peltier, 1974) that relate the displacements 3-vector $\vec{K}_{lm}$ to the perturbations that caused it, namely

$$\vec{K}_{lm}(a) = \vec{N}_{\mathrm{L}}\int_{r_{\mathrm{C}}}^{a}\vec{k}_l^L(r)\delta(r-a)\sigma_{lm}^{\mathrm{L}}dr + \vec{N}_{\mathrm{T}}\vec{k}^{\mathrm{T}}\left[\Phi_{lm}^{\mathrm{T}}(a) + \Phi_{lm}^{\mathrm{C}}(a)\right], \tag{1.126}$$

where $\vec{k}^{\mathrm{L}}$ and $\vec{k}^{\mathrm{T}}$ denote the load and tidal Green functions respectively, and we have also defined

$$\vec{N}_{\mathrm{L}} = \frac{G}{a}\,\mathrm{Diag}\left[\frac{1}{g(a)}, \frac{1}{g(a)}, 1\right],$$
$$\vec{N}_{\mathrm{T}} = \mathrm{Diag}\left[\frac{1}{g(a)}, \frac{1}{g(a)}, 1\right]. \tag{1.127}$$

With these definitions, the Green functions are expressed as

$$\vec{k}_l^{\mathrm{L}}(a) = \vec{N}_{\mathrm{L}}^{-1}\vec{B}_l(a)\vec{b}^{\mathrm{L}}, \tag{1.128}$$

$$\vec{k}_l^{\mathrm{T}}(a) = \vec{N}_{\mathrm{T}}^{-1}\vec{B}_l(a)\vec{b}^{\mathrm{T}}. \tag{1.129}$$

These Green functions have three components corresponding to radial, tangential, and gravitational proportionality functions between the perturbations and their responses, and they are denoted by h_l, l_l, k_l respectively such that

$$\vec{k}_l^{\mathrm{L}}(a) = \begin{pmatrix} h_l^{\mathrm{L}}(a) \\ l_l^{\mathrm{L}}(a) \\ 1 + k_l^{\mathrm{L}}(a) \end{pmatrix}. \tag{1.130}$$

The correspondence principle allows the transition into the viscoelastic framework via two steps: First, we take the same form of the solution in the frequency domain instead of the time domain, i.e., we replace the shear modulus $\mu(t)$ by $\mu(s)$ as defined in Eq. (1.66) to obtain

$$\tilde{\vec{k}}^{\mathrm{L}}(a,s) = \mathcal{L}\left[\vec{k}^{\mathrm{L}}(a,t)\right] = \vec{N}_{\mathrm{L}}^{-1}\vec{B}_l(a)\vec{b}^{\mathrm{L}}|_{\mu=\hat{\mu}(s)}. \tag{1.131}$$

Next, we perform an inverse Laplace transform[3] on the viscoelastic solution to obtain it in the time domain. This gives

$$\vec{k}^{\mathrm{L}}(t) = \mathcal{L}^{-1}\left[\tilde{\vec{k}}^{\mathrm{L}}(s)\right] = \frac{1}{2\pi i}\int_{c-i\infty}^{c+i\infty} \tilde{\vec{k}}^{\mathrm{L}}(s)e^{st}ds, \tag{1.132}$$

where a decision has to be made on the real constant c such that all the singularities of the integrand are on one side of the line going from $c - i\infty$ to $c + i\infty$. This leads us to a contour integration over the half-circle C_{R}:

$$\vec{k}^{\mathrm{L}}(t) = -\frac{1}{2\pi i}\lim_{R\to\infty}\int_{C_{\mathrm{R}}} \tilde{\vec{k}}^{\mathrm{L}}(s)e^{st}ds + \frac{1}{2\pi i}\int_{\Gamma} \tilde{\vec{k}}^{\mathrm{L}}(s)e^{st}ds, \tag{1.133}$$

[3]For the inverse Laplace transform, we use the Mellin's inverse formula, or the Bromwich integral defined as: $f(t) = \frac{1}{2\pi i}\int_{c-i\infty}^{c+i\infty} F(s)e^{st}ds$ (see Chapter 15 of Boas, 2006).

where the closed contour Γ contains all the singularities. We note that the limit of Eq. (1.131) for $|s| \to \infty$ converges to the elastic Green function $\vec{k}_{\rm E}^{\rm L}$ because the limit of $\tilde{\mu}(s)$ for $|s| \to \infty$ converges to the shear modulus μ. It is thus straightforward to show that the first term yields $\vec{k}_{\rm E}^{\rm L}\delta(t)$, and thus we have

$$\vec{k}^{\rm L}(t) = \vec{k}_{\rm E}^{\rm L}\delta(t) + \frac{1}{2\pi i}\int_{\Gamma}\tilde{\vec{k}}^{\rm L}(s)e^{st}ds. \tag{1.134}$$

The remaining problem for us is finding the singularities in the integral part of Eq. (1.134). A complete discussion on the physical origins of these singularities can be found in Cambiotti et al. (2009, 2010). Briefly, it has been shown that these singularities arise from two sources: *i)* the differential system of the propagator matrix being non–uniformly Lipschitzian, and this occurs when $s = 0$, $s = -\tau_{\rm M}^{-1}$ (Eq. 1.63), and for $s = \tau_{\rm M}\left(1 + \frac{4\mu}{3\kappa}\right)$; *ii)* the second source emerges from the constants of integration determined via the boundary conditions. The inverse of the matrix $\left[\vec{P}_1\vec{\Pi}_l(a,r)\vec{I}_C\right]|_{\mu=\hat{\mu}(s)}$ is singular for some values of the frequency. Thus the matrix $\vec{B}_l(r)$ can be re-written as

$$\vec{B}_l(r)|_{\mu=\hat{\mu}(s)} = \frac{\left[\vec{P}_2\vec{\Pi}_l(r,r_C)\vec{I}_C\right]\left[\vec{P}_1\vec{\Pi}_l(a,r)\vec{I}_C\right]^{\dagger}}{D(s)}, \tag{1.135}$$

where $D(s)$ is the so-called secular determinant defined as

$$D(s) = \det\left(\vec{P}_1\vec{\Pi}_l(a,r)\vec{I}_C\right)\Big|_{\mu=\hat{\mu}(s)}. \tag{1.136}$$

With this definition, the singularities would occur at the solutions of the secular equation

$$D(s) = 0. \tag{1.137}$$

It has been established that the solutions of the secular equation are real, finite, or at most infinite denumerable, and they are first-order roots (Tanaka et al., 2006). This implies that the Love numbers in the Laplace domain have first order poles at these roots, and each root contributes to the complex integration along the closed contour which appears in Eq. (1.134) as

$$\oint_{\Gamma_j}\tilde{\vec{k}}^{\rm L}(s)e^{st} = \vec{k}_j^{\rm L}e^{s_j t}, \tag{1.138}$$

where s_j and Γ_j denote the $j^{\rm th}$ root and the closed path containing the roots respectively, while $\vec{k}_j^{\rm L}$ are the residues. According to the residue theorem[4], these residues are

[4]The Cauchy residue theorem states that if a function $f(s)$ is analytical over a domain D, except for a number of distinguishable and isolated singularities, the integral of $f(s)$ over a curve Γ inside D, such

computed by

$$\vec{k}_j^{\mathrm{L}} = \lim_{s \to s_j} (s - s_j)\vec{k}^{\mathrm{L}}(s). \tag{1.139}$$

Each root is associated with a response of the viscoelastic model of the Earth model to the perturbation, and the set of the roots are referred to as the normal modes of the Earth with relaxation times τ_j. For simple layered incompressible models, the total number of normal modes is finite and can be determined as follows:

i) A buoyancy mode, labeled $\boldsymbol{M_i}$, emerges for density variations between adjacent viscoelastic layers. Two additional relaxation modes are triggered if the Maxwell times of both sides are different. The latter are called transient viscoelastic modes, with relatively short time-scales, and are denoted by $\boldsymbol{T_i}$ and $\boldsymbol{T_i^-}$.

ii) If one side of the layers interface is elastic, while the other is viscoelastic – which is the case in traditional Earth models between the uppermost viscoelastic mantle layer and the elastic Lithosphere – one buoyancy mode and one transient mode are triggered, and they are labelled as $\boldsymbol{M0}$ and $\boldsymbol{L0}$ respectively.

iii) The CMB contributes with one buoyancy mode labelled $\boldsymbol{C0}$

In what follows, we implement the recipe detailed thus far to compute the Love numbers for various Earth models. The most widely used spherically symmetric Earth model of physical parameters is the Preliminary Reference Earth Model, PREM (Dziewonski and Anderson, 1981), specifying the material parameters of the Earth's interior in terms of polynomials of the radial distance from the Earth's center. We consider an averaged-PREM model, which discretizes the material properties of the PREM model into layers with uniform values of all the parameters. In the models we use we shall consider an elastic Lithosphere, an inviscid core with no differentiation between the inner core and the outer core, and N_V viscoelastic layers in-between the core and the lithosphere. Regardless of the layering configuration we choose, we abide by the discontinuities that are clearly present in PREM. For example, in Table 1.1 we describe an 11-layer (11-L) model. The model is characterized by an elastic lithosphere of thickness $L = 120$ km; two shallow viscoelastic upper mantle layers, the first ending at depth $r = 220$ km, where the PREM shows the first density discontinuity, while the second ends at depth $r = 400$ km, the position of another discontinuity; then follows a transition zone that ends at depth $r = 670$ km, the major density discontinuity of the PREM. Six viscoelastic layers

that Γ does not pass through any of the singularities, is equal to $2\pi i$ times the sum of the residues of the singularities of $f(s)$ internal to the curve Γ (see e.g., Chapter 14 of Boas, 2006)

constitute the lower mantle, each with thickness around 370 km. Finally, we have the fluid core (Table 1.1).

We adopt the viscosity profile from Lau et al. (2016b), in which the authors constrain the mean of the upper mantle viscosity to $\approx 3\times10^{20}$ Pa s, the top 1500 km of the mantle to $\approx 10^{21}$ Pa s, and the mean lower mantle viscosity to around $\approx 5\times10^{21}$ Pa s. This profile is then volume averaged over any required layered model. For example, for the 11-L, the discretization is described in Table 1.1 and plotted in Figure 1.2.

Layer	Δr (km)	r (km)	ρ (kg/m^3)	μ (10^{11}N/m^2)	η (Pa.s)
Core-1	3480	0-3480	10932	0	0
LM-1	370.17	3480-3850.17	5436	2.82	3.11×10^{22}
LM-2	370.17	3850.17-4220.33	5252	2.61	2.81×10^{22}
LM-3	370.17	4220.33- 4590.50	5077	2.41	1.28×10^{22}
LM-4	370.17	4590.50-4960.67	4893	2.21	1.61×10^{21}
LM-5	370.17	4960.67-5330.83	4673	1.97	6.01×10^{20}
LM-6	370.17	5330.83-5701.00	4474	1.74	1.38×10^{21}
Trans.	270	5701.00-5971.00	3858	1.06	3.67×10^{21}
UM-1	180	5971.00-6151.00	3476	0.76	1.37×10^{20}
UM-2	100	6151.00-6251.00	3367	0.66	1.51×10^{21}
L-11	120	6251.00-6371.00	3234	0.61	0

TABLE 1.1: Parameters of our standard 11-layer volume averaged Earth model. For each layer of thickness Δr (second column), the radial boundaries are identified in the third column, while the constant density ρ, shear modulus μ, and viscosity η are identified in the third, fourth, and fifth columns respectively. The material parameters are derived from the PREM. The viscosity profile is adopted from Lau et al. (2016b). Variations are plotted in Figure1.2.

After prescribing the model, we numerically implement the analytical recipe detailed above. We start with a consistency check for our numerical code, computing the relaxation times for a specific model. In Figure 1.3, we plot the relaxation times of the normal modes as a function of the harmonic degree l going from $l = 2$ to $l = 100$, and we use a 9-L incompressible model with 7 viscoelastic layers. For this model, we expect 21 normal modes as follows:

i) The CMB will give rise to the mode $\boldsymbol{C0}$.

ii) The upper mantle/lithosphere boundary will give rise to two modes $\boldsymbol{L0}$ and $\boldsymbol{M0}$.

iii) Each of the 6 interfaces of the 7 viscoelastic layers will give rise to one buoyancy mode $\boldsymbol{M_i}$ and two transient modes $\boldsymbol{T_i}$ and $\boldsymbol{T_i^-}$, thus 18 modes.

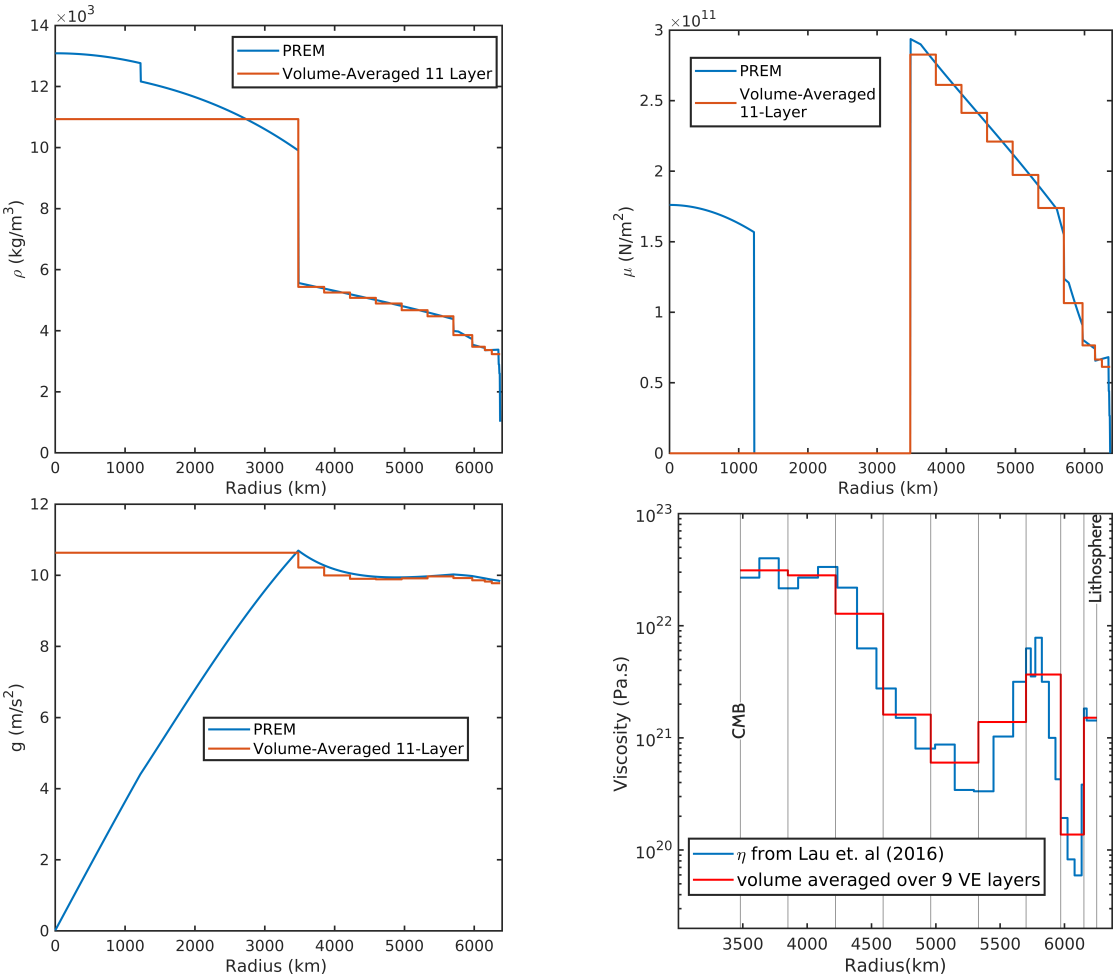

FIGURE 1.2: Radial profiles of the used Earth model. PREM profiles are plotted, and on top of them are the PREM-volume averaged density, shear modulus, and calculated gravitational acceleration for the used 11-layer model. Known discontinuities are respected in the layering, especially at 420 and 670 km of depth. Numerical values are presented in Table.1.1. The last panel shows the radial Viscosity profile adopted from Lau et al. (2016b), inferred from non-linear inversion of GIA observables. In Red we averaged their data over our 11-layered model (9 viscoelastic layers).

All of these modes were successfully captured by our code. The slowest modes are the buoyancy modes triggered between viscoelastic layers, and they range between $\tau_{M1} \approx 10^2$ kyr and $\tau_{M6} \approx 10^6$ kyr for small harmonic orders. The CMB triggered normal mode features a relaxation time τ_{C0} ranging between 10 and 100 kyr, while the modes triggered by density and rheological discrepancies between the mantle and the lithosphere feature smaller relaxation times on the order of less than one to few kyr.

The spectrum portrayed in Figure 1.3 is consistent with classic studies of viscoelastic relaxation (Sabadini et al., 2016). We therefore shift to study the effect of layering on the relaxation spectrum. In Figure 1.4, we plot the secular determinant as a function of the frequency for different layering models labelled N-L, and for different harmonic

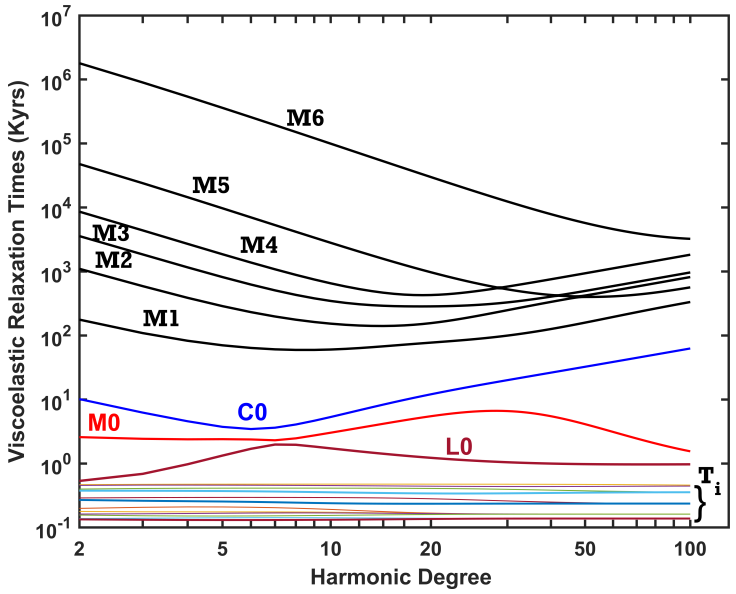

FIGURE 1.3: Relaxation times τ_i in kyr for the 9-L model as a function of the harmonic degree going from $l = 2$ to $l = 100$.

degrees. In particular, we do so for 4 models: 5-L, 9-L, 11-L, and 14-L. As expected, increasing the level of the model stratification naturally increases the number of normal modes, abiding by the analytical rules detailed above. A notable feature of all the used models is the relative stability of the transient modes when increasing the harmonic order, which can be also seen in Figure 1.3. This is evident when comparing the transient modes to the buoyancy modes, which compactify on the spectrum when we increase the harmonic order. When increasing the layering complexity, the secular determinant starts to feature a worrying erratic behavior at very small frequencies. This hinders root finding algorithms from determining the normal modes. A similar effect was observed in Spada and Boschi (2006), but for increasing the harmonic order. However, for the purpose of our dynamical ellipticity computations (associated with $l = 2$), we are not concerned with high harmonic orders, thus we focus next on the effect of increasing the layering. We do so by computing the Love numbers, starting with Eq. (1.134), where the normal modes enter as in Eq. (1.138). The explicit form of the Love numbers is written as (Peltier, 1974):

$$\begin{pmatrix} h_l \\ l_l \\ k_l \end{pmatrix}(s) = \begin{pmatrix} h_l \\ l_l \\ k_l \end{pmatrix}^{\mathrm{E}} + \sum_{j=1}^{N} \frac{1}{s - s_{lj}} \begin{pmatrix} h_{lj} \\ l_{lj} \\ k_{lj} \end{pmatrix}^{\mathrm{VE}} , \tag{1.140}$$

where the superscript E denotes the elastic component of the Love numbers, which, independent of the viscosity profile, describes the response of the Earth in the limit of

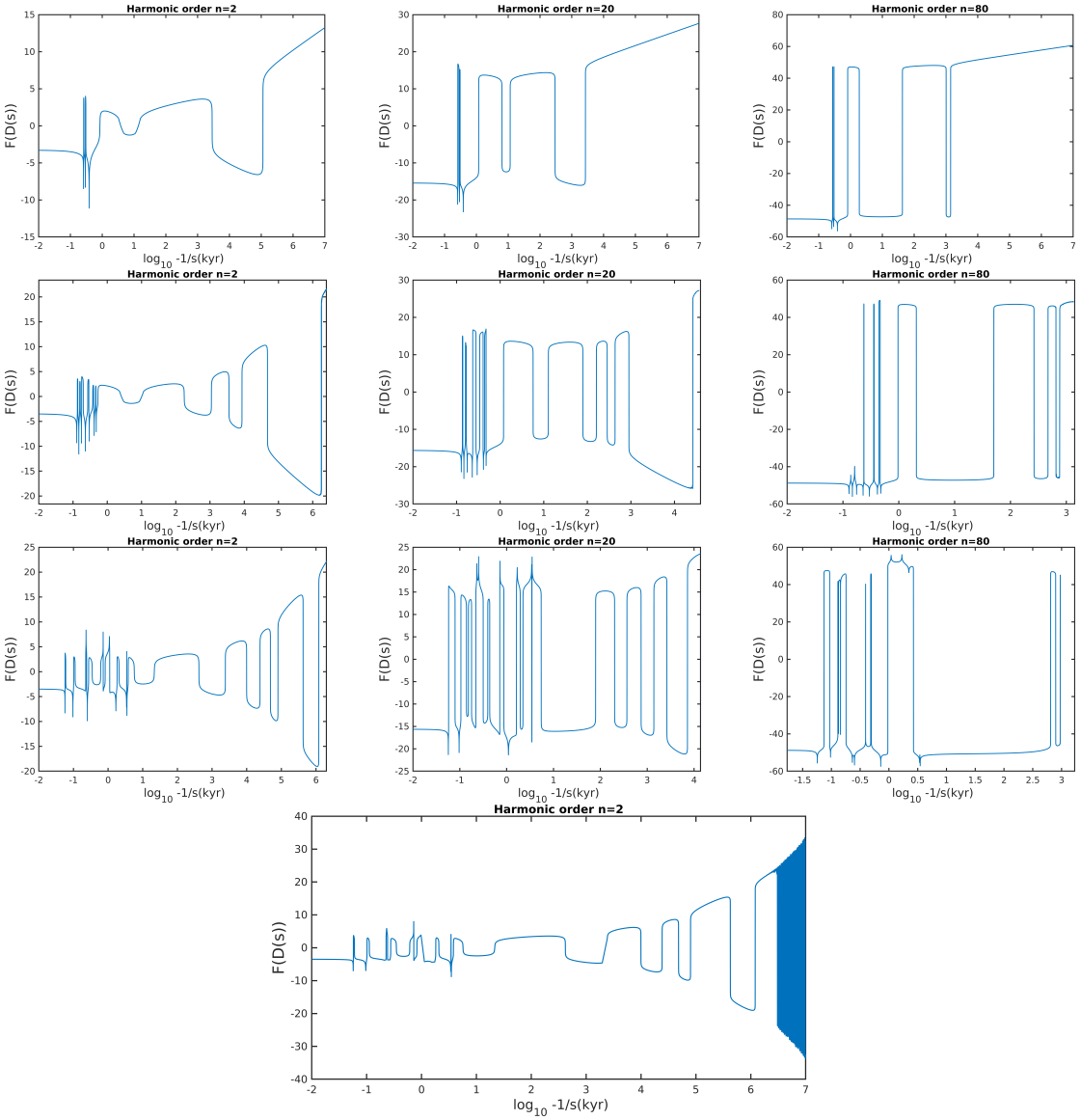

FIGURE 1.4: The secular determinant (1.136) computed for different harmonic degrees and different layering models. The y-axis represents a function of the secular determinant that is chosen as $F(D(s)) = \text{sign}(D(s)) \times \log_{10}|D(s)|$ if $|D(s)| > 10$ and $F(D(s)) = D(s)/10$ if $|D(s)| < 10$. Each row corresponds to a specific layering model where the first corresponds to a 5L model with 3-viscoelastic layers, the second refers to a 9L model, the third refers to 11L, while the fourth refers to 14L model. Each column represents a harmonic degree going left to right: $l = 2, 20, 80$.

infinite frequency or instantaneous time. On the other hand, the superscript VE denotes the viscous residues, which are dependent on the chosen viscosity profile, and they describe the relaxation spectrum. Finally, s_{lj} are the harmonic dependent normal modes described above. In the time domain we have:

$$\begin{pmatrix} h_l \\ l_l \\ k_l \end{pmatrix}(t) = \begin{pmatrix} h_l \\ l_l \\ k_l \end{pmatrix}^{\mathrm{E}} \delta(t) + \sum_{j=1}^{N} e^{s_{lj}t} \begin{pmatrix} h_{lj} \\ l_{lj} \\ k_{lj} \end{pmatrix}^{\mathrm{VE}} . \tag{1.141}$$

For the fluid limit of the Love numbers (Vermeersen and Sabadini, 1997b), we obtain:

$$\begin{pmatrix} h_l \\ l_l \\ k_l \end{pmatrix}^{\mathrm{F}} = \lim_{t\to\infty} \begin{pmatrix} h_l \\ l_l \\ k_l \end{pmatrix}(t) = \begin{pmatrix} h_l \\ l_l \\ k_l \end{pmatrix}^{\mathrm{E}} - \sum_{j=1}^{N} \frac{1}{s_{lj}} \begin{pmatrix} h_{lj} \\ l_{lj} \\ k_{lj} \end{pmatrix}^{\mathrm{VE}} . \tag{1.142}$$

The time dependent loading Love numbers can now be computed as the convolution between the Love numbers of Eq. (1.141), and the function $f(t)$ describing the temporal variation of the surface load:

$$\begin{pmatrix} h_l \\ l_l \\ k_l \end{pmatrix}^{\mathrm{L}} (t) = \begin{pmatrix} h_l(t) \\ l_l(t) \\ \delta(t) + k_l(t) \end{pmatrix} \otimes f(t). \tag{1.143}$$

For a Heaviside loading function of the form

$$f(t) = H(t), \tag{1.144}$$

the convolution is written as:

$$\begin{pmatrix} h_l \\ l_l \\ k_l \end{pmatrix}^{\mathrm{L}} (t) = H(t) \begin{pmatrix} h_l \\ l_l \\ k_l \end{pmatrix}^{\mathrm{F}} + H(t) \sum_{j=1}^{N} \frac{1}{s_{lj}} \begin{pmatrix} h_{lj} \\ l_{lj} \\ k_{lj} \end{pmatrix}^{\mathrm{VE}} e^{s_{lj}t}. \tag{1.145}$$

In Figures 1.5 and 1.6, we summarize the variation of the viscoelastic relaxation spectra for an increasing level of stratification in terms of the Love numbers and the relaxation times respectively. As before, the radial viscosity profile was adopted from the joint nonlinear inversions in Lau et al. (2016b), and volume averaged over the needed number of layers. For the Love numbers, the elastic limit is identical for the radial and transverse displacement parts h_2^{L} and l_2^{L}, while the signature of different layering can be identified in

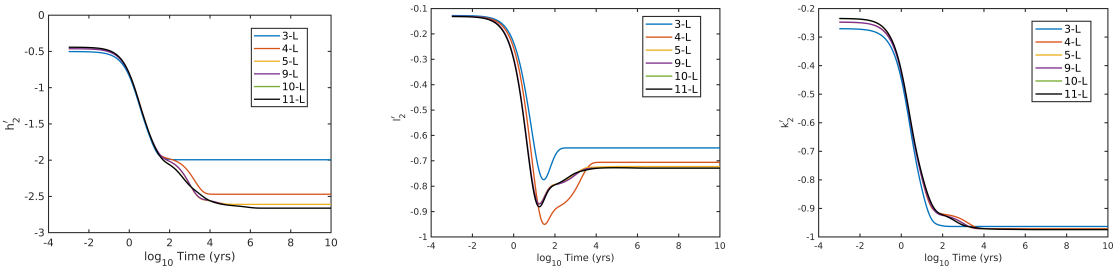

FIGURE 1.5: Time evolution of the three load Love numbers: The radial, tangential, and the gravitational, convoluted with the Heaviside step function, going as a function of time from the elastic limit to the fluid limit. The plots in each figure refer to a certain model of the Earth, going from simple stratification into more layering. All models used are PREM averaged and maintaining same viscosity profile. The convergence of the evolution of the Love numbers as we increase stratification is clear.

the elastic limit of k_2^{L}. In contrast, the fluid limit of k_2^{L} is identical when different layering is adopted, while the fluid limit of h_2^{L} and l_2^{L} clearly diverges. Transitioning between the limits, and around the timescales of relevance to our work, those corresponding to GIA, the three Love numbers exhibit clear discrepancies for different layering models, courtesy of the varying viscous residues. The latter is explored further in Figure 1.6. The $C0$, $L0$, and $M0$ modes, associated with the core-mantle and mantle-lithosphere boundaries, are of strongest viscous amplitudes (depicted by thickness), and converge towards constant values for a number of viscoelastic layers as small as three. With each added viscoelastic interface, a buoyancy mode M_i and a transient doublet $T_i^{\pm}$ emerge, though these modes feature viscous amplitudes that decay as i increases. This explains the discrepancies obtained in Figure 1.5, and proves the a larger number of viscoelastic layers (typically larger than 8) is not required to capture the essential viscoelastic response of the Earth, as the modes of strongest amplitudes converge fast enough with stratification. We proceed with a model of nine viscoelastic layers in the mantle, i.e., the 11-L model, for which the relaxation spectrum is detailed in Table 1.2.

Now that the viscoelastic response of the Earth is modelled, we move to quantify the surface loading perturbation. The variation of the latter features an intricate interplay between the ice caps and the oceans. We expand on this in the framework of the sea level variation theory.

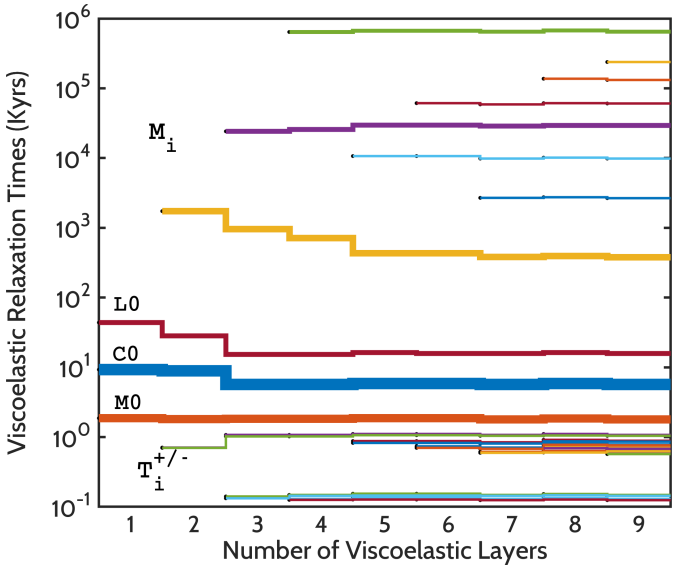

FIGURE 1.6: Viscoelastic relaxation times, $\tau_i = -1/s_i$, of harmonic degree $l = 2$ computed in the normal modes theory formalism, for an increasing stratification of the Earth's model. Zeroth modes are associated with the boundaries of the mantle with the core and the lithosphere. Buoyancy modes, M_i, and transient doublets, T_i, emerge at each added interface between viscoelastic layers, however, their contribution to the multi-exponential form (Eq. 1.141) decays with increasing layering. The labelling of modes is based upon the shear kernels derived on the basis of a viscoelastic extension of Rayleigh's elastic variational principle Peltier and Andrews (1976). The strength of each mode is indicated by its thickness. The partitioning of the viscoelastic layers is consistent with the detected seismological discontinuities of the PREM model.

1.3 Sea level variation theory

Changes of water volume in the oceans, along with changes in the volume of the ocean basins themselves drive sea level variation over a continuum of time scales that spans $10^{-3} \sim 10^{8}$ yr. On the longer timescale end of the spectrum, sea level variability is dominated by basin geometry and topography changes driven by tectonic plates (e.g., Douglas, 1991), sea floor spreading (e.g., Hays and Pitman, 1973), land erosion and consequently sedimentary transport into the oceans (Dalca et al., 2013), continental collisions and the subsequent compression of the continental areal extent (e.g., Van Andel, 1994), and mantle convection (e.g., Gurnis, 1990; Moucha et al., 2008).

Of interest to us here are variations over thousands to hundreds of thousands of years associated with surface mass distribution during glacial cycles, which result in the viscoelastic response of the solid Earth described in the previous section, and the consequent change in sea level as the planet isostatically compensates the effect of the

Mode	s (kyr^{-1})	k_2 VE-Residue (kyr^{-1})	Relaxation Time (kyr)
M8	-5.55×10^{-7}	-1.36×10^{-11}	1.80×10^{6}
M7	-1.62×10^{-5}	-3.25×10^{-8}	6.16×10^{4}
M6	-2.33×10^{-5}	-3.04×10^{-8}	4.29×10^{4}
M5	-4.03×10^{-5}	-5.58×10^{-8}	2.48×10^{4}
M4	-9.67×10^{-5}	-1.75×10^{-7}	1.03×10^{4}
M3	-2.98×10^{-4}	-2.37×10^{-6}	3.35×10^{3}
M2	-9.74×10^{-4}	-1.70×10^{-5}	1.03×10^{3}
M1	-0.0059	-1.90×10^{-5}	169.67
C0	-0.1018	-8.70×10^{-4}	9.816
L0	-0.4022	-0.1305	2.486
M0	-1.9183	-0.3427	0.521
T1	-2.1397	-0.0168	0.467
T2	-2.2153	-0.1093	0.451
T3	-2.5193	-0.0640	0.397
T4	-2.6987	-0.1290	0.370
T5	-3.4777	-0.0439	0.287
T6	-3.7364	-0.0040	0.268
T7	-4.9301	-0.0347	0.203
T8	-5.4766	-4.99×10^{-6}	0.183
T9	-5.7807	-8.23×10^{-4}	0.173
T10	-5.9606	-0.0244	0.169
T11	-6.4950	-0.0116	0.154
T12	-6.6772	-0.0141	0.150
T13	-7.2264	-0.0082	0.138
T14	-7.3872	-0.0061	0.135
T15	-7.9237	-0.0056	0.126
T16	-8.0635	-0.0032	0.124

TABLE 1.2: Relaxation spectrum of the Earth using an 11-layer model with 9 viscoelastic layers. 27 modes are retrieved, as expected from the analytical constraints. The normal modes are displayed in the second column, the associated Love number k_2 viscoelastic residue (non-normalized) in the third column, and the relaxation times in the fourth column.

loading-unloading cycles. The glacial isostatic adjustment of the planet exhibits a spatial pattern of sea-level variation that changes systematically from the near field to the far field pivots of the glacial cover (e.g., Mitrovica and Peltier, 1991).

For this spectrum of sea level variations, tide gauges have been used for centuries to establish an instrumental record by measuring the height of the sea level relative to the sea floor. The Proudman Laboratory at the University of Bristol maintains the repository of the Permanent Service for Mean Sea Level (PSMSL)[5], a database assimilating records

[5] www.psmsl.org.

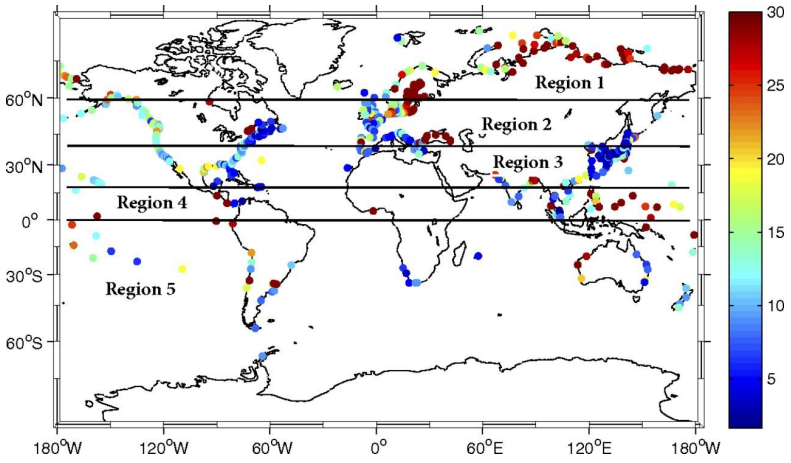

FIGURE 1.7: The variance [in cm^2] of detrended sea level observations at 596 tide gauge sites in the PSMSL (RLR) database. Figure adopted from Hay et al. (2013).

from a global network containing nearly two thousand tide gauges. The data-set is divided into two subsets: the metric records, which contain the raw observations in their individual reference frames; and the revised local reference (RLR) record, a smaller subset of 1166 tide gauges in which records have been reduced to a common height datum. For studies of global mean sea level variations (GMSL), it is proper to use the RLR subset as it allows a direct comparison between the tide gauge records.

Figure 1.7 shows the geographic distribution of nearly 600 gauges from the PSMSL RLR database with at least 20 years of data present in the last 50 years (Hay et al., 2013). Color coding corresponds to the variance of the tide gauge data computed from the annual records using all available data from 1807 to 2000. The largest variability is evident in the inner basins of the Baltic and Black seas, as well as along the coast of the Russian Arctic Ocean. The figure clearly establishes the regional variability of sea level, however, GMSL estimates are often used as a metric to describe the trends in sea level associated with climate variability. Different methods are used to compute the GMSL: the most common approach uses a small number of tide gauges that satisfy certain criteria of record continuity, duration, and consistency between neighboring sites, as well as a clear separation from tectonically active regions (e.g., Peltier and Tushingham, 1989; Douglas, 1997; Holgate and Woodworth, 2004); other approaches combine local averages of larger subsets (e.g., Jevrejeva et al., 2008), or establish spatial variability by combining altimetry with the tide gauge records (e.g., Church et al., 2011). Consistent among these approaches is the computed rate of sea level variation of 1.7 ± 0.2 mm/yr from 1900 to 1993. The rate increases to 2.8 ± 0.8 mm/yr as computed using tide gauges, and to 3.2 ± 0.4 mm/yr using altimetry data (Church et al., 2011).

Thermometric contributions, driven by the thermal expansion of the oceans due to increased heat content and the overflow of melt ice into the oceans, are thought to contribute around 25 percent of the sea-level trend over the past century, and up to 55 percent in the last decade of the 20th century (Antonov et al., 2005; Ishii and Kimoto, 2009; Cazenave and Llovel, 2010). This leaves changes in the mass of ice sheets and inland glaciers with a contribution of 75 percent to the century-scale trend, and 45 percent of the trend in the last decade of the century (Kaser et al., 2006; Bindoff et al., 2007). These GIA-related sea level changes deform the Earth, alter its rotational state, and perturb its gravitational field. The latter is exactly what we explore in the next section to compute variations in the Earth's dynamical ellipticity.

1.3.1 Sea level equation and the dynamical ellipticity

There exists, technically, two fundamental unknowns when modelling GIA: a model of the interior of the Earth describing its response to loading, i.e., its rheology, as detailed in Section 1.2, and a spatio-temporal function describing the evolution of the ice sheets. Once these are determined, a space-time variation of the relative sea-level change can then be obtained through a solution of the Sea Level Equation (SLE). This equation constructs the self-consistent gravitational redistribution of ice and water across the surface of the Earth. The SLE's mathematical theory and numerical implementation are undergoing continuous development by the community since its first introduction in the 1970s through a series of seminal papers (Peltier, 1974; Farrell and Clark, 1976; Peltier and Andrews, 1976; Clark et al., 1978; Milne and Mitrovica, 1998; Mitrovica and Milne, 2003; Kendall et al., 2005; Spada and Stocchi, 2007; Peltier, 2015; Adhikari et al., 2016; Whitehouse, 2018). We start with the definition of the relative sea level S as:

$$S = N - U, \tag{1.146}$$

N being the height of the sea surface relative to the center of mass of the Earth, and U being the height of the surface of the solid Earth. The variation of these two surfaces responds to ice and ocean changes, but because both the solid surface vertical displacement and sea surface variations are functions of the sea level itself, the SLE takes a more complicated form to account for this feedback:

$$\Delta S(\gamma, t) = \frac{\rho_{\mathrm{I}}}{\Gamma} G_{\mathrm{S}} \otimes_{\mathrm{I}} I(\gamma, t) + \frac{\rho_{\mathrm{w}}}{\Gamma} G_{\mathrm{S}} \otimes_{\mathrm{O}} \Delta S + C_{\mathrm{SL}}(t) \tag{1.147}$$

where $\Delta S(\gamma, t)$ is the change in relative sea level at position $\gamma = (\theta, \lambda)$ between time t and a reference t_0; $I(\gamma, t)$ is the spatio-temporal distribution of ice on the surface of the Earth; ρ_{I} and ρ_{w} are ice and water densities; G_{S} is a Green's function that combines a set of Love numbers to describe the perturbation of the Earth's solid surface in response to loading; $\otimes_{\mathrm{I}}$ and $\otimes_{\mathrm{O}}$ are convolutions in space and time over the ice sheets and oceans respectively. Finally, $C_{\mathrm{SL}}(t)$ is a time dependent uniform shift in sea level that is added to the equation to conserve the total mass transferring between ice sheets and the oceans, and is given by:

$$C_{\mathrm{SL}}(t) = -\frac{m_{\mathrm{I}}(t)}{\rho_{\mathrm{w}} A_{\mathrm{O}}(t)} - \frac{\rho_{\mathrm{I}}}{\Gamma}\overline{G_{\mathrm{S}} \otimes_{\mathrm{I}} I} - \frac{\rho_{\mathrm{w}}}{\Gamma}\overline{G_{\mathrm{S}} \otimes_{\mathrm{O}} \Delta S}. \tag{1.148}$$

The first term is often called the eustatic term, and it is the solution to the sea level equations when the other four terms are dropped, i.e., when the Green functions are zero. This physically corresponds to completely neglecting the deformation of the Earth and the time variations of the gravitational attractions between the solid earth and the oceans, the oceans and the ice sheets, and between the ice sheets and the solid earth. Thus this term describes a spatially uniform sea level that settles across the ocean with area $A_{\mathrm{O}}(t)$ due to variations in ice mass $m_{\mathrm{I}}(t)$. The oceanic area was time independent when the SLE was initially introduced in Farrell and Clark (1976), but further updates accounted for the expansion and retreat of marine-grounded ice (Milne and Mitrovica, 1998), and the effect of shoreline migration (Mitrovica and Milne, 2003). The final two terms are spatially averaged over the ocean, and these are subtracted because although the mean of the spatially varying terms could vanish when integrated over the surface of the Earth, the mean will not necessarily vanish when integrated over the ocean, thus this uniform shift is added to satisfy mass conservation.

The implicit nature of the SLE being a three dimensional non-linear integral equation, in the form of a Fredholm equation of the second kind, calls for an iterative approach in order to be solved. We adopt the theory and numerical code developed over the past two decades and called `SELEN`^{4} (Sea lEveL EquatioN solver, version 4.0, Spada and Stocchi, 2007; Spada et al., 2012; Spada and Melini, 2015, 2019). In `SELEN`^{4}, the SLE is solved by a pseudo-spectral iterative approach (Mitrovica and Peltier, 1991) over a spatially discretized Earth surface on a spherical grid of icosahedron shaped pixels (Tegmark, 1996). The gravitationally self-consistent surface loading is computed allowing for shoreline migration and the transfer of ice between grounded and marine-based. `SELEN`^{4} also accounts for the influence of the rotational feedback on sea level.

For a more elaborate explanation on the SELEN^4 scheme, the reader is referred to the supplementary material of Spada and Melini (2019).

Out of the various byproducts of the SLE solver, we are interested in computing the variation of the geoid response function defined as:

$$\mathcal{G}(\gamma, t) = \Gamma^g(\alpha, t) \otimes \mathcal{L}(\gamma, t), \tag{1.149}$$

where $\Gamma^g(\alpha, t)$ is the geoid Green's function (Peltier, 1974; Peltier and Andrews, 1976). It channels the solid interior response through the Love numbers computed in Section 1.2; specifically it is given by (Wu and Peltier, 1982):

$$\Gamma^g(\alpha, t) = \frac{R_\mathrm{E}}{M_\mathrm{E}} \sum_{l=0}^{\infty} \left[\delta(t) + k_l^\mathrm{L}(t)\right] P_l(\cos\alpha), \tag{1.150}$$

where α is the difference between the position of the measured sea level variation γ and the position of the load γ'. On the other hand, the surface loading function $\mathcal{L}$ describes the variation of the glacial and oceanic load on the Earth with respect to a reference state. In almost all numerical implementations of the SLE, continuous solutions in time have not been used, and a time discretization for all quantities is imposed over a piece-wise function ($n = 1..N$). With this time discretization and the pseudo-spectral approach, the geoid response function, expanded in spherical harmonics of degree l and order m, is written as:

$$\mathcal{G}_{lm} = \frac{3}{\rho^\mathrm{E}} \sum_{n}^{N} \frac{\Delta\mathcal{L}_{lm,n}}{2l+1} \left[1 + k_l^\mathrm{L} + \sum_{i=1}^{M} \frac{k_{l,i}^\mathrm{L}}{s_{l,i}} (e^{s_{l,i}(t-t_n)} - 1)\right] H(t - t_n), \tag{1.151}$$

where $\Delta\mathcal{L}_{lm,n} = \mathcal{L}_{lm,n+1} - \mathcal{L}_{lm,n}$, with $\mathcal{L}_{lm,n}$ representing the harmonic decomposition and temporal discretization of $\mathcal{L}$, and ρ^E being the average density of the Earth. Finding the variation in the geoid allows us to compute the variation in the geopotential Φ using the classic Bruns formula (Heiskanen, 1967):

$$\mathcal{G} = \frac{\Phi}{g}. \tag{1.152}$$

This allows us to write the geoid response function as

$$\mathcal{G}(\gamma, t) = R_\mathrm{E} \sum_{l=2}^{l_\mathrm{max}} \sum_{m=0}^{l} \left[\delta c_{lm}(t) \cos m\lambda + \delta s_{lm}(t) \sin m\lambda\right] P_{lm}(\cos\alpha). \tag{1.153}$$

Here, the Legendre polynomials are the fully normalized associated set, and c_{lm} and

s_{lm} are the well known Stokes' coefficients (Yoder, 1995). We note that the loading mass conservation law cancels the surface average of the load variation and equivalently the zeroth degree harmonic of the load's expansion. Furthermore, the first order also vanishes because we use a reference frame with an origin at the center of mass.

After computing the geoid response function via the SLE solver, the Stoke's coefficients in Eq. (1.153) are obtained by utilizing the general relationship between the coefficients of a complex spherical harmonics expansion of a time dependent scalar function; namely:

$$c_{lm}(t) + is_{lm}(t) = \sqrt{2 - \delta_{0m}}\mathcal{G}^*_{lm}(t). \tag{1.154}$$

Using the scaling relationship derived in Mitrovica and Peltier (1989), we find the gravitational zonal harmonics of the Earth as

$$J_l(t) = -\frac{1}{R_\mathrm{E}}\sqrt{2l+1}\mathcal{G}_{l0}(t). \tag{1.155}$$

More specifically, we are after the harmonic that corresponds to the equatorial flattening:

$$J_2(t) = -\frac{\sqrt{5}}{R_\mathrm{E}}c_{20}. \tag{1.156}$$

Hence the variation of the dynamical ellipticity (Eq. 1.8) relative to its present day value $H_0 \approx 3.27 \times 10^{-3}$ (Burša et al., 2008) can be written as:

$$\frac{\delta H(t)}{H_0} = \frac{\delta J_2(t)}{H_0\mathcal{K}}\left(1 - \frac{2}{3}H_0\right) \approx \frac{\delta J_2(t)}{H_0\mathcal{K}} = -\frac{\sqrt{5}}{H_0\mathcal{K}R_\mathrm{E}}\delta c_{20}(t), \tag{1.157}$$

where $\mathcal{K} = \frac{C}{M_\mathrm{E}R_\mathrm{E}^2}$ is the so-called structure constant. The problem of finding the relative variations in the dynamical ellipticity thus reduces for us to finding the geoid response function $\mathcal{G}$ in the framework of the SLE solver. Another contribution arises from variations in the centrifugal potential, but we ignore that based on the arguments in the following section.

1.3.2 The effect of the centrifugal potential variation on the dynamical ellipticity

In addition to the direct effect of surface loading, the dynamical ellipticity is also affected by the varying centrifugal potential as a consequence of altering the magnitude and direction of the angular velocity vector due to the mass redistribution. This rotational

effect was one of the additions that came about during the development of the sea level variation theory, and is of significance in TPW computations. However, on the basis of the following approximations, we argue that this effect is minimal on the dynamical ellipticity, and we then decide to ignore it in our calculations. It should be stressed that the variation of the angular velocity discussed here is merely related to the mass redistribution associated with surface loading. On the other hand, the angular velocity variation associated with the tidal interaction between the Earth and the Moon is the dominant contributor to the precession "constant" evolution over geological timescales; an effect that we detail on in Chapter 2.

Considering the rotating Earth and aligning the z-axis along the angular velocity vector $\mathbf{\Omega}_{\mathrm{E}}$, we re-write the centrifugal potential defined in Eq. (1.23) and felt by a point P at the surface, i.e., in the co-rotating frame as:

$$\phi^{\mathrm{C}}(P) = \frac{1}{2}\Omega^2 r_{\mathrm{p}}^2 = \frac{1}{2}\Omega^2 R_{\mathrm{E}}^2(1 - \cos^2\theta_{\mathrm{p}}), \tag{1.158}$$

where θ_{p} is the angular separation of P from the axis of rotation. Using the Legendre polynomials, this can be written as:

$$\phi^{\mathrm{C}}(P) = \frac{\Omega^2 R_{\mathrm{E}}^2}{3}\left[P_0(\cos\theta_{\mathrm{p}}) - P_2(\cos\theta_{\mathrm{p}})\right]. \tag{1.159}$$

The theory usually continues by expanding the potential variation into variations in the angular velocity vector and, to leading terms in the perturbation, this expansion is used in the problem of the true polar wander when solving the Liouville equations (see Section 1.1.2; Sabadini et al., 2016). But for our purposes here, we are considering only the variations in the second zonal harmonic. In a general sense, the variation in the dynamical ellipticity H due to variations in the surface loading potential ϕ^{L}, and the centrifugal potential ϕ^{C} can be derived from:

$$\begin{aligned} H &= \frac{R_{\mathrm{E}}^3}{GC}(1 + k_2^{\mathrm{L}})\phi_2^{\mathrm{L}} + \frac{R_{\mathrm{E}}^3}{GC}k_2^{\mathrm{T}}\phi_2^{\mathrm{C}} \\ &= \frac{R_{\mathrm{E}}^3}{GC}(1 + k_2^{\mathrm{L}})\phi_2^{\mathrm{L}} + k_2^{\mathrm{T}}\frac{\Omega^2 R_{\mathrm{E}}^5}{3GC}. \end{aligned} \tag{1.160}$$

The variation in the potential is driven by variations in the polar moment of inertia due to the following three contributions: A rigid Earth variation given by

$$\delta C^{\mathrm{r}} = \frac{2R_{\mathrm{E}}^3}{3G}\delta\phi_2^{\mathrm{L}}, \tag{1.161}$$

a viscoelastic compensation expressed as

$$\delta C^{\mathrm{ve}} = \frac{2R_{\mathrm{E}}^3}{3G} k_2^{\mathrm{L}} \delta\phi_2^{\mathrm{L}} = k_2^{\mathrm{L}} \delta C^{\mathrm{r}}, \tag{1.162}$$

and the rotational effect:

$$\delta C^{\mathrm{rot}} = \frac{2R_{\mathrm{E}}^3}{3G} k_2^{\mathrm{T}} \delta\phi_2^{\mathrm{C}} = \frac{4R_{\mathrm{E}}^5}{9G} k_2^{\mathrm{T}} \Omega \delta\Omega. \tag{1.163}$$

In a general sense too, the dynamical ellipticity can be split into the hydrostatic component H^{F}, and a residual part δH depending on all possible surface and internal irregularities:

$$H = H^{\mathrm{F}} + \delta H, \tag{1.164}$$

where the hydrostatic part can be found by taking the fluid limit of Eq. (1.160) such that:

$$\begin{aligned} H^{\mathrm{F}} =& \frac{R_{\mathrm{E}}^3}{GC}(1 + k_2^{\mathrm{L,F}})\phi_2^{\mathrm{L}} + k_2^{\mathrm{T,F}} \frac{R_{\mathrm{E}}^5}{3GC}\Omega^2 \\ \approx& k_2^{\mathrm{T,F}} \frac{R_{\mathrm{E}}^5}{3GC}\Omega^2. \end{aligned} \tag{1.165}$$

The last approximation is possible since $k_2^{\mathrm{L,F}} \approx -0.98$ while $k_2^{\mathrm{T,F}} \approx 0.97$. Ignoring the loss of angular momentum due to tidal dissipation, the variation in the angular velocity or the length of the day is accompanied by a variation in the moment of inertia to conserve the angular momentum, thus we can write:

$$\begin{aligned} \delta(C\Omega) &= C\delta\Omega + \Omega(1 + k_2^{\mathrm{L}})\delta C^{\mathrm{r}} + \Omega\delta C^{\mathrm{rot}} \\ &= \delta\Omega\left(C + \frac{4a^5}{9G} k_2^{\mathrm{T}}\Omega^2\right) + (1 + k_2^{\mathrm{L}})\Omega\delta C^{\mathrm{r}} \\ &= \delta\Omega C\left(1 + \frac{4}{3}\frac{k_2^{\mathrm{T}}}{k_2^{\mathrm{T,f}}} H^{\mathrm{f}}\right) + (1 + k_2^{\mathrm{L}})\Omega\delta C^{\mathrm{r}} \\ &\approx \delta\Omega C + (1 + k_2^{\mathrm{L}})\Omega\delta C^{\mathrm{r}} \equiv 0, \end{aligned} \tag{1.166}$$

where the approximation was based on the relatively small value of H^{F} (≈ 0.97). This allows us to write

$$\delta\Omega \approx -(1 + k_2^{\mathrm{L}})\Omega \frac{\delta C^{\mathrm{r}}}{C}. \tag{1.167}$$

With these quantities, we compute the ratio of the contributions to the polar inertia variation as:

$$\left|\frac{\delta C^{\mathrm{rot}}}{(1 + k_2^{\mathrm{L}})\delta C^{\mathrm{r}}}\right| = \left|\frac{4R_{\mathrm{E}}^5\Omega^2}{9GC} k_2^{\mathrm{T}}\right| = \left|\frac{4k_2^{\mathrm{T}}}{3k_2^{\mathrm{T,f}}} H^{\mathrm{f}}\right| \approx 10^{-3}, \tag{1.168}$$

where $k_2^{\mathrm{T}} \approx 0.3$. On this basis, we ignored the effect of rotation on the perturbation of dynamical ellipticity in our simulations.

1.4 Cenozoic glacial history

In this section, we give a historical overview of glaciation on the Earth's surface over the geological past. We focus on the last ice ages, the Cenozoic era, which extends over the past 65 million years. Starting 50 million years ago (Ma), the Earth entered a cooling phase that led to the inception of the grounded ice sheet on Antarctica around 34 Ma. Following that, the Earth witnessed a significant increase of the global ice volume during the Oligocene and the Miocene, with limited intervals of warming, and variations occurred almost completely on Antarctica due to the uni-polar ice configuration. To date, we have no geological evidence on continental scale glaciation in the northern hemisphere, except for Greenland, before 3 Ma. Since then, the Earth's climate oscillated strongly between glacial and interglacial stages. Towards the end of the Pliocene, glacial periods started to feature the expansion of ice caps on both hemispheres, whereas during interglacials, ice sheets were present only in Antarctica and Greenland, similar to the present interglacial: the Holocene. In what follows, we expand on this history in an attempt to have a detailed spatio-temporal evolution of ice that can be used as an input to the sea level equation developed in the previous section.

1.4.1 From benthic foraminiferal δ^{18}O to ice volume

Oxygen isotopic records measured with respect to the VPDB (Vienna Pee Dee Belemnite) standard and extracted from fossilised benthic foraminiferal shells have long been used as a primary proxy for climate variations (e.g., Emiliani, 1954, 1961; Shackleton, 1975; Zachos et al., 2001, 2008). The two main components affecting the uptake of δ^{18}O drawn from calcite shells are local temperature and sea water variations. Water evaporation preferentially removes the lighter isotope from water, thus the ratio given by

$$\delta^{18}\mathrm{O} = 1000 \times \frac{(\delta^{18}\mathrm{O}/\delta^{16}\mathrm{O})_{\mathrm{sample}} - (\delta^{18}\mathrm{O}/\delta^{16}\mathrm{O})_{\mathrm{standard}}}{(\delta^{18}\mathrm{O}/\delta^{16}\mathrm{O})_{\mathrm{standard}}} \tag{1.169}$$

will get more negative as the moisture heading to the polar regions passes across latitudes to accumulate mass on ice. On the other hand, the net evaporation enriches the sea water

with the heavier isotope, so the buildup of ice volume will cause the ratio extracted from the ocean to increase. Thus the isotopic ratio extracted from the ocean responds to climatic variations oppositely to that extracted from the ice . Following Fowler and Ng (2019), we use the mass conservation equation

$$\delta^{18}\mathrm{O}_{\mathrm{sw}} V_{\mathrm{O}} + \overline{\delta^{18}\mathrm{O}_{\mathrm{i}}} V_{\mathrm{i}} = K, \tag{1.170}$$

K being a constant, V_{O} and V_{i} being respectively the ocean and global ice volumes, $\delta^{18}\mathrm{O}_{\mathrm{sw}}$ is the ratio in sea water, and $\delta^{18}\mathrm{O}_{\mathrm{i}}$ is the mean ratio in ice sheet. The constant K can be defined at the present day, scaled with ice and ocean volume, thus:

$$\Delta\delta^{18}\mathrm{O}_{\mathrm{sw}} = -\frac{\overline{\delta^{18}\mathrm{O}_{\mathrm{i}}} V_{\mathrm{i}}}{V_{\mathrm{O}}} + \left.\frac{\overline{\delta^{18}\mathrm{O}_{\mathrm{i}}} V_{\mathrm{i}}}{V_{\mathrm{O}}}\right|_{\mathrm{PD}}. \tag{1.171}$$

The benthic ratios depend on ice volume through the sea water ratios, but they also depend on water temperature. In colder water the shells have a preferential uptake of the heavier isotope, hence an additional increase in the ratio. This contribution is parametrised as a linear relation between the change in deep-water temperature ΔT_{dw} and the change in the isotopic ratio from temperature $\Delta\delta^{18}\mathrm{O}_{\mathrm{T}}$ such that:

$$\Delta\delta^{18}\mathrm{O}_{\mathrm{T}} = \gamma \Delta T_{\mathrm{dw}}, \tag{1.172}$$

where the value of γ can be taken for example from Duplessy et al. (2002) so that $\gamma = -0.28‰^{\circ}\mathrm{C}^{-1}$. Thus the total change in benthic isotopes is the combination of the two effects giving us:

$$\Delta\delta^{18}\mathrm{O}_{\mathrm{bn}} = -\frac{\overline{\delta^{18}\mathrm{O}_{\mathrm{i}}} V_{\mathrm{i}}}{V_{\mathrm{O}}} + \left.\frac{\overline{\delta^{18}\mathrm{O}_{\mathrm{i}}} V_{\mathrm{i}}}{V_{\mathrm{O}}}\right|_{\mathrm{PD}} + \gamma \Delta T_{\mathrm{dw}}. \tag{1.173}$$

The latter equation means that the interpretation of climate variations from benthic isotopic ratios is ambiguous as to separate the contributions of temperature from those of ice volume. Consequently, an independent constraint on ice volume or deep ocean temperature is necessary to separate both components. A common approach is to use Mg/Ca ratios in benthic foraminifera as an independent proxy for deep ocean temperature (Lear et al., 2000, 2003; Shevenell et al., 2008; Sosdian and Rosenthal, 2009), though this method lacks sufficient constraints on the seawater Mg/Ca ratio creating a huge uncertainty in the temperature contribution to oxygen isotopic ratios. Cramer et al. (2011) demonstrated that benthic oxygen isotopic ratios combined with the available benthic Mg/Ca ratios and added to sea level variation curves are reconcilable under

reasonable assumptions. Thus $\mathrm{Mg/Ca_{bn}}$ can constrain temperature, and combined with $\delta^{18}\mathrm{O_{bn}}$ can constrain ice volume. In parallel, sea level curves can constrain ice volume, and combined with $\delta^{18}\mathrm{O_{bn}}$ can constrain temperature. Hence records of temperature and ice volume are almost independently constructed.

In our attempt to have a spatio-temporal distribution of ice on the Earth's surface over the Cenozoic, we will start with a constraint on the temporal evolution of global ice volume derived from benthic isotope oxygen ratios that use the same method explained above to separate the contributions from ice and temperature. The evolution of temperature as a function of Mg/Ca ratios is described in Cramer et al. (2011) by the following linear equations:

$$T = \frac{\mathrm{Mg/Ca} - 1.36}{0.106}, \tag{1.174}$$

$$T = \frac{\mathrm{Mg/Ca} - 1.27}{0.242}, \tag{1.175}$$

where Mg/Ca is to be corrected to account for the effect of variations in seawater carbonate ion saturation state. Following Miller et al. (2020), Eq. (1.175) is used. Once the temperature evolution is constructed, the required separation between the effects of temperature and ice volume variations can be established via a paleotemperature equation (O'Neil et al., 1969; Kim and O'Neil, 1997; Lynch-Stieglitz et al., 1999):

$$T = 16.1 - 4.76\left[\delta^{18}\mathrm{O_{bf}} - (\delta^{18}\mathrm{O_{sw}} - 0.27)\right]. \tag{1.176}$$

Using a linear relation between $\delta^{18}\mathrm{O_{sw}}$ and sea level variations associated with ice volume, glacial volume variations can be directly extracted. Based on this technique, we adopt the oxygen isotope splice and its associated sea level equivalent of ice compiled recently in Miller et al. (2020), covering the Cenozoic era, starting 66 Ma [6]. This compiled splice, denoted M20 hereafter, is similar to that in De Vleeschouwer et al. (2017), but is composed entirely of Pacific records, which compromise 60% of the modern and 80% of the early Cenozoic global reservoir, minimizing the effects of temperature and salinity present in other regions due to deep circulation changes. That said, uncertainties of the glaciation history we shall derive from the oxygen isotopic record mainly propagate from three different sources: uncertainties on the oxygen isotope record itself, uncertainties associated with filtering out the temperature contribution to the record, and uncertainties associated with the conversion of the remaining pure glacial

[6] we use the usual convention where ka, Ma (thousand, million years) denote dates in the past from now, while kyr, Myr denote durations

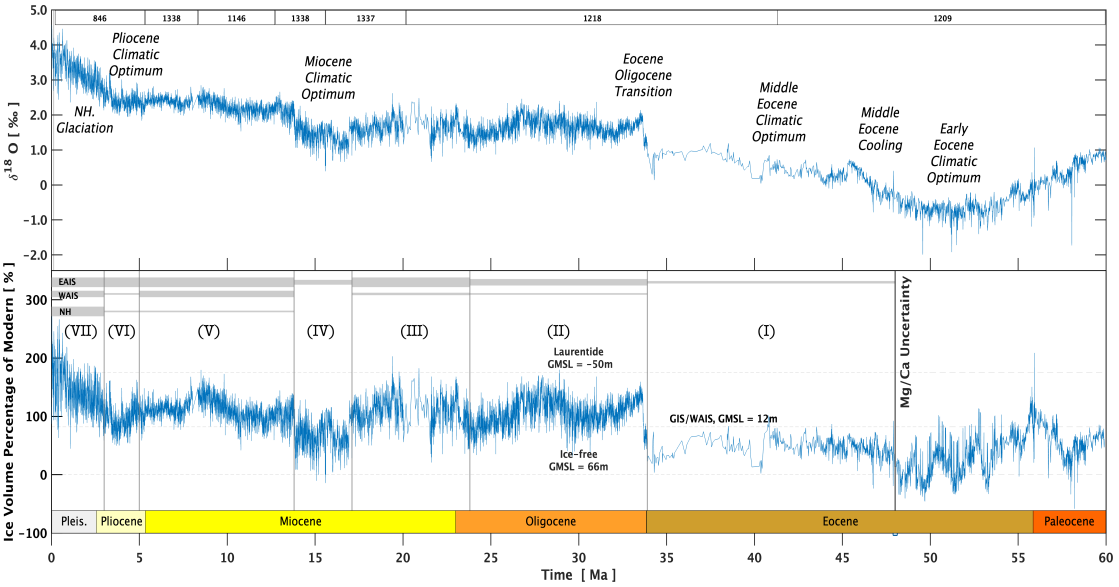

FIGURE 1.8: Cenozoic benthic foraminiferal δ^{18}O records from the splice compiled in Miller et al. (2020) [M20], and their ice volume contribution after the removal of the temperature contribution à la Cramer et al. (2011). The first panel is the isotope variation with time relative to the VPDB standard; the drilling sites are indicated on the top of the panel. The second panel is the ice variation with time in volume units on the right axis and in percentage relative to modern values on the left axis. The ice free line is equivalent to 66m of sea level increase above present, corresponding to the total increase in sea level if the Earth becomes ice free. The GIS/WAIS (Greenland and West Antarctic Ice Sheets) and the Laurentide lines are equivalent to 12m and -50m sea level variations. The gray bars on top of the second panel are rough sketches of the glacial evolution of the ice sheets across 8 intervals that we have defined for the spatio-temporal glacial function used in our simulations (more on that in Section 1.5). The 8$^{\text{th}}$ interval covers the last glacial cycle.

component to GMSL variations and eventually absolute ice volume (the calibration used in the M20 splice is 0.13‰/10m; see for e.g., Winnick and Caves, 2015).

1.4.2 Cenozoic Ma-scale climate

The M20 splice (Figure 1.8) is interpreted to distinguish between a mostly un-glaciated Cenozoic Hothouse with $\delta^{18}\text{O} < -0.5$‰, a moderate Warmhouse having ephemeral ice sheets with $-0.5 < \delta^{18}\text{O} < 1.8$‰, and an Icehouse with continental scale ice sheets on one or both of the Earth's poles with higher isotopic values (Miller et al., 1987; Huber et al., 2018) (the terms Hothouse, Warmhouse, and Icehouse have been adopted from Westerhold et al. 2020). A long term warming stage started in the late Paleocene (60 to 54 Ma) and led to the Paleocene-Eocene thermal maximum followed by a stable interval of minimum isotopic values during the Early Eocene climatic optimum (55 to 48 Ma).

The middle Eocene after that witnessed a cooling phase with an increase in δ^{18}O around 2‰, then the climate relatively stabilizes until the end of the Eocene with $\delta^{18}\text{O} \approx 1‰$.

During Middle to Late Eocene, although continental scale glaciation had not yet started in Antarctica, recent evidence suggests partial glaciation in high elevation regions (Rose et al., 2013, see Figure 1.9), and the expansion into marine terminating glaciers, specifically around the Aurora subglacial basin (Gulick et al., 2017). In their attempt to model the Eocene-Oligocene transition (EOT) and the continental scale glaciation of Antarctica, DeConto and Pollard (2003) simulated the glacial inception and the early growth of the East Antarctic ice sheet (EAIS) coupling components of the atmosphere, the oceans, and the ice sheets, while incorporating effects of paleogeography, greenhouse gas, orbital parameters variation, and ocean heat transport. Their model indicates that the declining CO_2 during that period leads to the formation of highly dynamic ice caps on high surface elevations, specifically on Dronning Maud Land and the Gamburtsev and Transantarctic mountains.

Ice on these separate caps slightly was fluctuating with orbital parameters. DeConto and Pollard (2003) explain that the transition into the ice-house of the Oligocene is only possible after crossing a CO_2 threshold that allows these ice caps to expand in volume and coalesce permanently. Hence this model can explain the existence of substantial amount of Antarctic ice volume even before the EOT, however, it cannot explain the large amplitude variations occurring during that period, which are most probably due to the error in the Mg/Ca record. This limitation is discussed in detail in Cramer et al. (2011), prescribing much larger errors on the record before 48 Ma, which explains the negative ice volumes obtained before this period in Figure 1.8. As such, we have limited our computations and model prediction of the evolution of the dynamical ellipticity to the interval covering the last 47 Myr.

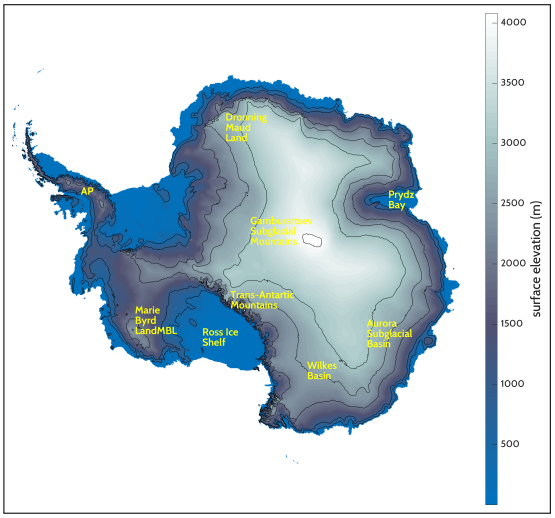

FIGURE 1.9: Surface elevation map of Antarctica. Data set is from bedmap2 (Fretwell et al., 2013), and the plot is generated using the Antarctic Mapping Tools (Greene et al., 2017)

On the opposite pole of the Earth, the growth of ice sheets in the Northern Hemisphere is thought to have initiated much later than that on Antarctica (Bailey et al., 2013). Ongoing

consensus suggests that the beginning of glaciation on southern Greenland only started in the late Miocene (Larsen et al., 1994), and it was until the late Pliocene when major glacial cycles and vast volume expansion culminated with the onset of the Laurentide ice sheet (Shackleton et al., 1984). However, recent evidence reports on sediment rafting by glacial ice on the south eastern end of Greenland dating back to 30 – 38 Ma (Eldrett et al., 2007). This was further supported by geochemical data and accurate source determinations of individual ice-rafted Fe-oxide grains giving evidence to episodic glaciation on Greenland beginning in the middle Eocene (Tripati and Darby, 2018). The relatively stable final phase of the Eocene was terminated by one of the major known Myr-scale features of the Cenozoic, the Eocene-Oligocene transition (EOT), around 34 Ma (Coxall et al., 2005), which is associated with the rapid glaciation of the Antarctic ice sheet (AIS) up to a continental scale, marking the onset of the Earth's Icehouse.

Following the EOT, a continental scale AIS was established, almost completely on the Eastern terrestrial region (Galeotti et al., 2016). During the Oligocene, the evolution shows that the EAIS was not yet permanently developed, as we have large scale oscillations that peaked at the loss of more than 60% of the AIS after the EOT around 30 Ma, indicating its long term instability. The extent to which the West Antarctic ice sheet (WAIS) participated in the mostly unipolar Oligocene glaciation is unknown. The model of DeConto and Pollard (2003) initiates glaciation as we mentioned on the high-elevation plateaus of East Antarctica. Oldest seismic stratigraphic evidence for ice in the Ross Sea is interpreted as late Oligocene (Bartek et al., 1992), or middle Miocene (Bart, 2003). However, glacial erosion going back to 28 Ma of dated volcanoes in the interior of Marie Byrd Land (MBL; see Figure 1.9) suggest a small Oligocene ice cap there (Rocchi et al., 2006). Moreover, seismic reflection data in Sorlien et al. (2007) suggests an episode of Oligocene grounded ice in West Antarctica far from the elevated plateau of MBL. The data also provides evidence for a higher elevation at the Ross Embayment for the early Cenozoic, which calls for the correction of the absence of ice accumulation in the existing GCMs (e.g., DeConto and Pollard, 2003).

During the Early to mid-Miocene, major variations occurred in Antarctic ice sheet volume and extent. The splice presented here estimates larger variations than those proposed in Pekar and DeConto (2006) (50% to 125% of modern EAIS values). GCMs previously failed to completely simulate such large scale variations because of strong hysteresis effects and glacial-interglacial symmetry, and the resultant stable ice sheet when the continental scale ice spread is achieved. Modelling this variability required adding more atmospheric components to account for ice sheet-climate feedback (Gasson

TABLE 1.3: A compilation of references used to constrain the spatio-temporal distribution of ice over the Earth's surface. Some elements of the list correspond to geological evidence of various ice sheets extent over the Cenozoic. Others correspond to numerical modelling of ice sheets, specifically used to simulate onsets of continental glaciation.

Geologic Evidence / Geographic Constraint	Reference
• Partial glaciation in Antarctic high elevation regions during the Early Eocene.	Rose et al. (2013)
• Antarctic expansion into marine terminating glaciers, specifically around the Aurora subglacial basin.	Gulick et al. (2017)
• Simulating the inception of the EAIS requires small ice caps on elevated plateaus.	DeConto and Pollard (2003)
• Sediment rafting by glacial ice on the S-E end of Greenland dating back late Eocene.	Eldrett et al. (2007)
• Middle Eocene episodic glaciation on Greenland from ice-rafted Fe-oxide grains.	Tripati and Darby (2018)
• Seismic stratigraphic evidence for ice in the Ross Sea during Oligocene-Miocene.	Bartek et al. (1992) Bart (2003)
• Oligocene grounded ice in the WAIS around and far from Marie Byrd Land.	Rocchi et al. (2006); Sorlien et al. (2007)
• Terrestrial retreat of the EAIS during the Miocene Climatic Optimum.	Levy et al. (2016)
• Expansion of terrestrial ice across the Ross Sea continental shelf around 24.5–24 Ma.	Hauptvogel et al. (2017)
• Terrestrial AIS stability for the past 8 Ma from cosmogenic isotope data.	Shakun et al. (2018)
• Early Pliocene loss of ice from WAIS and Greenland.	Naish et al. (2009)
• Substantial marine ice retreat in the EAIS during Early Pliocene.	Cook et al. (2013)
• Simulating the AIS evolution over the last 3 Myr: Separation between polar caps' contributions to the global volume.	Pollard and DeConto (2009)

et al., 2016b). These large oscillations were punctuated by the Miocene Climatic Optimum (17 - 13.8 Ma). The latter was a period of reduced ice volume where near ice free conditions were attained around 15 Ma, probably establishing the most recent ice-free Earth. Records from around the Antarctic margin support this terrestrial retreat of the EAIS (Levy et al., 2016; Gulick et al., 2017). GCMs and simulated AIS are much more stable than the geologic record for this period, calling for more work in order to understand how the AIS responded to past climate changes and what drove the terrestrial retreat (Gasson and Keisling, 2020).

Following that warm period, the Middle Miocene Climatic Transition (MMCT) involved three major steps of cooling and consequently sea level falls (Mi3a, Mi3, Mi4, 14.8-12.8 Ma) resulting in a permanent EAIS (Miller et al., 2020) and a global ice volume a bit higher that today ($\sim$ 120%). The ice volume then remained approximately constant

until early Pliocene. This scenario of Antarctic stability for the past 8 million years is supported by cosmogenic isotope data from the Ross Sea (Shakun et al., 2018). Consequently, any ice loss during this interval would be from the marine sectors either in the WAIS, or the large basins of East Antarctica, and the Wilkes and Aurora subglacial basins. This was the case of the Early Pliocene, when sea level rose to levels above 12 m, indicating the loss of ice from WAIS and Greenland (Naish et al., 2009). Some peaks were even higher, requiring the melting of the marine parts of the EAIS. Although the sea level maximum of this period remains poorly constrained (Dutton et al., 2015), there is physical evidence for substantial ice retreat in the marine sectors of East Antarctica (Cook et al., 2013).

During the last 3 Ma, build-ups of ice volume were associated with sea level lowering up to 130 m below present, indicating the onset of a continental scale northern hemispheric ice sheets. The largest of these build-ups were during the past 800 kyr. The last glacial maximum (LGM, 21 ~ 26 Ka) is not only a local maximum of glaciation but a global one across Cenozoic ice history as it is associated with the maximum sea level drop ~130 m (Austermann et al., 2013). We summarize this brief Cenozoic glacial history in Table 1.3.

1.5 Evolution of Cenozoic dynamical ellipticity

In the framework of the SLE solver, the ice volume input should be temporally discretized as we discussed, but also spatially distributed over the surface of the Earth in order to facilitate the computation of the surface integrals by the pseudo spectral approach (Mitrovica and Peltier, 1991). Since an exact distribution is currently impossible to obtain over such a prolonged history, we approximate the input by conserving the global limit from the M20 splice (Figure 1.8), and abiding by major known glacial events and available geological constraints that help model the glacial spatial distribution (Table 1.3). The global estimate of ice volume is thus distributed over the spherically pixelated grid on the surface of the Earth. `SELEN`^{4} adopts a grid of equal-area, icosahedron-shaped pixels (Tegmark, 1996). This grid is characterized by a resolution parameter R such that the total number of pixels on the surface P is

$$P = 40R(R-1) + 12. \tag{1.177}$$

All our simulations were performed with $R = 30$, yielding $P = 34812$. For such a large number of pixels, each pixel can be thought of as a disk of radius $r_{\rm disk} \approx 2R_{\rm E}/\sqrt{P}$. Thus each pixel approximately covers a surface area of 14600 km^2.

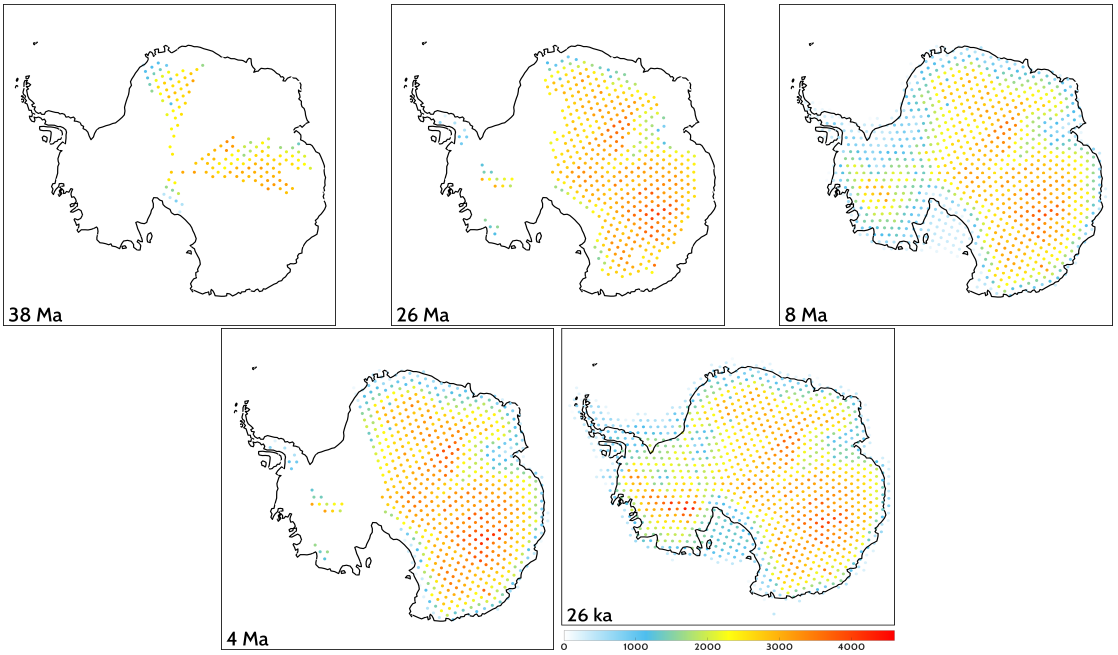

FIGURE 1.10: Time slices of the Antarctic ice distribution on the pixelated surface of the Earth. Color coding represents the ice thickness in meters. Each spatial spread in used over a specific interval of time (see text).

Over the time interval of our simulations (47 Myr), we scale our glacial input with the global limit of M20, however, we separate between 8 intervals of spatial distribution (marked by the vertical gray lines in Figure 1.8). Samples of the distribution over these intervals are plotted via MATLAB's Mapping Toolbox (Greene et al., 2017) and shown in Figure 1.10 for the Antarctic ice sheet, and in Figure 1.11 of the northern ice cap. Before the Eocene-Oligocene transition, ice is distributed over the high elevation regions of the East Antarctic Ice Sheet (EAIS); specifically on the Dronning Maud Land, the Gamburtsev Mountain, and parts of the Trans-Antarctic Mountains. The second interval, the Oligocene, witnesses continental scale spread on the EAIS, with minimal glaciation on the high elevation plateaus of the western part (WAIS), and on the Eastern side of the Greenland Ice Sheet (GIS). The third interval, covering the Early Miocene, only differs from the second interval by the expansion of the EAIS into marine terminating glacial spread. The fourth interval represents the warm period of the Middle Miocene Climatic Optimum (MMCO), and is characterized by Antarctic glacial retreat reaching the spread of the first interval. Following the MMCO, the stable EAIS is established, and ice fully covers the WAIS and the GIS for the first time. The sixth interval represents the warm period of the Early Pliocene, and it witnessed the retreat of the WAIS. Starting 3 Ma,

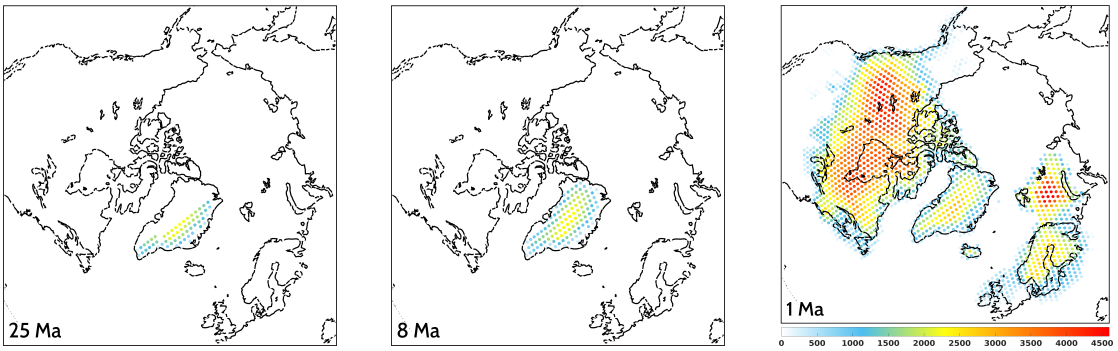

FIGURE 1.11: Same as Figure 1.10, but for the glacial spread over the northern hemisphere.

the seventh interval highlights the maximum glacial spread over the Cenozoic, with the glaciation of the Laurentide and the Fennosacida ice sheets (Figure 1.11). In this interval, for the separation of the global ice volume between the northern and southern regions, we use the simulation of Pollard and DeConto (2009) as an estimate of Antarctic ice. Subtracting this estimate from the global limit leaves us with the contribution of the northern cap. Finally, we terminate our established history with the ICE-6G model (Peltier et al., 2015), and we use the distribution of the Last Glacial Maximum (LGM) as the limit of the maximum possible ice spread. In each interval, the distribution of the allocated ice volume over the pixels of the corresponding region is controlled by the relative distribution among the same pixels at the LGM.

It is noteworthy that such a distribution may not be adequate for high precision geodetic computations. However, we are after the second degree harmonic decomposition of the load, which is characterized by even parity and symmetry under rotation. Also, the change in oblateness reflects long wavelength deformation, so abiding by major climatic events, it is safe to assume that we are capturing the backbone of the evolution of the dynamical ellipticity. Our sensitivity tests will later show that variations in the spatial distribution are only higher order corrections.

Using SELEN^4, the SLE is solved over two nested loops, and the convergence of the solution as a function of the number of iterations is discussed in Milne and Mitrovica (1998); Spada and Melini (2019). Based on the convergence tests in these studies, all of our simulations were performed over three internal and three external loops. We use the 11-layer Earth model described earlier, and we provide SELEN^4 with the needed Green's functions based on the viscoelastic response of this model.

Global ice input uncertainty propagates from the uncertainty of the sea level variation. Estimates of uncertainty on the latter vary between ±10m and ±20m (Kominz et al.,

2008; Miller et al., 2012; Raymo et al., 2018). Thus we consider these limits as 1σ and 2σ error estimates respectively, and we consequently create a white Gaussian noise with these amplitudes to perform 40 simulations of the SLE solver. In addition to this error, sea level variation is under a systematic uncertainty propagating from the variation in the volume of the oceans basins and a contribution from tectonic changes (Conrad, 2013). Constraining the former was already done in the M20 data set based on Cramer et al. (2011) by limiting the ice contribution to the sea level variation through end member scenarios. To remove the tectonic contribution, we apply a LOESS regression filter (a generalized moving polynomial regression; Cleveland and Devlin, 1988), with a window of 20 Myr, to isolate and then remove variability occurring over plate tectonic timescales, thus only keeping short timescale variability that is most likely due to the ice volume contribution.

In Figure 1.12, we plot in red the evolution of the relative perturbation in the dynamical ellipticity based on our SLE solutions. In black are solutions with 1σ correction, and 2σ solutions are in gray. Since the present Earth is in an interglacial period, the mean of the perturbation across the Cenozoic is negative, as glaciation involves a net transfer of mass into the poles, reducing the dynamical ellipticity. As discussed earlier, the viscoelastic response attempts to compensate for this reduction by increasing the flattening again, but the overall perturbation nonetheless remains negative. The mean of the oscillations over the Eocene approaches zero, with relatively high amplitude oscillations attributable to the poor constraint of the Mg/Ca ratios. The first major amplification in our model prediction of the perturbation occurs in a step-function like jump and is, as expected, across the Eocene-Oligocene transition (34 Ma), upon the initiation of a continental scale glaciation on Antarctica. After that, the unstable terrestrial East Antarctic Ice sheet results in moderate amplitude oscillations averaging around -0.04% (Figure 1.12). The following major Myr-scale variation in the secular trend occurs around the Miocene climatic optimum when the Earth enters a period of reduced glaciation reaching near ice-free conditions. During this period, the relative perturbation in the ellipticity trend drops to around -0.012%, then attains its global average again with the initiation of a larger scale glaciation on West Antarctica and Greenland, and with the stabilization of the EAIS. The final major variation in the trend occurs when the Earth transitions into its bipolar glaciation. During the last 3 Myr, the dynamical ellipticity enters a regime of extremely high amplitude oscillations that are maximized during the last million years. The average value during this period drops to around -0.05% (second panel of Figure 1.12), and reaches -0.07% during the most recent glacial cycles. Glacial peaks over the same period average around -0.11%, and reach -0.17% within the 2σ envelope. The

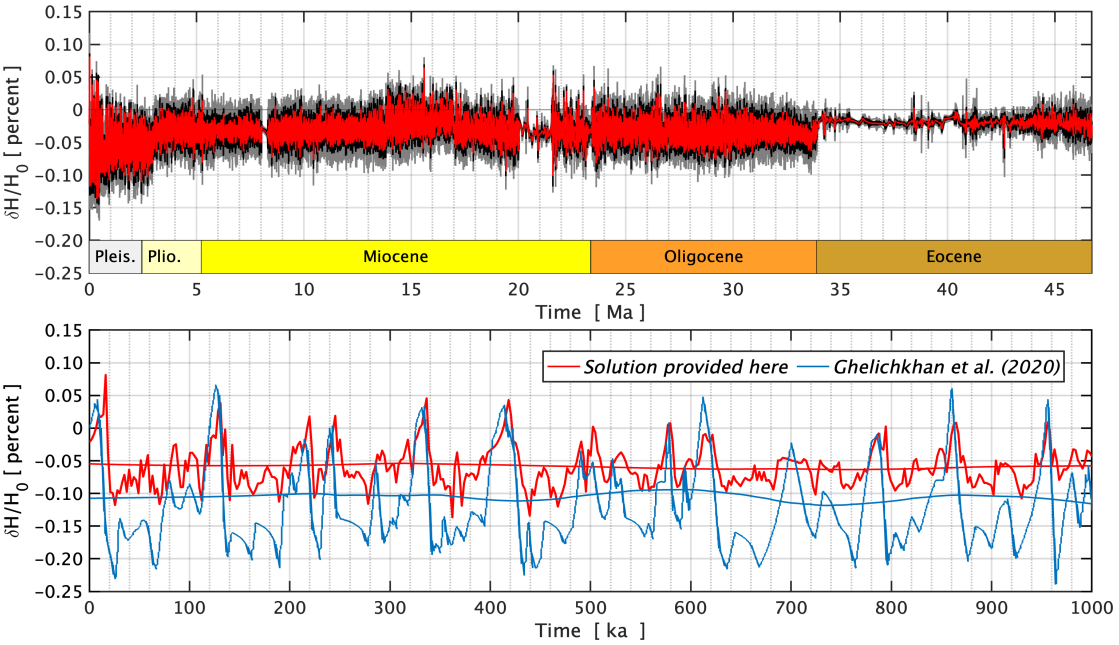

FIGURE 1.12: Model prediction of the evolution of the relative perturbation in dynamical ellipticty due to GIA over the past 47 Myr (the limit beyond which Mg/Ca data is compromised by large errors). *Top:* Evolution in red corresponds to the ice load variation derived from the M20 $\delta^{18}O$ splice of Figure 1.8 and internal profiles averaged from the PREM model with viscosity variation adopted from Lau et al. (2016b) . In black and gray are 40 other simulations accounting for 1σ and 2σ uncertainty in ice as discussed in the text. *Bottom:* A smaller window over the past million years only. Plotted is our solution compared to that provided in Ghelichkhan et al. (2020), each with their smoothed secular trends.

last interglacial period is marked with a global maximum with a relative perturbation of +0.08‰. We note that using simpler geometries of glacial spread yields results that are well confined within this uncertainty envelope. For instance, replacing the spatial evolution of the Antarctic glacial distribution by the spread of the Last Glacial Maximum (LGM), which almost represents a spherical cap confined within a circle of latitude at $-66°$, yields an evolution of the dynamical ellipticity within the 2σ uncertainty envelope for the Eocene and parts of the Miocene, and within 1σ for the rest of the Cenozoic.

In a similar procedure to that adopted here, Ghelichkhan et al. (2020) also derived the evolution of the dynamical flattening due to GIA over the last 3 Myr. In the second panel of Figure 1.12, we compare their solution to the present work over the past million years only. By visual inspection, the two solutions appear to evolve in-phase along the glacial cycles within the same order of magnitude. We also investigated the periodicity of both solutions and they matched identically. However, the evolution in Ghelichkhan et al. (2020) involves more amplified oscillations and a larger secular reduction in the dynamical ellipticity. In fact, the plotted secular trends show that our estimate is around

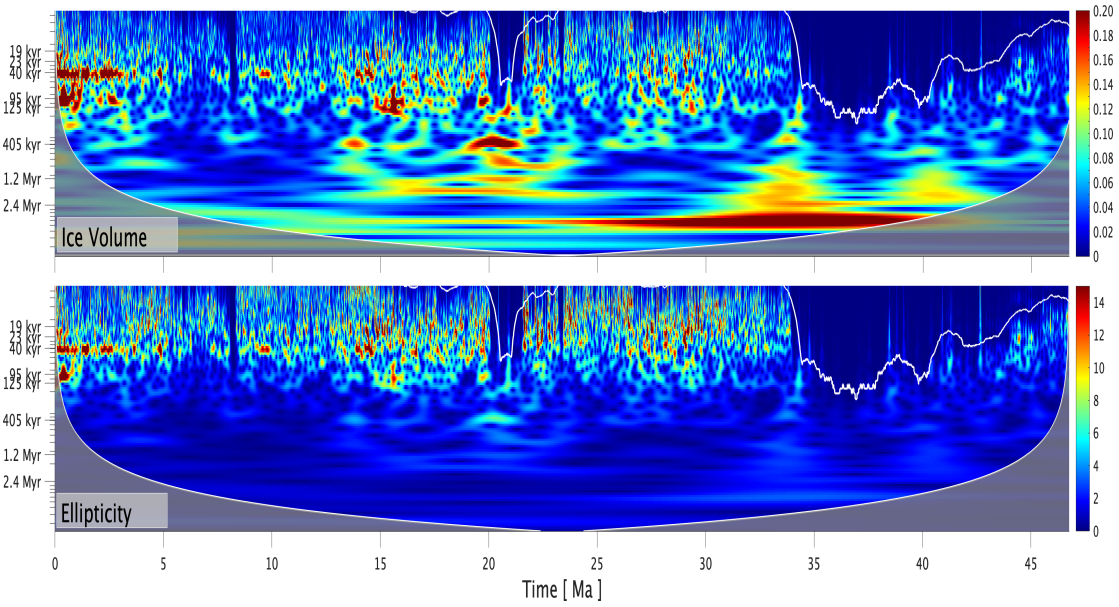

FIGURE 1.13: Continuous Wavelet Transforms (CWT) performed for the ice volume input provided to our simulations and the computed dynamical ellipticity evolution. The color mapping shows the relative power of varying amplitudes of spectral components of the data. Major spectral components associated with orbital forcing are identified on the y-axis. On top of the scalogram, the top white curve corresponds to the computed local nyquist frequency. The bottom shaded area represents the cone of influence, which is the area potentially affected by edge-effect artifacts, and is suspected to have time-frequency misinformation.

half that produced in their analysis (around -0.055% compared to -0.11%). Their study adopts an ice history from Raymo et al. (2011), which is also developed from foraminiferal oxygen data. However, it is not clear whether their direct scaling took into account the contribution of temperature or not, so that could partially justify the discrepancy. However, as our ice sensitivity envelope well constrains the long term trend, we expect the difference to have emerged from adopting different viscosity profiles for the Earth, thus we perform a viscosity sensitivity analysis in the following sections.

1.5.1 Pacing by astronomical beats

On timescales of $10^1 \sim 10^3$ kyr, the climatic state behaves as a nonlinear system that responds to quasi-periodic astronomical forcing. To better understand this modulation and its influence on the dynamical ellipticity variation, we perform a continuous wavelet transform (CWT) using MATLAB for both the ice input data and our dynamical ellipticity evolution solution. That of the former is similar to that present in Miller et al. (2020), and on a Myr timescale, it shows the general transition in the power spectrum from a

climate that was mostly dominated by long period orbital forcing, into a regime of short period forcing dominance. The long eccentricity and obliquity cycles are clearly present before the Eocene-Oligocene transition, along with a less prominent shorter eccentricity (405-kyr) modulation. The long periodicity dominance continued across the Oligocene, where large amplitude oscillations in ice volume were paced by the long obliquity cycle, along with an emerging dominance of the eccentricity period modulation (Boulila et al., 2011). During this period, we also identify the short eccentricity (100-kyr) and obliquity (40-kyr) bands being present to a lesser power (Pälike et al., 2006; Liebrand et al., 2017).

Across the Miocene, the attenuation of the long period orbital forcing control is clear, in favor of a growing effect for the 405-kyr eccentricity and 40-kyr obliquity cycles. While the first major expansion of terrestrial ice across the Ross Sea continental shelf took place at 24.5–24 Ma (Naish et al., 2001; Hauptvogel et al., 2017), Levy et al. (2019) suggested that the pacing by short obliquity forcing increases when ice sheets margins extend into marine environments, a persistent feature after the Miocene Climatic Transition (MCT, 15 Ma). Accordingly, our spectrogram is consistent with this analysis showing more power at the 40 kyr modulation starting around this period. During the last 3 Myr, blow-ups of ice volume were associated with extreme sea level falls and the onset of a continental scale northern hemispheric ice sheets. The 40-kyr obliquity cycle continued to be dominant with the 100-kyr eccentricity cycle which takes over across the last 800 kyr, although it was already present before this transition. We note the clear attenuation of the 405-kyr eccentricity cycle that was dominant during intervals of the Miocene, and the almost complete muting of the long eccentricity and obliquity cycles. This general trend was also identified in another compiled oxygen splice (Westerhold et al., 2020), explained by the spectrum of different nonlinear responses of the climate system to orbital forcing during different climate states: Eccentricity cycles should dominate the pacing of the Hothouse and the WarmHouse, as the eccentricity dominates temperature responses in low latitudes, while obliquity cycles dominate over the CoolHouse and the IceHouse, as high latitude glaciation is mostly influenced by the obliquity. This feature is also clear in our spectral analysis, except for the fact that long term obliquity pacing was also prominent even before the Oligocene.

As for our dynamical ellipticity evolution, its CWT is a filtered version of that of the ice input. Since its evolution is dictated by the evolution of the surface loading, one can expect to have an identical pacing for both signals. However, the solid Earth's response behavior is orchestrated by the relaxation spectrum of the normal modes whose timescales range between $10^{-1} \sim 10^{5}$ kyr (Figure 1.6). We also note that the

modes with the longest relaxation times correspond to buoyancy modes with very low normalized viscous amplitudes $k^L_{2,i}/s_{2,i}$, and thus minimal contribution to the summation in Eq. (1.151). Hence the viscous relaxation of the solid Earth acts as a high pass filter that will only keep short periodicities at play. Thus the CWT of the dynamical ellipticity attenuates the imprints of long orbital forcing and maintains the pacing by the short obliquity and eccentricity cycles. It must be stressed that this frequency filter is only associated with the physics under study. A complete study of solid Earth deformation would incorporate low frequency signals associated with mechanisms like mantle convection and plate tectonics.

1.5.2 Viscosity profiles sensitivity test

To better constrain the evolution of the dynamical ellipticity, we investigate the effect of mantle viscosity on the presented solution. The literature is very dense with modelled profiles, and we present a sample of them in Figure 1.14. The problem of inferring this radial profile from GIA observables dates back to Daly (1925). In general, relative sea level histories and post glacial rebound data, specifically those from Fennoscandia or Antarctica, constrain the upper mantle's viscosity, while post glacial signals from Canada are used to constrain the upper part of the lower mantle. Other geophysical observables, including the rate of change of J_2 and the polar wander are used to constrain the viscosity of the rest of the lower mantle, though these constraints may be challenged (Nakada et al., 2015; Adhikari et al., 2018). Other radial profiles were derived from joint inversion of data that include these GIA effects along with data related to mantle convection (Mitrovica and Forte, 1997, 2004; Moucha et al., 2008). Based on that, a community consensus has been established that the viscosity's radial profile increases some orders of magnitudes along the Earth's depth. However, precise accounts of this transition are almost irreconcilable in the literature (Figure 1.14). Particularly, some models infer a viscosity jump of two orders of magnitude (Lambeck et al., 2014; Nakada et al., 2015), while others advocate a less acute transition (e.g. the VM5a model Peltier et al., 2015)).

The low contrast viscosity profile we have used so far is presented in Lau et al. (2016b), and was constructed by analyzing GIA data using a combination of forward predictions and inversions based on nonlinear Bayesian inference. The result is constraining the upper mantle viscosity to around 3×10^{20} Pa s, the depth in between the mid-upper mantle and mid-lower mantle to around 10^{21} Pa s, and the bottom half of the lower

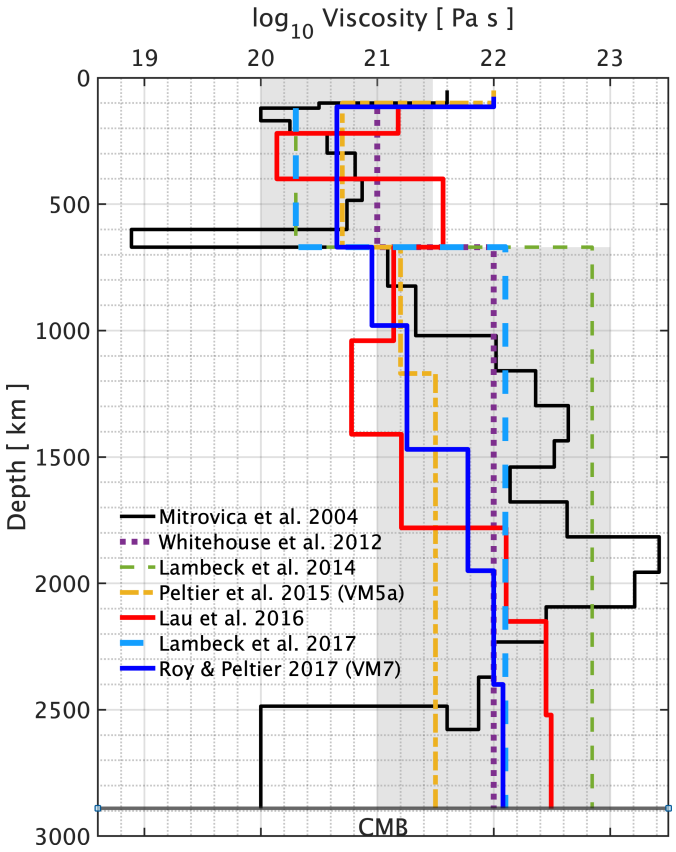

FIGURE 1.14: Mantle radial viscosity profiles from six different models in the literature (Mitrovica and Forte, 2004; Whitehouse et al., 2012; Lambeck et al., 2014; Peltier et al., 2015; Lau et al., 2016b; Lambeck et al., 2017; Roy and Peltier, 2017). Most models are inferred from inversions of GIA observables including sea level variations, rebound, rate of change of the second zonal harmonic, and polar wander. Almost all models involve at least an order of magnitude viscosity transition between the mean of the upper mantle and the mean of the lower mantle, however some models advocate more acute jumps than others, especially around the 660 Km seismic discontinuity. Shaded are the areas we cover in our sensitivity analysis.

mantle to a mean value in excess of 10^{22} Pa s. This low contrast viscosity model of Lau et al. (2016b) is very similar to the VM7 model of Roy and Peltier (2017) and the VM5a of Peltier et al. (2015), especially in the upper part of the lower mantle. In contrast, the profile used in Ghelichkhan et al. (2020) is the high viscosity contrast model of Mitrovica and Forte (2004) (further updated in Moucha et al. (2008) and Forte et al. (2009) removing the soft layer at the 660 km discontinuity). The latter model was derived from joint inversions of mantle convection and GIA constraints, but it is argued that it overestimates solid Earth relaxation times inferred from shoreline displacement histories in the James Bay area (Pendea et al., 2010). Models inferring more pronounced contrast across the seismic discontinuity are completely ruled out by the present true polar wander constraints and global positioning system (GPS) observations of the crustal

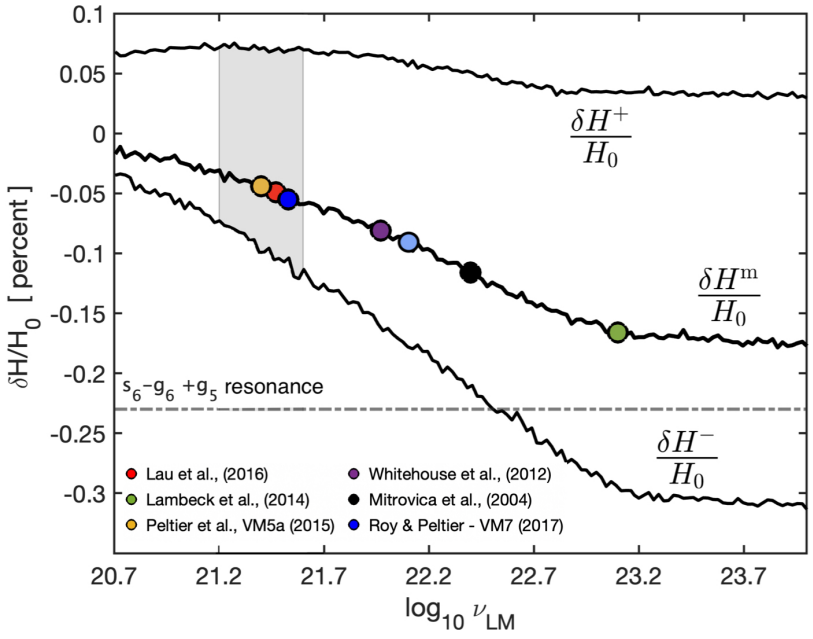

FIGURE 1.15: Relative perturbation in dynamical ellipticity over the past 3 Myr as a function of the lower mantle viscosity $\nu_{\rm LM}$. The upper mantle viscosity is fixed at $\nu_{\rm UM} = 0.5 \times 10^{21}$ Pa s. The middle branch, $\delta H^m/H_0$, represents the mean of the evolution, while the upper and lower branches represent the highest and lowest peaks in the evolution, denoted by $\delta H^+/H_0$ and $\delta H^-/H_0$ respectively. For each value of $\nu_{\rm LM}$ we perform 20 simulations that differ in the ice input to account for a random uncertainty in the interval $[0\ 2\sigma]$ as discussed in the text. Each point on the branches is thus the average of these simulations. Specified points on the branch refer to the specific viscosity profiles in Figure 1.14 using the same color coding. The shaded area refers to a part of the identified region $\mathcal{R}_1$ after constraining the lower mantle viscosity to $\log_{10}\nu_{\rm LM} \in [21.2, 21.6]$ by observed values of $\dot{J}_2$ (see text). We also marked the threshold value of $\delta H/H_0$, which if attained, the Earth could have crossed the $s_6 - g_6 + g_5$ resonance described in Eq. (1.18) (Laskar et al., 1993a).

vertical motion over the North American continent (Argus et al., 2021).

We proceed by performing a systematic exploration of the dynamical ellipticity solution's sensitivity to mantle viscosity variations. We perform simulations for effective viscosity values, namely a single value for the upper mantle and another single value for the lower mantle. For the specified models with more layering, volumetric averaging was performed over concentric spherical shells. As previously predicted by Mitrovica and Forte (1995), the results are mostly insensitive to viscosity variations in the upper mantle and almost entirely dependent on the lower mantle. The contribution of the upper mantle is expected to arise for higher order harmonics. Thus in Figure 1.15, we show the results of a suite of simulations for a span of lower mantle effective viscosity $\nu_{\rm LM}$ for fixed upper mantle effective viscosity $\nu_{\rm UM} = 0.5 \times 10^{21}$ Pa s. Considering a time interval covering the most recent 3 Myr, we plot the mean ($\delta H^m/H_0$), the upper envelope ($\delta H^+/H_0$), and

the lower envelope ($\delta H^{-}/H_0$) values of the evolution of our model predictions of the relative perturbation for each viscosity value. Each point on each branch is the average of 20 simulations that covered the ice uncertainty envelope. The negative values of $\delta H^{m}/H_0$ and $\delta H^{-}/H_0$ get more negative as the viscosity contrast between the upper and lower mantle increases. However, the slope of this monotonic trend is smaller for smaller values of ν_{LM} than it is for larger values. In contrast, $\delta H^{+}/H_0$ is less sensitive to viscosity variations. The time evolution of each simulation also shows that the difference between the long term trends grows in time, and this has two causes: the general feature of ice volume increase with time, and the accumulation of the non-linear effects due to the solid Earth's relaxation response.

Besides the reduction in the mean, Figure 1.15 shows that larger values of lower mantle viscosity, corresponding to a larger viscosity jump across the 660 km discontinuity, are associated with a broader separation between the peaks, $(\delta H^{+} - \delta H^{-})/H_0$. This behavior of the cycles' amplitudes, along with that of $\delta H^{m}/H_0$, is understandable when increasing the viscosity. The latter results in an increase in the relaxation times which reduces the value of the fluid Love number, and consequently the magnitude of the viscoelastic compensation effect. The larger the viscosity value, the more we approach the limit of elastic compensation only, which is characterized by a larger relative perturbation in the geoid and in the dynamical ellipticity. This justifies the plateau that we reach for $\log_{10}\nu_{\mathrm{LM}} > 23.2$ Pa s. In contrast, decreasing the viscosity results in decreasing the relaxation times and increasing the viscoelastic compensation effect, thus shrinking the relative perturbation. Accounting for this viscosity effect explains the difference we obtain with the larger amplitude oscillations in Ghelichkhan et al. (2020). The authors use the viscosity profile of Mitrovica and Forte (2004), characterized by a larger lower mantle viscosity than our volume averaged profile from Lau et al. (2016b). The offset between the two solutions in Figure 1.12 is now clear in Figure 1.15, where the black dot of the former profile corresponds to $\delta H^{m}/H_0 = -0.116\%$, while the red of the latter profile corresponds to $\delta H^{m}/H_0 = -0.05\%$.

Investigating the possibility of the past occurrence of the resonance scenario discussed after Eq. (1.18), we also mark in Figure 1.15 the threshold value required to cross the $s_6 - g_6 + g_5$ resonance exhibited by Laskar et al. (1993a). It is evident that the average value of the ellipticity variation does not cross this threshold, as it plateaus for large values of ν_{LM} as explained above. Values of $\delta H^{-}/H_0$, plotted on the lower curve, only cross the threshold value when $\log_{10}\nu_{\mathrm{LM}} > 22.6$ Pa s, i.e., for lower mantle viscosity

values excluded by the observational constraints (Argus et al., 2021), as we will further confirm in the following section.

1.5.3 Constraining the evolution of H by $\dot{J}_2$

The average and the amplitude of the ellipticity perturbation cycles are highly sensitive to the chosen viscosity profile. The presented solution in Figure 1.12 is based on a recent inference of the viscosity profile. To justify this choice in the context of our viscosity sensitivity study, we attempt to constrain our effective viscosity freedom by the observed values of $\dot{J}_2$, which as discussed earlier, is the major constraint used for lower mantle viscosity (Peltier, 1983). The first Satellite Laser Ranging (SLR) based estimate of the variation of J_2 was reported in Yoder et al. (1983) as a linear trend of $-3 \times 10^{-11}\mathrm{yr}^{-1}$. As time proceeded, further analysis of SLR data over longer time spans and using more satellites provided more estimates of the secular trend. In Figure 1.16 we compiled an inter-study comparison of this trend from different references. All studies until the late 1990s approximated the trend by a negative linear drift that is most likely an outcome of GIA (Peltier, 1983; Yoder et al., 1983; Cheng et al., 1989). However, analyses of the time span after 1995 showed a systematic decrease in this trend suggesting non-linearity (Cheng et al., 2013). The likely cause of this swing was attributed to modern melting of glaciers as an outcome of global warming (Roy and Peltier, 2011; Matsuo et al., 2013; Loomis et al., 2019; Chao et al., 2020). It is suggested that obtaining a pure GIA signal of $\dot{J}_2$ requires isolating this "contamination" of glaciers' modern melting (Ivins et al., 1993). This can lead to a pure GIA contribution of larger negative values [e.g. $-5.4 \pm 0.7 \times 10^{-11}\mathrm{yr}^{-1}$ (Lau et al., 2016b) ; $-(6.0 - 6.5) \times 10^{-11}\mathrm{yr}^{-1}$(Nakada et al., 2015)]. However, in our effective model, we restrict our study to the trend of $\dot{J}_2$ before the departure from linearity, and we consider this trend to be a pure GIA signal (Roy and Peltier, 2011).

On a grid covering the ranges of mantle viscosity values (Figure 1.14), and using the already developed ice distribution, we compute present day rates of variation of J_2. In Figure 1.16, we contour the surface of $\dot{J}_2$ in this effective viscosity space, and we specify level curves of relevance with respect to the observed values. The latter appear to be concentrated around two regions, which as discussed earlier, are mostly dependent on the lower mantle viscosity. This sensitivity is clear with the vertical structure of the level curves. Thus in total, two regions of viscosity combinations are preferred for the best fit with observational data: $\mathcal{R}_1$, a region enclosed by $\log_{10} \nu_{\mathrm{LM}} \in [21.2, 21.6]$ for

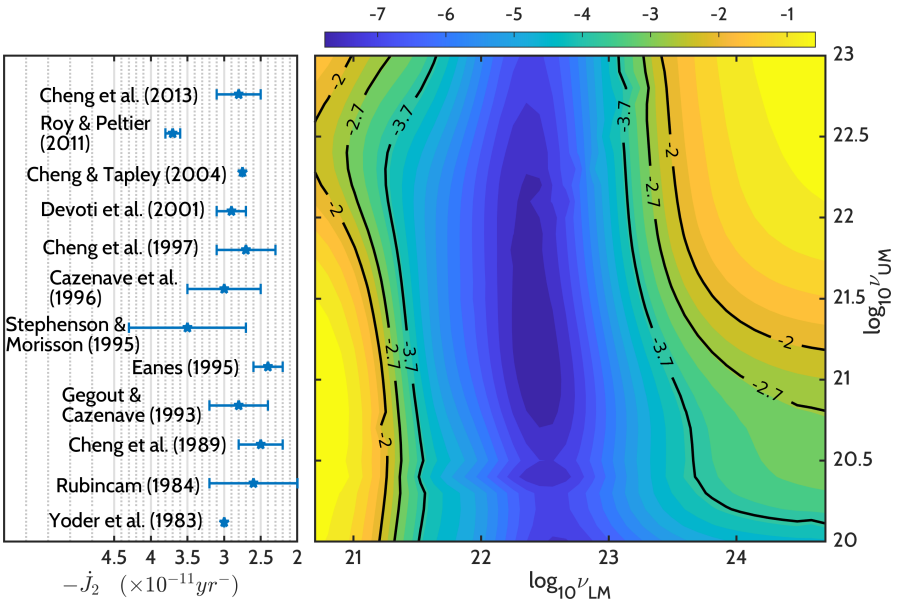

FIGURE 1.16: Constraining the choice of the viscosity profile by a comparison with observational estimates of $\dot{J}_2$. Left: an inter-study of computed values of the secular trend. We note that more recent analyses were based on larger time spans of SLR measurements and more satellites. In studies that showed the quadratic form of the variation, we only took the negative linear trend that is most likely attributed to the post glacial rebound (Roy and Peltier, 2011). We also note that, unlike the rest, the estimate of Stephenson et al. (1995) is based on the analysis of the Earth's rotational data over the recent centuries, which features a much larger uncertainty compared to other studies. Right: Level curves of the surface of computed $\dot{J}_2$ on a grid of combinations of viscosity values for the upper and lower mantle parts. We specified curves corresponding to relevant limits of observational values.

any value of ν_{UM}, and a region $\mathcal{R}_2$, enclosed by $\log_{10}\nu_{\mathrm{LM}} \in [23.1, 23.6]$ with large values of upper mantle viscosity. $\mathcal{R}_2$ diverges for lower values of upper mantle viscosity corresponding to an Earth with a very acute jump between the mantle parts (three to four orders of magnitude). Thus for values of upper mantle viscosity well constrained within the shaded region of Figure 1.14, $\mathcal{R}_1$ best fits the observed $\dot{J}_2$. Moreover, as explained earlier, the region $\mathcal{R}_2$ is ruled out by taking the second rotational datum into account (Peltier, 2015; Argus et al., 2021). Namely, modern observations of the speed (0.98° Myr^{-1}) and direction (79.9° W) of the true polar wander (Argus and Gross, 2004) can only be fitted using low viscosity contrast models. We identified $\mathcal{R}_1$ in the dynamical ellipticity evolution space in Figure 1.15. This region is consistent with the inferred low contrast viscosity profiles: VM5a (Peltier et al., 2015), VM7 (Roy and Peltier, 2017), and that of Lau et al. (2016b). This rectangular region represents our constrained estimates for the average and amplitude of the variation in the dynamical ellipticity. It clearly shows that the pure GIA contribution cannot drive the Earth into the $s_6 - g_6 + g_5$ resonance.

1.6 Summary

In this chapter, we provide the evolution of the dynamical ellipticity of the Earth over the past 47 Myr due to the varying glacial surface load. We start by computing the viscoelastic Love numbers in the normal modes theory. There we identified an essential limitation of the propagator matrix method when solving the differential deformation system: increasing the stratification level of the Earth's model produced erratic response spectra in the high frequency regime. However, we proved that this limitation can be judiciously avoided due to the convergence of the viscoelastic response with the modelled layering of the Earth.

After computing the surface loading viscoelastic Love numbers, we constructed a detailed history of the glacial variation during the Cenozoic starting from benthic foraminiferal records. We used a recently-compiled far-field record of benthic oxygen isotopes (Miller et al., 2020). As both oceanic temperature and ice volume take part in the isotopic variation, the contributions were deconvolved using benthic Mg/Ca records as an independent temperature proxy. Though we translated the glacial contribution to ice volume, we proceed with caution noting the following:

- Our inference of the global glacial volume from the isotopic record is only a rough estimate of glacial volume that gains more precision when accompanied by a record of oxygen isotope composition in the ice sheets (Langebroek et al., 2010).
- This global ice volume inference could be compromised by variations in atmospheric moisture transport and the thickness of ice sheets yielding an overestimate of glacial volume (Winnick and Caves, 2015). Uncertainties in using this isotope record can also propagate from the used temperature contribution correction (Cramer et al., 2011), especially given evidence on discrepancies between ice growth reconstruction and the isotopic record over the last glacial cycle (Pico et al., 2017), or over the Pliocene (Gasson et al., 2016a).
- The comparison of the sea level equivalent of the record with the sea level construction from continental margins (Miller et al., 2020) can also be compromised by effects of mantle dynamic topography rather than pure glacial dynamics (Forte et al., 1993; Moucha et al., 2008).
- However, our ice sensitivity tests proved that the correction to the dynamical ellipticity evolution due to an ice uncertainty propagating from an error of ±20

m in eustatic sea level equivalence does not corrupt model predictions (Figure 1.12). Moreover, uncertainties in the spatial distribution of ice are minimized by the symmetries of the second zonal harmonic. The geological evidence employed (see Table 1.3) is also a critical backbone of the analysis we report here.

Based on this ice history, we used the sea level equation solver of Spada and Melini (2019) to self-consistently trace the evolution of the surface loading between the ice caps and the oceans. Once the sea level variation is established, we directly recover the evolution of the geopotential of the Earth, from which we isolate the dynamical ellipticity.

The viscoelastic response of the Earth features the major uncertainty in retrieving an accurate evolution of the dynamical ellipticity. The predicted evolution of the dynamical ellipticity mostly depends on the Earth's viscosity profile, specifically on the lower mantle viscosity. As the latter is not well determined in the literature, we studied the sensitivity of our prediction of the dynamical ellipticity perturbation to lower mantle viscosity variations. We then proceeded with a misfit analysis of model predictions of $\dot{J}_2$ with recent observational estimates. The final outcome is constraining the average relative perturbation of the dynamical ellipticity over the past 3 Myr to $[-0.031\%, -0.055\%]$, with a lower boundary inside $[-0.07\%, -0.13\%]$, and a less sensitive upper limit around $+0.07\%$. Scrutinizing our model dynamical ellipticity perturbation evolution over the past 700 Kyr, and using the same viscosity profiles, our mean and peak-to-peak estimates are smaller than those computed by Mitrovica and Forte (1995) (for the averaged viscosity profile of Mitrovica and Forte (2004), our maximum negative perturbation of $\delta H/H_0$ is -0.21%, while their maximum is -0.3%). In contrast, our estimates are larger than those less acute in Peltier and Jiang (1994).

These intervals also account for the uncertainty propagating from the used ice distribution. Our evolution extends to the mostly unipolar interval of the Cenozoic with an average inside $[-0.02\%, -0.045\%]$. Going beyond 47 Ma, our ice input, and consequently our prediction of the ellipticity evolution are compromised by the growing error in the Mg/Ca record.

CHAPTER 2

REVISITING THE LONG-TERM TIDAL EVOLUTION OF THE EARTH-MOON SEPARATION

2.1 Introduction

The Earth-Moon duo represents, to a large extent, a unique system. Setting aside Pluto & Charon, the satellite to planet radius ratio in the Earth-Moon system is the largest among all known analogues (Peale, 1999). The ambiguous nature and -most probably tiny- size of the lunar core (e.g., Viswanathan et al., 2019), the large total angular momentum, the partially molten early Moon with a deep magma ocean (e.g., Maurice et al., 2020), and the current orbital configuration of the system, all along with other features require an intricate lunar formation and evolution theory to be satisfactorily explained. Here, we brief on the history and state-of-the-art of some perplexing challenges in modelling the Earth-Moon system. We focus on three “conundrums" associated with reconciling presently measured observables of the Earth-Moon system with formation, early, and long term evolution models.

❖ *The isotopic crisis and the angular momentum reconciliation*

Pre-Apollo theories of lunar formation were largely based on dynamical scenarios, since little was established on the chemical composition of the lunar building blocks (Cummings, 2019). Theories included, but were not limited to:

- rotational fission, in which the rapidly rotating proto-Earth flung away the lunar forming material by the mere act of the centrifugal force. The theory is primarily accredited to Darwin (1879) who, aided by the work of Poincaré (1885) on the equilibrium forms of rotating fluids, argued that the rapid rotation of the proto-Earth can bring its spheroidal equilibrium into an unstable pear-shaped mass distribution. Consequently, for 4-5 hr length of day, resonances between the solar semi-diurnal tide and the free oscillations of the fluid may rupture

the unstable configuration into two or more parts. Although the theory was later challenged on the basis of the insufficient amplitudes of the resonance tides when tamed by core-fluid friction (Jeffreys, 1930), it remained alive, with various modifications, until the beginning of the Apollo explorations. Perhaps the reason for the staying power had to do with linking the rupture scenario during the lunar genesis with the formation of oceanic basins (Fisher, 1882; Wise, 1963).

- collisional fission; the less recognized fission scenario, whereby fission occurred after the Earth collided with another "planetoid" (Daly, 1946).
- co-accretion, in which the Earth and the Moon formed simultaneously, close to each other within the circumsolar cloud of dust and gas (Schmidt, 1958; Urey, 1962). Namely, satellite formation is the result of particles encountering the planetary embryos with certain velocities such that they do not agglomorate on them, but rather join a swarm revolving around the planet. The swarm particles also collide amongst themselves, and accumulated to form independent embryos, the future satellites. Schmidt (1958) argues on the same basis that the ring of Saturn is the exception of the process where the swarm particles did not agglomerate due to the strong Saturnian tides. On the same day of writing this paragraph, the work of Wisdom et al. (2022) was published arguing, in contrast, that the rings are the byproduct of a long-lived satellite that was shattered upon approaching Saturn.
- capture; as a correction to the theory of the Earth and the Moon co-accreting in the same region, pre-Apollo estimates of the density of the Moon suggested the simultaneous accretion in different regions of the solar accretion disk. Namely, the lunar low iron content is an anomaly among terrestrial solar system objects (Kaula, 1969), and thus it should have formed elsewhere. Subsequently, its orbit was disrupted so that it crossed the Earth's orbit, and it was eventually captured by the Earth (Urey, 1963).

The genesis of the Moon via a giant impact with the Earth emerged as the leading theory at the 1984 "Origin of the Moon" conference, as it seemed best able to explain several features of the system (Wood, 1986). A class of simulated impact models demonstrated that a giant collision can leave behind an iron-poor disk around the Earth (Benz et al., 1986), thus explaining the iron content anomaly of the Moon (Kaula, 1969). This class of models required the impact to occur when the Earth was half-grown (Cameron, 1997, 2001), such that they can explain the lunar mass. However, these models could not explain the accretion of lunar siderophile-rich material. It

was then suggested that the impact scenario should involve a grazing, Mars-sized impactor, having a very small relative velocity at infinity (Canup and Asphaug, 2001), and it should have happened at the end of the Earth's accretion phase (Canup, 2004). Namely, an oblique impact, characterized with a total Earth-Moon angular momentum (AM) roughly the same as the present, can generate a debris disk up to twice the mass of the Moon. This disk would later follow classic accretion scenarios to form the a Moon depleted in iron and volatile elements, and would account for the AM in the current Earth-Moon system (Ida et al., 1997; Salmon and Canup, 2012; Canup et al., 2015).

The tale does not end here because this so-called "canonical impact" scenario presents a conundrum: the simulated disk composition is predominated by that of the impactor, while the Earth largely maintains its pre-impact composition. This means that the produced Moon would be compositionally distinct from the Earth's mantle, in contrast with high-precision measurements of lunar isotopes (Zhang et al., 2012; Herwartz et al., 2014). This quandary was later coined by some as the "isotopic crisis" of the giant impact model (Melosh, 2014). The likely resolution of the problem is another modification of the giant impact scenario by increasing the impact AM. This allows for a disk and a planet that have close to equal proportions of impactor material and consequently similar isotopic signatures (Ćuk and Stewart, 2012).

Yet again, the high AM impact scenario solves a chemical problem but poses another dynamical one: the consistency with the current AM requires significant loss of AM post-impact. Capture into the evection resonance was the first promising mechanism proposed to solve this problem (along with another problem described below; Touma and Wisdom, 1998; Touma and Sridhar, 2015). This resonance occurs when the apsidal precession period of the Moon is equal to the orbital period of the Earth, and during which the luni-solar angle at the lunar apse maintains a value of $-\pi/2$. AM is thus transferred to the Earth-Sun system by virtue of the solar tidal torque as the Moon migrates outwards. The resonance would occur at 4.6 Earth radii ($R_\oplus$) for an initial 5 hr LOD (Touma and Wisdom, 1998), but increasing the initial AM by decreasing the initial LOD and increasing the Earth's oblateness shifts its location outwards (Ćuk and Stewart, 2012). However, the scenario requires maintaining a high lunar eccentricity which may be challenging (Tian et al., 2017; Ward et al., 2020), thus near-resonant dynamics are currently emerging as the more plausible scenario (Wisdom and Tian, 2015; Rufu and Canup, 2020).

❖ *The present and post-impact inclination reconciliation*

When classic tidal models trace the current 5 degrees of lunar inclination backwards in time, the inclination of the Moon when it was close to the Earth is found to be $\sim$ 12 degrees (Goldreich, 1966; Touma and Wisdom, 1998; Rubincam, 2016). However, in the canonical giant impact theory described above, the Moon should have formed by re-accretion in the Earth's equatorial plane, thus with a zero-inclination orbit. Reconciling the inclination upon formation with the long term inclination evolution until the present of the outwards-migrating Moon is often coined as the inclination problem. Proposed theories of inclination excitation ranged from scenarios involving resonances: capture into the evection then eviction resonances (Touma and Wisdom, 1998), or resonances between the proto-Moon and the debris disk (Ward and Canup, 2000); to scenarios involving a high obliquity (60-80 degrees), high AM Earth (Ćuk et al., 2016), which can produce a lunar orbit inclined by 30 degrees via the notorious Laplace plane instabilities (Tremaine et al., 2009; Farhat and Touma, 2021) [see also Tian and Wisdom, 2020 for arguments against this scenario based on vertical AM constraints]. Other scenarios involve inclination excitation via collisionless encounters with planetesimals over a period of tens of millions of years post-formation (Pahlevan and Morbidelli, 2015). In all cases, any posited inclination excitation scenario should also account for inclination damping as a result of tidal heating during the lunar magma ocean phase (Tyler, 2008), or the high lunar obliquity during the Cassini state transition (Chen and Nimmo, 2016). Other constrains on the the orbital history can also be derived from the lunar figure (Matsuyama et al., 2021; Downey et al., 2022).

2.2 The time-scale problem of the lunar origin

The third problem of the Earth-Moon evolution that is the focus of our work here is the time-scale problem of lunar origin. Namely, it corresponds to the difficulty in modelling the tidal history of the Earth-Moon separation such that the presently measured rate of increase in the lunar semi-major axis is properly evolved in the past to predict the correct formation age of the Moon. This is exactly the problem we address and expand on next in this chapter.

Ever since the Moon has formed close to the Earth, the energy dissipation[1] of gravitational tides on Earth has been depleting the Earth's rotational AM and pumping the

[1]Hereafter, when we discuss energy dissipation we refer to that only driven by astronomical forcing; i.e. that dependent on the Earth's rotation and lunar semi-major axis, which is described at the present as anomalously high.

lunar orbital AM. This net outcome is the effect of the axial component of the torque exerted by the lunar tidal potential on the mass redistribution of the Earth produced by the deformational action of the tidal potential itself. This deformation response is delayed relative to the forcing potential because of the dissipative mechanisms in the Earth's constituent layers. Consequently, the torque retards the Earth's rotational velocity (LOD increases), and the reciprocal torque on the Moon causes its semi-major axis to increase (e.g., Spencer Jones, 1939; Dickey et al., 1994). The rate of the latter variation is measured at the present to sub-mm-precision and is well constrained to 38.30 ± 0.08 mm/year using lunar laser ranging (LLR; e.g., Williams and Boggs, 2016). This rate is associated with an energy dissipation rate of 3.7 TW (Egbert and Ray, 2003).

It is now well established that the present dissipation rate is largely dominated by the effect of oceanic tides, with much smaller contributions from solid Earth dissipation. Ray et al. (1999) estimated the oceanic signature in the present ΔLOD to be 2.28 ms/century. The contribution due to solid Earth represents only 6% of the total tidal variation of LOD (Mathews and Lambert, 2009). During most of the 20th century, oceanic dissipation was thought to occur solely in shallow seas, and dissipation in deep oceans was neglected (Jeffery, 1921; Lamb, 1945). However, with TOPEX/Poseidon altimetry, it was shown that up to 30% of dissipation comes from the deep ocean (Egbert and Ray, 2000).

The total dissipative-driven variation in LOD is often associated with a series of $k \sin \chi$ – or more commonly k/Q – factors for the phase-delayed potential of tides (Williams and Boggs, 2016). The whole time-scale problem of the lunar origin reduces to how these factors, the tidal Love number k, the quality factor Q, and the phase lag χ are modeled. The traditional theory of tides is characterized by two essential features: First, the tidal response is decomposed into a Fourier series with harmonic modes; then each mode is associated with a separate magnitude and phase delay (Darwin, 1879; Kaula, 1964). When adopted to bodily tides, this procedure was often reduced into models associated with ad hoc tools such as the constant geometric lag model (MacDonald, 1964; Goldreich, 1966), or the constant time lag model (Mignard, 1979, 1980, 1981; Hut, 1981). The former assumes a uniform tidal response independent of orbital and rotational variations (frequency independent phase lag, or quality factor), except for a mere change of sign at the 1:1 resonance. As Efroimsky and Makarov (2013) demonstrated, the constant geometric lag model implicitly sets the time lag of the response to be also constant when used with the traditional expression of the polar component of the torque (for e.g., Eq. (4.159) of Murray and Dermott, 1999). Both the quality factor and the time lag cannot be

simultaneously frequency independent and thus this model is inherently contradictory. Another commonly used model for long-term studies of the Earth-Moon system is the constant time lag (Δt) model (e.g., Mignard, 1979; Neron de Surgy and Laskar, 1997), where Δt represents the interval between the time of lunar stress on the Earth and the time at which the Earth establishes its equilibrium.

A variety of these models were employed by Touma and Wisdom (1994a) to study the evolution of the Earth-Moon system. As also noted earlier by Goldreich (1966), Touma and Wisdom (1994a) demonstrated that different tidal models bring little differences into the evolution history. In Figure 2.1 we adopt their results that summarize the time-scale problem, which is vividly encountered for any of the used tidal models. Namely, integrating the lunar semi-major axis backwards from the present, it collapses onto the Earth in between one and two billion years ago, an event coined previously by Munk (1968) as a “Gerstenkorn event". This modelled prediction of a younger Moon was not completely discredited pre-Apollo missions. While advocating for the theory of lunar capture, Gerstenkorn (1955) estimated the age of the Moon at 1.4 Ga. Similar estimates from tidal modelling of 1.68 Ga (MacDonald, 1966), 1.78 Ga (Baldwin, 1965), and 1.4-2.3 Ga (Slichter, 1963), were also present, along with estimates of the age of the lunar maria at 3.6 Ga (Hartmann, 1965). All these estimates raised questions about lunar formation theories discussed at the time.

With Apollo came strict geological and geochemical constraints on the lunar age, revealing it has roughly the same age of the Moon (e.g., Tera and Wasserburg, 1972; Hertogen et al., 1977; Turcotte and Kellogg, 1986; Halliday et al., 1996; Lee et al., 1997; Nemchin et al., 2009; Barboni et al., 2017; Maurice et al., 2020). The problem now shifted from being a lunar formation problem to a tidal modelling problem. Namely, the tidal theory was required to address the following issue: how to reconstruct a history of the Earth-Moon distance with an associated tidal dissipation rate that is higher at the present than it was in the past with a closer Moon. More specifically, it should be elucidated how tidal dissipation can have a non-monotonic dependence on the Earth-Moon separation. The transition to oceanic tidal modelling was then inevitable, especially given that the analytical theory of oceanic tides was simultaneously being developed (e.g., Doodson, 1958; Wunsch, 1967; Longuet-Higgins, 1968; Longuet-Higgins and Pond, 1970; Cartwright, 1977; Platzman, 1983, 1984). The likely resolution of the problem of explaining the “anomalous" high dissipation at the present was then attributed to an enhanced resonant state of dissipation in the oceans.

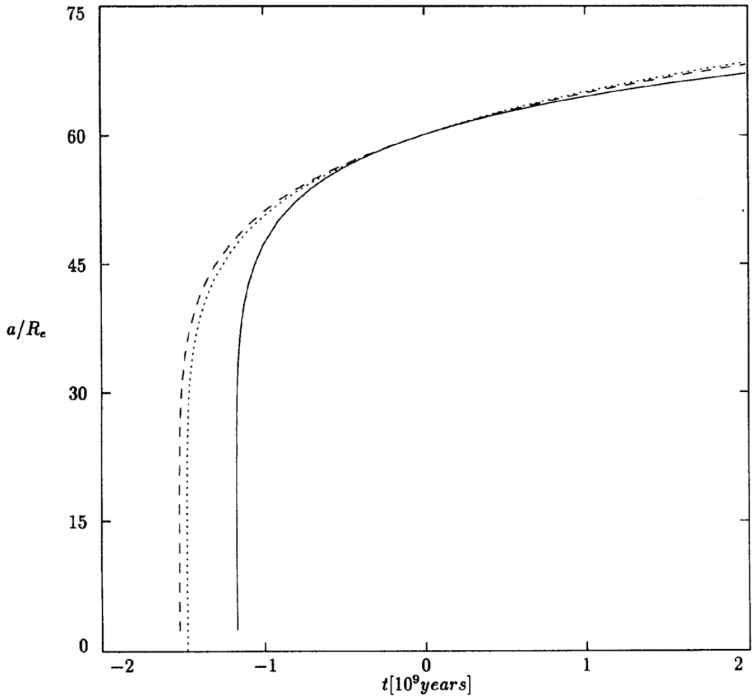

FIGURE 2.1: The time-scale problem of the Lunar origin. The semi-major axis of the lunar orbit is tidally evolved forward and backward in time, and plotted on the y-axis normalized by the Earth radius. The solid line corresponds to the tidal evolution with the constant time lag model. The dotted and dashed lines correspond to the evolutions assuming constant phase shifts and geometric lags. In the three curves, the backward evolution depicts that the lunar orbit collapses onto the Earth between 1 and 2 Ga. Figure reproduced from Touma and Wisdom (1994a).

There is no established consensus to date, however, on the reason behind pushing the oceans into this resonant state. A long standing hypothesis is the re-organization of the oceanic eigenoscillation spectrum that accompanied the variation in the continental configuration (e.g., Brosche and Sündermann, 1984; Ooe, 1989). Namely, the periodic build up and disintegration of super-continents and the associated opening and closing of oceans (Wilson cycles) should impose a spectral shift, attenuation, or amplification in oceanic normal modes (Gotlib and Kagan, 1985). Evidence supporting the role of continentality in establishing the resonance can be drawn from the frequency overlap between the forcing frequency and the oceanic normal models computed for realistic configurations (Sanchez, 2008).

Early models of the Earth-Moon tidal evolution that took into account the varying oceanic resonant properties were proposed by Webb (1980, 1982a,b) and Hansen (1982). In Webb's series of papers, the dynamical equations of tides were solved for a hemispherical ocean of constant depth to evaluate the tidal torque. The hemispherical ocean was first fixed about the equator to mimic the present pacific ocean, then later allowed to vary

on the surface between equatorial and polar configurations. For each oceanic position, tidal energy distribution was averaged over a tidal cycle, and then weighted averaging was performed over the oceanic position to reflect the average response, in a statistical sense, to luni-solar tidal forcing. The dependence of this average response on the tidal frequency was then used to compute the Earth-Moon tidal evolution. Thus the model of Webb can be considered the first to incorporate, rather implicitly, the effect of continental drift. Besides the prescribed uniform oceanic depth, Webb's model was also tuned by another free parameter: a bottom friction coefficient that enters linearly in the momentum equation.

A similar procedure was adopted in Hansen (1982), where the tidal torque was also derived for an idealized hemispherical ocean bounded by a continental counterpart, with a center either at the equator or at the pole. The results reported in both works, though ignoring the effect of solid Earth deformation on the ocean and dissipation in the mantle itself, provided evidence to the fact that a Gerstenkorn's event was not necessary, i.e. the modelled closest encounter between the Earth and the Moon occurs beyond 4.5 Ga. The idealized models of Webb and Hansen opened a can of worms on studying the effect of continental drift on Earth-Moon evolution, and left the field with a series of novel works on how to evade the Gerstenkorn event (e.g., Kagan and Maslova, 1994; Kagan, 1997; Abe et al., 1997; Poliakow, 2004). The circle was recently closed back onto numerical modelling, with the growing sophistication and resolution of tidal numerical simulations (e.g., `OTIS`, Egbert et al., 1994). The possible added value of numerical modelling over analytical modelling lies in the capacity to account for realistic continental configurations, and that the inclusion of dissipation is not restricted to a linear term. However, both the drag coefficient and the tidal conversion dissipative terms in the numerical models are also free parameters that need to be prescribed (Green and Huber, 2013). Paleo-tidal dynamics were simulated for the LGM (21 ka), Pliocene (3 Ma), Miocene (25 Ma), Eocene (50 Ma), Cretaceous (116 Ma) and the Permian-Triassic (252 Ma) in Green et al. (2017). Tidal dissipation was then computed for each simulation and interpolated in-between to establish a history of the Earth-Moon system. More recently. Daher et al. (2021) used the same continental configurations in Green et al. (2017) to compute possible histories of the Earth-Moon system assuming each of the configurations is fixed in time, or using MCMC sampling between them. The results of the latter work with all possible continental sampling indeed avoids any close Earth-Moon encounter, but the Moon would still have a high orbit around its formation time.

Along with the spectral shifting due to continental drift, it is argued that paleo-dissipation might have also varied significantly during ice ages, as areas of continental shelves vary with sea level (Griffiths and Peltier, 2009; Arbic and Garrett, 2010). However, both ice ages and basin geometry cycles have much smaller periodicities compared to the Earth's age (Boulila et al., 2018; Farhat et al., 2022b). Accurately accounting for such level of realism in deep-time modeling is hindered by the accumulating uncertainty. It is estimated that the "world uncertainty", that is the lithospheric percentage that has already been subducted at given time and is consequently unavailable for use to constrain tectonic and paleo-continental reconstructions, is as high as 60% by $\sim$ 140 Ma and 65% by $\sim$ 220 Ma (Müller et al., 2016; Tetley et al., 2019). Thus if it is indeed that the effect of continentality dominates controlling the tidal response, then it might very well be impossible to accurately model the tidal history of the Earth-Moon system, and sampling/statistical optimization is where the field should be heading.

Fortunately, as we are concerned with the long term tidal modelling, the explanation provided by continental drift for the current resonant state does not involve a robust mechanism. As Tyler (2021) argues, the frequency overlap between the tidal forcing and the basin normal modes is not sufficient to enhance resonances, but an overlap in spatial form is required too. Namely, basin modes that shift with continental drift do not feature the same degree-two harmonic form of the tidal forcing, and thus are not directly forced by tidal forces. In fact, long wavelength tides are excited first, and these can then scatter energy into basin modes. Therefore, the effect of continental drift should be secondary in driving paleo-dissipation. The primary player would then be the spin rate of the Earth. The latter establishes a robust mechanism of exciting tidal resonances (e.g., Auclair-Desrotour et al., 2018, 2019a; Tyler, 2021), and thus the decreasing spin rate of the Earth has played the dominant role in driving the Earth into its current enhanced resonance.

With the question of the hierarchy of contributions to paleo-disspation still open-ended, and with our quest to compute the tidal history over geological timescales, we attempt in our work below to compromise between the practicality of effective models that parametrize continentality, and the realism of costly numerical models that depend on paleogeographic reconstruction. We thus undertake a systematic exploration of the time varying tidal dissipation in the oceans by studying two configurations: a hemispherical ocean that migrates on the Earth mimicking continental drift, and a global ocean. We first expand on the theory of computing the tidal flows for these two configurations below, then we detail on the model of the evolution over geological timescales.

2.3 Oceanic tidal dynamics

2.3.1 The tidal response of a hemispherical ocean

We start with the computation of the tidal response of a hemispherical ocean on the surface of the Earth. The formalism is heavily based on earlier works (Longuet-Higgins and Pond, 1970; Webb, 1980) describing the free oscillations and the tidal response of a hemispherical ocean symmetric about the equator; we expand upon it here by adopting the true polar wander scenario (Webb, 1982a) to solve for a general oceanic position. We note that the mathematical formulation of the referenced works (Longuet-Higgins and Pond, 1970; Webb, 1980, 1982a) contains several misprints that we correct here.

In the co-planar problem under study (ignoring the Earth's obliquity and the lunar orbital inclination), we define a frame of reference co-rotating with the Earth, with a spin vector of $\vec{\Omega} = \Omega\hat{z}$, Ω being the Earth's spin rate and $\hat{z}$ as the unit vector along its figure axis. In this frame, we use the spherical coordinates (r, θ, λ) denoting the radius, the co-latitude, and the longitude respectively, and their corresponding unit vectors $(\hat{r}, \hat{\theta}, \hat{\lambda})$. We start with the linearized system of equations that describe the conservation of momentum and mass in a tidally forced shallow oceanic layer[2] (e.g., Laplace, 1798; Lamb, 1945; Longuet-Higgins, 1968; Tyler, 2011):

$$\partial_t \vec{u} + \sigma_R \vec{u} + \vec{f} \times \vec{u} + g\boldsymbol{\nabla}\zeta = g\boldsymbol{\nabla}\zeta_{eq}, \tag{2.1a}$$

$$\partial_t \zeta + \boldsymbol{\nabla} \cdot (H\vec{u}) = 0, \tag{2.1b}$$

where $\vec{u} = u_\theta\hat{\theta} + u_\lambda\hat{\lambda}$ is the horizontal velocity field, g is the gravitational acceleration at the surface, ζ is the oceanic depth variation, ζ_{eq} is the equilibrium depth variation, H is the uniform oceanic thickness (the first of only two free parameters in our model), and σ_R is the Rayleigh (or linear) drag frequency (Matsuyama, 2014; Auclair-Desrotour et al., 2018); the latter is an effective dissipation parameter characterizing the damping of the oceanic tidal response by dissipative mechanisms (the second free parameter in our model). On Earth, σ_R mainly accounts for the loss of energy of the barotropic flow by bottom friction in the shallow seas and the loss of energy over ridges in the deep oceans through the conversion of barotropic tidal flows into internal gravity waves (which in some local areas represents nearly 85% of the total dissipation; see for e.g., Carter et al., 2008). For the latter mechanism, the Rayleigh drag frequency can actually be related to

[2]In the rest of this chapter, we use the notation ∂_x^n for $\frac{\partial^n}{\partial x^n}$.

physical parameters such as the Brunt-Väisälä frequency, which quantifies the stability of the ocean's stratification against convection (see, e.g., Gerkema and Zimmerman, 2008), and to the length-scale of topographical patterns at the oceanic floor (Bell Jr, 1975; Palmer et al., 1986). In Eq. (2.1), the Coriolis parameter $\vec{f}$ is given by

$$\vec{f} = 2\Omega \cos\theta \hat{r}, \tag{2.2}$$

the horizontal gradient operator $\boldsymbol{\nabla}$ is defined as

$$\boldsymbol{\nabla} = R^{-1}\left[\hat{\theta}\partial_\theta + \hat{\lambda}\,(\sin\theta)^{-1}\,\partial_\lambda\right], \tag{2.3}$$

and the horizontal divergence of the velocity field $\boldsymbol{\nabla}\cdot\vec{u}$ as

$$\boldsymbol{\nabla}\cdot\vec{u} = (R\sin\theta)^{-1}\left[\partial_\theta\left(\sin\theta u_\theta\right) + \partial_\lambda u_\lambda\right], \tag{2.4}$$

with R being the Earth's radius. Finally, we remark that the interaction of tidal flows with the mean flows of the oceanic circulation are ignored in the momentum equation, namely, Eq. (2.1a).

For $\vec{u} = \partial_t\vec{x}$, where $\vec{x}$ is the horizontal tidal displacement field, the momentum equation (2.1a) is rewritten as

$$\left[\partial_t^2 + (\sigma_\mathrm{R} + \vec{f}\times)\partial_t\right]\vec{x} + g\left(\boldsymbol{\nabla}\zeta - \boldsymbol{\nabla}\zeta_\mathrm{eq}\right) = 0. \tag{2.5}$$

Following Proudman (1920b), we use Helmholtz's theorem at this step (e.g., Arfken and Weber 1999, Chapter 1) to decompose the horizontal displacement vector field into

$$\vec{x} = \boldsymbol{\nabla}\Phi + \boldsymbol{\nabla}\Psi\times\hat{r}, \tag{2.6}$$

where $\boldsymbol{\nabla}\Phi$ is a curl-free vector field ($\boldsymbol{\nabla}\times(\boldsymbol{\nabla}\Phi) = \vec{0}$) and $\boldsymbol{\nabla}\Psi\times\hat{r}$ is a divergence-free vector field ($\boldsymbol{\nabla}\cdot(\boldsymbol{\nabla}\Psi\times\hat{r}) = 0$). In the above equation, we introduce the divergent displacement potential Φ and the rotational displacement streamfunction Ψ (e.g., Gent and McWilliams 1983; Webb 1980; Tyler 2011), with the latter accounting for the vortical component of the tidal displacement field (e.g., Vallis 2017). As discussed by Fox-Kemper et al. (2003), while the Helmholtz decomposition is unique for infinite domains, this is not true for bounded domains such as hemispherical oceanic shells due to lack of additional physical constraints on the boundary conditions for either of the components of the sum. There are boundary conditions only on the total flux at

coastlines. Impermeability is a typical boundary condition: the net flux normal to the coast is zero, which is expressed as $\vec{x} \cdot \hat{n} = 0$, where $\hat{n}$ designates the outward pointing unit vector defining the normal to the coast. Following Webb (1980, 1982a), we assume that both components of the flux satisfy this condition, namely

$$\hat{n} \cdot \boldsymbol{\nabla}\Phi = 0, \qquad \hat{n} \cdot (\boldsymbol{\nabla}\Psi \times \hat{r}) = 0. \tag{2.7}$$

We note that the second condition of the above equation can be rewritten as $(\hat{r} \times \hat{n}) \cdot \boldsymbol{\nabla}\Psi = 0$, which implies that Ψ is constant along the coastline (in the following, we set $\Psi = 0$ at the oceanic boundary). This condition thus means that the coastline corresponds to a closed streamfunction contour, which depicts a distinct gyre of the tidal flow.

Although arbitrary, the assumption that both components of the flux satisfy the impermeability condition has been widely used to study the dynamics of ocean basins because of its convenience relative to other possible conditions (e.g., Gent and McWilliams 1983; Watterson 2001; Han and Huang 2020). In particular, this assumption provides a unique decomposition apart from an arbitrary additive constant to each function, Φ and Ψ. Moreover, the second condition given by Eq. (2.7) enforces the orthogonality of the curl-free and divergence-free components of the tidal flow. By combining together the identity $\boldsymbol{\nabla} \cdot (\Phi \boldsymbol{\nabla}\Psi \times \hat{r}) = (\boldsymbol{\nabla}\Psi \times \hat{r}) \cdot \boldsymbol{\nabla}\Phi$ and Gauss' theorem (e.g., Arfken and Weber 1999)

$$\int_O \boldsymbol{\nabla} \cdot (\Phi \boldsymbol{\nabla}\Psi \times \hat{r})\, dA = \oint_{\partial O} \Phi\, (\boldsymbol{\nabla}\Psi \times \hat{r}) \cdot \hat{n}\, d\ell, \tag{2.8}$$

with dA and $d\ell$ being the infinitesimal area element of the hemispherical oceanic domain, O, and length element of the coastline, ∂O, respectively, we obtain

$$\int_O (\boldsymbol{\nabla}\Phi) \cdot (\boldsymbol{\nabla}\Psi \times \hat{r})\, dA = \oint_{\partial O} \Phi\, (\boldsymbol{\nabla}\Psi \times \hat{r}) \cdot \hat{n}\, d\ell. \tag{2.9}$$

As the second condition of Eq. (2.7) enforces $(\boldsymbol{\nabla}\Psi \times \hat{r}) \cdot \hat{n} = 0$ along the coastline, it follows that

$$\int_O (\boldsymbol{\nabla}\Phi) \cdot (\boldsymbol{\nabla}\Psi \times \hat{r})\, dA = 0, \tag{2.10}$$

meaning that the components $\boldsymbol{\nabla}\Phi$ and $\boldsymbol{\nabla}\Psi \times \hat{r}$ each belong to one of the two orthogonal subspaces that form the space of horizontal displacements satisfying the assumed boundary conditions. We remark that the orthogonality of the Helmholtz decomposition is not necessarily verified in the general case since it is itself a consequence of the

specific boundary condition chosen for the divergence-free component of the tidal flow.

The functions Φ and Ψ are expanded in terms of complete sets of eigenfunctions over the domain O such that:

$$\Phi(\theta, \lambda, t) = \sum_{r=1}^{\infty} p_r(t)\phi_r(\theta, \lambda), \tag{2.11}$$

$$\Psi(\theta, \lambda, t) = \sum_{r=1}^{\infty} p_{-r}(t)\psi_r(\theta, \lambda). \tag{2.12}$$

The eigenfunctions (ϕ_r, ψ_r) satisfy, over the oceanic domain (O), the Helmholtz equations given by (e.g., Riley et al. (1999), Chapter 21)

$$\nabla^2\phi_r + \mu_r\phi_r = 0, \tag{2.13}$$

$$\nabla^2\psi_r + \nu_r\psi_r = 0, \tag{2.14}$$

and, along the coastline (∂O), the boundary conditions given by Eq. (2.7)

$$\hat{n} \cdot \nabla\phi_r = 0, \qquad \psi_r = 0. \tag{2.15}$$

Here we introduced the horizontal Laplacian

$$\nabla^2 = (R\sin\theta)^{-2}\left[\sin\theta\,\partial_\theta\left(\sin\theta\,\partial_\theta\right) + \partial_{\lambda\lambda}\right], \tag{2.16}$$

and the real eigenvalues, μ_r and ν_r, associated with the eigenfunctions ϕ_r and ψ_r, respectively. We note that the eigenfunctions are normalized such that

$$\int_O \phi_r\phi_s dA = \int_O \psi_r\psi_s dA = \delta_{rs}, \tag{2.17}$$

where the notation δ_{rs} referring to the Kronecker δ-symbol is $\delta_{rs} = 1$ for $r = s$ and 0 otherwise. Using these conditions, the eigenfunctions are defined as:

$$\phi_r = \frac{\alpha_{n,m}}{R} P_n^m(\cos\theta)\cos m\lambda, \tag{2.18}$$

$$\psi_r = \frac{\alpha_{n,m}}{R} P_n^m(\cos\theta)\sin m\lambda, \tag{2.19}$$

with eigenvalues $\mu_r = \nu_r = n(n+1)/R^2$ and the normalization coefficient

$$\alpha_{n,m} = \sqrt{\frac{2n+1}{\pi}\frac{(n-m)!}{(n+m)!}\frac{1}{1+\delta_{m0}}}. \tag{2.20}$$

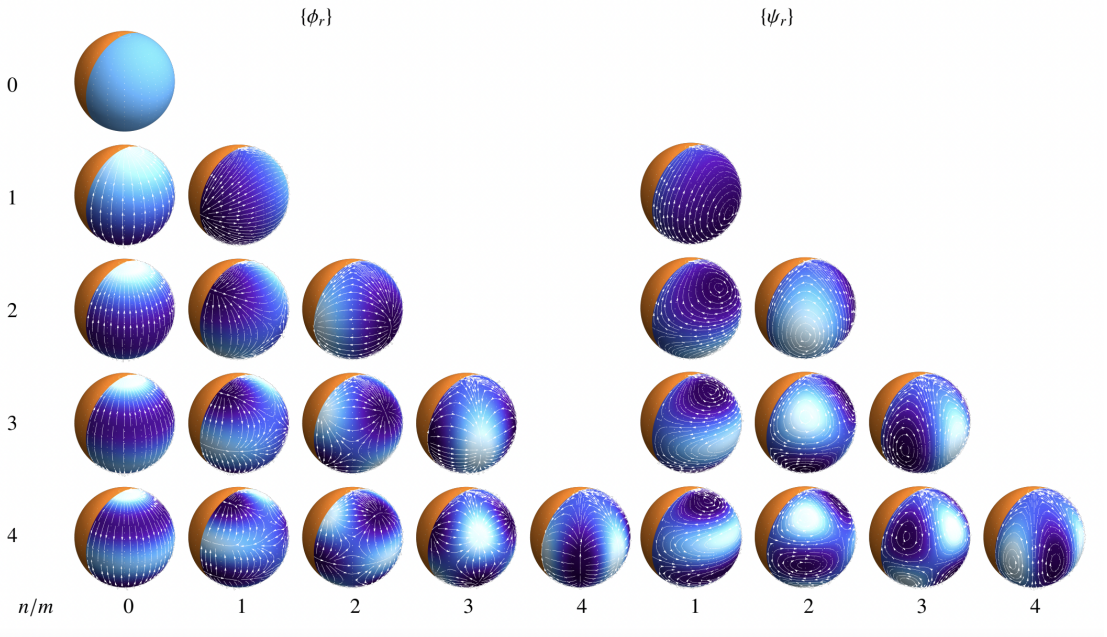

FIGURE 2.2: Eigenfunctions ϕ_r (left) and ψ_r (right), and the associated tidal flows. The eigenfunctions defined by Eqs. (2.18) and (2.19) are plotted over the hemispherical oceanic domain for $0 \leq n \leq 4$ (from top to bottom) and $0 \leq m \leq n$ (from left to right). Bright or dark colors designate positive or negative values of the eigenfunctions, respectively. Streamlines indicate the tidal flows corresponding to $\boldsymbol{\nabla}\phi_r$ for the set $\{\phi_r\}$ and to $\boldsymbol{\nabla}\psi_r \times \hat{r}$ for the set $\{\psi_r\}$.

In Eqs. (2.18) and (2.19), each harmonic index, r, of the eigenfunctions is associated with a degree, n, and order, m, and the expansion functions are the associated Legendre functions (defined in Section 2.3.1.2). In the definition of ϕ_r Eq. (2.18), $n \in \mathbb{N}$ and $m = 0, 1, ..., n$ while in the expression of ψ_r Eq. (2.19), $n \in \mathbb{N}^*$ and $m = 1, 2, ..., n$. By convention, we set $\psi_0 = 0$ hereafter. Figure 2.2 shows the eigenfunctions ϕ_r and ψ_r for $1 \leq m \leq n \leq 4$ and the streamlines of the associated tidal flows.

The eigenfunctions (ϕ_r, ψ_r) can be split into two sets describing tidal solutions that are symmetric or anti-symmetric about the equator, and thus one can decide, based on the symmetry of the tidal forcing, on the associated set of eigenfunctions that need to be considered using a classification scheme (Longuet-Higgins, 1968; Longuet-Higgins and Pond, 1970) for the pairs (n, m). However, in our model, where the ocean is no longer symmetric about the equator, both symmetric and anti-symmetric eigenfunctions are required. In substituting the definitions of Eqs. (2.11), (2.12), and (2.13) into the continuity equation (2.1b), we find that:

$$\zeta = H \sum_{r=1}^{\infty} \mu_r p_r \phi_r. \tag{2.21}$$

What is left to complete the solution is finding the coefficients p_r and p_{-r} by substituting the series expansions in the momentum equation (2.1a) and multiplying by $\boldsymbol{\nabla}\phi_r$ and $\boldsymbol{\nabla}\psi_r \times \hat{r}$, then integrating over the oceanic area. Starting with the former, we get

$$\begin{aligned}
&\sum_{s=0}^{\infty} \left(\partial_t^2 p_s + \sigma_{\mathrm{R}} \partial_t p_s + g H p_s \mu_s - g\zeta_{\mathrm{eq},s}\right) \boldsymbol{\nabla}\phi_s \cdot \boldsymbol{\nabla}\phi_r \\
&\quad + \left(\partial_t^2 p_{-s} + \sigma_{\mathrm{R}} \partial_t p_{-s}\right) (\boldsymbol{\nabla}\psi_s \times \hat{r}) \cdot \boldsymbol{\nabla}\phi_r \\
&\quad + \partial_t p_s \left(\vec{f} \times \boldsymbol{\nabla}\phi_s\right) \cdot \boldsymbol{\nabla}\phi_r + \partial_t p_{-s} \left[\vec{f} \times (\boldsymbol{\nabla}\psi_s \times \hat{r})\right] \cdot \boldsymbol{\nabla}\phi_r = 0.
\end{aligned} \tag{2.22}$$

The product of the gradients of two eigenfunctions is computed using Green's first identity (e.g., Strauss (2007), Chapter 7)

$$\int_O \boldsymbol{\nabla}\phi_s \cdot \boldsymbol{\nabla}\phi_r dA = \int_{\partial O} \phi_s \left(\boldsymbol{\nabla}\phi_r \cdot \hat{n}\right) d\ell - \int_O \phi_s \boldsymbol{\nabla}^2 \phi_r dA. \tag{2.23}$$

The first term on the right-hand side vanishes as it includes the boundary condition at the coast (Eq. 2.15). The second term is computed using the eigenvalue equation (Eq. 2.13) and the normalization condition, thus

$$\int_O \boldsymbol{\nabla}\phi_s \cdot \boldsymbol{\nabla}\phi_r dA = \mu_r \delta_{rs}. \tag{2.24}$$

Rearranging the other terms using vector identities, we rewrite Eq. (2.22) as

$$\begin{aligned}
&\sum_{s=0}^{\infty} \left(\partial_t^2 p_s + \sigma_{\mathrm{R}} \partial_t p_s + g H p_s \mu_s - g\zeta_{\mathrm{eq},s}\right) \mu_r \delta_{r,s} \\
&+ \left(\partial_t^2 p_{-s} + \sigma_{\mathrm{R}} \partial_t p_{-s}\right) \int_O (\boldsymbol{\nabla}\psi_s \times \hat{r}) \cdot \boldsymbol{\nabla}\phi_r \, dA + \partial_t p_s \int_O \vec{f} \cdot (\boldsymbol{\nabla}\phi_s \times \boldsymbol{\nabla}\phi_r) \, dA \\
&+ \partial_t p_{-s} \int_O \left(\vec{f} \cdot \hat{r}\right) (\boldsymbol{\nabla}\phi_r \cdot \boldsymbol{\nabla}\psi_s) \, dA = 0.
\end{aligned} \tag{2.25}$$

The third term vanishes due to orthogonality (see Eq. 2.10), while upon replacing the Coriolis term by its definition in Eq. (2.2) we are left with

$$\begin{aligned}
&\left(\partial_t^2 p_r + \sigma_{\mathrm{R}} \partial_t p_r + g H p_r \mu_r - g\zeta_{\mathrm{eq},r}\right) \mu_r - 2\Omega \sum_{s=1}^{\infty} \partial_t p_s \int \cos\theta \hat{r} \cdot (\boldsymbol{\nabla}\phi_r \times \boldsymbol{\nabla}\phi_s) \, dA \\
&+ 2\Omega \sum_{s=1}^{\infty} \partial_t p_{-s} \int \cos\theta \, (\boldsymbol{\nabla}\phi_r \cdot \boldsymbol{\nabla}\psi_s) \, dA = 0.
\end{aligned} \tag{2.26}$$

To close the system, we multiply the momentum equation with $\boldsymbol{\nabla}\psi_r \times \hat{r}$ to get

$$\begin{aligned}
&\sum_{s=0}^{\infty} \left(\partial_t^2 p_s + \sigma_{\mathrm{R}} \partial_t p_s + g H p_s \mu_s - g\zeta_{\mathrm{eq},s}\right) \boldsymbol{\nabla}\phi_s \cdot (\boldsymbol{\nabla}\psi_r \times \hat{r}) \\
&+ \partial_t p_s \left(\vec{f} \times \boldsymbol{\nabla}\phi_s\right) \cdot (\boldsymbol{\nabla}\psi_r \times \hat{r}) + \partial_t p_{-s} \left[\vec{f} \times (\boldsymbol{\nabla}\psi_s \times \hat{r})\right] \cdot (\boldsymbol{\nabla}\psi_r \times \hat{r}) \\
&+ \left(\partial_t^2 p_{-s} + \sigma_{\mathrm{R}} \partial_t p_{-s}\right) (\boldsymbol{\nabla}\psi_s \times \hat{r}) \cdot (\boldsymbol{\nabla}\psi_r \times \hat{r}) = 0. \qquad (2.27)
\end{aligned}$$

Integrating Eq. (2.27) over the area of the ocean and using basic vector calculus, we get

$$\begin{aligned}
&\sum_{s=0}^{\infty} \left(\partial_t^2 p_s + \sigma_{\mathrm{R}} \partial_t p_s\right) \int \boldsymbol{\nabla}\psi_s \cdot \boldsymbol{\nabla}\psi_r dA - \partial_t p_s \int \left(\vec{f} \cdot \hat{r}\right) (\boldsymbol{\nabla}\phi_s \cdot \boldsymbol{\nabla}\psi_r)\, dA \\
&\quad - \partial_t p_{-s} \int \left(\vec{f} \cdot \hat{r}\right) \hat{r} \cdot (\boldsymbol{\nabla}\psi_r \times \boldsymbol{\nabla}\psi_s)\, dA = 0, \qquad (2.28)
\end{aligned}$$

where upon replacing the Coriolis term as before we finally obtain

$$\begin{aligned}
&\partial_t^2 p_{-r} + \sigma_{\mathrm{R}} \partial_t p_{-r} - \frac{2\Omega}{\nu_r} \sum_{s=1}^{\infty} \partial_t p_s \int \cos\theta\, (\boldsymbol{\nabla}\phi_s \cdot \boldsymbol{\nabla}\psi_r)\, dA \\
&- \frac{2\Omega}{\nu_r} \sum_{s=0}^{\infty} \partial_t p_{-s} \int \cos\theta \hat{r} \cdot (\boldsymbol{\nabla}\psi_r \times \boldsymbol{\nabla}\psi_s)\, dA = 0. \qquad (2.29)
\end{aligned}$$

We identify in Eqs. (2.26) and (2.29) the so-called "gyroscopic coefficients" (e.g., Proudman, 1920a,b) that are defined as

$$\begin{aligned}
\beta_{r,s} &= -\int_O \cos\theta\, \hat{r} \cdot (\boldsymbol{\nabla}\phi_r \times \boldsymbol{\nabla}\phi_s)\, dA, \\
\beta_{r,-s} &= \int_O \cos\theta\, \boldsymbol{\nabla}\phi_r \cdot \boldsymbol{\nabla}\psi_s dA, \\
\beta_{-r,s} &= -\int_O \cos\theta\, \boldsymbol{\nabla}\psi_r \cdot \boldsymbol{\nabla}\phi_s dA, \\
\beta_{-r,-s} &= -\int_O \cos\theta\, \hat{r} \cdot (\boldsymbol{\nabla}\psi_r \times \boldsymbol{\nabla}\psi_s)\, dA, \qquad (2.30)
\end{aligned}$$

with $\beta_{-s,r} = -\beta_{r,-s}$. These coefficients carry the effect of rotational distortion to the tidal waves and the boundary conditions imposed by the coastlines. Using these definitions, Eqs. (2.26) and (2.29) form an infinite linear system in the coefficients $p_r(t)$ and $p_{-r}(t)$ that is expressed as

$$\partial_t^2 p_r + \sigma_{\mathrm{R}} \partial_t p_r + g H \mu_r p_r - g\zeta_{\mathrm{eq},r} + \frac{2\Omega}{\mu_r} \sum_{s=-\infty}^{s=\infty} \beta_{r,s} \partial_t p_s = 0, \qquad (2.31)$$

$$\partial_t^2 p_{-r} + \sigma_R \partial_t p_{-r} + \frac{2\Omega}{\nu_r} \sum_{s=-\infty}^{s=\infty} \beta_{-r,s} \partial_t p_s = 0. \tag{2.32}$$

This system is then transformed to the frequency domain, truncated, and solved spectrally as a function of the tidal forcing frequency σ. We re-write it as

$$\begin{aligned} &- \sigma^2 p_r - i\sigma\sigma_R p_r + gH\mu_r p_r - g\zeta_{\mathrm{eq},r} - \frac{2i\sigma\Omega}{\mu_r} \sum_{s=-\infty}^{s=\infty} \beta_{r,s} p_s = 0, \\ &- \sigma^2 p_{-r} - i\sigma\sigma_R p_{-r} - \frac{2i\sigma\Omega}{\nu_r} \sum_{s=-\infty}^{s=\infty} \beta_{-r,s} \partial_t p_s = 0. \end{aligned} \tag{2.33}$$

Once the series p_r is found, the root mean squared tidal amplitude is computed via (Webb, 1980)

$$H_{\mathrm{rms}} = \sqrt{\frac{H}{\pi R^2} \sum_{r=1}^{\infty} \mu_r^2 p_r^* p_r}, \tag{2.34}$$

where * represents complex conjugation.

2.3.1.1 Coupling the hemispherical ocean response with solid Earth deformation

In the tidal theory under study, the solid component of the Earth is subject to viscoelastic deformation as a result of three contributions: the direct tidal effect of the tidal perturber, the loading effect of the perturbed oceanic shell, and the effect of gravitational self-attraction between the oceanic shell and the solid part (Farrell, 1972; Zahel, 1980). If we were to take these into account when studying oceanic tides, ζ becomes a function of two moving surfaces: the free oceanic surface, ζ_{os}, and the vertically deforming solid surface ζ_{ss}.

In the frame co-rotating with the Earth, the gravitational potential is expressed as (e.g., Auclair-Desrotour et al., 2019a)

$$U(\vec{r}, \vec{r}\,') = \frac{GM}{|\vec{r} - \vec{r}\,'|} - \frac{GM}{r'^2} r \cos\theta\,, \tag{2.35}$$

where G is the gravitational constant, M is the mass of the tidal perturber (the Sun or the Moon), and r' is the distance between the Earth and the perturber. In the shallow ocean approximation, the tidal potential at the Earth's surface ($r = R$) is

$$U^{\mathrm{T}}(\theta, \lambda, \vec{r}\,') = U(R, \theta, \lambda, \vec{r}\,') - \frac{GM}{r'}\,, \tag{2.36}$$

where a constant offset was removed as it does not contribute to the tidal force. In the frequency domain, the associated complex gravitational potential U^{T}, such that $\mathcal{U}^{\mathrm{T}} = \mathrm{Re}\{U^{\mathrm{T}}\}$, is expanded spectrally in Fourier series and spatially in spherical harmonics, with complex coefficients $U_n^{m;s}$ as (Kaula, 2013; Auclair-Desrotour et al., 2019a)

$$U^{\mathrm{T}} = \sum_{n=2}^{\infty} \sum_{m=-n}^{n} \sum_{s=-\infty}^{\infty} U_n^{m;s} P_n^m(\cos\theta) \exp\{i(\sigma_m^s t + m\lambda)\}, \tag{2.37}$$

where s is an integer and the tidal forcing frequency $\sigma_m^s = m\Omega - sn_{\mathrm{orb}}$, the frequency n_{orb} being the orbital mean motion of the tidal perturber. In the absence of obliquity, the n^{th} harmonic of the tidal potential $U_n^{m;s}$ is given by (Ogilvie, 2014)

$$U_n^{m;s} = \frac{GM}{a}\left(\frac{R}{a}\right)^n A_{n,m,s}(e). \tag{2.38}$$

Here a is the semi-major axis of this perturber and $A_{n,m,s}(e)$ are dimensionless functions of the orbital eccentricity of the perturber e computed via the Hansen coefficients $X_s^{n,m}$(Laskar, 2005). The functions $A_{n,m,s}(e)$ read as (Correia et al., 2014)

$$A_{n,m,s}(e) = (2-\delta_{m,0}\,\delta_{s,0})(1-\delta_{m,0}\,\delta_{s<0})\sqrt{\frac{2(n-m)!}{(2n+1)(n+m)!}} P_n^m(0) X_s^{-(n+1),m}(e) \tag{2.39}$$

Here $\delta_{k,l}$ is the usual Kronecker delta symbol such that $\delta_{k,l} = 1$ if $k = l$ and 0 otherwise; analogously, $\delta_{s<0} = 1$ if $s < 0$. In our study, we restrict the tidal potential to the dominant contribution of the semi-diurnal component identified by $n = m = s = 2$ and corresponding to the tidal frequency $\sigma_2^2 = 2(\Omega - n_{\mathrm{orb}})$. For this component, while neglecting the small orbital eccentricity of the Sun and the Moon, $A_{2,2,2}(0) = \sqrt{3/5}$. Hereafter, we use U_n^{T} to represent a single harmonic (n, m, s) of the tidal potential. This harmonic of degree n is defined as

$$U_n^{\mathrm{T}} = U_n^{m;s} P_n^m(\cos\theta) \exp\left\{i(\sigma_m^s t + m\lambda)\right\} . \tag{2.40}$$

In what follows, we use σ instead of σ_m^s to simplify the notation. Subject to U_n^{T} only, the equilibrium oceanic depth would be $\bar{\zeta} = U_n^{\mathrm{T}}/g$. However, the loading effect of the deforming oceanic shell adds to the tidal potential and they both affect the ocean surface $\bar{\zeta}_{\mathrm{os}}$ and the ocean floor corresponding to the solid surface $\bar{\zeta}_{\mathrm{ss}}$. The former is expressed as (Matsuyama, 2014)

$$\bar{\zeta}_{\mathrm{os}} = \frac{h_n^{\mathrm{T}} U_n^{\mathrm{T}}}{g} + \sum_l \frac{3\rho_{\mathrm{oc}}}{(2l+1)\rho_{\mathrm{se}}} h_l^{\mathrm{L}} \zeta_l, \tag{2.41}$$

where $\rho_{\rm oc}$ and $\rho_{\rm se}$ stand for the uniform oceanic and solid Earth densities, respectively. In this equation, the oceanic depth variation, ζ, is decomposed into spherical harmonics (defined by Eq. (2.98)) such that

$$\zeta_l(\theta,\lambda,t) = \sum_{m=-l}^{l} \zeta_l^m(t) P_l^m(\cos\theta)\exp(im\lambda)\,. \tag{2.42}$$

Although ζ given in (2.21) is only defined over the oceanic hemisphere, this decomposition over the whole sphere is required when applying the Love numbers. Using the orthogonality of spherical harmonics, and the fact that $\zeta(\theta,\lambda,t)=0$ over the continental hemisphere, Eq. (2.42) may also be expressed as

$$\zeta_l(\theta,\lambda,t) = \frac{1}{2}\sum_{m=0}^{l}\alpha_{lm}^2 \int_O \zeta(\theta',\lambda',t) P_l^m(\cos\theta) P_l^m(\cos\theta')\times\cos(m(\lambda-\lambda'))\,d\Omega\,, \tag{2.43}$$

where the integral is computed over the solid angle spanned by the ocean. The second contribution to the equilibrium tide, which is due to the solid redistribution of mass, is

$$\bar{\zeta}_{\rm ss} = (1+k_n^{\rm T})\frac{U_n^{\rm T}}{g} + \sum_l \frac{3\rho_{\rm oc}}{(2l+1)\rho_{\rm se}}(1+k_l^{\rm L})\zeta_l. \tag{2.44}$$

In equations (2.41) and (2.44), we used the tidal Love numbers $k_n^{\rm T}$ and $h_n^{\rm T}$, and the surface-loading Love numbers $k_n^{\rm L}$ and $h_n^{\rm L}$, where the first of each set is the transfer function corresponding to the gravitational response, and the second codes for the vertical displacement. We emphasize that here the Love numbers are defined in the Fourier domain, therefore, they correspond to the intrinsic mechanical impedances of the solid part that relate its visco-elastic tidal response to tidal forcings in the permanent regime and they characterise both the elastic deformation of the body and its anelastic deformation resulting from energy dissipation due to viscous friction in the Earth's interior. In the general case, the four Love numbers ($k_n^{\rm T}$, $h_n^{\rm T}$, $k_n^{\rm L}$, and $h_n^{\rm L}$) can be computed from internal structure models (e.g., Tobie et al., 2005, 2019; Bolmont et al., 2020). In our work, for the sake of simplicity, we use the closed-form solutions derived for a uniform solid interior (Munk and MacDonald, 1960)

$$\left\{k_n^{\rm T}, h_n^{\rm T}, k_n^{\rm L}, h_n^{\rm L}\right\} = \frac{1}{(1+\tilde{\mu}_n)}\left\{\frac{3}{2(n-1)}, \frac{2n+1}{2(n-1)}, -1, -\frac{2n+1}{3}\right\}, \tag{2.45}$$

where $\tilde{\mu}_n$ is a complex dimensionless effective shear modulus, with a form that is dependent on the chosen solid rheology (Efroimsky, 2012; Renaud and Henning, 2018). To

specify $\tilde{\mu}_n$, we consider an Andrade rheology (Andrade, 1910), which has an advantage over the commonly used Maxwell rheology in attenuating the rapid decay of the anelastic component of the deforming solid Earth for high tidal frequencies (Castillo-Rogez et al., 2011; Auclair-Desrotour et al., 2019a). This is particularly useful with regard to avoiding an overestimation of the tidally dissipated energy of the solid part during early eons. For this rheology, $\tilde{\mu}_n$ takes the following form (Findley et al., 1977; Efroimsky, 2012):

$$\tilde{\mu}_n = \frac{4(2n^2+4n+3)\pi R^4}{3nGM_{\rm E}^2}\frac{\mu_{\rm E}}{1+(i\sigma\tau_{\rm A})^{-\alpha_{\rm A}}\Gamma(1+\alpha_{\rm A})+(i\sigma\tau_{\rm M})^{-1}}, \tag{2.46}$$

where $M_{\rm E}$ is the mass of the Earth, $\mu_{\rm E}$ its average rigidity, and Γ is the gamma function (Abramowitz et al., 1988); $\alpha_{\rm A}$ is a dimensionless rheological exponent determined experimentally (Castelnau et al., 2008; Petit and Luzum, 2010); $\tau_{\rm A}$ is the anelastic Andrade timescale; and $\tau_{\rm M}$ the Maxwell relaxation time defined as the ratio of viscosity to rigidity. For a volumetric average of the mantle's shear modulus $\mu_{\rm E} = 17.3\times10^{10}$ Pa, and volumetric average of viscosity deduced from inversions of Lau et al. (2016b), we have $\tau_{\rm M} = 685$ yrs. The values $\alpha_{\rm A} = 0.25$ and $\tau_{\rm A} = 2.19\times10^4$ yrs that we use in our model are adopted from Auclair-Desrotour et al. (2019a). All the applied parameter values are summarized in Table 2.3.

Taking the effect of solid Earth deformation into account, we replace the equilibrium tide $\zeta_{\rm eq}$ in the momentum equation (2.1a) by the difference $\bar{\zeta}_{\rm os} - \bar{\zeta}_{\rm ss}$ of Eqs.(2.41) and (2.44) and we resolve it in the Fourier domain using the forcing tidal frequency, σ. The modified momentum conservation equations is then expressed as

$$i\sigma\vec{u} + \sigma_{\rm R}\vec{u} + \vec{f}\times\vec{u} = -g\boldsymbol{\nabla}\left(-\gamma_n^{\rm T}\bar{\zeta} + \sum_l \gamma_l^{\rm L}\zeta_l\right), \tag{2.47}$$

with $\bar{\zeta} = U_n^{\rm T}/g$, and where the loading and tidal tilt factors are defined as (Matsuyama, 2014)

$$\gamma_n^{\rm T} = 1 + k_n^{\rm T} - h_n^{\rm T} \quad ; \quad \gamma_l^{\rm L} = 1 - \frac{3\rho_{\rm oc}}{(2l+1)\rho_{\rm se}}(1 + k_l^{\rm L} - h_l^{\rm L}). \tag{2.48}$$

Just like the Love numbers, $\gamma_n^{\rm T}$ and $\gamma_l^{\rm L}$ are complex in the general case and tend toward unity as the deformability of the solid and oceanic layers decreases. Now we get to the added contribution of the ocean-solid coupling to the linear system of p_r and p_{-r}. Multiplying the added contribution of loading and self-attraction effects by $\boldsymbol{\nabla}\phi_r$ and $\boldsymbol{\nabla}\psi_r\times\hat{r}$, then resolving the added terms in the frequency domain, after a number of manipulations, we can finally re-write the expression of the system of Eqs. (2.31) and

(2.32) as

$$-\sigma^2 p_r - i\sigma\sigma_{\rm R} p_r + gH\mu_r\left(1-\frac{\gamma_r^{\rm L}}{2}\right)p_r - g\gamma_n^{\rm T}\bar{\zeta}_r - \frac{2i\sigma\Omega}{\mu_r}\sum_{s=-\infty}^{s=\infty}\beta_{r,s}p_s$$
$$-\frac{1}{2}gH\sum_{\substack{s'=1\\ s'\neq r}}^{\infty}\mu_{s'}F_r^{s'}p_{s'} = 0 \tag{2.49}$$

$$-\sigma^2 p_{-r} - i\sigma\sigma_{\rm R} p_{-r} - \frac{2i\sigma\Omega}{\nu_r}\sum_{s=-\infty}^{s=\infty}\beta_{-r,s}\partial_t p_s = 0 \tag{2.50}$$

where we define

$$F_r^{s'} = 4\alpha_{n,m}\alpha_{n',m'}\sum_p\sum_q \gamma_p^{\rm L} q^2\alpha_{p,q}^2\frac{O_{p,q}^{n,m}O_{p,q}^{n',m'}}{(q^2-m^2)(q^2-m'^2)}\,, \tag{2.51}$$

with $O_{p,q}^{n,m}$ corresponding to the Gram matrix of the ALFs,

$$O_{n,m}^{u,v} = \int_{-1}^{1} P_n^m(\mu)P_u^v(\mu)d\mu, \tag{2.52}$$

for which the method of computation is detailed in Section 2.3.1.3. Coupled to the orbital dynamical evolution, the tidal frequency σ is determined at each point in time in the hemispherical phase of the model, then the system is truncated at $r_{\rm max}$ and solved numerically (see Section 2.3.1.5). We re-write the linear system as

$$(a^{(1)}+a_r^{(2)})p_r + a_r^{(3)}\sum_{s=-\infty}^{s=\infty}\beta_{r,s}p_s + a^{(5)}\sum_{\substack{s'=1\\ s'\neq r}}^{\infty}\mu_{s'}F_r^{s'}p_{s'} = c_r, \tag{2.53}$$

$$a^{(1)}p_r + a_r^{(4)}\sum_{s=-\infty}^{s=\infty}\beta_{r,s}p_s = 0, \tag{2.54}$$

where the first equation is for $r > 0$ and the second is for $r < 0$, and we have introduced the following coefficients:

$$\begin{aligned} a^{(1)} &= -\sigma^2 - i\sigma\sigma_{\rm R}, & a_r^{(2)} &= gH\mu_r(1-\gamma_r^{\rm L}/2),\\ a_r^{(3)} &= -2i\sigma\Omega\mu_r^{-1}, & a_r^{(4)} &= -2i\sigma\Omega\nu_{-r}^{-1},\\ a^{(5)} &= -\frac{1}{2}gH, & c_r &= g\gamma_n^{\rm T}\bar{\zeta}_r. \end{aligned} \tag{2.55}$$

2.3.1.2 The gyroscopic coefficients

The gyroscopic coefficients introduced in Eq. (2.30) characterize the rotational distortion of tidal waves via the Coriolis force term and the effect of boundary conditions imposed by the oceanic geometry. This coupling is dependent on the position of the ocean on the sphere and the relative position of the tidal perturber with respect to the tidally forced ocean. Since we are after a generic configuration describing the response of the oceanic hemisphere at any position, the expressions of Eq. (2.30) should be written for any frame rotating with the ocean. We start with the definition of the ALFs (Chapter 8 of Abramowitz et al., 1988)

$$P_n^m(\mu) = \frac{(-1)^m}{2^n n!}(1-\mu^2)^{m/2}\partial_\mu^{n+m}(\mu^2-1)^n, \tag{2.56}$$

which are solutions to the Legendre equation,

$$\partial_\mu\left[(1-\mu^2)\partial_\mu P_n^m\right] + \left[n(n+1) - \frac{m^2}{1-\mu^2}\right]P_n^m = 0. \tag{2.57}$$

Upon differentiation, we obtain

$$\partial_\mu P_n^m = -\frac{m\mu}{1-\mu^2}P_n^m - \frac{P_n^{m+1}}{\sqrt{1-\mu^2}}. \tag{2.58}$$

Substituting Eq. (2.58) in Eq. (2.57) we get the recurrence relation

$$P_n^{m+2} - \frac{2m\mu^2(m+1)}{1-\mu^2}P_n^m - 2\mu(m+1)\partial_\mu P_n^m + [n(n+1) - m(m+1)]\,P_n^m = 0,$$

which gives the useful relation

$$\mu\partial_\mu P_n^m = \frac{P_n^{m+2}}{2(m+1)} + \left[\frac{n(n+1)+m(m+1)}{2(m+1)} - \frac{m}{1-\mu^2}\right]P_n^m. \tag{2.59}$$

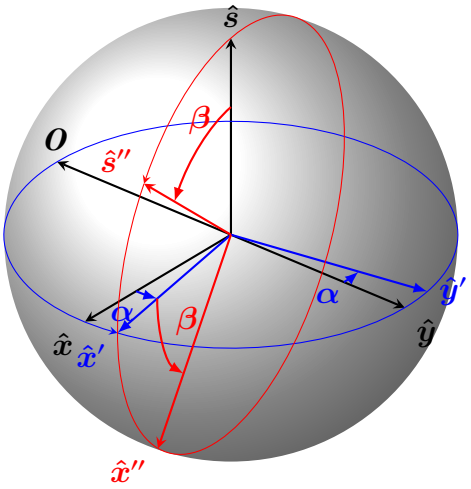

FIGURE 2.3: Adopted transformation scheme that allows recovering the tidal response of a hemispherical ocean with an arbitrary center on the sphere. We use an Eulerian transformation of the form $\mathcal{R}_3(\alpha)\mathcal{R}_2(\beta)\mathcal{R}_3(\gamma)$ with $\gamma = 0$, allowing us to shift the latitude of the oceanic center O by shifting the spin axis from $\hat{s}$ to $\hat{s}''$ in a true polar wander scenario (Webb, 1982a).

From Eqs. (2.56-2.59), it is straightforward to obtain the following ALFs recurrence relations that are necessary to compute the integral equations of the gyroscopic coefficients,

$$\frac{\mu P_n^m}{\sqrt{1-\mu^2}} = -\frac{1}{2m}\left(P_n^{m+1} + (n-m+1)(n+m)P_n^{m-1}\right), \tag{2.60}$$

$$\frac{P_n^m}{\sqrt{1-\mu^2}} = -\frac{1}{2m}\left(P_{n-1}^{m+1} + (n+m-1)(n+m)P_{n-1}^{m-1}\right), \tag{2.61}$$

$$\sqrt{1-\mu^2}\partial_\mu P_n^m = -\frac{1}{2}P_n^{m+1} + \frac{1}{2}(n+m)(n-m+1)P_n^{m-1}, \tag{2.62}$$

$$(1-\mu^2)\partial_\mu P_n^m = \frac{1}{2n+1}\left((n+1)(n+m)P_{n-1}^m - n(n-m+1)P_{n+1}^m\right). \tag{2.63}$$

The theory of the hemispherical tidal response is based on an ocean bound by two meridians. Thus for an oceanic center moving on the sphere, we instead rotate the spin axis relative to the center of the ocean, and accordingly the frame of the tidal perturber to maintain the coplanar configuration of the dynamical system. These rotations will enter the system through the Coriolis term, specifically through the gyroscopic coefficients, along with the tidal forcing term. We define an arbitrary rotation $\{\theta, \lambda\} \rightarrow \{\theta', \lambda'\}$ using an Eulerian rotation matrix of the form $\mathcal{R}_3(\alpha)\, R_2(\beta)\, R_3(\gamma)$, with $(0 \leq \alpha \leq 2\pi)$

and $(0 \leq \beta \leq \pi)$, and we fix $\gamma = 0$ (see Figure 2.3). For a vector J defined as

$$J = \mathcal{R}_3(\alpha)\mathcal{R}_2(\beta)\begin{pmatrix}0 & 0 & 1\end{pmatrix}^T = \begin{pmatrix}\sin\beta\cos\alpha & \sin\beta\sin\alpha & \cos\beta\end{pmatrix}^T,$$

the transformed gyroscopic coefficients are:

$$\frac{R^2}{\alpha_r\alpha_s}\beta_{r,s} = J_z\,\beta^{(1)}_{r,s} + J_x\,\beta^{(2)}_{r,s} + J_y\,\beta^{(3)}_{r,s}, \tag{2.64}$$

$$\frac{R^2}{\alpha_r\alpha_s}\beta_{r,-s} = J_z\,\beta^{(1)}_{r,-s} + J_x\,\beta^{(2)}_{r,-s} + J_y\,\beta^{(3)}_{r,-s}, \tag{2.65}$$

$$\frac{R^2}{\alpha_r\alpha_s}\beta_{-r,-s} = J_z\,\beta^{(1)}_{-r,-s} + J_x\,\beta^{(2)}_{-r,-s} + J_y\,\beta^{(3)}_{-r,-s}, \tag{2.66}$$

$$\beta_{-r,s} = -\beta_{s,-r}, \tag{2.67}$$

where, for r associated with the harmonic pair of integers (n, m) and s associated with (u, v), we introduce the coefficients:

$$\beta^{(1)}_{r,s} = \frac{2}{m^2 - v^2}\int \left[v^2 P^v_u \partial_\mu P^m_n + m^2 P^m_n \partial_\mu P^v_u\right]\mu d\mu, \tag{2.68}$$

$$\beta^{(2)}_{r,s} = \frac{\pi}{4}\int \left[mK^{(1)}_{m,v} P^m_n \partial_\mu P^v_u \bar{\mu}^{1/2} - vK^{(2)}_{m,v}\partial_\mu P^m_n P^v_u \bar{\mu}^{1/2}\right] d\mu, \tag{2.69}$$

$$\beta^{(3)}_{r,s} = \int \left[mK^{(3)}_{m,v} P^m_n \partial_\mu P^v_u \bar{\mu}^{1/2} - vK^{(4)}_{m,v}\partial_\mu P^m_n P^v_u \bar{\mu}^{1/2}\right] d\mu, \tag{2.70}$$

$$\beta^{(1)}_{r,-s} = \frac{-2v}{m^2 - v^2}\int \left[\partial_\mu P^v_u \partial_\mu P^m_n \mu\bar{\mu} + m^2 P^m_n P^v_u \frac{\mu}{\bar{\mu}}\right] d\mu, \tag{2.71}$$

$$\beta^{(2)}_{r,-s} = \frac{\pi}{4}\int \left[K^{(2)}_{m,v}\partial_\mu P^m_n \partial_\mu P^v_u \bar{\mu}^{3/2} - mvK^{(1)}_{m,v} P^m_n P^v_u \bar{\mu}^{-1/2}\right] d\mu, \tag{2.72}$$

$$\beta^{(3)}_{r,-s} = \int \left[K^{(4)}_{m,v}\partial_\mu P^m_n \partial_\mu P^v_u \bar{\mu}^{3/2} - mvK^{(3)}_{m,v} P^m_n P^v_u \bar{\mu}^{-1/2}\right] d\mu, \tag{2.73}$$

$$\beta^{(1)}_{-r,-s} = \frac{2mv}{m^2 - v^2}\int \left[P^v_u \partial_\mu P^m_n + P^m_n \partial_\mu P^v_u\right]\mu d\mu, \tag{2.74}$$

$$\beta^{(2)}_{-r,-s} = \frac{\pi}{4}\int \left[vK^{(1)}_{m,v}\partial_\mu P^m_n P^v_u \bar{\mu}^{1/2} - mK^{(2)}_{m,v} P^m_n \partial_\mu P^v_u \bar{\mu}^{1/2}\right] d\mu, \tag{2.75}$$

$$\beta^{(3)}_{-r,-s} = \int \left[vK^{(3)}_{m,v}\partial_\mu P^m_n P^v_u \bar{\mu}^{1/2} - mK^{(4)}_{m,v} P^m_n \partial_\mu P^v_u \bar{\mu}^{1/2}\right] d\mu, \tag{2.76}$$

with $\bar{\mu} = 1 - \mu^2$ and

$$K^{(1)}_{m,v} = (1 + \delta_{v,0})\delta_{m-v,1} - \delta_{m-v,-1}, \tag{2.77}$$

$$K^{(2)}_{m,v} = K^{(1)}_{v,m}, \tag{2.78}$$

$$K^{(3)}_{m,v} = m\left(\frac{1}{m^2 - (v^2+1)^2} + \frac{1}{m^2 - (v^2-1)^2}\right), \tag{2.79}$$

$$K^{(4)}_{m,v} = K^{(3)}_{v,m}. \tag{2.80}$$

Under the terms of this transformation, the latitude of the center of the ocean in the rotating frame is given by

$$\cos\theta' = \cos\theta\cos\beta + \sin\theta\sin\beta\cos(\lambda - \alpha). \tag{2.81}$$

To compute the integrals involved in the gyroscopic coefficients, we make use of the essential condition[3] (e.g., Longuet-Higgins and Pond, 1970)

$$P^m_n P^v_u\big|_{\mu=\pm1} = 0, \tag{2.82}$$

and we use the overlap integral of two ALFs (Eq. 2.52), which we compute using the closed form relations provided in the following section. Now we have at hand all the elements to compute the gyroscopic coefficients harmonically. The final form of the three coefficients with superscript $^{(1)}$ are identical to those in Webb (1980) and similar to those in Longuet-Higgins and Pond (1970) up to certain misprints. For the rest of the terms, the expressions given in Webb (1982a) involve numerous typographical errors and inconsistencies, so we provide here the full set of the gyroscopic coefficients. The coefficients $\beta^{(1)}_{r,s}$ and $\beta^{(2)}_{r,s}$ are expressed as

$$\beta^{(1)}_{r,s} = \left[\frac{u(u+1) + v(v+1)}{v+1} - 2v\frac{n(n+1) - u(u+1) + v}{m^2 - v^2}\right] O^{u,v}_{n,m} + \frac{1}{v+1} O^{u,v+2}_{n,m},$$

$$\beta^{(2)}_{r,s} = \frac{\pi}{4}\left[mK^{(1)}_{m,v}\int P^m_n \partial_\mu P^v_u \bar{\mu}^{1/2} d\mu - vK^{(2)}_{m,v}\int \partial_\mu P^m_n P^v_u \bar{\mu}^{1/2} d\mu\right], \tag{2.83a}$$

$$= \frac{\pi}{8}\Big\{mK^{(1)}_{m,v}\left[(u+v)(u-v+1)O^{u,v-1}_{n,m} - O^{u,v+1}_{n,m}\right]$$
$$-vK^{(2)}_{m,v}\left[(n+m)(n-m+1)O^{u,v}_{n,m-1} - O^{u,v}_{n,m+1}\right]\Big\}, \tag{2.83b}$$

[3] we note that this general condition is invalid in the case where $n = m = u = v = 0$. However, this case is excluded here by the definition of the eigenfunctions in Eqs. (2.18) and (2.19).

where we used Eq. (2.62) for each integrand in Eq. (2.83a) to obtain Eq. (2.83b). The coefficients $\beta^{(3)}_{r,s}$, $\beta^{(1)}_{r,-s}$, and $\beta^{(2)}_{r,-s}$ read as:

$$\beta^{(3)}_{r,s} = \frac{1}{2}\Big\{ mK^{(3)}_{m,v}\left[(u+v)(u-v+1)O^{u,v-1}_{n,m} - O^{u,v+1}_{n,m}\right] - vK^{(4)}_{m,v}\left[(n+m)(n-m+1)O^{u,v}_{n,m-1} - O^{u,v}_{n,m+1}\right]\Big\}, \tag{2.84}$$

$$\beta^{(1)}_{r,-s} = \frac{-2v}{(m^2-v^2)(2n+1)}\left\{(n+1)(n-1)(n+m)O^{u,v}_{n-1,m} + n(n+2)(n-m+1)O^{u,v}_{n+1,m}\right\}, \tag{2.85}$$

$$\beta^{(2)}_{r,-s} = \frac{\pi}{4}\left[K^{(2)}_{m,v}\int \partial_\mu P^m_n \partial_\mu P^v_u \bar{\mu}^{3/2} d\mu - mvK^{(1)}_{m,v}\int P^m_n P^v_u \bar{\mu}^{-1/2} d\mu\right], \tag{2.86a}$$

$$= \frac{\pi}{4}\left[K^{(2)}_{m,v}\int \partial_\mu P^m_n \bar{\mu}\partial_\mu P^v_u \bar{\mu}^{1/2} d\mu - mvK^{(1)}_{m,v}\int P^m_n P^v_u \bar{\mu}^{-1/2} d\mu\right], \tag{2.86b}$$

$$\begin{aligned} &= \frac{\pi K^{(2)}_{m,v}}{8(2n+1)}\Bigg\{(n+1)(n+m)\left[(u+v)(u-v+1)O^{u,v-1}_{n-1,m} - O^{u,v+1}_{n-1,m}\right] \\ &\quad + n(n-m+1)\left[O^{u,v+1}_{n+1,m} - (u+v)(u-v+1)O^{u,v-1}_{n+1,m}\right]\Bigg\} \\ &\quad + \frac{\pi v K^{(1)}_{m,v}}{8}\left\{O^{u,v}_{n-1,m+1} + (n+m-1)(n+m)O^{u,v}_{n-1,m-1}\right\}, \end{aligned} \tag{2.86c}$$

where we used the recurrence relations of Eq. (2.62) and Eq. (2.63) to compute the first integral of Eq. (2.86b), and the relation of Eq. (2.61) to compute the second integral. Finally, the remaining terms $\beta^{(3)}_{r,-s}$, $\beta^{(1)}_{-r,-s}$, $\beta^{(2)}_{-r,-s}$, and $\beta^{(3)}_{-r,-s}$ are expressed as:

$$\begin{aligned} \beta^{(3)}_{r,-s} = &\frac{K^{(4)}_{m,v}}{2(2n+1)}\Bigg\{(n+1)(n+m)\left[(u+v)(u-v+1)O^{u,v-1}_{n-1,m} - O^{u,v+1}_{n-1,m}\right] \\ &+ n(n-m+1)\left[O^{u,v+1}_{n+1,m} - (u+v)(u-v+1)O^{u,v-1}_{n+1,m}\right]\Bigg\} \\ &+ \frac{vK^{(3)}_{m,v}}{2}\left\{O^{u,v}_{n-1,m+1} + (n+m-1)(n+m)O^{u,v}_{n-1,m-1}\right\}, \end{aligned} \tag{2.87}$$

$$\beta^{(1)}_{-r,-s} = \frac{-2mv}{m^2-v^2}O^{u,v}_{n,m}, \tag{2.88}$$

$$\beta^{(2)}_{-r,-s} = \frac{\pi}{8}\left\{-mK^{(2)}_{m,v}\left[(u+v)(u-v+1)O^{u,v-1}_{n,m} - O^{u,v+1}_{n,m}\right] + vK^{(1)}_{m,v}\left[(n+m)(n-m+1)O^{u,v}_{n,m-1} - O^{u,v}_{n,m+1}\right]\right\}, \tag{2.89}$$

$$\beta^{(3)}_{-r,-s} = \frac{1}{2}\left\{-mK^{(4)}_{m,v}\left[(u+v)(u-v+1)O^{u,v-1}_{n,m} - O^{u,v+1}_{n,m}\right] + vK^{(3)}_{m,v}\left[(n+m)(n-m+1)O^{u,v}_{n,m-1} - O^{u,v}_{n,m+1}\right]\right\}. \tag{2.90}$$

2.3.1.3 The overlap integral $O^{u,v}_{n,m}$

Here, we provide a closed form solution for the computation of the overlap integral of Eq. (2.52). The procedure is assimilated from tools of angular momentum quantization (Varshalovich et al., 1988). Following Dong and Lemus (2002) and introducing the notation $q = v - m$, we have

$$O^{u,v}_{n,m} = C^{u,v}_{n,m}\sum_{l}(2l+1)\mathcal{D}(|q|,l)\cdot\begin{pmatrix} n & u & l \\ 0 & 0 & 0\end{pmatrix}\begin{pmatrix} n & u & l \\ -m & v & m-v\end{pmatrix}, \tag{2.91}$$

where the factors $C^{u,v}_{n,m}$ are given by:

$$C^{u,v}_{n,m} = (-1)^{\kappa}2^{|q|-2}|q|\sqrt{\frac{(n+m)!(u+v)!}{(n-m)!(u-v)!}}, \tag{2.92}$$

and the coefficients $\mathcal{D}(|q|,l)$ by

$$\mathcal{D}(|q|,l) = \left[1+(-1)^{l+|q|}\right]\sqrt{\frac{(l-|q|)!}{(l+|q|)!}}\frac{\Gamma(l/2)\Gamma((l+|q|+1)/2)}{((l-|q|)/2)!\Gamma((l+3)/2)}. \tag{2.93}$$

We note here that the phase κ introduced in Dong and Lemus (2002) as

$$\kappa = \begin{cases} m & \text{if } v \geq m, \\ v & \text{otherwise,}\end{cases} \tag{2.94}$$

corrects the phase given in Mavromatis and Alassar (1999) and Crease (1966), where the latter was used for the computation of the gyroscopic coefficients in Longuet-Higgins and Pond (1970) and Webb (1980, 1982a).

In Eq. (2.91), the summation over l runs for $|n-u| \leq l \leq (n+u)$; $l \geq |q|$; and $|l+n+u|$ is even. Finally, the Wigner 3-jm symbols are determined from Varshalovich et al. (1988)

by

$$\begin{pmatrix} a & b & c \\ d & e & f \end{pmatrix} = (-1)^{R_{21}+R_{31}+R_{32}} \left[\frac{R_{31}!R_{32}!R_{33}!R_{13}!R_{23}!}{(J+1)!R_{11}!R_{12}!R_{21}!R_{22}!} \right]^{1/2} \times \sum_z (-1)^z \frac{(R_{21}+z)!(R_{11}+R_{31}-z)!}{z!(R_{31}-z)!(R_{23}-z)!(R_{13}-R_{31}+z)!}, \tag{2.95}$$

where $J = a + b + c$, and R_{ij} are the elements of the so-called Regge $\mathfrak{R}$-symbol (Regge, 1958) defined as

$$\begin{aligned} R_{11} &= -a + b + c, & R_{12} &= a - b + c, & R_{13} &= a + b - c, \\ R_{21} &= a + d, & R_{22} &= b + e, & R_{23} &= c + f, \\ R_{31} &= a - d, & R_{32} &= b - e, & R_{33} &= c - f. \end{aligned} \tag{2.96}$$

The summation in Eq. (2.95) runs over all integer values of z for which all the factorial arguments are non-negative. Finally, we note that using Eq. (2.91), $O^{u,v}_{n,m} = 0$ when $v = m$. In that case, we alternatively use

$$O^{u,m}_{n,m} = \frac{2}{2n+1} \frac{(n+m)!}{(n-m)!} \delta_{n,u} \,. \tag{2.97}$$

This method for the computation of the overlap integral was verified numerically using MATLAB's ALFs package.

2.3.1.4 The tidal forcing term $\bar{\zeta}_r$

As in Webb (1980), considering the equilibrium tide $\bar{\zeta}$ to have a unit root mean square amplitude, and to be driven by a spherical harmonics term of the form

$$Y^q_p(\theta, \lambda) = \sqrt{\frac{2p+1}{4\pi} \frac{(p-q)!}{(p+q)!}} P^q_p(\cos\theta) \, \exp(iq\lambda) \,, \tag{2.98}$$

with angular frequency σ, we define

$$\bar{\zeta} = \sqrt{2\pi} Y^q_p(\theta, \lambda) \exp(i\sigma t). \tag{2.99}$$

Under the rotation of the coordinate system described by the Euler angles (α, β, γ) (see Section 2.3.1.2 and Figure 2.3), the spherical harmonics transform as (Varshalovich

et al., 1988)

$$Y_p^s(\theta', \lambda') = \sum_{q=-p}^{p} Y_p^q(\theta, \lambda) D_{s,q}^p(\alpha, \beta, \gamma), \tag{2.100}$$

or

$$Y_p^q(\theta, \lambda) = \sum_{s=-p}^{p} Y_p^s(\theta', \lambda') D_{s,q}^{p*}(\alpha, \beta, \gamma), \tag{2.101}$$

where $D_{q,s}^p$ designate the Wigner D-functions. These functions are themselves the product of three functions (Varshalovich et al., 1988), each depending on one argument: α, β, or γ such that

$$D_{s,q}^p(\alpha, \beta, \gamma) = e^{-iq\alpha} d_{sq}^p(\beta) e^{-is\gamma}. \tag{2.102}$$

In this expression, the functions $d_{sq}^p(\beta)$ are given by

$$\begin{aligned} d_{sq}^p(\beta) = {} & (-1)^{p-s} \left[(p+q)!(p-q)!(p+s)!(p-s)!\right]^{1/2} \\ & \times \sum_j (-1)^j \frac{(\cos\beta/2)^{q+s+2j} (\sin\beta/2)^{2p-q-s-2j}}{j!(p-q-j)!(p-s-j)!(q+s+j)!}, \end{aligned} \tag{2.103}$$

with j running over all integer values for which the factorial arguments are positive. This sum involves $N+1$ terms, where N is the minimum of $(p+q)$, $(p-q)$, $(p+s)$, and $(p-s)$. Since we are studying the semi-diurnal tide ($p = q = 2$), we are left with one term only. Expanding the harmonic factor $Y_p^s(\theta', \lambda')$ of Eq. (2.101) in terms of the basis eigenfunctions, we get the expression of the equilibrium oceanic depth variation in the rotated frame of reference,

$$\bar{\zeta} = \sqrt{\frac{\pi R^2}{2}} \exp(i\sigma t) \sum_{s=-p}^{p} D_{s,q}^{p*}(\alpha, \beta, \gamma) \left(1 + \delta_{s,0}\right)^{1/2} \left[\phi_p^s + i\psi_p^s\right]. \tag{2.104}$$

Then, invoking the definition of the component $\bar{\zeta}_r$,

$$\bar{\zeta}_r = \int_O \phi_r \bar{\zeta} dA, \tag{2.105}$$

we get its expression in the rotated frame of reference as

$$\begin{aligned} \bar{\zeta}_r = {} & \sqrt{\frac{\pi R^2}{2}} \exp(i\sigma t) \sum_{s=-p}^{p} D_{s,q}^{p*}(\alpha, \beta, \gamma) \left(1 + \delta_{s,0}\right)^{1/2} \\ & \times \left[\int_O \phi_p^s \phi_n^m dA + i \int_O \psi_p^s \phi_n^m dA\right], \end{aligned} \tag{2.106}$$

where the dot products of the eigenfunctions are simplified as follows:

$$\int_O \phi_p^s \phi_n^m \, dA = \begin{cases} \delta_{n,p}, & \text{if } s = m, \\ (-1)^m \delta_{n,p}, & \text{if } s = -m, \\ 0, & \text{otherwise,} \end{cases} \tag{2.107}$$

and

$$\int_O \psi_p^s \phi_n^m \, dA = \begin{cases} 0, & \text{if } m + s = \text{even}, \\ \alpha_{p,s} \, \alpha_{n,m} \dfrac{2s}{s^2 - m^2} O_{p,s}^{n,m} & \text{otherwise.} \end{cases} \tag{2.108}$$

We note that as the index s takes negative values, we use

$$P_p^{-s} = (-1)^s \frac{(p-s)!}{(p+s)!} P_p^s \tag{2.109}$$

in the overlap integral of Eq. (2.52).

2.3.1.5 Tidal torque of a hemispherical ocean

Once the gyroscopic coefficients are computed, the linear system of the coefficients (p_r, p_{-r}) in Eq. (2.53) is truncated and solved numerically. What we are after are the tidal torques that enter in the dynamical equations of the Earth-Moon system (see Section 2.5.2), which depend on the rotational angular velocity of the Earth and the orbital frequency of the tidal perturber. Defining the tidal torque transferring power from the Earth's rotational momentum to the perturber's orbital angular momentum by $\mathcal{T}$, the power lost by the Earth would be $\mathcal{T}\Omega$, and the power gained by the perturber is $\mathcal{T} n_{\text{orb}}$. The difference between them is the dissipative work of the total tidal mass redistribution $\mathcal{W}_{\text{diss}}$, thus

$$\mathcal{T} = \frac{\mathcal{W}_{\text{diss}}}{\Omega - n_{\text{orb}}}. \tag{2.110}$$

The total dissipative work is the sum of two contributions: the dissipative work of oceanic tidal currents, $\mathcal{W}_{\text{diss}}^{\text{oc}}$, and dissipation in the deforming viscoelastic mantle. In the formalism established thus far, we calculated the self-consistently coupled tidal responses of the ocean and solid part for the Earth's half hosting the hemispherical ocean, which corresponds to the effective tidal response of the planet for this hemisphere. The tidal response of the continental hemisphere is simply described by the solid Love numbers introduced in Eq. (2.45), since there is no oceanic tide in that case. The coupled solid-oceanic tidal response accounts for both the direct gravitational tidal

forcing generated by the perturber on the solid part and ocean and the mutual forcings of the two layers through the variations of the loading exerted by the latter on the former, and the variations of the Earth's self-gravitational potential due to mass redistribution. For simplicity, we ignore the energy dissipated in the solid part in the calculation of the tidal torque and we only consider that which is occurring within the oceanic shell, namely, $\mathcal{W}^{\rm oc}_{\rm diss}$. This is justified by the predominance of the oceanic response over the solid part over the time interval covered by the hemispherical ocean configuration in our model (see Section 2.5). This hierarchy of contributions is only jeopardized by the emerging significance of the solid dissipation when moving backwards in time and increasing the Earth's rotational velocity Ω. Solid Earth dissipation would also be amplified with an early less viscous mantle due to higher Hadean-Archean temperatures (Ross and Schubert, 1989). Eventually, a regime transition may lead to the predominance of the mantle's elastic response (Lau et al., 2015, 2016a). In our nominal model described in Section 2.5, we switch from the hemispherical ocean configuration to the global ocean configuration during mid-Archean, beyond which we self-consistently account for the dissipative contribution of the solid part (Section 2.3.2). Thus, we have only ignored the dissipative contribution of the mantle when it is insignificant. The oceanic dissipative work is given by (Webb, 1980)

$$\begin{aligned}\mathcal{W}^{\rm oc}_{\rm diss} &= \left\langle \int_O \vec{u}(t)\cdot\sigma_{\rm R}\vec{u}(t)dA \right\rangle \\ &= \frac{1}{2}\sigma_{\rm R}\sigma^2 \sum_{r=1}^{\infty}\left(\mu_r p_r p_r^* + \nu_r p_{-r} p_{-r}^*\right), \end{aligned} \tag{2.111}$$

where $\langle\rangle$ denotes time averaging over the tidal period. This work should be equal to the work done by the tidal force on the ocean

$$\begin{aligned}\mathcal{W}^{\rm oc}_{\rm tide} &= \left\langle \rho_{\rm oc} g H \int_O \nabla\bar{\zeta}(t)\cdot\vec{u}(t)dA \right\rangle \\ &= \frac{1}{2}\rho_{\rm oc} g H \sigma\, {\rm Im}\left\{\sum_{r=1}^{\infty} p_r \mu_r \bar{\zeta}_r^*\right\}. \end{aligned} \tag{2.112}$$

Hence, the tidal torque associated with the lunar semi-diurnal frequency $\sigma = 2(\Omega - n_{\rm M})$, $n_{\rm M}$ being the lunar mean motion, is

$$\mathcal{T}_{\rm M} = \rho_{\rm oc} g H\, {\rm Im}\left\{\sum_{r=1}^{\infty} p_r \mu_r \bar{\zeta}_r^*\right\}, \tag{2.113}$$

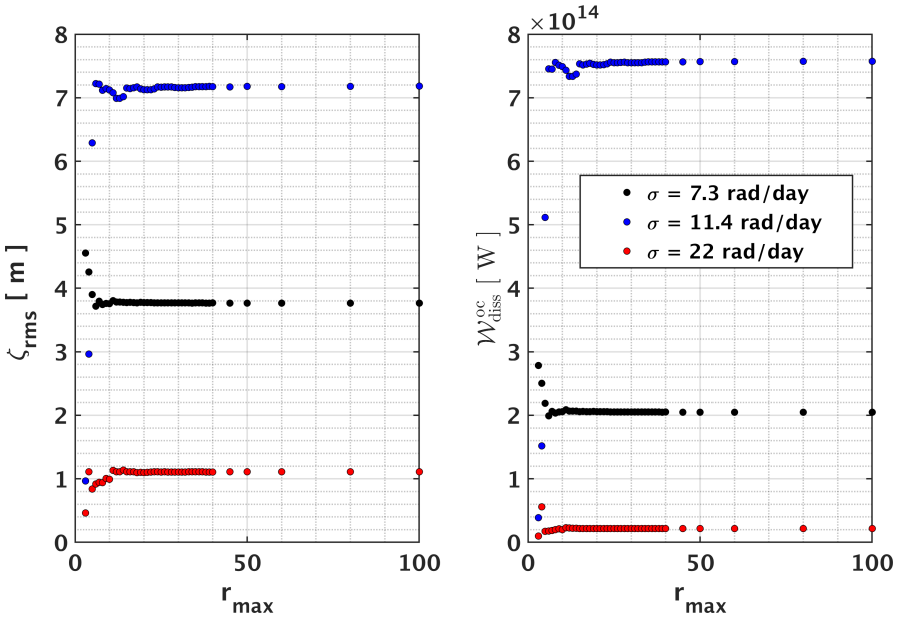

FIGURE 2.4: Numerical analysis on the dependence of the tidal response computation on the truncation order $r_{\max}$. The response is quantified by the root mean square tidal amplitude, $\zeta_{\rm rms}$, (Eq. 2.114) and the dissipative work, $\mathcal{W}^{\rm oc}_{\rm diss}$, (Eq. 2.111), and plotted for three tidal frequencies: 7.3, 11.4, and 22 rad/day that correspond to the vicinity of a tidal resonance, the peak of a resonance, and the background spectrum respectively.

and we obtain a similar expression for the solar tides $\mathcal{T}_{\rm S}$ when solving the system with the solar tidal frequency component $\sigma = 2(\Omega - n_{\rm S})$, $n_{\rm S}$ being the solar mean motion that generates the solar tidal work.

Besides the tidal torque, the tidal response can also be quantified by the root mean square tidal height variation, $\zeta_{\rm rms}$, given as

$$\zeta_{\rm rms} = \sqrt{\frac{H}{\pi R^2} \sum_{r=1}^{\infty} \mu_r^2 p_r^* p_r}. \tag{2.114}$$

As these quantities are computed numerically, a truncation order, $r_{\max}$, is required. In Figure 2.4, we show the numerical dependence of the tidal response on $r_{\max}$. Since the response is dominated by gravity modes, the tidal solution converges fast enough with $r_{\max}$. To avoid any truncation effect in our computation, and to properly account for the resonances, we adopted $r_{\max} = 50$. In Figure 2.5, we plot the torque of the hemispherical configuration for two scenarios: accounting for the oceanic response only and accounting for both the oceanic and solid responses self-consistently. As explained in Section 2.3.1.1, the effects of self-attraction and loading interactions between the solid mantle and the oceanic shell are evident in attenuating the amplitude of the response and slightly shifting the position of resonances. This delay effect is due to the influence of

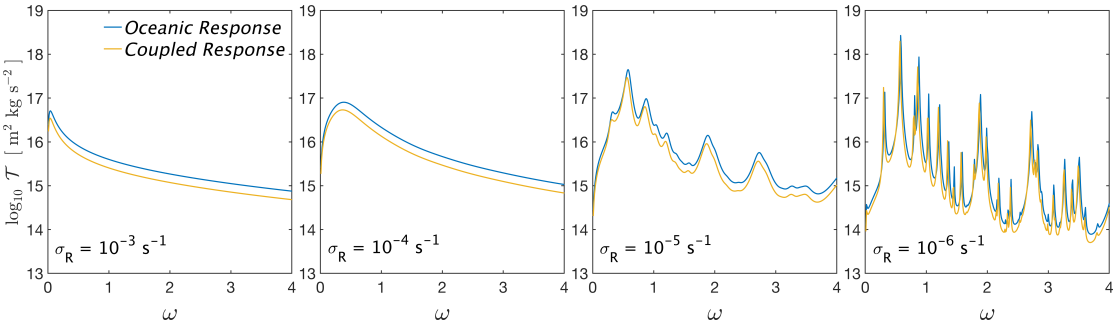

FIGURE 2.5: Tidal torque between the Earth and the Moon. We compare the torque of the hemispherical ocean model between a pure oceanic response, and the response of the ocean when accounting for loading and self-attraction effects arising from solid Earth deformation assuming an Andrade rheology. The procedure of this coupling for the hemispherical configuration is detailed in Section 2.3.1.1. We recall that the energy tidally dissipated in the solid part is ignored in the hemispherical configuration. The thickness of the oceanic shell is set to $H = 4000$ m. The ocean is symmetric around the equator and bounded by longitudes $\lambda = 0$ and $\lambda = \pi$. Energy dissipation is quantified by the linear Rayleigh drag frequency σ_R. The logarithm of the torque is plotted as a function of the normalized frequency $\omega = (\Omega - n_{\rm orb})/\Omega_0$, where the Earth's spin rate varies with the tidal forcing frequency $\Omega = n_{\rm orb} + \sigma/2$ at fixed $n_{\rm orb}$, and Ω_0 being the present spin rate of the Earth.

this coupling on the phase of resonance depths of near-resonant free oscillations (Müller, 2008).

In Figure 2.6, we plot the tidal torque for a hemispherical ocean at different surface positions. With longitudinal symmetry, the latter is defined by the latitude of the oceanic center. The drifting effect on the resonances ranges from position shifting and attenuation for small forcing frequencies to major distortion in the spectrum at larger frequencies. Extreme distortion occurs in the polar oceanic scenario: the major resonance around 11 rad/day reaches a maximum relative to other configurations and the rest of the resonances are absorbed into the background leaving a unimodal spectrum. This behavior makes it important to take into account the position of the hemispherical cap into the model we develop next.

2.3.2 The tidal response of a global ocean

We next describe the oceanic tidal dynamics assuming a spherical fluid shell, also of uniform thickness H, covering the Earth's surface. The reason we are interested in this configuration will become clearer when we describe our evolution model later on. The premise of the analytical treatment of the problem can be found in its gory details in several works (e.g., Tyler, 2011; Matsuyama, 2014; Auclair-Desrotour et al., 2014,

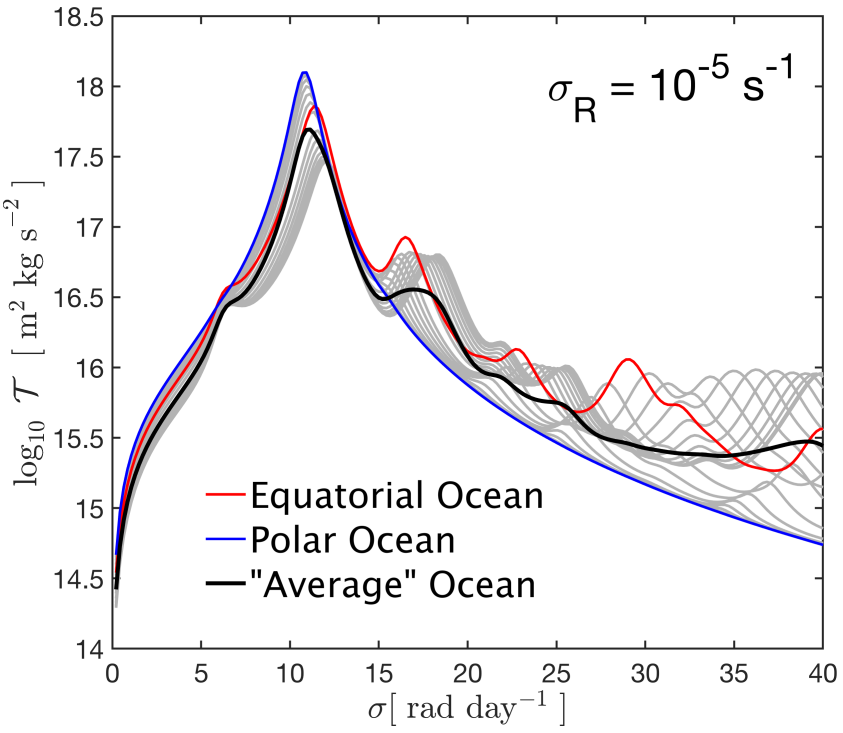

FIGURE 2.6: Drifting effect of the continental cap on the oceanic response: the tidal torque of a hemispherical ocean is plotted as a function of the forcing semi-diurnal frequency for different positions of the center of the ocean.

2018, 2019a). Adopting this formalism for the Earth-Moon system was recently done in Motoyama et al. (2020) for the first half of the system's age where the removal of continents was justified due to the timing of continental formation and evolution. Tyler (2021) used the formalism for the full age of the system arguing that "continentality" can be implicitly parametrized. We provide here a brief recipe of this analytical formalism necessary for constructing our model.

In the global ocean configuration, solving the governing system of Eq. (2.1) is done by expanding the velocity field, the tidal elevation, and the forcing gravitational tidal potential in Fourier series of time and longitude, with the tidal frequency serving as the expansion frequency[4]. This is justified by the imposed linear approximation, where the response of each given mode is proportional to the corresponding component of the

[4]We remind the reader that we proceed with this theory by studying dynamics in the coplanar setting. The theory requires further development if one were to account for the Earth's obliquity and lunar inclination.

forcing. Thus, we have

$$\begin{aligned}\vec{u} &= \sum_{m,\sigma} \vec{u}^{\,m,\sigma}(\theta)\exp\{i(\sigma t + m\lambda\},\\ \zeta &= \sum_{m,\sigma} \zeta^{m,\sigma}(\theta)\exp\{i(\sigma t + m\lambda\},\\ \zeta_{\rm eq} &= \sum_{m,\sigma} \zeta_{\rm eq}^{m,\sigma}(\theta)\exp\{i(\sigma t + m\lambda\}.\end{aligned} \tag{2.115}$$

Defining the complex tidal frequency $\tilde{\sigma}$ and the complex spin parameter $\tilde{\nu}$ as in Auclair-Desrotour et al. (2018) by

$$\tilde{\sigma} = \sigma - i\sigma_{\rm R} \quad \text{and} \quad \tilde{\nu} = \frac{2\Omega}{\tilde{\sigma}}, \tag{2.116}$$

and replacing the tidal quantities by their expansions, the governing system reduces to an eigenvalue-eigenfunction problem, known classically (when ignoring friction) as the Laplace tidal equation (e.g., Lee and Saio, 1997). We assume that the Fourier components can be expanded spatially using a set of the latitudinal complex Hough functions $\{\Theta_n^{m,\tilde{\nu}}(\theta)\}$ (Hough, 1898), associated with a set of eigenvalues $\{\Lambda_n^{m,\tilde{\nu}}\}$. Hough functions arise as natural solutions of the Laplace tidal equation when describing horizontal dynamics:

$$\mathcal{L}^{m,\tilde{\nu}}\Theta_n^{m,\tilde{\nu}}(\theta) = -\Lambda_n^{m,\tilde{\nu}}\Theta_n^{m,\tilde{\nu}}(\theta), \tag{2.117}$$

where the operator $\mathcal{L}^{m,\tilde{\nu}}$ is defined as

$$\mathcal{L}^{m,\tilde{\nu}} = \frac{1}{\sin\theta}\frac{d}{d\theta}\left(\frac{\sin\theta}{1-\tilde{\nu}^2\cos^2\theta}\frac{d}{d\theta}\right) - \frac{1}{1-\tilde{\nu}^2\cos^2\theta}\left(m\tilde{\nu}\frac{1+\tilde{\nu}^2\cos^2\theta}{1-\tilde{\nu}^2\cos^2\theta} + \frac{m^2}{\sin^2\theta}\right). \tag{2.118}$$

With the complex nature of $\tilde{\nu}$, it follows that the Hough functions and their eigenvalues upon the introduction of dissipation are complex too, in contrast with earlier studies. To compute the Hough functions and their associated eigenvalues, we adopt the method developed in Wang et al. (2016), where Hough functions are expanded in terms of Associated Legendre Functions

$$\begin{aligned}\Theta_n^{m,\tilde{\nu}}(\theta) &= \sum_{m\le l} A_{n,l}^{m,\tilde{\nu}} P_l^m(\cos\theta),\\ P_l^m(\cos\theta) &= \sum_n B_{l,n}^{m,\tilde{\nu}}\Theta_n^{m,\tilde{\nu}}(\theta),\end{aligned} \tag{2.119}$$

with $A_{n,l}^{m,\tilde{\nu}}$ and $B_{l,n}^{m,\tilde{\nu}}$ being complex coefficients defining a change of basis . In Figure 2.7 we plot a sample of these functions associated with the symmetric modes of degree

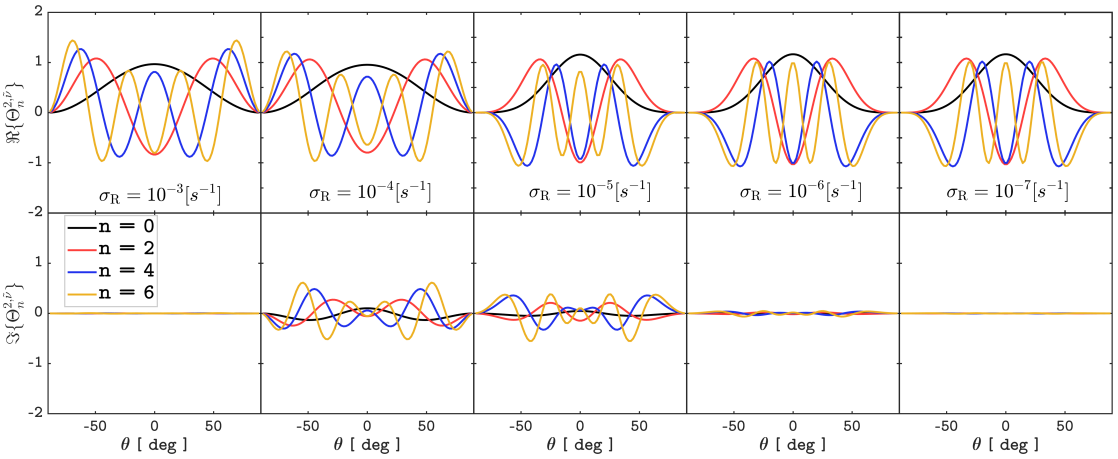

FIGURE 2.7: A sample from the set of Hough functions $\{\Theta_n^{m,\tilde{\nu}}(\theta)\}$. Real and imaginary parts of even mode Hough functions (n being even), plotted as a function of the latitudinal angle θ. The functions are associated with the quadrupolar ($m = 2$) perturbation, which is relevant for the semi-diurnal tidal forcing. Each column corresponds to a different value of the dissipative frequency σ_R, such that going from left to right is equivalent to going from a strongly to a weakly frictional regime.

$m = 2$ for various values of σ_R. In a weakly dissipative regime, where $\sigma \gg \sigma_R$, the Hough functions and their eigenvalues are pure real. The real spin parameter for this case of a perfect fluid can be approximated as $\nu = 2\Omega/\sigma$. This is the classic case usually studied in the linear theory of tides (e.g., Lee and Saio, 1997; Auclair-Desrotour et al., 2014; Matsuyama, 2014), where viscous friction only slightly modifies the horizontal structure of the tides. The tidal modes in this case are divided into families of gravity modes and inertial modes that correspond to $n \geq 0$ and $n < 0$ respectively. Gravity modes can further be defined in the regime of super-inertial waves, where $|\nu| \leq 1$, or in the regime of sub-inertial waves, with $|\nu| > 1$. In contrast, the inertial modes can only be defined in the regime of sub-inertial waves. In the limit of slow rotation, with $\nu \longrightarrow 0$, the Hough functions associated with gavity modes can be represented by the associated Legendre Polynomials P_l^m with $n = l - m$. Thus the Hough functions have been often described on the sphere as Legendre Polynomials distorted by rotation.

In the limit of strong dissipation, where $\sigma_R > \sigma$, friction significantly affects the horizontal structure of tidal waves. In the limit of $\sigma_R \longrightarrow \infty$, gravity and Rossby Hough functions merge asymptotically and converge towards the associated Legendre Polynomials again (Volland, 1974). Thus strong friction also tames the Coriolis effects, as if the planet is stationary.

Using the change of basis coefficients $A_{n,l}^{m,\tilde{\nu}}$, the tidal displacement solution is expressed as

$$\zeta_l^{m,\sigma} = \sum_n A_{n,l}^{m,\tilde{\nu}} \zeta_n^{m,\sigma}, \tag{2.120}$$

where the components $\zeta_n^{m,\sigma}$ are solutions to the linear algebraic system

$$\left(\sigma\tilde{\sigma} \boldsymbol{I}_N - \begin{bmatrix} \sigma_{1,1}^2 & \dots & \sigma_{1,n}^2 & \dots & \sigma_{1,N}^2 \\ \vdots & \ddots & \vdots & & \vdots \\ \sigma_{n,1}^2 & \dots & \sigma_{n,n}^2 & \dots & \sigma_{n,N}^2 \\ \vdots & & \vdots & \ddots & \vdots \\ \sigma_{N,1}^2 & \dots & \sigma_{N,n}^2 & \dots & \sigma_{N,N}^2 \end{bmatrix} \right) \begin{bmatrix} \zeta_1^{m,\sigma} \\ \vdots \\ \zeta_n^{m,\sigma} \\ \vdots \\ \zeta_N^{m,\sigma} \end{bmatrix} = \begin{bmatrix} \mathcal{F}_1^{m,\sigma} \\ \vdots \\ \mathcal{F}_n^{m,\sigma} \\ \vdots \\ \mathcal{F}_N^{m,\sigma} \end{bmatrix}. \tag{2.121}$$

In this linear system, $\boldsymbol{I}_N$ denotes the identity matrix of size $N \times N$, the forcing terms of the studied tidal potential $U_l^{m,\sigma}$ (Eq. 2.37) are expressed as

$$\mathcal{F}_n^{m,\sigma} = -\frac{H\Lambda_n^{m,\tilde{\nu}}}{R^2} \sum_{m \le l} B_{l,n}^{m,\tilde{\nu}} \gamma_l^T U_l^{m,\sigma}, \tag{2.122}$$

and the complex characteristic frequencies $\sigma_{n,k}$ as

$$\sigma_{n,k} = \sqrt{gH\hat{k}_n^2 \sum_{l \ge m} \gamma_l^L A_{k;l}^{m,\tilde{\nu}} B_{l,n}^{m,\tilde{\nu}}}, \tag{2.123}$$

where the horizontal wave-number of the degree-n mode $\hat{k}_n = \sqrt{\Lambda_n^{m,\tilde{\nu}}}/R$, and the coupling coefficients γ_l^{T} and γ_l^{L} are defined in Eq. (2.48). Once the solution of this algebraic system is obtained, the self-consistent tidal response of the Earth is quantified by the total frequency dependent complex Love number defined, for each order, m, and degree, l, as

$$k_{l,m}^{O} = k_l^{\mathrm{T}} + \left(1 + k_l^{\mathrm{L}}\right) \frac{3g}{2l+1} \frac{\rho_{\mathrm{oc}}}{\rho_{\mathrm{se}}} \frac{\zeta_l^{m,\sigma}}{U_l^{m,\sigma}}. \tag{2.124}$$

The first term of the above expression accounts for the direct tidal gravitational forcing of the solid part by the perturber. The second term is related to the oceanic tidal response, which is coupled to that of the solid part through gravitational and surface loading interactions via the loading Love number k_l^{L} (see Section 1.2.7). We remark that the effective Love number characterizing the full tidal response of the planet (Eq. 2.124) depends on both the latitudinal and longitudinal harmonic degrees, l and m, in contrast with the solid tidal Love number, k_l^{T}. This results from the fact that Coriolis

forces alter the oceanic tidal response, which is not the case for the solid tidal response. A more typical parameter often associated with tidal dissipation is the quality factor Q. The definition of the latter varies in the literature, and is confusingly referred to as the dissipation parameter. As Tyler (2021) points out, Q is related to both kinetic and potential energy densities (KE and PE, respectively), thus it is linked to the partition of energy between gravity and rotational modes. However, studying tidal dynamics is often the study of the tidal flow and therefore kinetic energy rather than the potential energy. Hence, if the definition of Q as $Q = \sigma(\mathrm{KE} + \mathrm{PE})/W$, where W is the work done by the tidal potential, is adopted (Egbert et al., 2004), then Q quantifies not only the dissipation timescale but also the relative importance of rotation in the dynamics. Consequently, it is not a good parameter for comparing tidal dissipation of two bodies that have different rotational motion, and it should be used with caution only to quantify the number of cycles to obtain an e-folding decay of the tidal amplitude, i.e. only to describe the damping, rather than being a fundamental parameter characterizing dissipation. In our formulation, it is the Love number, and more specifically its imaginary part that characterizes the process of dissipative deformation. The tidal quality factor Q can now be defined in terms of the Love number as (Mathis and Le Poncin-Lafitte, 2009)

$$Q = \left| \frac{k^O_{l,m}}{\mathrm{Im}\left\{k^O_{l,m}\right\}} \right|. \tag{2.125}$$

In Figure 2.8, we plot the frequency spectrum of Q. The figure clearly depicts the resonances associated with surface-gravity modes modified by rotation. These resonances are situated around the pairs of complex eigen-frequencies $\sigma_n^{\pm}$ defined as (Auclair-Desrotour et al., 2018)

$$\sigma_n^{\pm} = i\frac{\sigma_\mathrm{R}}{2} \pm \sqrt{gH\hat{k}_n^2 - \left(\frac{\sigma_\mathrm{R}}{2}\right)^2}, \tag{2.126}$$

which depicts explicitly the predominance of friction over the rotational distortion of tidal waves in a strong friction regime. The spectral coverage of the non-resonant background of the response increases with increasing σ_R. In the opposite limit, resonant peaks are spelled out intensifying in amplitude as friction is weakened[5]. Besides, when $\sigma_\mathrm{R} \to 0$, the frequencies $\sigma_n^{\pm}$ become real and positive, and we recover the eigen-frequencies of high-wavelength surface gravity modes travelling around the sphere.

[5] Auclair-Desrotour et al. (2015) studied the dependence of the resonant peaks on the frequencies of dissipative mechanisms in a fluid box. The authors showed that the heights of resonant peaks scale as the inverse of the frequency associated with viscous friction, while the widths of the peaks and the non-resonant background are proportional to this frequency. Though the setting in their study is idealized, the resonances of the global ocean are expected to behave in a similar way.

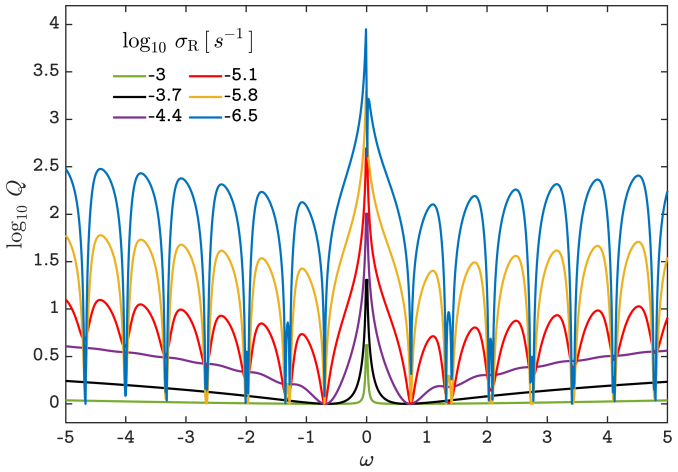

FIGURE 2.8: The tidal quality factor Q associated with the semidiurnal oceanic tide of the Earth. The logarithms of Q is plotted as functions of the normalized tidal frequency $\omega = \Omega - n_{\rm orb}/\Omega_0$ (where Ω_0 designates the present spin rate of the Earth) for different orders of magnitude of the dissipative frequency $\sigma_{\rm R}$. The frequency spectrum of Q is computed via the Love number function of Eq. (2.125). The mean motion of the Moon, $n_{\rm orb}$, is assumed to be constant and the variation in σ (consequently ω) is driven by variations in Ω. The excitation of resonances is clear for moderate values of $\sigma_{\rm R}$.

2.3.2.1 The pure oceanic response

Before wrapping up on our oceanic analytics, we pause briefly to comment again on the effect of solid tides on the global oceanic response, as we did in Section 2.3.1.1 for the hemispherical configuration. Looking back at Eq. (2.124), the Love number for the pure oceanic response can be computed in the limit of an infinitely rigid mantle ($\mu \longrightarrow \infty$). Furthermore, the Cowling approximation is assumed (e.g., Cowling, 1941; Unno et al., 1989), whereby the term with $\rho_{\rm oc}/\rho_{\rm se}$, which results from the action of the self-attraction variations due to the oceanic tidal mass redistribution on the oceanic tides themselves, is ignored. Consequently, the tidal and loading Love numbers would vanish, and the tilt coefficients $\gamma_n^{\rm T}$, $\gamma_l^{\rm L}$ of Eq. (2.48) would be equal to unity. We focus for now on the semi-diurnal forcing which corresponds to $l = m = 2$, and thus Eq. (2.124) can then be re-written as

$$k_{2,2}^{\mathcal{O}} = \frac{3g}{5}\frac{\rho_{\rm oc}}{\rho_{\rm se}}\frac{\zeta_2^{2,\sigma}}{U_2^{2,\sigma}}. \tag{2.127}$$

By virtue of the imposed approximations, the complex characteristic frequencies $\sigma_{n,k}$ of Eq. (2.123) vanish for $n \neq k$, and the algebraic system of Eq. (2.121) simplifies to

$$\zeta_n^{2,\sigma} = \frac{\mathcal{F}_n^{2,\sigma}}{\sigma\tilde{\sigma} - \sigma_{n,n}^2}, \tag{2.128}$$

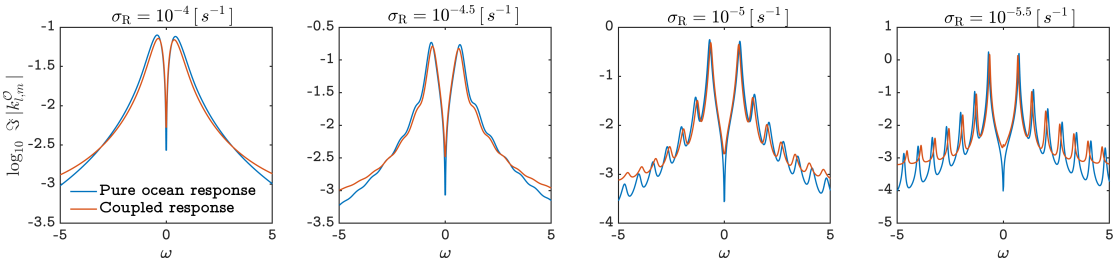

FIGURE 2.9: The tidal response of the Earth, quantified by the imaginary part of the Love number. In each panel, we plot the logarithm of the absolute value of the imaginary part of the Love number as a function of the normalized frequency $\omega = (\Omega - n_{\rm orb})/\Omega_0$, where the Earth's spin rate varies with the tidal forcing frequency $\Omega = n_{\rm orb} + \sigma/2$ at fixed $n_{\rm orb}$, and Ω_0 being the present spin rate of the Earth. The panels differ by the prescribed value of the $\sigma_{\rm R}$. In each panel, we plot the Love number in two settings: that of Eq. (2.124), where the tidal response of the Earth is that self-consistently computed when accounting of oceanic tides and solid Earth deformation and dissipation; and that of Eq. (2.130), which is retrieved from the former under the rigid mantle and Cowling approximations, i.e. when the mantle is taken to be non-deformable and the gravitational feedback of the tidal response due to the induced self-attraction variation is ignored. The effects of solid Earth deformation and self-attraction can thus be seen in the attenuation and spectral shift of the resonances, while the effect of solid dissipation can be noticed at high frequencies with the divergence of the two Love numbers in each panel.

where the forcing terms $\mathcal{F}_n^{2,\sigma}$ reduce to

$$\mathcal{F}_n^{2,\sigma} = -\frac{H\Lambda_n^{m,\tilde{\nu}}}{R^2} B_{2,n}^{2,\tilde{\nu}} U_2^{2,\sigma}. \tag{2.129}$$

These expressions allow us to re-write the Love number of the coupled response in Eq. (2.124) in the limit of the pure oceanic response as

$$k^{\mathcal{O}}_{l,m} = -\frac{3g}{5}\frac{\rho_{\rm oc}}{\rho_{\rm se}}\frac{H}{R^2}\sum_n \frac{\Lambda_n^{2,\tilde{\nu}} B_{2,n}^{2,\tilde{\nu}} A_{n,2}^{2,\tilde{\nu}}}{\sigma\tilde{\sigma} - \frac{gH}{R^2}\Lambda_n^{2,\tilde{\nu}}}. \tag{2.130}$$

In Figure 2.9, we plot the Love numbers of the pure (Eq. 2.130) and coupled responses (Eq. 2.124) for different values of the dissipation frequency $\sigma_{\rm R}$. Solid Earth deformation via the effects of self-attraction and loading has its robust signature on the oceanic response spectrum: attenuation of the response in terms of the background spectrum and the peaks and a slight shift in the peaks spectral position. We have observed the same effect when studying the hemispherical ocean in Section 2.3.1.1 (Figure 2.5). However, the added signature here is that of the tidal dissipation in the solid itself. In the hemispherical configuration, we have ignored the dissipation of the solid part and considered only the effects of loading and self-attraction. In Figure 2.9, the effect of solid dissipation is amplified at higher frequencies. The difference between the two

Love number grows with σ, reaching half an order of magnitude for $4 \leq \omega \leq 5$. This is physically expected as the mantle approaches the fluid limit for an extremely rapid rotation, and can start dissipating like a fluid. As we mentioned earlier, solid Earth dissipation would also be amplified with an early less viscous mantle due to higher Hadean-Archean temperatures (Ross and Schubert, 1989). Eventually, a regime transition may lead to the predominance of the mantle's elastic response (Lau et al., 2015, 2016a).

With the tidal response now properly characterized, the remaining part is to compute the tidal torque. The contribution of the component $U_l^{m,\sigma}$ of the tidal potential to the total tidal torque exerted on the Earth scales as the imaginary part of the associated Love number and is expressed as (Efroimsky and Williams, 2009; Correia et al., 2014)

$$\mathcal{T}_l^m = \frac{3}{2} G M^2 \frac{R^5}{a^6} \operatorname{Im}\left\{k_{l,m}^O\right\}. \tag{2.131}$$

In Figure 2.10, we summarize the spectra of the tidal torques of the two configurations: the global and the hemispherical oceans. Comparing the two spectra in the limit of weak friction reveals the highly irregular nature of the waveforms in the hemispherical response against the fairly regular resonance periodicity in the global configuration. Several resonances can be encountered in the hemispherical configuration due to the spatially inhomogeneous response where the hemispherical continent is a barrier on propagation of tidal pathways. This can happen in between only two resonant peaks of the global configuration. These spectral differences will have important signatures in the model of the Earth-Moon system evolution that we describe next.

2.3.2.2 The high friction asymptotic regime

We provide here a brief interlude on the tidal spectrum in a high friction regime. Looking at Figure 2.10, the first two panels correspond to regimes of high friction, and are characterized with a smooth spectrum, relative to those of moderately or weakly dissipative regimes in the panels on the right. The spectrum is also characterized with a single peak in the response which is close to spin-orbit synchronization. Thus we can study this regime by ignoring the Coriolis term in the tidal equations as the friction term dominates and as we are in the slow rotation regime. Under these assumptions, we

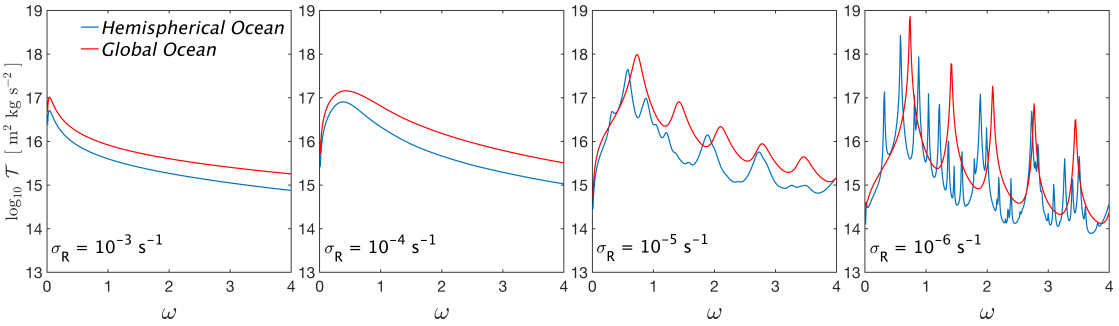

FIGURE 2.10: Tidal torque between the Earth and the Moon corresponding to the coupled oceanic-solid response in two configurations: a global oceanic shell of thickness $H = 4000$ m (shown in red), and a hemispherical ocean with the same thickness, symmetric around the equator and bounded by longitudes $\lambda = 0$ and $\lambda = \pi$ (in blue). Energy dissipation is quantified by the linear Rayleigh drag frequency σ_{R}. The logarithm of the torque is plotted as a function of the normalized frequency $\omega = (\Omega - n_{\mathrm{orb}})/\Omega_0$, where the Earth's spin rate varies with the tidal forcing frequency $\Omega = n_{\mathrm{orb}} + \sigma/2$ at fixed n_{orb}, and Ω_0 being the present spin rate of the Earth.

re-write the governing system of Eq. (2.1) as:

$$\partial_t \vec{u} + \sigma_{\mathrm{R}} \vec{u} = \boldsymbol{\nabla}(U - g\boldsymbol{\nabla}\zeta), \tag{2.132a}$$

$$\partial_t \zeta + \boldsymbol{\nabla} \cdot (H\vec{u}) = 0. \tag{2.132b}$$

Transforming to the Fourier domain we obtain

$$\vec{u} = \frac{\boldsymbol{\nabla}(U - g\zeta)}{\sigma_{\mathrm{R}} + i\sigma}, \tag{2.133a}$$

$$\boldsymbol{\nabla} \cdot \vec{u} = -\frac{i\sigma\zeta}{H}. \tag{2.133b}$$

Taking the divergence of Eq. (2.133a) and equating it with Eq. (2.133b) we obtain a solution for the tidal amplitude ζ of the form

$$\frac{g\zeta}{U} = \frac{\mu_n H/R^2}{\sigma(i\sigma_{\mathrm{R}} - \sigma) + \mu_n g H/R^2}. \tag{2.134}$$

In the preceding equation, we use the set of eigenvalues of spherical harmonics $\mu_n = n(n+1)$. We further define the characteristic frequency $\sigma_{\mathrm{p;n}}$

$$\sigma^2_{\mathrm{p;n}} = \mu_n g H/R^2, \tag{2.135}$$

and we use the definition of the complex tidal frequency $\tilde{\sigma}$ (Eq. 2.116) to re-write the solution of Eq. (2.134) as

$$\frac{g\zeta}{U} = -\frac{\sigma_{\mathrm{p;n}}^2}{\sigma\tilde{\sigma} - \sigma_{\mathrm{p;n}}^2}. \tag{2.136}$$

Looking at the expression of the Love number in Eq. (2.124), and dropping the superscripts and the subscripts while ignoring the effect of solid deformation, we use the tidal solution of Eq. (2.136) to write the quadrupolar Love number as

$$k_{2,2}^{O} = \frac{3g}{5}\frac{\rho_{\mathrm{oc}}}{\rho_{\mathrm{se}}}\frac{\zeta}{U} = -\frac{3}{5}\frac{\rho_{\mathrm{oc}}}{\rho_{\mathrm{se}}}\frac{\sigma_{\mathrm{p}}^2}{\sigma\tilde{\sigma} - \sigma_{\mathrm{p}}^2}, \tag{2.137}$$

which can be also expressed as

$$k_{2,2}^{O} = -\frac{3}{5}\frac{\rho_{\mathrm{oc}}}{\rho_{\mathrm{se}}}\left[\frac{\sigma^2\sigma_{\mathrm{p}}^2 - \sigma_{\mathrm{p}}^4 + i\sigma\sigma_{\mathrm{R}}\sigma_{\mathrm{p}}^2}{(\sigma^2 - \sigma_{\mathrm{p}}^2)^2 + \sigma^2\sigma_{\mathrm{R}}^2}\right]. \tag{2.138}$$

Since we use the imaginary part of the Love number to describe the tidal response, we easily extract the imaginary part from Eq. (2.138) to obtain

$$\mathrm{Im}\left\{k_{2,2}^{O}\right\} = -\frac{3}{5}\frac{\rho_{\mathrm{oc}}}{\rho_{\mathrm{se}}}\left[\frac{\sigma\sigma_{\mathrm{R}}\sigma_{\mathrm{p}}^2}{(\sigma^2 - \sigma_{\mathrm{p}}^2)^2 + \sigma^2\sigma_{\mathrm{R}}^2}\right]. \tag{2.139}$$

We are interested in retrieving a closed form solution for the position of the single peak near synchronization, thus we straightforwardly proceed to compute the derivative of Eq. (2.139) to obtain

$$\left[\mathrm{Im}\left\{k_{2,2}^{O}\right\}\right]' = -\frac{3}{5}\frac{\rho_{\mathrm{oc}}}{\rho_{\mathrm{se}}}\sigma_{\mathrm{R}}\sigma_{\mathrm{p}}^2\left[\frac{-3\sigma^4 + \sigma^2(2\sigma_{\mathrm{p}}^2 - \sigma_{\mathrm{R}}^2) + \sigma_{\mathrm{p}}^4}{\left((\sigma^2 - \sigma_{\mathrm{p}}^2)^2 + \sigma^2\sigma_{\mathrm{R}}^2\right)^2}\right], \tag{2.140}$$

for which the solution is

$$\sigma_{\otimes} = \pm\sqrt{\frac{1}{6}\left[2\sigma_{\mathrm{p}}^2 - \sigma_{\mathrm{R}}^2 \mp \sqrt{(2\sigma_{\mathrm{p}}^2 - \sigma_{\mathrm{R}}^2)^2 + 12\sigma_{\mathrm{p}}^4}\right]}, \tag{2.141}$$

where only the plus sign inside the square root gives a real frequency. Noting that $\sigma_{\mathrm{p}} \sim 10^{-4}$ s^{-1}, we re-arrange the latter expression using powers of the ratio $\sigma_{\mathrm{p}}/\sigma_{\mathrm{R}}$, and we ignore terms of order 3 and more. Doing so, the peak frequency $\sigma_{\otimes}$ simplifies drastically to

$$\sigma_{\otimes} \simeq \frac{\sigma_{\mathrm{p}}^2}{\sigma_{\mathrm{R}}}. \tag{2.142}$$

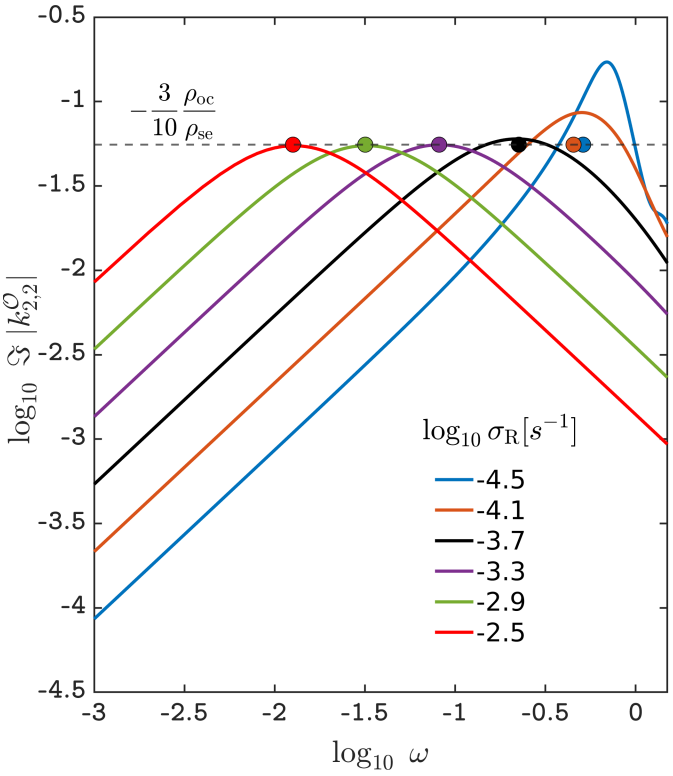

FIGURE 2.11: The spectrum of the imaginary part of the Love number in the high friction regime. As seen in Figure 2.10, the spectrum in this regime is characterized by a smooth regularity, and a single peak near synchronization. We zoom here logarithmically around this peak, and we plot the spectrum along with our analytical estimates of the position and the value of the peak derived in Eq. (2.142) and Eq. (2.143) respectively. The figure shows the accuracy of these estimates for values of $\log_{10}\sigma_R > -3.7$, beyond which we start observing the discrepancy.

Substituting σ by $\sigma_\otimes$ in Eq. (2.139), we retrieve the value of the imaginary part of the Love number at this peak, which is the maximum value of the spectrum in the high friction regime, as

$$\mathrm{Im}\left\{k^{\mathcal{O}}_{2,2}\right\}\Big|_{\sigma=\sigma_\otimes} = -\frac{3}{10}\frac{\rho_{oc}}{\rho_{se}}. \tag{2.143}$$

In Figure 2.11 we plot the imaginary part of the Love number for the pure oceanic response in the form given by Eq. (2.130). We focus on the spectrum near synchronization, and we mark the solutions for the position of the peak and its value, for different values of σ_R. Evidently, our analytical characterization of the peak is accurate in matching the full solution of the Love number. The interesting solution of the value at the peak (Eq. 2.143), being merely a ratio of the ocean and solid Earth densities, serves as a precise threshold of the maximum value of the Love number, as long as $\log_{10}\sigma_R < -3.7\ \mathrm{s}^{-1}$, beyond which the position of the peak and its value no longer match our estimates, as seen for the blue and orange markers.

2.4 Geological snapshots

Before embarking on the implementation of the the oceanic tidal theory to model the past evolution of the Earth-Moon system, we pause for an essential geological window. Besides the fact that we have no geological evidence on the possible cataclysmic features accompanying a Gerstenkorn's event, certain sets of geological data provided the earliest evidence against any suggestion of a younger Moon, even before the Apollo era. Namely, sedimentary structures were identified as associated with tidal deposition in Archean sand-stones, mud-stones, and carbonate rocks (e.g., Eriksson, 1977). The time-scale problem was not an actual problem in the geological studies, in contrast with geophysical modelling, due to the abundance of data, of various nature, that indicated the non-uniformity of tidal dissipation in the geological past.

The earliest established bundle of these data sets are the so-called paleontological "clocks" associated with studying sequences of different coloring in fossil corals, bivalves and brachiopods for the Phanerozoic eon, and in stromatolites for the Proterozoic eon. Namely, studying growth increments in invertebrate fossils can indicate the number of solar days per year and the length of the synodic month (e.g., Wells et al., 1963); a methodology that presumes certain periodicities across different bands. Although these data sets have proved the variation of the tidal dissipation rate during the past 500 Myrs, the quantitative interpretation of these growth increments is widely controversial (Lambeck, 1980; Scrutton, 1978; Williams, 2000).

Another data set is established through the study of cyclic rhythmites with tidal origin (e.g. Williams, 1989; Sonett and Chan, 1998; Williams, 2000; Eulenfeld and Heubeck, 2022); a methodology that has been providing another scope into the geological past since the 1980s. Namely, tidal laminae, or vertically accreted thin beds were generated by the alternating deposition of fine-grained sandstone, siltstone, and mudstone. The periodic nature of these thickness alternations reflects the strong tidal influence on sedimentation during phases of strong and weak tidal currents. These cyclicities were later labelled as tidal rhythmites, and were studied to identify the past tidal periodicities. For instance, diurnal laminae are related to the lunar day, while synodic tides leave a distinctive signature in the rhythmite record. Determining the periodicities is optimized for long records of tidal deposits that span several years such that several independent astronomical parameters can then be computed and cross-verified. The earliest of these data points is that of Eriksson and Simpson (2000), where tidal bundles from an exposed outcrop in the Moodies Group of the Barberton Greenstone Belt in South Africa, which

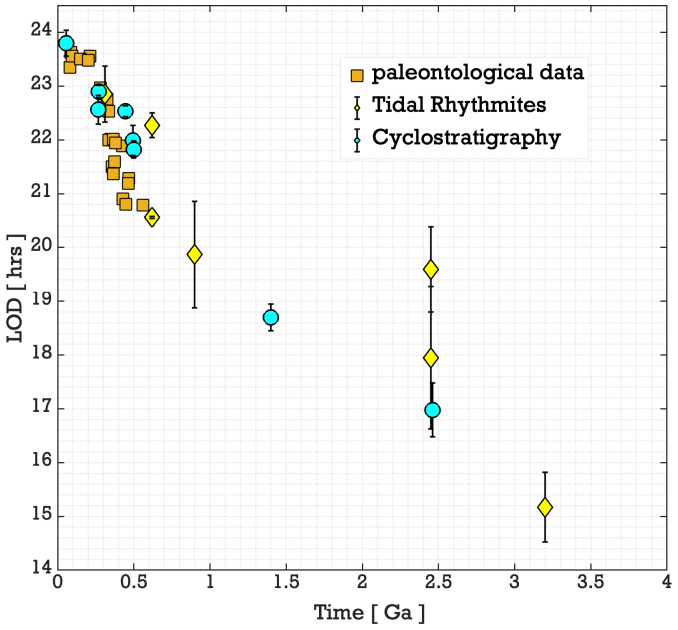

FIGURE 2.12: A compilation of proxies of the deep time history of the Earth-Moon system, plotted in terms of the LOD. The data are split into the three sets discussed in the text: the paleonotlogical clocks that include fossil corals, bivalves and brachiopods, and stromatolites (Williams, 2000; Denis et al., 2011); the tidal rhythmites data set (Williams, 1989, 1990, 1997, 2000; Sonett and Chan, 1998; Walker and Zahnle, 1986; de Azarevich and Azarevich, 2017), and the cyclostratigraphic data set (Meyers and Malinverno, 2018; Zhong et al., 2020; Sørensen et al., 2020; Huang et al., 2020; Lantink et al., 2022).

dates back to about 3.22 billion years old, were analyzed. The data point was recently revisited in Eulenfeld and Heubeck (2022) to provide a LOD estimate around 13 hours, and an Earth-Moon separation of $\sim 42 R_{\mathrm{E}}$. Although the inference methodology in tidal bundles avoids some of the uncertainties associated with paleontological data, it is still subject to the way the cycles are interpreted and the possible detorioration of the laminae, which has led to divergent astronomical quantities inferred from the same record (e.g., Walker and Zahnle, 1986; Sonett and Chan, 1998).

An alternative, and to our understanding more robust scope into deep geological time is based on the study of Milankovitch cycles. Namely, quasi-periodic variations in insolation driven by astronomical cyclicity leave behind climate variations that are recorded in sedimentary strata (see Section 1.5.1 for the analogy in glacial cycles). The study of these strata, now well known as the field of cyclostratigraphy, involves contrasting the variability and constructing the deep-time ratios between the periodicities of the Earth's eccentricity, climatic precession, and obliquity cycles (e.g., Hinnov, 2018; Sinnesael et al., 2019). Namely, climatic precession and obliquity periods depend on the precession frequency of the Earth, which varies along the tidal history, while the

TABLE 2.1: Cyclostratigraphic data. In boldface, we display the direct observables we used: the precession frequency p in arcsec/yr. The time of observation, T, is in the second column. The semi-major axis of the Moon ($a_{\rm M}$) given in Earth radius ($R_{\rm E}$) or in km, and the length of the solar day (LOD), in hours, are derived from the observed quantities using the model that is presented in the text. These values may thus differ from the corresponding values published in the referenced publications; IC denotes the initial conditions (Laskar et al., 2004). The two values (a,b) for the Lucaogou data set correspond to different analyses (a): TimeOptMCMC (Meyers and Malinverno, 2018); (b) obliquity and precession cycle counting (Huang et al., 2020). Whenever it is specified in the original publication, the uncertainty in p is set to 2σ. The uncertainty of the other variables is propagated through the nominal solution of the present study. The references for the datasets, indicated by superscripts are as follows: 1- Laskar et al. (2004), 2- Meyers and Malinverno (2018), 3- Huang et al. (2020), 4- Zhong et al. (2020), 5- Sørensen et al. (2020), 6- Fang et al. (2020), 7- Lantink et al. (2022).

dataset	T [Ga]	p [arcsec/yr]	$a_{\rm M}$ [$R_{\rm E}$]	$a_{\rm M}$ [km]	LOD [hr]
IC$^{(1)}$	0.000	**50.467718**	60.142611	383598	24.00
Walvis Ridge$^{(2)}$	0.055	**51.28 ± 1.02**	59.94 ± 0.26	382284 ± 1650	23.80 ± 0.24
Lucaogou(a)$^{(3)}$	0.268	**57.01 ± 1.37**	58.57 ± 0.31	373538 ± 2000	22.56 ± 0.27
Lucaogou(b)$^{(3)}$	0.270	**55.36 ± 0.51**	58.95 ± 0.12	375967 ± 750	22.90 ± 0.11
Yangtze Block$^{(4)}$	0.445	**57.19 ± 0.53**	58.52 ± 0.12	373277 ± 750	22.53 ± 0.10
Alum shale$^{(5)}$	0.493	**60.11 ± 1.59**	57.88 ± 0.34	369153 ± 2200	21.99 ± 0.28
Luoyixi$^{(6)}$	0.500	**61.06 ± 0.94**	57.67 ± 0.20	367854 ± 1300	21.82 ± 0.16
Xiamaling$^{(2)}$	1.400	**85.79 ± 2.72**	53.27 ± 0.41	339777 ± 2600	18.70 ± 0.25
Joffre$^{(7}$	2.460	**108.91 ± 8.28**	50.24 ± 0.96	320452 ± 6100	16.98 ± 0.50

eccentricity cycles of the Earth are largely stable (Laskar et al., 2011a). The robustness of this method is of course dependent on how well preserved these sedimentary successions are; a feature that is less and less established the deeper we head in geological time, especially given the need of independent high-precision geochronological verification. At the time of writing this manuscript, the oldest cyclostratigraphic reconstructions studied the records in the 1.4-billion-year-old Xiamaling Formation from the North China Craton (Zhang et al., 2015; Meyers and Malinverno, 2018), and the 2.46-billion-year-old Joffre Member of the Brockman banded iron formation (Lantink et al., 2022).

In Figure 2.12 we plot samples of these three data sets (paleontological data set, tidal rhythmites, and cylcostratigraphic inferences) in terms of the inferred LOD. We first note that the LOD is not the directly inferred quantity for the tidal rhythmites or the cyclostratigraphy data, but it is rather the length of the synodic month for the former and the precession frequency for the latter. That said, the LOD is computed for each data point in the corresponding study based on different assumptions about tidal evolution that are usually model dependent. By visual inspection, the data empirically trace a delicate history of the long term evolution of the LOD that involves a rich variation behavior. However, it is impossible to accept all the data points at face value, as several data points coincide in time (or are in each other's vicinity), but vary in their LOD

TABLE 2.2: Tidal rhythmites data. In boldface, we display the observables. In general, the observable is the number of synodic lunar months per year or in an equivalent way, as quoted here, the number of sidereal lunar months per year (col. 3). The values are issued from the referenced publications (col. 1). For the Moodies Group, we could not infer this quantity from the original publication, and the corresponding estimate of the lunar semi-major axis was taken from de Azarevich and Azarevich (2017). The semi-major axis, $a_{\rm M}$, is obtained through Kepler's law ($n_{\rm M}^2 a_{\rm M}^3 = G(M_{\rm M} + M_{\rm E})$). As for the cyclostratigraphic data (Table.2.1), all other quantities (p, LOD) are derived from the observed quantities using the model that is presented in the text. These values may thus differ from the corresponding values published in the referenced publications. The uncertainty of the observables are propagated to the derived variables through the nominal solution of the present study. The values at the origin ($T = 0$) are from Laskar et al. (2004). It should be noted that the present value of sidereal lunar months per year and lunar semi-major axis provided here for $T = 0$ differs from some published value because here we consider averaged values, which should be the case for such long-term studies (see Figure 18 from Laskar et al., 2004). The references for the datasets, indicated by superscripts are as follows: 1- Laskar et al. (2004), 2-Sonett and Chan (1998), 3- Williams (1997), 4- Williams (2000), 5- Williams (1990), 6- Walker and Zahnle (1986), 7- Eriksson and Simpson (2000), 8- de Azarevich and Azarevich (2017).

dataset	T [Ga]	smo/yr	p [arcsec/yr]	$a_{\rm M}$ [$R_{\rm E}$]	LOD [hr]
IC$^{(1)}$	0.000	13.4289	50.467718	60.142611	24.00
Mansfield$^{(2)}$	0.310	**13.86 ± 0.21**	55.60 ± 2.55	58.89 ± 0.59	22.85 ± 0.52
Elatina$^{(2)}$	0.620	**14.93 ± 0.01**	69.24 ± 0.13	56.04 ± 0.03	20.56 ± 0.02
Elatina$^{(3,4)}$	0.620	**14.10 ± 0.10**	58.55 ± 1.24	58.22 ± 0.28	22.27 ± 0.23
Cottonwood$^{(2)}$	0.900	**15.33 ± 0.60**	74.68 ± 8.32	55.06 ± 1.44	19.87 ± 0.99
Weeli Wolli$^{(4,5)}$	2.450	**16.70 ± 1.10**	94.71 ± 17.19	52.01 ± 2.29	17.95 ± 1.32
Weeli Wolli$^{(6)}$	2.450	**15.50 ± 0.50**	77.04 ± 7.03	54.66 ± 1.18	19.59 ± 0.79
Moodies Group$^{(7,8)}$	3.200		148.36 ± 18.61	**46.45 ± 1.50**	15.17 ± 0.65

inference drastically. As we are faced with the model-dependence of the data and our inability to judge their accuracy, we decide not to take the geological data into account when building our tidal model, and rather see independently the matching between them and our modelled evolution history afterwards. Furthermore, we only consider hereafter the data sets of tidal rhythmites and cyclostratigraphy, as they are, potentially, more robust than the paleontological data. We summarize the two data sets in Tables 2.1 and 2.2.

2.5 Model description

2.5.1 Continental drift and oceanic geometry shifting

We are now fully geared to construct and describe our model for the long term tidal evolution of the Earth-Moon system. The tidal theory detailed earlier serves as the

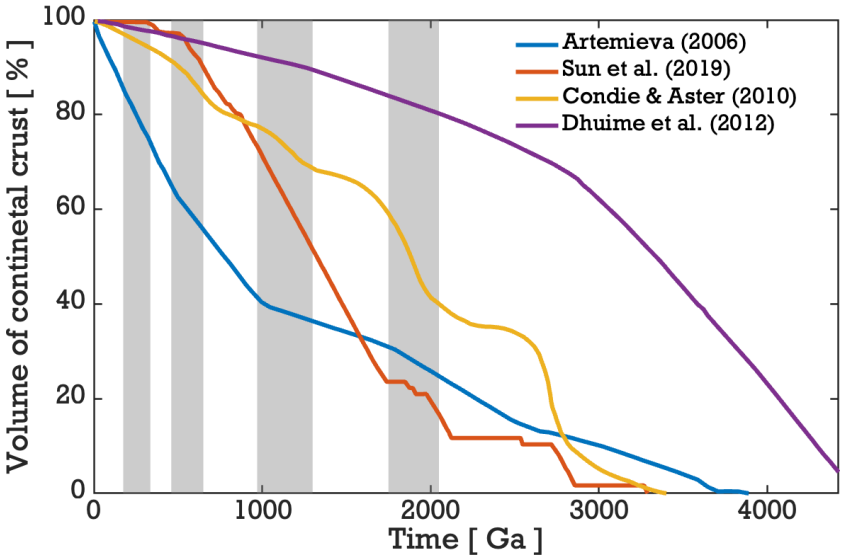

FIGURE 2.13: A sample of crustal growth curves representing those that rely on age distributions preserved in present day geology (Artemieva, 2006; Condie and Aster, 2010), and those that constrain the volumes of crust in the past independent of present day age distributions (Dhuime et al., 2012; Sun et al., 2019). While acknowledging the discrepancies in the predictions arising from each approaches, all curves agree on transitioning from a global ocean in the earliest eons to the present continental volume. Gray patches mark major super-continental cycles.

foundation of the model. Focusing on the dependence of tidal dissipation on the Earth's spin rate, we combine the two analytical formulations detailed earlier that describe long-wavelength barotropic tidal flows over shallow spherical and hemispherical shells. Both configurations are parameterized by two free parameters: the oceanic uniform thickness H and the dissipation frequency σ_{R}. The spherical shell describes a global ocean that we assume had existed in the earliest eons of the lifetime of the Earth similar to the recent study in (Motoyama et al., 2020). The existence of an early ocean is supported by models on planetary atmosphere formation and the early solidification of the magma ocean (e.g., Hamano et al., 2013), evidence from the analysis of detrital zircon around 4.4 Ga (Wilde et al., 2001), evidence on the interaction between the ocean and continental crust 4 billion years ago (Mojzsis et al., 1996), and from isotopic studies on Earth's early surface environment (Oxygen isotopes: Peck et al., 2001; Bindeman et al., 2018; Johnson and Wing, 2020; Hydrogen isotopes: Pope et al., 2012; Kurokawa et al., 2018. The stability of isotopic compositions are indicative of the subaqueous nature of almost all large igneous province volcanism pre-Archean (e.g., Kump and Barley, 2007). Moreover, to date, the Earth's earliest extensive platform sedimentary successions correspond to the late Archean, indicative of the continents becoming exposed at that time.

The voluminous nature of early oceans is supported by experimental thermodynamic

models studying water storage capacities in the mantle and its dependence on the pressure-temperature effects (e.g., Townsend et al., 2016; Muir and Brodholt, 2018; Chen et al., 2020). Recently, Dong et al. (2021) established a temperature-dependent water storage capacity model for the Earth's mantle. Their experiments depicted that the early – significantly hotter – mantle was characterized by a water storage capacity that is lower than that at present. Due to the continuous exchange and redistribution of water between the ocean and the mantle reservoirs over geological time (van Keken et al., 2011), estimates of water content in the mantle today being greater than its storage capacity in the early Archean means that early Archean oceans must have been voluminous and possibly larger than at present, with very probable excessive flooding over the existing continents, if any (Dong et al., 2021). The "globality" of the early ocean is justified by the analysis of continental crust growth curves based on geochemical evidence in radiogenic isotope ratios (e.g., Hawkesworth et al., 2020). In Figure 2.13 we plot a sample of curves for the modelled growth of the continental crust from the literature (Artemieva, 2006; Condie and Aster, 2010; Dhuime et al., 2012; Sun et al., 2019), all anchored to the present day volume. The curves are based on the presently preserved proportions of rocks with either different geological or crust formation ages. One of the controversial issues among these models is whether the predicted crustal growth is more realistic when based on archives in the crust or in the mantle, and the role of the underlying assumptions in the application of such archives (e.g., Payne et al., 2016; Korenaga, 2018). The discrepancies we observe in the sampled curves thus arise based on different assumptions. A limitation with these models is that they account for the cumulative growth of the crust summing ultimately to unity at the present, hence by construction, they do not allow for a past crustal volume greater than the current one. It is thus likely that such curves represent minimum estimates for the volumes (Guo and Korenaga, 2020). Nonetheless, these curves typically agree on two asymptotic limits: a near-to-full global ocean in the Archean, and a long term transition towards the present configuration. It is also noteworthy that the curve of Dhuime et al. is representative of a larger ensemble of models in the literature (e.g., Pujol et al., 2013), all agreeing that 65–75% of the present volume had been generated by 3 Ga. Thus taking these curves into account, we use the hemispherical ocean configuration to model the Earth's surface at the present, and we transition to the global ocean configuration in the earliest eons.

In the hemispherical ocean phase of the model, we still have one variable to constrain: the position of the center of the ocean. As seen in Figure 2.6, the surface position of the ocean on the sphere can distort the tidal spectrum by shifting the spectral position and changing the amplitude of resonances. In particular, in the limit of a polar ocean, the

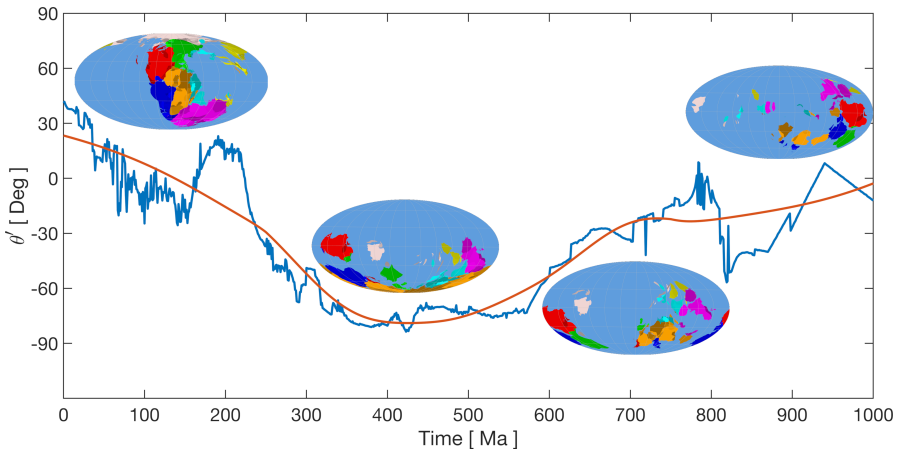

FIGURE 2.14: Temporal evolution of the latitude of the surface "paleo-barycenter" over the last one billion years. The plate tectonics reconstruction is adopted from Merdith et al. (2021), which establishes the first kinematically continuous tectonic motion model across multiple super-continental cycles. The evolution is smoothed in red using a moving polynomial regression filter with a window of 200 Myr. In our effective model, this curve maps the evolution of the center of the hemispherical continental cap that transitions from being symmetric about the equator during the Mesozoic, to being almost polar during the Paleozoic.

spectrum is uniquely characterized by a single resonant peak and a smooth response in the remainder of the spectrum where all the resonances are absorbed into the background. Thus it is essential for us to take this variation into account in our model. For this purpose, we adopt a recent model that reconstructs the first kinematically continuous history of plate tectonics and continental drift over the last one billion years (Merdith et al., 2021). We use the modeled tectonic boundaries provided by the authors, and we construct a history of the geographic center by computing the surface projection of the "barycenter" of the continental distribution. We use the `GPlates` open-source reconstruction software (Boyden et al., 2011; Gurnis et al., 2012) to post-process the data of Merdith et al. (2021). In Figure 2.14 we plot the evolution of the latitude of the continental barycenter in time, along with sketches of the continental distribution. The evolution is also smoothed using a `LOESS` regression filter (a generalized moving polynomial regression subroutine for `MATLAB`; Cleveland and Devlin, 1988), and it shows a regime transition between a near-equatorial continental cap around the present, to a near polar one during the Paleozoic, and then back again to the equatorial configuration during the Neo-Proterozoic. When the hemispherical configuration is adopted for the ocean, we anchor the center of the continental cap to this barycenter evolution history. As the model of Merdith et al. (2021) covers the interval of 0-1 Ga only, we fix the hemispherical ocean to its position at 1 Ga beyond that.

In summary, the tidal response of the Earth is initiated with the hemispherical ocean

configuration from the present till 1 Ga, with a center of the continental cap that follows the continental drift, and we call that Phase 1 of the model. In Phase 2, we continue to use the hemispherical configuration, but due to the lack of a continuous tectonic reconstruction, we fix the ocean to its position at 1 Ga. During Phase 2, the tidal responses of the hemispheric and global configurations are computed, but only the former is used as the response of the Earth. Phase 2 terminates when the responses of the two configurations equate, signaling the transition into the global ocean configuration and the initiation of Phase 3. We denote by t_{switch} this transition epoch, which is determined implicitly and autonomously by the integrator, and it takes a different value for different combinations of the pair of free parameters (H, σ_{R}).

2.5.2 Orbital dynamics

For the reconstruction of the Earth-Moon distance, we use a reduced secular dynamical model describing the exchange of angular momentum between the Earth's rotation and the lunar orbital motion (Webb, 1982a; Tyler, 2021). Similar to Goldreich (1966), the equations for tidal friction are averaged over the tidal timescale, ignoring lunar eccentricity. We further assume co-planarity, i.e. we ignore the Earth's obliquity and lunar inclination as we are, at this stage, only focused on the time-scale problem and the lunar distance evolution. The tidal evolution model of Touma and Wisdom (1994a) made the same approximations as Goldreich (1966), but their formulation was carried out in a canonical framework. They computed, numerically, the full (un-averaged) tidal evolution, including planetary perturbations, and the full rigid-body dynamics of the Earth. They further enhanced their model by carrying out the integrations using the symplectic mapping methods of Wisdom and Holman (1992) and Touma and Wisdom (1994b). Their results depicted that the full numerical integrations are in good agreement with the averaged model of Goldreich (1966). Thus we proceed with the averaged model as a fairly adequate description of this highly non-linear system.

While the predominance of oceanic dissipation over terrestrial and lunar solid dissipation is established, we mainly focus on terrestrial oceanic tides in our reduced dynamical model. This simplification allows for a systematic understanding of the hierarchically complex contributions of multiple intervening players. The contribution of eccentricity tides becomes significant when the orbit of the Moon was highly eccentric. Accounting for lunar tides and lunar core-mantle boundary dissipation would counteract the effect of terrestrial tides and increase the lunar eccentricity when going backwards in time,

but only to moderate values ($e \leq 0.1$) (e.g., Daher et al., 2021). Attaining a highly eccentric lunar orbit is possible through an evection resonance, which occurs when the precession period of the perigee of the Moon equals 1 year, the orbital period of the Earth. Touma and Wisdom (1998) studied this regime and showed that the capture into such a resonance could have been encountered for a lunar semi-major axis $a_{\rm M} \approx 4.6 R_{\rm E}$, exciting the lunar eccentricity to $e_{\rm M} \approx 0.5$. However, the timescale of capture and escape from this evection resonance is $10^4 \sim 10^5$ yr, after which the lunar orbit tends to circularization again (Rufu and Canup, 2020). Furthermore, the evection regime can only be encountered by integrating forwards, while we integrate backwards in our model due to the lack of constrained initial conditions in the forward integration.

Dissipation within the Moon is also rendered significant at the early stage of the system with the Earth fully molten and the moon having little to no atmosphere, forcing it to quickly cool into a highly dissipative body. However, this also occurs over a relatively short time interval, specifically when $a_{\rm M} < 20 R_{\rm E}$ (Zahnle et al., 2015). The timescale of these mechanisms that can render our approximations invalid is much smaller than that associated with the long-term tidal evolution we model in our work. Furthermore, a key feature of the lunar distance evolution is the runaway effect encountered in the backward integration, with $a_{\rm M}$ collapsing rapidly when reaching $30 R_{\rm E}$ to the formation site, slightly beyond the Roche limit, within few million years. This effect is a robust one regardless of the tidal model (see for e.g., Webb, 1982a; Touma and Wisdom, 1994a). We also observe the same effect in our results (see Figure 2.16). Our evolution prediction in the next section also shows that the Moon spends 97% of its lifetime with $a_{\rm M} > 30 R_{\rm E}$. Thus, as much as early stage mechanisms are essential to constrain the formation scenarios of the system, the robustness of the runaway evolution beyond $30 R_{\rm E}$ renders the reduced dynamical model a safe and sufficient approach for the long-term study. This model should provide the skeleton of the secular evolution in the system around which full spatial dynamics can flesh. Other effects such as climate friction (Levrard and Laskar, 2003) and core-mantle coupling (Neron de Surgy and Laskar, 1997; Touma and Wisdom, 2001) are also ignored, as well as halts of tidal interaction due to Laplace plane transitions (Ćuk et al., 2016). We also ignore periods of extensive glaciation, where the Earth could be potentially covered by a thick ice shell altering the generated oceanic tides (Tyler, 2020).

Under these assumptions, the governing dynamical system of equations is expressed as

$$\frac{dL_\Omega}{dt} = -\left(\mathcal{T}_\mathrm{M} + \mathcal{T}_\mathrm{S}\right) \ , \tag{2.144}$$

$$\frac{dL_\mathrm{M}}{dt} = \mathcal{T}_\mathrm{M} \ , \tag{2.145}$$

where $\mathcal{T}_\mathrm{M}$ is the lunar semi-diurnal tidal torque coupling between the oceanic and the solid response of the Earth, and $\mathcal{T}_\mathrm{S}$ is its solar counterpart, both computed for the hemispherical configuration as detailed in Section 2.3.1.5 and for the global configuration as described in Section 2.3.2. The orbital angular momentum of the Moon $L_M = \beta\sqrt{G(M_\mathrm{E} + M_\mathrm{M})a_\mathrm{M}}$, where $\beta = M_\mathrm{E}M_\mathrm{M}/(M_\mathrm{E}+M_\mathrm{M})$ is the Earth-Moon system's reduced mass. The rotational angular momentum of the Earth is defined as $L_\Omega = C(\Omega)\Omega$, with the time-varying principal moment of inertia given by (Goldreich, 1966)

$$C(\Omega) = C(\Omega_0) + \frac{2k_2^f R_\mathrm{E}^5}{9G}(\Omega^2 - \Omega_0^2). \tag{2.146}$$

Here, k_2^f is the second-degree fluid Love number of centrifugal/tidal deformation and G is the gravitational constant. The differential equation is integrated backwards in time using the Runge-Kutta 9(8) method, starting from the present and stopping at $a_\mathrm{M} = 3R_\mathrm{E}$. The tidal torque computation is coupled to the orbital integrator and is computed simultaneously at each step. It takes the model parameters (H, σ_R) as input, and the system's variables, a_M and Ω, to compute the tidal frequency and, consequently, the coupled tidal response.

Once the lunar semi-major axis (a_M) and the rotation speed of the Earth (Ω) are determined, we compute the obliquity of the Earth (ϵ) and the precession frequency (p) as derived quantities (Laskar et al., 2004). Starting with Equations (40) and (46) from Correia and Laskar (2010) in the case of zero eccentricity, we obtain

$$\frac{d\epsilon}{dt} = \frac{Kn}{C(\Omega)\Omega}\sin\epsilon\left(\frac{\Omega}{2n_\mathrm{M}}\cos\epsilon - 1\right), \tag{2.147}$$

and

$$\frac{da_\mathrm{M}}{dt} = \frac{2K}{\beta a_\mathrm{M}}\left(\frac{\Omega}{n_\mathrm{M}}\cos\epsilon - 1\right), \tag{2.148}$$

that is

$$\frac{d\epsilon}{da_\mathrm{M}} = \frac{\beta n_\mathrm{M} a_\mathrm{M}}{4C(\Omega)\Omega}\sin\epsilon\frac{\Omega\cos\epsilon - 2n_\mathrm{M}}{\Omega\cos\epsilon - n_\mathrm{M}}. \tag{2.149}$$

We note that the tidal response parameter, K, disappears from the equations. This would also be the case if K depended on Ω. The obliquity evolution equation (2.149) is integrated using the values of a_{M} and Ω that result from the tidal flows and orbital dynamics coupled system. The precession frequency, p, is then derived using Equations (6) and (8) from Laskar et al. (2004) with zero eccentricity and inclination, that is

$$p = \frac{3}{2}\left(\frac{GM_{\mathrm{S}}}{a_{\mathrm{E}}^3} + \frac{GM_{\mathrm{M}}}{a_{\mathrm{M}}^3}\right) E_d(\Omega_0)\frac{\Omega}{\Omega_0^2}\cos\epsilon. \tag{2.150}$$

In (2.149) and (2.150), the constant values taken for the Earth's radius R_{E}, the gravitational constant of the Moon, GM_{M}, and the Sun, GM_{S}, the mass ratio $M_{\mathrm{E}}/M_{\mathrm{M}}$, the rotational velocity Ω_0, the Earth's semi-major axis a_{E}, and the inertia parameter $C(\Omega_0)/M_{\mathrm{E}}R_{\mathrm{E}}^2$ are adopted from INPOP21 (Fienga et al., 2021). The dynamical ellipticity at the origin of date, $E_d(\Omega_0) = 0.003243$, is determined from the initial conditions for the obliquity (ϵ_0) and precession (p_0) adopted from the La2004 solution (Laskar et al., 2004). All the values of applied parameters are summarized in Table 2.3.

This derivation of the obliquity and precession frequency evolutions is only valid in the limit of a distant Moon, that is, when the Moon is beyond its Laplace radius (Tremaine et al., 2009; Farhat and Touma, 2021) and its Laplace plane is the ecliptic rather than the Earth's equatorial plane (Boué and Laskar, 2006). In our a_{M} evolution of Figure 2.16, the Laplace regime transition occurs very early in the evolution ($t > 4$Ga); thus, when we compute and plot the precession frequency evolution in the next section, we do so over the interval between the present and 3.5 Ga. We also note that for cyclostratigraphic data points, the precession frequency is the direct observable (Table 2.1).

2.6 Model prediction

2.6.1 Constraining effective parameters

With the tidal-orbital coupled model properly described, what remains is to constrain the two free effective parameters. We recall that the first of these is the effective frequency σ_{R}, which parameterizes oceanic dissipation by globally modeling the bottom friction and the conversion of barotropic flows into internal gravity waves (e.g., Carter et al., 2008). This frequency can also be interpreted as the inverse of a dissipation timescale, τ, that quantifies the time needed to deplete the kinetic energy budget of tidal oscillations

TABLE 2.3: Values of constant parameters used in the numerical implementation of the theory. Astronomical values are adopted from INPOP21 (Fienga et al., 2021). Oceanic and rheological parameters are adopted from Auclair-Desrotour et al. (2019a). The average rigidity is computed from the PREM model (Dziewonski and Anderson, 1981), while the average viscosity is computed from mantle viscosity inversions in Lau et al. (2016b). The initial conditions of the orbital integration are the mean elements from the La2004 astronomical solution (Laskar et al., 2004).

Parameter	**Value**
Surface gravitational acceleration (g)	9.81 m s^{-2}
Earth radius (R_E)	6378.1366 km
Solar gravitational constant (GM_S)	$2.95912208285381355\times10^{-4}$ AU^3 day^{-2}
Earth-Moon gravitational constant ($G[M_\mathrm{E}+M_\mathrm{M}]$)	$8.99701139522114438\times10^{-10}$ AU^3 day^{-2}
Earth to Moon mass ratio ($M_\mathrm{E}/M_\mathrm{M}$)	81.30056789872074318737
Uniform oceanic density (ρ_oc)	1022 kg m^3
Andrade characteristic time (τ_A)	2.19×10^4 yr
Andrade rheological exponent (α_A)	0.25
Average rigidity of the deformable mantle (μ_E)	17.3×10^{10} Pa
Average viscosity of the deformable mantle (η_E)	3.73×10^{21} Pa s
Present day mean lunar semi-major axis (a_0)	60.142611 R_E
Present day mean sidereal length of the day (LOD_s)	23.934468 hr
Present day mean obliquity (ϵ_0)	23.2545°
Present day mean precession frequency (p_0)	50.467718 arcsec yr^{-1}
Earth's semi-major axis (a_E)	1.495978707×10^8 km
Earth's inertia parameter ($C_0/(M_\mathrm{E}R^2)$)	0.3306947357075918999972
Earth's fluid Love number (k_2^f)	0.93

after switching off the forcing. Although σ_R is probably a function of local topography, its spatial variation can be averaged out longitudinally over the Earth's fast rotation and latitudinally over precession and plate tectonics. The second free parameter in our model is the uniform effective oceanic thickness, H. The imprints of these two parameters on the tidal response spectrum are distinguishable: variations in H smoothly shift the positions of the resonant peaks while slightly varying their amplitudes. In contrast, as we have seen in Figure 2.10, variations in σ_R can completely reshape the tidal spectrum, amplifying the resonant peaks by several orders of magnitude when σ_R decreases or, otherwise, completely absorbing the resonant peaks into the background spectrum.

To constrain these parameters, we compute the evolution of the Earth-Moon system that results from the luni-solar semi-diurnal tidal torque over a two-dimensional grid defined by ranges of values of (H, σ_R). We do so for three models that ascend in realism: a global ocean model across the full geological history (similar to Tyler, 2021); an "average" hemispherical ocean model across the full geological history (similar to Webb, 1982a), for which the response at any tidal frequency is averaged over all possible oceanic positions on the sphere; and our combined model that starts at the present with the hemispherical ocean evolving with the mimetic continental drift, then switches to

the global ocean (further details on the combined model in Section 2.5). For each pair of (H, σ_R), we extract from the corresponding constructed dynamical history of the Earth-Moon distance the resulting present rate of lunar recession, $\dot{a}_0$, and the lunar formation time, t_f (the time at which the Moon reaches $3R_E$), and then we compute the mean square weighted deviation χ^2, taking two data points into account: the Lunar Laser Ranging (LLR) estimate of lunar orbital recession, which gives $\dot{a}_0^{LLR} \pm \sigma^{LLR} = 38.30 \pm 0.08$ mm/year (Williams and Boggs, 2016); and geochemical estimates of lunar formation time, which we denote by $t_f^{geo} \pm \sigma^{geo} = 4.425 \pm 0.025$ Ga (Maurice et al., 2020). χ^2 is then computed as

$$\chi^2 = \frac{1}{2}\left[\left(\frac{\dot{a}_0 - \dot{a}_0^{LLR}}{\sigma^{LLR}}\right)^2 + \left(\frac{t_f - t_f^{geo}}{\sigma^{geo}}\right)^2\right]. \tag{2.151}$$

Misfit surfaces of χ^2 for the three models are shown in Figure 2.15. Two χ^2 local minima exist for the global oceanic response; however, one of them corresponds to an unreasonably large average oceanic depth $H \approx 5500$ m, leaving us with a global minimum of $(H, \log_{10}\sigma_R)$= (2273 m, -4.89), where σ_R is in s^{-1}. The global minimum in the "average" hemispherical ocean model corresponds to $(H, \log_{10}\sigma_R)$= (3816 m, -4.54), which is close to the average depth of the Pacific Ocean (Amante and Eakins, 2009). For the combined model, the global minimum corresponds to $(H, \log_{10}\sigma_R)$=(4674 m, -5.19), where H is the oceanic thickness for the hemispherical phase of the model, which is twice that of the global ocean phase during earlier eons. The switch between the two geometries occurs at t_{switch}, which is implicitly determined by the dynamical integrator as we explained in Section 2.5.1. For the best-fit solution, we have $t_{switch} = 3.25$ Ga, which is consistent with the discussed evidence on the existence of a global ocean until the late Archean. If we assume that the oceanic volume is conserved over time, the best-fit value of H for the combined model corresponds to a volume of 1.19×10^{18} m^3, which is only 10% off from the currently estimated value of 1.33×10^{18} m^3 based on global relief models (Amante and Eakins, 2009). The fitted dissipation frequency, σ_R, corresponds to a decay time $\tau = 43.1$ hr, which is consistent with real oceanic studies (Garrett and Munk, 1971; Webb, 1973) that offer a range between 24 and 60 hr (or $\log_{10}\sigma_R \in [-4.93, -5.33]$). The best-fit values for the combined model correspond to a lunar trajectory characterized by a current rate of recession $\dot{a}_0 = 3.829$ cm/yr and an impact time at 4.431 Ga. We summarize the numerical results of this experiment in Table 2.4.

For the combined model only, we evaluate the uncertainties on the fitted parameters from those on the observables following the standard propagation of uncertainty method.

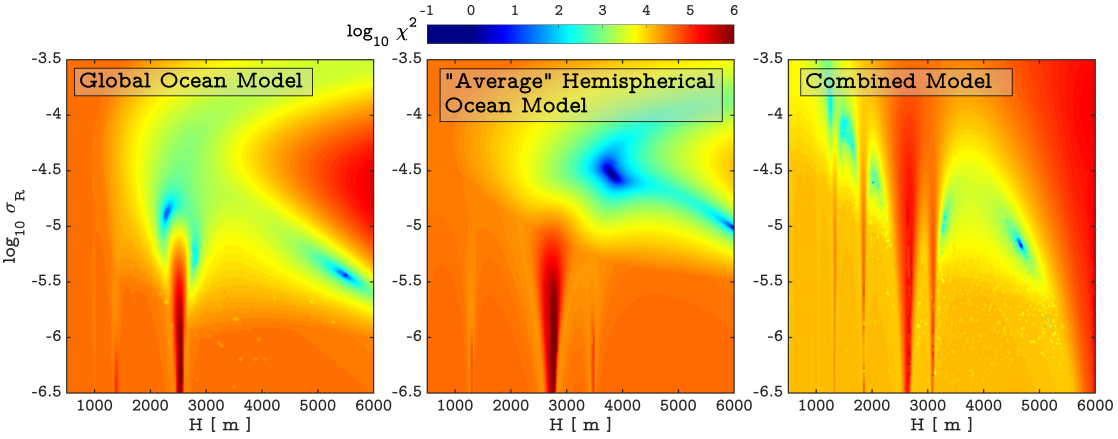

FIGURE 2.15: Misfit surfaces of χ^2 for the three studied geometric models. The past dynamical evolution of the Earth-Moon system is reconstructed for the shown ranges of our two free model parameters H and σ_R. The misfit is established using the currently measured lunar recession rate via LLR, and the lunar age as described in the text. The three models differ in the imposed geometry of the oceanic shell over the geological history, with the combined model featuring more physical realism that the other two. The numerical results of this analysis are summarized in Table 2.4. The dynamical evolution associated with each of the misfit minima is plotted in terms of: the lunar semi-major axis in Figure 2.16, length of the day in Figure 2.18, and obliquity and precession frequency in Figure 2.19.

TABLE 2.4: Misfit analysis summary. Best-fit values of the two free parameters, σ_R and H, for each of the three studied models are shown, along with the corresponding value of χ^2, as well the resulting lunar recession rate at the present $\dot{a}_0$ and the impact time, t_f.

Model	**Global Ocean**	**Hemispherical Ocean**	**Combined Model**
σ_R [s^{-1}]	1.2770×10^{-5}	2.8860×10^{-5}	6.4417×10^{-6}
H [m]	2273	3816	4674
$\dot{a}_0$[cm yr^{-1}]	3.833	3.828	3.829
t_f [Ga]	4.422	4.432	4.431
χ^2	0.0775	0.0705	0.0345

Because of the absence of correlation between the two data $\dot{a}_0$ and t_f, the entries of the variance matrix,

$$\Sigma = \begin{bmatrix} \mathrm{var}(H) & \mathrm{cov}(H, \sigma_R) \\ \mathrm{cov}(H, \sigma_R) & \mathrm{var}(\sigma_R) \end{bmatrix}, \tag{2.152}$$

are given by:

$$\mathrm{var}(H) = \left(\frac{\partial H}{\partial \dot{a}_0}\right)^2 \left(\sigma^{\mathrm{LLR}}\right)^2 + \left(\frac{\partial H}{\partial t_\mathrm{f}}\right)^2 (\sigma^{\mathrm{geo}})^2 \,, \tag{2.153a}$$

$$\mathrm{var}(\sigma_\mathrm{R}) = \left(\frac{\partial \sigma_\mathrm{R}}{\partial \dot{a}_0}\right)^2 \left(\sigma^{\mathrm{LLR}}\right)^2 + \left(\frac{\partial \sigma_\mathrm{R}}{\partial t_\mathrm{f}}\right)^2 (\sigma^{\mathrm{geo}})^2 \,, \tag{2.153b}$$

$$\mathrm{cov}(H, \sigma_\mathrm{R}) = \frac{\partial H}{\partial \dot{a}_0}\frac{\partial \sigma_\mathrm{R}}{\partial \dot{a}_0} \left(\sigma^{\mathrm{LLR}}\right)^2 + \frac{\partial H}{\partial t_\mathrm{f}}\frac{\partial \sigma_\mathrm{R}}{\partial t_\mathrm{f}} (\sigma^{\mathrm{geo}})^2 \,. \tag{2.153c}$$

The partial derivatives entering in these formulae are computed numerically from the fit of $(\dot{a}_0 \pm \sigma^{\mathrm{LLR}}, t_\mathrm{f})$ and $(\dot{a}_0, t_\mathrm{f} \pm \sigma^{\mathrm{geo}})$. The marginal uncertainties on parameters H and σ_R are $\sigma_H = \mathrm{var}(H)^{1/2} = 32.75$ m and $\sigma_{\sigma_\mathrm{R}} = \mathrm{var}(\sigma_\mathrm{R})^{1/2} = 0.2631 \times 10^{-6}$ s^{-1}, respectively. We use the variance matrix Σ to evaluate the 2σ-confidence ellipsoid around the best-fit parameters (H, σ_R). When providing the uncertainties on the evolution of the Earth-Moon distance a_M, and the length of the day LOD in the next section, we integrate 25 pairs of the parameters (H, σ_R) chosen at the boundary of this 2σ-confidence region.

2.6.2 Earth-Moon separation: A history of surfing resonances

For each of the global minima of the misfit parametric studies, we plot the evolution of the Earth-Moon distance in Figure 2.16. At the top of the evolution, we spread the earlier discussed compilation of geological proxies from tidal rhythmites and cyclostratigraphy (Tables 2.1 and 2.2). The associated evolution of the LOD, precession frequency, and obliquity are plotted in Figures 2.18 and 2.19. The three models are constrained at the end points, thus differences arise mostly in between. To better elaborate on the models' discrepancies, we plot in Figure 2.17 the temporal evolution of the tidal torque (normalized by its present value) associated with the combined model. As it is directly proportional to tidal dissipation, the long-term evolution of the torque is characterized by a non-monotonic variation, characteristic of the shrinking Earth-Moon separation, that is interrupted by multiple crossings of resonances. The distribution of resonances in the hemispherical configuration, $t < t_{\mathrm{switch}}$, is less regular than that in the global configuration, $t > t_{\mathrm{switch}}$, (see also Figs. 2.10 and 2.5 for a global description of the tidal response spectrum). Each resonance crossing in the torque generates an inflection point in the evolution of a_M, which depends on the width and to a lesser degree on the amplitude of the resonance peak (Auclair-Desrotour et al., 2014).

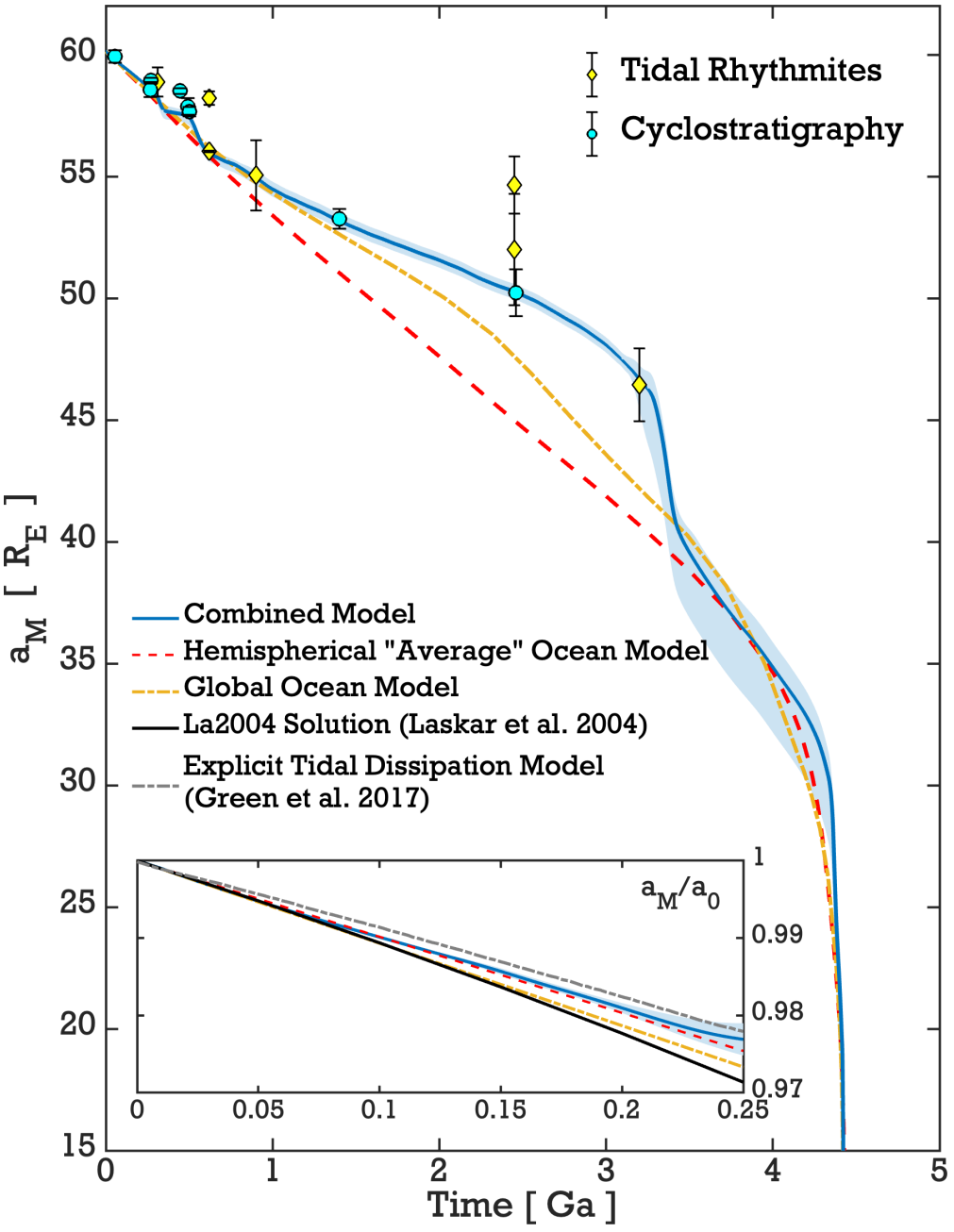

FIGURE 2.16: Evolution of the lunar semi-major axis over time. The Earth-Moon separation, a_{M}, is plotted for the three studied models, taking the best-fit values of the free parameters (H, σ_{R}) as described in Figure 2.15. Plotted on top of the evolution curves are geological inferences of a_{M} from cyclostratigraphy and tidal laminae data (Tables 2.1 and 2.2). The shaded envelope corresponds to 2σ-uncertainty in the fitted parameters of the combined model (Section 2.6.1). In the narrow window, we zoom over the most recent 250 Myr of the evolution and make a comparison with the evolution corresponding to explicit numerical tidal modeling using paleogeographic reconstructions (Green et al., 2017) and the prediction of the numerical solution La2004 (Laskar et al., 2004). We note that the integration of a_{E} extends to $3R_{\mathrm{E}}$, but the y-axis is trimmed to start at $15R_{\mathrm{E}}$ for a better visualization of the geological data.

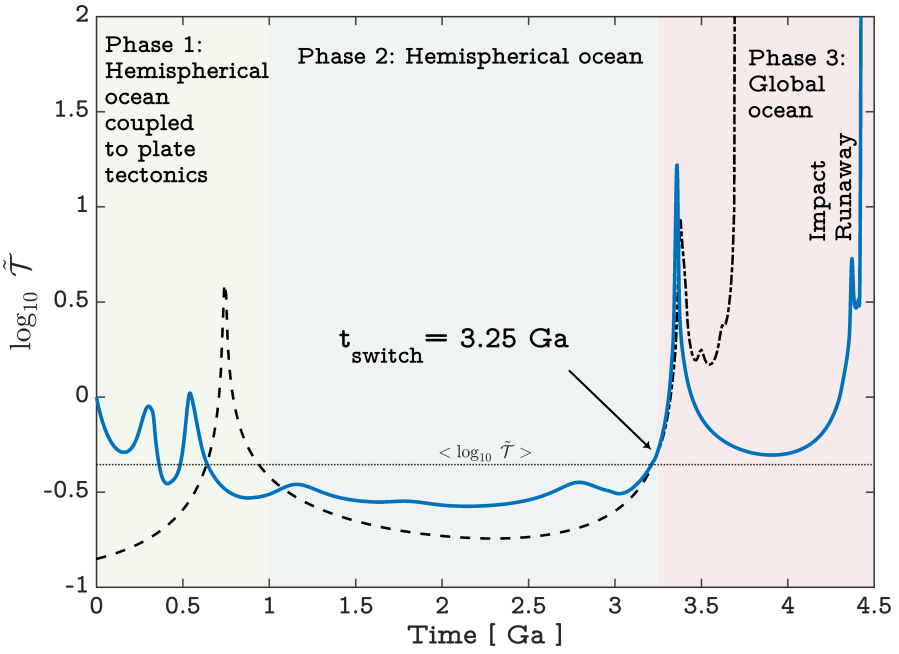

FIGURE 2.17: History of the tidal torque. The logarithm of the semi-diurnal tidal torque of the Earth (normalized by its present value: $\tilde{\mathcal{T}} = \mathcal{T}/\mathcal{T}(t = 0)$) is plotted as a function of time. The solid curve corresponds to the torque of the combined model that involves three phases: in the first phase, a hemispherical ocean migrates on the surface of the Earth following the evolution of the continental barycenter of Figure 2.14. Given that we lack a continuous plate tectonics model beyond 1 Ga, in Phase 2, we fix the hemispherical ocean to its configuration at 1 Ga to avoid discontinuities in the modeling. It is noteworthy that the attenuated tidal torque over this phase is not due to the fixed oceanic position but due to the tidal response occupying the non-resonant background of the spectrum for the tidal frequencies associated with this interval. Beyond $t_{\rm switch}$, we enter Phase 3 of the model with the global ocean configuration. The dashed and dashed-dotted curves correspond, respectively, to the global and hemispherical oceanic torques that are ignored over the specified intervals by the selective combined model.

Figure 2.17 depicts a critical feature of the combined model: starting with the hemispherical geometry at present, the torque is located around a resonance peak, which provides a higher dissipation rate than for the global ocean configuration. This models the anomalous present rate of dissipation attributed to the blocking of westward tidal propagation by the current continental distribution and the effect of enhanced dissipation by continental shelves (Arbic et al., 2009). The first phase of the model involves two major resonances between the present and 700 Ma, resulting in cascade falls of $a_{\rm M}$ of $2.8R_{\rm E}$ within 330 Myr. These resonances are associated with rapid variations of the Earth's obliquity (Figure 2.19) that could have triggered major climatic events. We observe that the first resonance overlaps with the Paleozoic oxygenation event ($\sim$ 350 Ma), while the second overlaps with the Neoproterozoic major oxygenation event ($\sim$ 600 Ma) and the Cambrian Explosion (Wood et al., 2019). Possible correlation between the

Earth's LOD and the benthic ecosystem should thus be considered (Klatt et al., 2021). The second resonance peak is almost half an order of magnitude lower than in the global configuration. This is an essential feature of the combined model by which it preserves the lunar angular momentum budget at this stage and better matches the cyclostratigraphic proxy estimates at 1.4 and 2.5 Ga, which clearly cannot be explained by the other, more dissipative models considered in Figure 2.15.

Following these resonances, the torque enters a long non-resonant interval associated with the intrinsic tidal response occupying the background of the spectrum (Figure 2.10). This "dormant" torque phase covers the interval of the so-called "boring billion years" associated with stabilized rates of atmospheric oxygenation (Alcott et al., 2019). Entering the oceanic global geometry phase of the combined model occurs at 3.25 Ga, namely after covering all significant super-continental cycles, although t_{switch} is implicitly determined by the dynamical integrator. Samples of continental growth curves predict a fast decay in continental crust volume beyond t_{switch} (Sun et al., 2019; Hawkesworth et al., 2020). After switching to the global ocean response spectrum, the torque passes through a major resonance around 3.35 Ga, resulting in a significant and abrupt drop in a_{M} of $6.5R_{\text{E}}$ within 250 Myr. Beyond this age, the evolution again follows the tidal dissipation background spectrum before terminating with the impact.

2.6.3 New target for geological studies

As elucidated thus far, our semi-analytical physical model was fitted only to the most accurate constraints of the Earth-Moon evolution: the present tidal dissipation rate and the age of the Moon. We deliberately avoided fitting our model to any of the available geological data. The unique solution of our combined model is nearly a perfect match to a large set of those geological data (Figure 2.16 and Figs. 2.18 and 2.19). This solution will provide a new target for geological studies, as it clearly validates the cyclostratigraphic approach, which estimates the Earth's precession frequency from stratigraphic sequences (Meyers and Malinverno, 2018; Huang et al., 2020; Sørensen et al., 2020; Lantink et al., 2022) (Table 2.1). In particular, the cyclostratigraphic evaluation of the Earth-Moon distance at 2459 ± 1.3 Ma in the Joffre banded iron formations (BIF, Lantink et al., 2022) is in remarkable agreement with our model, compared to the equivalent estimates deciphering tidal rhythmites in the (~ 2450 Ma) Weeli Wooli BIF in Australia (Walker and Zahnle, 1986; Williams, 2000). Our target curve can probably now be used to elaborate robust procedures for the analysis of these tidal rhythmites that led sometimes

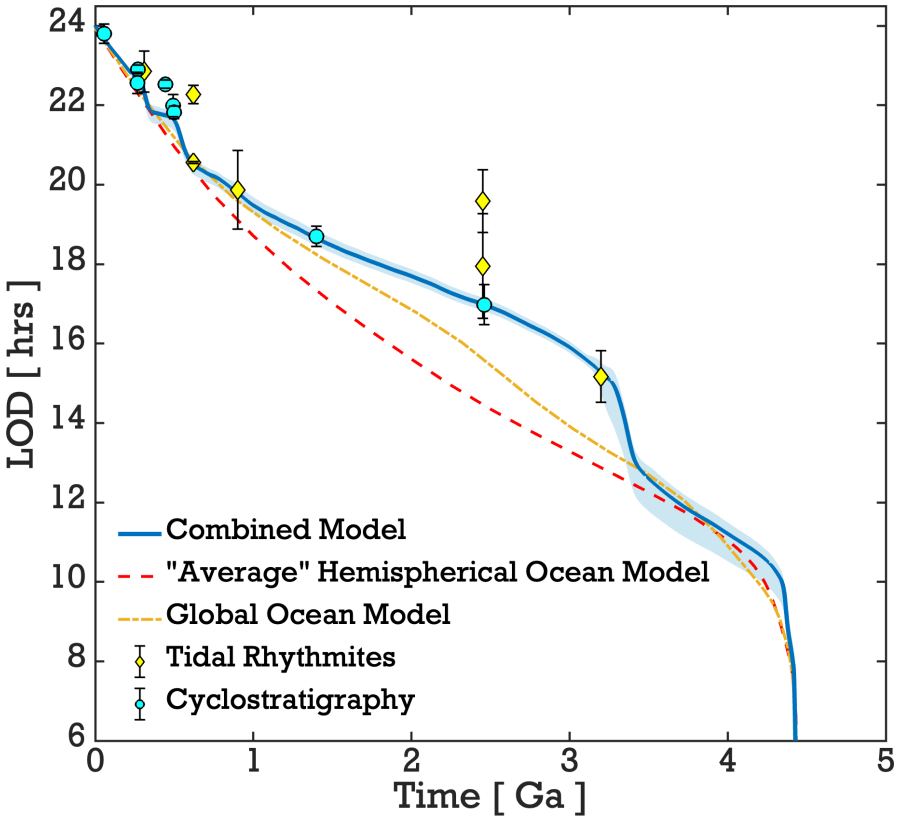

FIGURE 2.18: Evolution of the Earth's length of the day with time. Similar to Figure 2.16, but here for the LOD evolution associated with the three studied oceanic models. Geological data on the LOD are summarized in Tables 2.1 and 2.2. The minimal value reached for the LOD when the integration is terminated at 3 Earth radii is 5.25 hr.

to divergent interpretations (Walker and Zahnle, 1986; Sonett and Chan, 1998; Williams, 2000) (Table 2.2).

We obtained a striking fit with the estimate of a_{M} at 3.2 Ga obtained through the analysis of the Moodies group rhythmites (Eriksson and Simpson, 2000; de Azarevich and Azarevich, 2017), but we do not deny that this agreement could be coincidental and a new analysis of these sections in association with cyclostratigraphic estimates is required. We expect that substantial progress will be made in the near future with the analysis of many cyclostratigraphic records, which could then be used to further constrain our physical model. The sequences that occur during the resonant states (or in their vicinity), corresponding to the steep slopes in Figure 2.16, are of particular interest. This coherence between the geological data and the present scenario for the Earth-Moon evolution will also promote the use of these geological data and, in particular, the cyclostratigraphic geological data as a standard observational window for recovering the past history of the solar system.

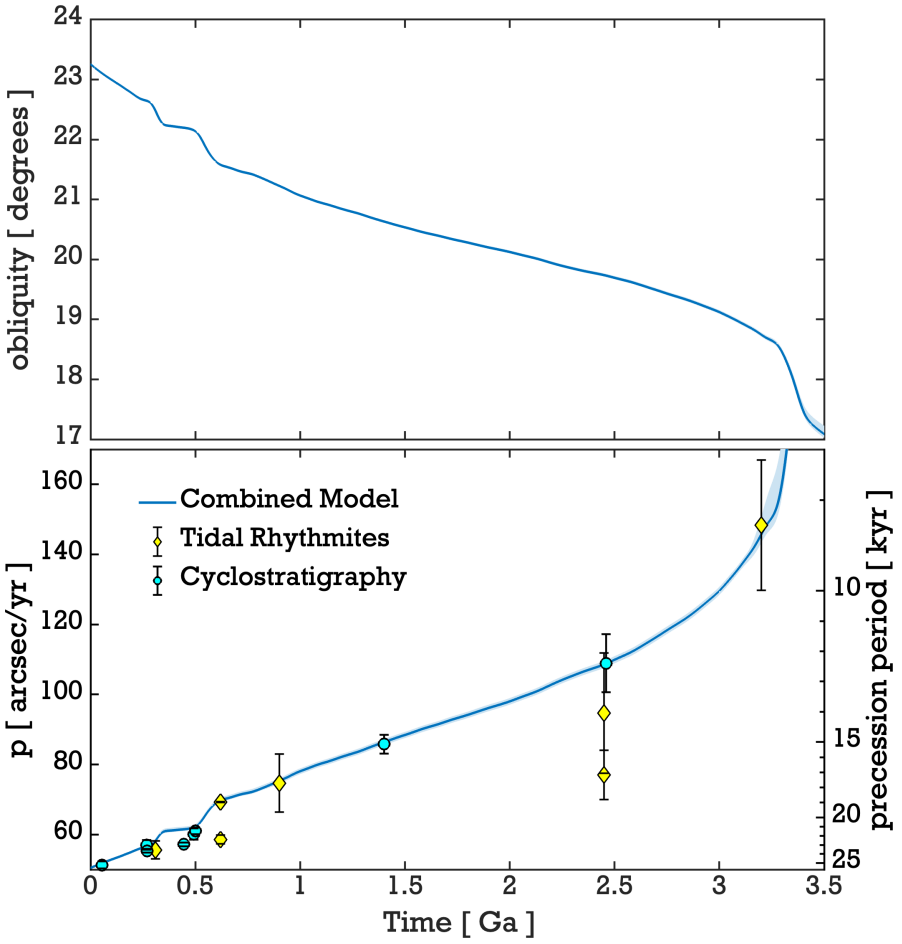

FIGURE 2.19: Evolution of the Earth's obliquity, precession frequency, and precession period with time. The evolution of a_{M} (Figure 2.16) and LOD (Figure 2.18) are used to compute the evolution of obliquity and precession by Eqs. (2.149) and (2.150). The geological data of the precession frequency from tidal rhythmites and cyclostratigraphy are also plotted on top of the curve (Tables 2.1 and 2.2). We note that the precession frequency is the directly measured observable in cyclostratigraphy.

2.7 Summary

In this chapter, we revisited the classic time-scale problem of the lunar origin by taking a different modelling route than what is traditionally considered. Namely, we chose to study the tidal evolution history of the Earth-Moon system by constraining it to its most certain points: the well constrained present and the well constrained genesis epoch. In between, we studied the Earth's tides in the oceans and the mantle to recover a history of dissipation in the Earth-Moon system that allowed us to trace the system's orbital and rotational dynamics.

We followed the semi-analytic tradition of the linear theory of tides in solving the governing system of tidal equations. The tradition was initiated by Laplace, whose

work on the eigen-oscillations of fluids ushered a stream of works that extended from solid, then oceanic, to atmospheric tides. We recovered the behavior of fluid tides in two geometric configurations of the ocean: spherical and hemispherical shells. In both geometries, we adopted a uniform oceanic thickness and a constant Rayleigh drag frequency that parameterizes oceanic dissipation. The two effective parameters were considered as the free parameters of the model with which we fitted the orbital history of the Moon to its formation age and current recession rate. The two geometries required different solutions for the tidal equations, an endeavour that took us on a wild analytical roller-coaster.

The two geometries were adopted to mimic the continental evolution on the Earth's surface. We used the hemispherical geometry to model the present configuration moving backwards, and we further coupled the position of the hemispherical continent with plate tectonic models. Abiding by predictions of continental crust evolution, we switch to the spherical oceanic shell in the earlier eons, allowing for a global Archean ocean.

Though we allowed for the effect of continental drift on tidal dissipation, the predominant regulator of dissipation is the evolving spin rate of the Earth. The latter controls the evolution of the tidal frequency, laying down an erratic spectrum of dissipation. The spectrum involves multiple crossings of resonances associated with frequency overlaps between the eigenmodes of the oceans and the forcing frequency. Modelled histories of the lunar orbit and the Earth's LOD live on this spectrum: smooth variations in the dissipation translate to a smooth evolution of the lunar distance and the LOD; while resonance crossings in the spectrum trigger abrupt (~Myr-timescale) and significant changes.

Having isolated these players, we then coupled our oceanic dynamics solver with our mimetic continental drift tracer, along with an orbital dynamics integrator. We then imposed the aforementioned constraints on this rich dynamical system, and provided a tidal history of the Earth-Moon system that evades the time-scale "conundrum". Though we decided to be completely agnostic of the geological proxies on the Earth-Moon history when building the model, our predicted tidal history was in good agreement with the geological data. It specifically demonstrates the robustness of the cyclostratigraphic machinery in unravelling astronomical quantities from sedimentary sequences, and further suggests interesting intervals for future investigations.

CHAPTER 3

A FIXED PRECAMBRIAN LOD FOR THE EARTH?

3.1 Introduction

Resonances are tempting; or at least we would like to believe that they appeared as such in the previous chapter, as they managed to save us from the time-scale problem. They were also appealing to Kelvin (1882), who invoked a very similar theory of resonances to explain his barometric observations on the relatively large semi-diurnal pressure oscillations, compared to the diurnal component variation. The latter is by far much larger than the former in the harmonic analysis of air temperature variations that cause both these pressure variations (Figure 3.1). These typical oscillations in the atmosphere are majorly produced by either the luni-solar gravitational forcing, or the solar thermal forcing (thus the corresponding gravitational and thermal atmospheric tides). The semi-diurnal variation of barometric pressure is certainly not in response to the gravitational influence of the sun, because if it were the case, then there should be a much larger component associated with the lunar analogue, while in reality there is not. As such, according to Kelvin, it is the thermal influence driving modes of oscillation whereby an overlap between the semi-diurnal term and the corresponding forcing frequency can explain this modal amplification. Investigating the normal modes spectrum of the atmosphere might have been unfeasible at the time of Kelvin, thus onwards started a community debate on the resonance theory, neatly and authoritatively summarized in Chapman and Lindzen (1969), henceforth CL69.

Early tests of Kelvin's theory of the resonance were performed by Rayleigh (1890) and Margules (1892). Rayleigh's results failed Kelvin's hypothesis as he estimated the free period of oscillation for the semi-diurnal and the diurnal components to be 13.7 hrs and 23.8 hrs respectively, thus establishing a stronger overlap in the diurnal type of oscillations. Margules predicted a closer resonance for the semi-diurnal component. However, both attempts were fraught with unrealistic approximations, such as the non-rotation in the case of Rayleigh's work, and the uniformity of the tidal phase with height

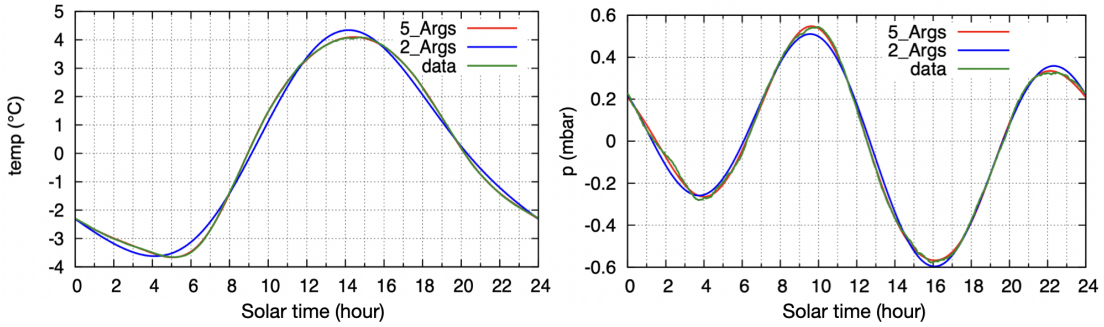

FIGURE 3.1: Daily variations in temperature and pressure recorded over one year and averaged over a day, with the subsolar point anchored to 12 h. The data was recorded every minute over the year 2013 with a Vantage Pro 2 weather station at latitude 48.363° N. The average values of temperature (10.8973° C) and pressure (1015.83 mbar) have been removed keeping only the variations. In both panels, the raw data is plotted in green, while a Fourier decomposition over the solar day is plotted in blue for two harmonics, and in red for five harmonics. Temperature is dominated by the diurnal component, with a maximum value around 14h26mn. The largest harmonics of the pressure variations is the semi-diurnal term, followed by the diurnal term (Auclair-Desrotour et al., 2017a).

in the case of Margules. It took a couple of decades until Lamb (1911) significantly improved Laplace's theory of free oscillations by abstracting from the problem the Earth's rotation and sphericity via his plane-based formalism. Lamb is probably the first to assert that the propagation of long waves in the atmosphere are indeed similar to those of a liquid ocean of depth H if and when the density variations occur isothermally for an atmosphere in adiabatic equilibrium. The latter of course being not realistic, one of Lamb's major contributions to the theory was his discovery of the existence of an infinite series of long waves with different speeds, thus an infinite series of values for the equivalent depth[1] h. This step was necessary to relax the assumptions considered in the case study of Laplace, and it allowed Taylor (1929, 1932) to estimate the period of oscillation of the semi-diurnal component to be greater than 12 hrs, thus establishing serious doubts around the resonance hypothesis.

The revival of the theory was possible by adopting variations on the temperature profile of the atmosphere. Pekeris (1937) applied Taylor's method to determine the atmospheric free oscillations for which the temperature increases upwards in the stratosphere. He showed that, conditionally, the atmosphere can be characterized by two equivalent oceanic depths, one of which gives a period very close to 12 hours and is characterized by surface distribution of quadrupolar nature. The exact estimate of the oscillation period

[1]The original definition of h dates back to Laplace (1798) who, when studying the tidal oscillations of an isothermal atmosphere, showed that they can be inferred from those of a liquid ocean of uniform depth h, hence the nomenclature of h as the tidally equivalent depth of the atmosphere. We provide its mathematical definition in Eq. (3.44).

was subject to the large uncertainty on the upper atmospheric data. The condition referred to was that the atmospheric temperature, after increasing upward above the stratosphere, should reach a maximum and thereafter start decreasing. The same calculation was performed a decade later by Weekes and Wilkes (1947) and Jacchia and Kopal (1952), who had better constraints on the temperature profile with the advent of some of the earliest rockets used for upper atmospheric characterization (Best et al., 1947). Their estimates on the free oscillation period provided a temporary support of the resonance theory. Later, Holmberg (1952) used these estimates to suggest that the torque arising from the resonant thermal response at the present is equal in magnitude and opposite in sign to that generated by terrestrial gravitational tides, thus placing the Earth into a rotational equilibrium with a stabilized spin rate. With the accurate determination of the atmospheric temperature profile that followed, the theory was completely abandoned, along with any possibility of the magnification of the present semi-diurnal tide by a resonance, giving the deathblow to a track of work over 80 years initiated by Kelvin.

Though the resonance theory was proven to be inapplicable to the Earth at the present, could it still be valid in other settings, and its total dismissal too hasty? The semi-diurnal tide, generated via the atmospheric pressure waves, describes the movement of atmospheric mass away from the substellar point. As a result, mass culminates forming bulges on the nightside and the dayside, generating a torque that acts to accelerate the Earth's rotation. As such, the thermally generated torque counteracts the luni-solar gravitational torque associated with solid and oceanic Earth tides. The latter components typically act to drive the closed system of the tidally perturbing-perturbed players towards its equilibrium states of circularity, coplanarity, and synchronous rotation via dissipative mechanisms[2] (e.g., Hut, 1980, 1981). In contrast, the inclusion of the stellar flux as an external source of energy renders the system an open system with radiative energy converted, by the atmosphere, into mechanical deformation and gravitational potential energy in the tidal response. Though the competition between the torques is established on Earth, the thermal torque remains, at least currently, orders of magnitude smaller. However, the afore-summarized long series of studies advanced the theory of thermal tides for it to be applied to Venus (Goldreich and Soter, 1966; Gold and Soter, 1969; Dobrovolskis and Ingersoll, 1980; Ingersoll and Dobrovolskis, 1978; Correia and Laskar, 2001; Correia et al., 2003; Correia and Laskar, 2003b), hot Jupiters (e.g., Arras and Socrates, 2010; Auclair-Desrotour and Leconte, 2018; Gu et al., 2019; Lee, 2020), or near-synchronous and Earth-like rocky exoplanets (Cunha et al., 2015; Leconte et al., 2015; Auclair-Desrotour et al., 2017a, 2019b). Namely, for planetary systems within the

[2]A fourth tidal evolution scenario involves orbital spiralling (see e.g., Hut, 1980).

– misleadingly coined – habitable zone, the gravitational tidal torque diminishes in the regime near synchronization and becomes comparable in magnitude to the thermal tide torque. Consequently, the latter may actually prevent the planet from entering a precisely synchronous state (Laskar and Correia, 2004; Correia and Laskar, 2010; Cunha et al., 2015; Leconte et al., 2015).

Going back home, Zahnle and Walker (1987) – hereafter ZW87 – revived Holmberg's hypothesis of the rotational equilibrium for the Earth by applying the resonant theory of thermal tides to the distant past. Their suggestion relied on two factors needed to close the gap between the thermal and gravitational torques. The first hypothesis is that an atmospheric resonance occurred when the LOD was around 21 hrs, exciting the thermal torque to large values. Secondly, the gravitational tidal torque must have been, on average, much lower in the Precambrian. In the absence of a complete tidal evolution model for the Earth-Moon system at the time, ZW87 relied, for the second factor, on the rotational deceleration estimates of Lambeck (1980), fitted to match the distribution of geological data available then. While most of the datasets used to support this claim are questionable[3] (Section 2.4), we have shown in the previous chapter that this claim still holds, since the larger interval of the Precambrian is associated with what we called a "dormant" torque phase, lacking any significant resonances (Figure 2.17). This rotational stabilization scenario is what we aim to investigate in what follows.

In general, long wavelength ($\lesssim$ few days) free atmospheric oscillations take the form of Rossby waves, while those with shorter periods are associated with gravity waves. The term 'Lamb wave', corresponding to large-scale horizontally propagating acoustic modes (i.e. restored by the fluid compressibility), is usually associated with the latter. Intermediately, the smallest wavelength, large-scale Rossby waves exhibit a common vertical structure with Lamb waves (Deland, 1970). In the isothermal approximation, this vertical structure is associated with a velocity profile of horizontal waves that grows with altitude z as $\exp\{\kappa z/H\}$, where κ is an atmospheric parameter function of the adiabatic exponent Γ_1 (the ratio of heat capacities); namely $\kappa = (\Gamma_1 - 1)/\Gamma_1$, and the pressure height scale H is defined as

$$H(z) = \frac{\mathcal{R}_s T_0(z)}{g}, \tag{3.1}$$

[3]To estimate the Precambrian torque, ZW87 specifically used the tidal rhythmite record preserved in the Weeli-Wolli Banded Iron formation. As we show in Figure 2.12 and Table 2.2, this record is fraught with multiple inferences featuring significantly different values for the LOD, altogether different from the cyclostratigraphic inference from the Joffre member that is estimated to have roughly the same age (Lantink et al., 2022).

where $\mathcal{R}_s = \mathcal{R}_{GP}/\mathcal{M}$ is the specific gas constant, with $\mathcal{R}_{GP}$ and $\mathcal{M}$ being the perfect gas and molar mass constants respectively (Vallis, 2017); T_0 is the equilibrium temperature, and g the gravitational acceleration (we note that the vertical dependence of H propagates only from that of the temperature based on the approximations discussed in Section 3.2.1). This growth profile corresponds to energy decay such that most of the energy of free oscillations is concentrated within a few scale heights from the ground. This is due to the fast decay of density compared to that of the tidal energy as the altitude increases, facilitating the movement of a parcel of smaller density with the same amount of energy, and consequently inducing horizontal oscillations of larger velocities and amplitudes. The increase of oscillation amplitude is substantial (Lindzen and Blake, 1972), which suggests that small scale oscillations near the surface boundary might imply very significant oscillations at ionospheric heights via upwards-propagating gravity waves. Noting that the tidal equivalent depth is approximated as[4]

$$h \simeq \frac{4R_E^2\Omega_E^2}{g\Lambda}, \tag{3.2}$$

where Λ is the eigenvalue of the tidal horizontal wave structure (as defined in Section 2.3.2), R_E is the radius of the Earth, Ω_E is the spin rate of the Earth, and that the equivalent depth of the fundamental symmetric semi-diurnal tidal oscillation is currently estimated as $h_0 = 7.852$ km, the equivalent depth in the past would have been

$$h(t) = h_0 \left(\frac{24}{\mathrm{LOD}(t)}\right)^2. \tag{3.3}$$

Since the Lamb waves at the present have an equivalent depth of $\sim$ 10 km, the atmosphere would evidently resonate with the semi-diurnal thermal tide for LOD= 21.26 hr. Using the model of LOD evolution of Lambeck (1980), ZW87 made this back-of-the-envelope calculation to establish the scenario of the rotational equilibrium for the Earth at 600 Ma. They used an idealized atmospheric model to allow for a significant enhancement in the semi-diurnal thermal torque by amplifying the amplitude of surface pressure oscillations from roughly 1 to $\sim$ 20 mbar.

If the occurrence of the resonance is surmised, the trapping and the consequent rotational stabilization hinges on other factors: the resonance width, where a sufficient timescale over which restoring forces must act, should be granted; atmospheric composition, contributing via the scaling and the efficiency of radiation/absorption; surface temperature, and dissipative mechanisms of radiative transfer. The more recent work

[4]the exact definition given later in Eq. (3.44)

of Bartlett and Stevenson (2016) – hereafter BS16 – followed up on the suggestion of ZW87 and investigated the effect of temperature fluctuations, i.e. thermal noise, on the resonance trapping. They concluded that the rotational stabilization could have lasted 1 billion years, only to be distorted again by a drastic deglaciation event (on the scale the follows a snowball Earth), thus allowing the LOD to increase again from $\sim$ 21 hr to the present value. In Figure 3.2 we plot a summary of the results of their model. Using a simplified tidal model of the lunar gravitational forcing, with a strength weighed by the scaling factor τ_0, BS16 studied the stability of the resonance trapping when combining the thermal torque with the lunar gravitational tidal torque, along with thermal noise. Of interest to us in this Figure is the evident mismatch between the LOD inference from the earliest cyclostratigraphic data points and the various curves of LOD evolution. Specifically, smack within the interval of the trapping lies the data point of Meyers and Malinverno (2018) with an inferred LOD of 18.7 hr, instead of the supposed resonant $\sim$ 21 hr. The incompatibility between these cyclostratigraphic records and the resonance trapping theory leads us to consider one, or more, of the following explanations:

- The resonance-trapping scenario did occur, and the mismatch is due to the wrong cyclostratigraphic LOD inference. We recall here that the directly inferred quantity of the cyclostratigraphic method is the precession frequency of the Earth. Translating the latter to an LOD estimate is often model-dependent, and thus any caveats in the used model would propagate to the LOD estimate [see Section 2.4 for further details].

- The resonance-trapping did occur, but at a different LOD, or at the same LOD at a different time interval. If the cyclostratigraphic estimates are taken at face value, they can be fitted by a tidal evolution history that allows for resonance trapping at a different semi-diurnal tidal frequency. Namely, the used equivalent depth of the atmosphere depends primarily on its tropospheric scale height, which in turn depends on the surface temperature and composition (Eq. 3.1). In the model used by ZW87, an isothermal atmosphere was adopted (in which case the pressure height H is independent of altitude) to make use of the relation $h = \Gamma_1 H$ (see for e.g., Siebert, 1961). The resonant behavior of a realistic atmosphere is most probably different with a more realistic temperature and composition profiles. Such probable variations would translate to variations in the spectral position of the resonance, and thus the LOD at which it occurs.

- The resonance did occur, but was highly unstable for trapping to endure over a geologic time-scale. The stability of the resonance straddles several factors. The

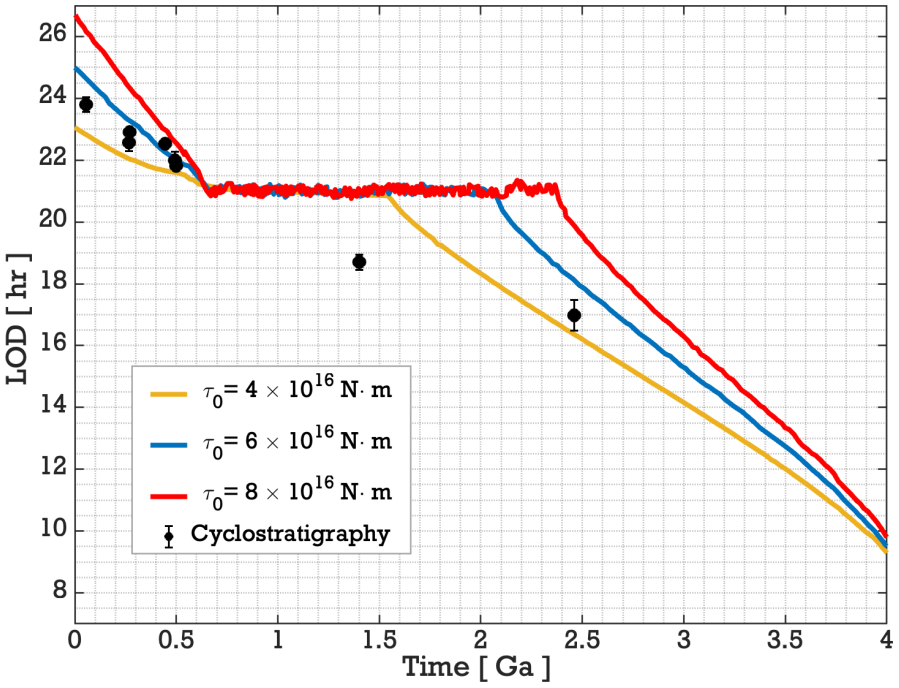

FIGURE 3.2: The evolution of the LOD in the resonance trapping scenario. We regenerate the results of Bartlett and Stevenson (2016), where the authors use a simplified lunar tidal forcing scaled to the present by the coefficient τ_0 [see their Section 4], along with a thermal torque that encounters a resonance when the LOD reached $\sim$ 21 hr. Their integration is performed forward in time; thus when the resonance is encountered, a thermal noise is applied to test for the stability of the trapping. The escape from resonance is guaranteed by an ad-hoc severe temperature drop that the authors assume is associated with snowball Earth scenarios. Plotted against the generated LOD curves is our compiled data set of cyclostratigraphic inferences.

effect of thermal high frequency fluctuations was investigated in BS16, and the resilience of the resonance against them was established. However, this resilience is also dependent on the width of the resonance, which provides a frequency buffer such that thermal-induced variations in the spectrum would not break the resonance. It was assumed in ZW87 that the width of the resonance is independent of the dissipative mechanisms. However, as proven later (e.g., Auclair-Desrotour et al., 2014), and as we shall confirm next, this assumption is invalid.

Another factor that can destabilize the trapping is due to the other player in the torque balance, the oceanic gravitational tide. We argued in the previous chapter for the tidal frequency to be the dominant modulator of the oceanic tidal spectrum. As such, when the Earth enters the resonance trap, the tidal frequency is stabilized, and consequently the oceanic tidal torque. However, continental drift as we also saw in the previous chapter can independently induce spectral shifts, and thus the resonance stability would hinge upon the competition between the thermal

resonance width and the paleogeographic-induced spectral shift. This effect was not explored in earlier studies.

- The resonance never occurred, or did occur but with a pressure anomaly amplitude such that the resulting thermal torque never matched the oceanic gravitational torque. This is the scenario we plan to explore next. It should be noted here that the local tidal spectrum (in the vicinity of the resonance) shown in ZW87 and BS16 is symmetric about the resonant frequency (or equivalently the LOD). In Figure 3.3, left panel, we show the local spectrum obtained for the Lamb resonance by BS16. The panel predicts: *i)* the occurrence of the Lamb resonance during the Precambrian (for LOD $\in [20.5, 21.5]$ hr); *ii)* The possibility of this resonance to amplify the thermal torque to values greater than the oceanic torque; *iii)* The symmetry of the resonance, such that a positive and a negative peak of the torque are present, both acting oppositely to accelerate and decelerate the Earth's rotation, respectively. Namely, the phase of the semi-diurnal tide reverses upon passage through the resonance. Starting with faster and moving to slower rotation before reaching the resonant frequency, the thermal tide acts to decelerate the Earth, complementing the gravitational tide. At the position of the resonance, the pressure maximum is reached, and the phase of the tide then reverses (and consequently the sign of the torque), such that the thermal tide starts accelerating the Earth.

Since the pioneering work of Gold and Soter (1969) on Venus, only a handful of works studied the frequency spectrum of the thermal torque for rocky planets. Progress has been achieved through analytical models well founded in the classical theory of tides (Ingersoll and Dobrovolskis, 1978; Dobrovolskis and Ingersoll, 1980; Auclair-Desrotour et al., 2017a,b), parameterized models that captured essential spectral features (e.g., Correia and Laskar, 2001, 2003a), and fully numerical approaches that made use of the advancing sophistication of general circulation models (GCM; e.g., Leconte et al., 2015; Auclair-Desrotour et al., 2019b). The latter two works are, to our knowledge, the only attempts on establishing the tidal torque numerically. Interested in the response of habitable-zone planets, Leconte et al. (2015) focused on the low frequency spectrum. Auclair-Desrotour et al. (2019b) – henceforth ALM19 – characterized the dependence of the tidal torque interpolating between the low and high frequency regimes. ALM19's study is thus the first, and perhaps the only study that numerically computed the tidal response and torque at the Lamb resonance. Of interest to us is a perplexing feature that ALM19 established (Figure 3.3 right panel): the torque at the Lamb resonance featured

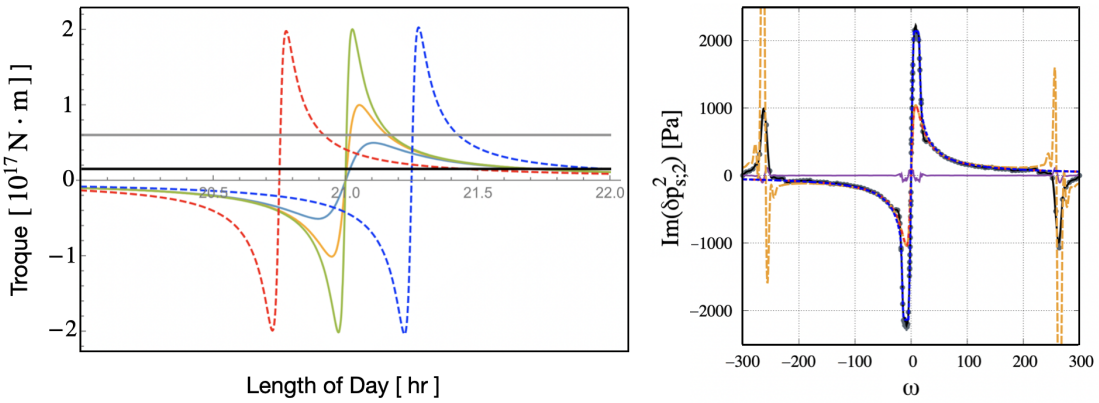

FIGURE 3.3: The spectrum of the thermal tidal response. *Left:* The spectrum of the tidal torque is plotted as a function of the length of day on Earth, as computed by the model of BS16 (panel adapted from their Figure 1). The panel is zoomed over the part of the spectrum where the Lamb resonance occurs. Solid curves correspond to different prescribed damping factors of the atmospheric tide. Dashed curves differ by the prescribed atmospheric temperature. The black horizontal line marks the assumed value of the Precambrian oceanic tidal torque, while the gray horizontal line marks the present value, both multiplied by −1. The panel shows the occurrence of the Lamb resonance in the Precambrian with a symmetric positive and negative peaks for the torque. *Right:* The spectrum of the pressure anomaly, which is directly proportional to the tidal torque (via Eq. 3.55) is plotted as a function of the normalized tidal frequency ω (panel adapted from Figure 3 of ALM19). In contrast with the left panel, the full spectrum is plotted here, with the Lamb resonance occurring in the high frequency regime for $\omega = 260..$ The spectrum in blue interpolates the data points in black, which were retrieved via GCM simulations for a dry Venus-sized planet with a surface of bare rocks, and a 10 bar atmosphere. The GCM-spectrum shows that the resonance is asymmetric, with a single negative peak that acts to complement the oceanic tidal torque. In contrast, the spectrum in yellow, obtained from an analytical model assuming an isothermal atmosphere, shows the existence of the two peaks.

a single peak, specifically the peak that acts in the same direction of gravitational tides; i.e. the peak required for the rotational stabilization was gone with the wind!

With view to greater physical realism, we intend to analytically establish the frequency spectrum of the thermal tidal torque, from first principles, to specifically characterize the Lamb resonance, bearing in mind that the models used in ZW87 and BS16 were idealized. The specific goal is to unravel the cause of the resonance asymmetry observed in ALM19, and to provide a new physical model for the thermal tidal torque that better matches the GCM-computed response. We next start where we should, with the primitive equations of atmospheric waves.

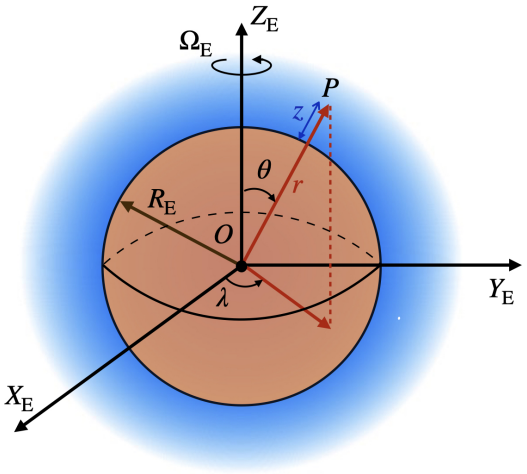

FIGURE 3.4: Reference frame of atmospheric dynamics. Spherical coordinate system co-rotating with the Earth.

3.2 Atmospheric dynamics

3.2.1 Minimal model and essential structure

For the atmosphere enveloping the Earth (Figure 3.4), and similar to the set-up in Auclair-Desrotour et al. (2017a), we define the reference frame $\mathcal{R}_E$ co-rotating with the Earth, i.e. $\mathcal{R}_E : \{O, \boldsymbol{X}_E, \boldsymbol{Y}_E, \boldsymbol{Z}_E\}$, with O at the Earth's center, $\boldsymbol{X}_E$ and $\boldsymbol{Y}_E$ in the equatorial plane and $\boldsymbol{Z}_E = \boldsymbol{\Omega}_E/|\Omega_E|$. In this frame, the position of an atmospheric parcel P is defined by the position vector $\boldsymbol{r}$ in the spherical coordinates (r, θ, λ), where $r = |OP|$ designates the radial distance, θ the co-latitude, and λ the longitude. The position of the same parcel in the atmospheric shell is defined by the altitude z, where $r = R_E + z$.

The atmosphere is characterized by the scalar fields of pressure p, temperature T, density ρ, and the vectorial velocity field $\boldsymbol{\mathcal{V}}$. Each of these variables varies with time and space, and can be decomposed into two terms: an equilibrium state field, for which we used the subscript 0; and a perturbation term, for which we add the prefix δ (except for the velocity, for which the perturbation is simply denoted by $\boldsymbol{V}$. We thus have:

$$p = p_0 + \delta p \qquad T = T_0 + \delta T \qquad \rho = \rho_0 + \delta\rho \qquad \boldsymbol{\mathcal{V}} = \boldsymbol{V}_0 + \boldsymbol{V}. \tag{3.4}$$

In order to simplify the analytical treatment of tidal dynamics of the atmosphere, we make the following assumptions to define the hitherto arbitrary atmospheric structure. Namely (CL69):

(i) The background equilibrium fields are uniform in time. This assumption relies on the hierarchy of variation timescales between the relatively short period perturbative tidal dynamics and the long period adjustment of equilibrium fields. That said, this approximation is valid as long as we do not get very close to synchronization.

(ii) Only lowest order perturbations are considered. The atmospheric response to tidal forcing is considered relatively small and is linearized near equilibrium. We recall here Figure 3.1 where the amplitude of the pressure oscillations at latitude 48° N peaks at ~ 0.5 mbar, thus corresponding to 0.05% (it would be ~ 1 mbar at the equator, thus 0.1%). Nonlinear effects are consequently ignored, including those corresponding to the interactions between tidal waves. Thus we have:

$$|\delta p(\boldsymbol{r},t)| \ll p_0(\boldsymbol{r}), \quad |\delta\rho(\boldsymbol{r},t)| \ll \rho_0(\boldsymbol{r}), \quad |\delta T(\boldsymbol{r},t)| \ll T_0(\boldsymbol{r}). \tag{3.5}$$

(iii) No differential rotation between the atmosphere and the solid counterpart. With this imposed solid rotation, we set $\boldsymbol{V}_0 = 0$.

(iv) Hydrostatic equilibrium is assumed. The background fields are adjusted by gravity such that the weight of the air column balances ground pressure. Namely:

$$\frac{dp_0}{dz} = -g\rho_0. \tag{3.6}$$

Using the ideal gas law, $p_0 = \mathcal{R}_s\rho_0 T_0$, (3.6) is re-written as

$$\frac{d\ln p_0}{dz} = -\frac{g}{\mathcal{R}_s T_0}, \tag{3.7}$$

which allows us to identify the definition of the pressure height scale in Eq. (3.1). It is noteworthy that the ideal gas approximation is valid for the Earth up to an atmospheric altitude of 95 km, where the molecular weight starts varying (US standard atmosphere; NOAA, 1976). The hydrostatic approximation implicitly dictates neglecting the variation rates of vertical flows and the vertical component of Coriolis acceleration. It is thus closely related to the thin-layer approximation which we adopt for our model described in Section 3.2.2.

(v) Spherical symmetry is imposed (the Earth's ellipticity is ignored). As such, only radial atmospheric variations are considered as we ignore temperature and gravity gradients between the poles and the equator. Further more, the atmosphere is regarded as a thin fluid shell ($H_{\text{atm}} \sim 100$ km), radial variations in gravity can be ignored. One can justify the latter by computing the difference in g between the

ground and the upper atmospheric limit. Defining the gravitational acceleration as $\boldsymbol{g} = -g(r)\hat{r}$, where $g(r) = GM_{\mathrm{E}}/r^2$, the relative difference in g is:

$$\frac{\Delta g}{g} \approx \frac{2H_{\mathrm{atm}}}{R_{\mathrm{E}}}, \tag{3.8}$$

which is on the order of 3‰.

(vi) Weather fluctuations are ignored. There is a separation of time scales and length scales, which prevents the meteorological patterns and the tidal patterns from overlapping and interacting. Furthermore, compared to the background profiles, the mean flow, and tidal oscillations, meteorological fluctuations correspond to chaotic variations that average to zero on the considered timescales (Figure 3.1; see also North et al., 2014).

(vii) Surface topography is ignored such that the effects of mountains and the land-sea distribution are not taken into account. These effects, however, are expected to influence the atmospheric tidal response of the planet, with earlier suggestions on affecting tidal amplitudes and phases for the Earth (Zharov and Gambis, 1996) and Mars (Guzewich et al., 2016).

With these approximations, we introduce the reduced altitude x defined as:

$$x = \int_0^z \frac{dz}{H(z)}, \tag{3.9}$$

and we can thus define the background distributions of pressure, density, and temperature as:

$$p_0(x) = p_0(0)e^{-x}, \quad \rho_0(x) = \frac{p_0}{gH}, \quad T_0(x) = \frac{gH}{\mathcal{R}_{\mathrm{s}}}. \tag{3.10}$$

3.2.1.1 The buoyancy frequency

Essential to our atmospheric structure definition and central in the analytical model we develop next is the buoyancy frequency, N, a measure of the strength of vertical density stratification (chapter 2.9 of Vallis, 2017). Also known as the Brunt–Väisälä frequency, N is used as an indicator of the local gravitational stability of a fluid, with a vertical density gradient, with respect to convection.

A fluid can be labelled as stably stratified if a parcel tends to return to its original position after being displaced under the action of the Archimedean force. In contrast, the fluid is

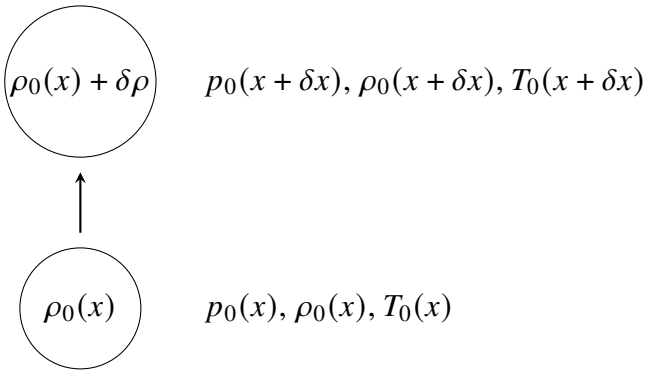

FIGURE 3.5: Vertical displacement of a parcel in a stratified atmosphere.

unstably stratified if the fluid parcel tends to diverge away from its original position upon displacement, and neutrally stratified if it tends to settle where it is. To quantify this description, we consider the background density profile $\rho_0(x)$ discussed above. A parcel moves upward in the atmosphere from x to $x + \delta x$ as described in Figure 3.5. Initially, the parcel has the same density $\rho_0(x)$ as the surrounding. Its vertical displacement in the atmosphere incurs a density change of $\delta\rho$. The parcel of volume V_p will therefore feel the buoyancy force

$$\delta F = -\big[\rho_0(x) + \delta\rho - \rho(x + \delta x)\big]V_\mathrm{p} g\,. \tag{3.11}$$

The parcel will move back towards its initial position if it is heavier than the surrounding fluid ($\delta F < 0$); thus the stability condition can be expressed as

$$\rho_0(x) + \delta\rho > \rho_0(x + \delta x), \tag{3.12}$$

which upon Taylor expansion gives

$$\rho_0(x) + \delta\rho > \rho_0(x) + \frac{d\rho_0}{dx}\delta x + \cdots\,. \tag{3.13}$$

In the case of infinitesimal parcel displacements ($\delta x \to 0$), this condition becomes:

$$-\frac{d\rho_0}{dx} + \frac{\delta\rho}{\delta x} > 0. \tag{3.14}$$

The first density gradient in this condition simply corresponds to the rate at which the static density varies with height. The second term denotes the rate at which the parcel's own density changes during its vertical displacement. It is thus the difference between the two density gradients that determines the stability of the stratification.

The vertical motion of the parcel satisfies the equation

$$\rho_0(x) V_\mathrm{p}\, \delta\ddot{z} = \delta F \tag{3.15}$$

with $\delta z = H\delta x$. Subsituting the buoyancy force δF by its expression (3.11) expanded at first order in δx, we recover the equation of an harmonic oscillator

$$\delta\ddot{x} + N^2 \delta x = 0\,, \tag{3.16}$$

where N is the buoyancy frequency defined as

$$N^2 = -\frac{g}{\rho_0 H}\left(\frac{d\rho_0}{dx} - \frac{\delta\rho}{\delta x}\right). \tag{3.17}$$

In terms of this frequency, the stability condition (3.14) reduces to: local stability if $N^2 > 0$, local instability if $N^2 < 0$, and neutral stratification when $N^2 = 0$. To simplify this expression of the buoyancy frequency, we recall that variations of pressure in a gas are balanced much quicker than those of temperature. Therefore, we can consider the transformation of the gas inside the parcel to be adiabatic with a pressure always at equilibrium with the atmosphere, i.e., $p_0(x) + \delta p = p_0(x + \delta x)$. According to the Laplace law, the transformation is thus subject to

$$p_0(x + \delta x)\,[\rho_0(x) + \delta\rho]^{-\Gamma_1} = p_0(x)\rho_0(x)^{-\Gamma_1}. \tag{3.18}$$

Expanding to first order in δx and $\delta\rho$, we get

$$\frac{\delta\rho}{\delta x} = \frac{1}{\Gamma_1}\frac{\rho_0}{p_0}\frac{dp_0}{dx}\,. \tag{3.19}$$

From this result, the buoyancy frequency of Eq. (3.17) can be expressed in terms of the density gradient and the pressure gradient. To highlight the role of the temperature gradient, we substitute the density gradient using the ideal gas law

$$\frac{d\ln\rho_0}{dx} = \frac{d\ln p_0}{dx} - \frac{d\ln T_0}{dx}\,, \tag{3.20}$$

then the buoyancy frequency reads

$$N^2 = \frac{g}{H}\left(\frac{d\ln T_0}{dx} - \kappa\frac{d\ln p_0}{dx}\right). \tag{3.21}$$

As such, if the atmosphere were to be isothermal i.e., $T_0(x) = T_0(0)$, then the buoyancy

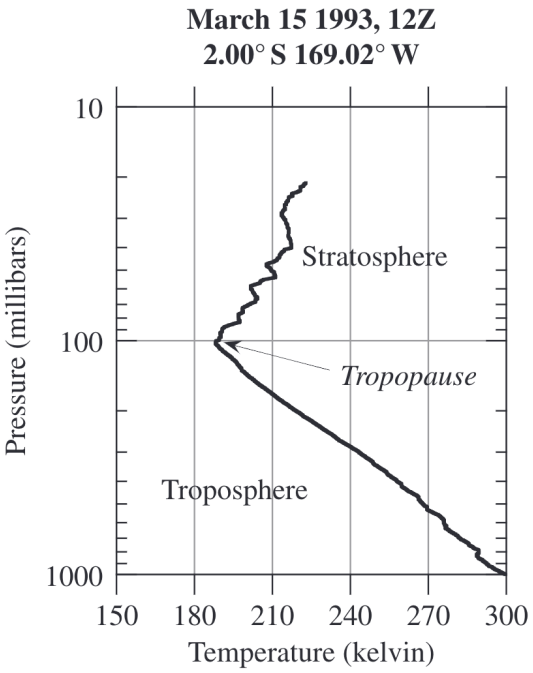

FIGURE 3.6: Temperature profile measured in the tropical Pacific. The measurements were obtained from a radiosonde ("weather balloon") launched on March 15, 1993. Figure adapted from Pierrehumbert (2010).

frequency reduces to $N = \sqrt{\kappa g/H}$, recalling that $p_0(x) = p_0(0)e^{-x}$ gives to $d \ln p_0/dx = -1$. It should be also stressed that the most appropriate thermodynamical quantity to express the buoyancy frequency is not the temperature T_0 but the potential temperature Θ_0 defined as the asymptotic temperature that a parcel would attain if it were adiabatically brought to a reference pressure p_{ref}, namely (Vallis, 2017, Section 1.7.1),

$$\Theta_0 = T_0 \left(\frac{p_{\text{ref}}}{p_0} \right)^{\kappa} . \tag{3.22}$$

Indeed, in terms of this potential temperature, the buoyancy frequency is simply expressed as (Vallis, 2017, Eq. 2.244[5])

$$N^2 = \frac{g}{H} \frac{d \ln \Theta_0}{dx} \tag{3.23}$$

and therefore, the stability is controlled by the slope of Θ_0. In what follows, we focus on the neutrally stratified scenario where $\Theta_0(x)$ is uniform and $N^2 = 0$, and we adopt it for our tidal model developed next. The neutral stratification case is a limiting case, the other limiting case being the stably isothermal case. With the massive troposphere

[5]We note that we use the reduced altitude in our Eq. (3.23), compared to the equation in Vallis where the geometric altitude is used.

controlling the tidal response of the Earth, we adopt the neutral stratification limiting case because it is closer to the actual structure of the Earth's troposphere than the isothermal approximation. In Figure 3.6 we show the vertical profile of temperature obtained via weather balloon measurements (Pierrehumbert, 2010). The profile clearly depicts the negative temperature gradient of the troposphere, which is evidently closer to an idealised adiabatic profile than to an idealised isothermal profile. In fact, it is the heating of the troposphere by the surface which generates convective motions and efficient turbulent mixing, thus enhancing energy transfer and driving the layer towards an adiabatic temperature profile. Furthermore, the temperature profile being adiabatic would prohibit the propagation of gravity waves, i.e. waves restored by the Archimedean force, which compose the baroclinic component of the atmospheric tidal response. This leaves the atmosphere with barotropic tidal flows, which is consistent with the tidal dynamics generated under the shallow water approximation.

Closing this interlude, we provide an essential condition on the scale height H that will be deemed useful in our model. We evoke the hydrostatic equilibrium condition on Eq. (3.17) to re-write the Brunt–Väisälä frequency as

$$N^2 = \frac{g}{H}\left(\kappa + \frac{1}{H}\frac{dH}{dx}\right). \tag{3.24}$$

With the adopted neutral stratification scenario, $N^2 = 0$, Eq. (3.24) implies that

$$\frac{d\ln H}{dx} = -\kappa. \tag{3.25}$$

3.2.2 Tidal waves and the primitive equations

Now we are fully geared to explore the governing system of dynamical equations. In the co-rotating reference frame $\mathcal{R}_\mathrm{E}$ described earlier, the atmosphere is subject to the total gravitational potential[6] $\mathcal{U} = U_\mathrm{g} + U_\mathrm{T} + U$, where U_g is the equilibrium self-gravitational potential of the Earth ($\boldsymbol{\nabla} U_\mathrm{g} = -\boldsymbol{g}$), U_T is the gravitational tidal potential, and U is the tidal response potential, arising from the mass redistribution. With these potentials, the motion of a fluid parcel is described by the horizontal momentum equation for a

[6]We note that the notations and conventions used to describe the potentials in this chapter are not identical to those in the previous one.

compressible gas (e.g., Vallis, 2017):

$$\partial_t \boldsymbol{\mathcal{V}} + \boldsymbol{\mathcal{V}} \cdot \boldsymbol{\nabla}\boldsymbol{\mathcal{V}} + 2\boldsymbol{\Omega} \times \boldsymbol{\mathcal{V}} = -\frac{1}{\rho}\boldsymbol{\nabla} p - \boldsymbol{\nabla}\mathcal{U}, \tag{3.26}$$

where the effect of centrifugal acceleration, $\boldsymbol{\Omega}\times(\boldsymbol{\Omega}\times\boldsymbol{r})$, along with dissipative processes such as molecular and turbulent viscosity and ion drag are ignored. The momentum equation is accompanied by the continuity equation of mass conservation:

$$\partial_t \rho + \boldsymbol{\nabla} \cdot (\rho \boldsymbol{\mathcal{V}}) = 0. \tag{3.27}$$

Poisson's equation defines the relation between the gravitational potential and the redistribution of mass:

$$\boldsymbol{\nabla}^2 \mathcal{U} = 4\pi G \rho. \tag{3.28}$$

As the atmosphere is thermally forced by the sun, we decompose the absorbed thermal power per unit mass $\mathcal{J}$ into the sum of the average power absorbed, J_0 that defines thermal equilibrium, and the thermal tide component J, i.e., $\mathcal{J} = J_0 + J$. Heat transport follows (CL69):

$$\frac{C_\mathrm{p}}{\Gamma_1}(\partial_t T + \boldsymbol{\mathcal{V}} \cdot \boldsymbol{\nabla} T) = \frac{gH}{\rho}(\partial_t \rho + \boldsymbol{\mathcal{V}} \cdot \boldsymbol{\nabla}\rho) + \mathcal{J}. \tag{3.29}$$

In this equation, we used the specific heat capacity C_p defined as $C_\mathrm{p} = \mathcal{R}_\mathrm{s}/\kappa$. As we mentioned earlier, hydrostatic equilibrium is assumed, and tidal fields are considered as relatively small perturbations. We thus linearize the governing equations keeping only first order terms; we further ignore fluctuations in the self-gravity field of the Earth induced by the tidal density variations (which correspond to the Cowling approximation we adopted for the oceanic tidal dynamics in Section 2.3.2.1). Under these assumptions, Eq. (3.26) is re-written as:

$$\partial_t \boldsymbol{V} + 2\boldsymbol{\Omega} \times \boldsymbol{V} = -\frac{1}{\rho_0}\boldsymbol{\nabla}\delta p - \frac{g}{\rho_0}\delta\rho\hat{\boldsymbol{r}} = -\boldsymbol{\nabla} U_\mathrm{T}. \tag{3.30}$$

Projecting this equation onto the basis vectors, we obtain the system provided in CL69:

$$\partial_t V_\theta - 2\Omega V_\lambda \cos\theta = -\frac{1}{R_\mathrm{E}}\partial_\theta\left(\frac{\delta p}{\rho_0} + U_\mathrm{T}\right), \tag{3.31}$$

$$\partial_t V_\lambda + 2\Omega V_\theta \cos\theta + 2\Omega V_r \sin\theta = -\frac{1}{R_\mathrm{E}\sin\theta}\partial_\lambda\left(\frac{\delta p}{\rho_0} + U_\mathrm{T}\right), \tag{3.32}$$

$$\partial_t V_r - 2\Omega V_\lambda \sin\theta = -\frac{1}{H\rho_0}\partial_x \delta p - g\frac{\delta\rho}{\rho_0} - \frac{1}{H}\partial_x U_\mathrm{T}. \tag{3.33}$$

The parcel's displacement in one direction is dependent on the characteristic length scale of the atmosphere in that direction. As such, with the adopted *thin-shell approximation* (CL69), the vertical acceleration V_r is neglected in the momentum constituent equations. Furthermore, we adopt the *traditional approximation* (e.g., Unno et al., 1989; Mathis et al., 2008), thus ignoring the Coriolis coupling terms between the equations. Furthermore, for the vertical momentum equation, this amounts to assuming the hydrostatic approximation for the tidal perturbation in addition to the background profiles[7]. This approximation is justified as long as the buoyancy term given by $-g\delta\rho/\rho_0$ is strong compared to the Coriolis term in the vertical direction; and as long as the tidal velocity is essentially horizontal. For further details on the reasoning and the validity behind these approximations, the reader is referred to CL69, Unno et al. (1989), Mathis and Le Poncin-Lafitte (2009), Tort and Dubos (2014), Prat et al. (2016), and Auclair-Desrotour (2016).

We continue our system's linearization to obtain for the mass conservation,

$$\partial_t \delta p + \frac{1}{H}\partial_x \left(\rho_0 V_r\right) = -\frac{\rho_0}{R_\mathrm{E}\sin\theta}\left[\partial_\theta\left(\sin\theta V_\theta\right) + \partial_\lambda V_\lambda\right], \tag{3.34}$$

and for the heat transport equation,

$$\frac{C_\mathrm{p}}{\Gamma_1}\left(\partial_t \delta T + \frac{1}{H}\frac{dT_0}{dx}V_r\right) = \frac{gH}{\rho}\left(\partial_t \delta\rho + \frac{1}{H}\frac{d\rho_0}{dx}V_r\right) + J. \tag{3.35}$$

Along with the aforementioned approximations, we further ignore the gravitational tide as its effect is negligible compared to the thermal counterpart. In sum, the perturbed and linearized system of momentum and mass conservation, and heat transfer governing

[7]We note that the hydrostatic approximation is implicitly applied to both components, the tidal perturbation and the background profile, in GCMs solving the hydrostatic primitive equations (e.g., LMD GCM, Hourdin et al., 2006).

the dynamics of tidal waves under the ideal gas law reads:

$$\partial_t V_\theta - 2\Omega V_\lambda \cos\theta = -\frac{1}{R_\mathrm{E}}\partial_\theta \frac{\delta p}{\rho_0}\,, \tag{3.36}$$

$$\partial_t V_\lambda + 2\Omega V_\theta \cos\theta = -\frac{1}{R_\mathrm{E}\sin\theta}\partial_\lambda \frac{\delta p}{\rho_0}\,, \tag{3.37}$$

$$0 = -\frac{1}{H\rho_0}\partial_x \delta p - g\frac{\delta\rho}{\rho_0}\,, \tag{3.38}$$

$$\partial_\mathrm{t}\delta p + \frac{1}{H}\partial_x\left(\rho_0 V_r\right) = -\frac{\rho_0}{R_\mathrm{E}\sin\theta}\left[\partial_\theta\left(\sin\theta V_\theta\right) + \partial_\lambda V_\lambda\right]\,, \tag{3.39}$$

$$\frac{C_\mathrm{p}}{\Gamma_1}\left(\partial_\mathrm{t}\delta T + \frac{1}{H}\frac{dT_0}{dx}V_r\right) = \frac{gH}{\rho_0}\left(\partial_\mathrm{t}\delta\rho + \frac{1}{H}\frac{d\rho_0}{dx}V_r\right) + J\,, \tag{3.40}$$

$$\frac{\delta p}{p_0} = \frac{\delta T}{T_0} + \frac{\delta\rho}{\rho_0}. \tag{3.41}$$

The analytical treatment of this system is classical in the literature, and best depicted in CL69. It follows that the variation of the Lagrangian pressure G is adopted as a convenient quantity in tidal theory. It is defined as:

$$G = -\frac{1}{\Gamma_1 p_0}\left(\partial_t \delta p + \frac{1}{H}\frac{dp_0}{dx}V_r\right). \tag{3.42}$$

Next, the tidal response, assumed to be linear to thermal forcing, is Fourier-decomposed in time and longitude using the tidal frequency σ and the longitudinal order m. Thus all the physically varying quantities take the form:

$$f = \sum_{\sigma,m} f^{\sigma,m}(x,\theta)e^{i(\sigma t + m\lambda)}. \tag{3.43}$$

We refer the reader to CL69 for the full and classic procedure that follows; a procedure that leads to the decomposition of the response into a horizontal component described by the Laplace tidal equation (see Section 2.3.2), where the Hough functions $\{\Theta_n(\theta)\}$ serve as eigenfunctions[8], and a vertical component characterized by the vertical structure equation. The two equations are coupled by the eigenvalues $\{\Lambda_n\}$ defined in Section 2.3.2, where for each mode of index n an equivalent depth h_n is defined as

$$h_n = \frac{R_\mathrm{E}\sigma^2}{g\Lambda_n}. \tag{3.44}$$

[8]We note that unlike the case of the global ocean model, the Hough functions and their associated eigenvalues are in this case real.

As such, the coefficients of the Fourier expansion in of each variable in Eq. (3.43) are expanded in terms of the Hough eigenfunctions whereby

$$f^{\sigma,m} = \sum_{n\in\mathbb{Z}} f_n^{\sigma,m}(x)\,\Theta_n^{\sigma,m}(\theta). \tag{3.45}$$

Essential to the tidal model we develop next is the vertical structure equation, which is obtained by straightforward manipulations of Eqs. (3.38) and (3.39). It reads as:

$$H\partial_{zz}G^{\sigma,m} + \left(\frac{dH}{dz} - 1\right)\partial_z G^{\sigma,m} = \frac{g}{R_{\rm E}^2\sigma^2}\mathcal{L}^{\sigma,m}\left[\left(\frac{dH}{dz} + \kappa\right)G^{\sigma,m} - \frac{\kappa J^{\sigma,m}}{\Gamma_1 g H}\right], \tag{3.46}$$

where the horizontal operator $\mathcal{L}^{\sigma,m}$ is the same operator[9] defined in Eq. (2.118). The vertical structure equation is an in-homogeneous equation which, given two boundary conditions at the ground and the uppermost layer, has a unique solution for the vertical structure for each Hough mode. We follow the common practice of reducing it to a canonical form by a change of variables defined as:

$$y_n(x) = G_n(x)e^{-x/2}. \tag{3.47}$$

Thus the vertical structure equation becomes:

$$\frac{d^2y_n}{dx^2} + \hat{k}_{x;n}^2(x)y_n = \frac{\kappa J_n}{\Gamma_1 g h_n}e^{-x/2} \tag{3.48}$$

where the dimensionless vertical wavenumber $\hat{k}_{x;n}$ is defined by

$$\hat{k}_{x;n}^2 = \frac{1}{4}\left[\frac{4}{h_n}\left(\kappa H + \frac{dH}{dx}\right) - 1\right]. \tag{3.49}$$

The vertical structure equation thus reduces to an equation describing a forced harmonic oscillator with a wavenumber that determines the nature of tidal waves. We will come back to the wavenumber characterization later when we extend the theory to build our mode.

For now, we close this section by moving to the solution of the perturbed quantities, which are easily obtained, for each Hough and Fourier mode, from the system of equations (3.36-3.41), after solving the vertical structure equation for $y(x)$. We hereafter drop the subscripts and superscripts identifying the modes. Of particular interest is the delayed mass redistribution resulting from the thermal forcing and generating the tidal

[9] in the case where $\sigma_{\rm R} = 0$.

torque. With the hydrostatic balance imposed, i.e. with the pressure and gravitational forces exactly compensating each other, and assuming that the Earth is rigid enough to support atmospheric variations without noticeable distortions, it follows that the mass distribution is directly proportional to the surface pressure variation, which we denote by $\delta p_{\rm s}$. The latter can be retrieved from the solution of the pressure perturbation[10]:

$$\delta p(x) = \frac{p_0(0)}{H}\left[\frac{\Gamma_1 h}{i\sigma}e^{-x/2}\left(\frac{dy(x)}{dx} - \frac{1}{2}y(x)\right)\right]. \tag{3.50}$$

The velocity field components on the other end read as:

$$V_r = \Gamma_1 h e^{x/2}\left[\frac{dy}{dx} + \left(\frac{H}{h} - \frac{1}{2}\right)y\right], \tag{3.51}$$

$$V_\theta = \frac{\Gamma_1 h p_0(0)}{R_{\rm E} H\sigma^2}e^{-x/2}\left(\frac{dy}{dx} - \frac{1}{2}y\right), \tag{3.52}$$

$$V_\lambda = i\frac{\Gamma_1 h p_0(0)}{R_{\rm E} H\sigma^2}e^{-x/2}\left(\frac{dy}{dx} - \frac{1}{2}y\right). \tag{3.53}$$

The generated tidal torque $\mathcal{T}$ about the Earth's spin axis is obtained by integrating the gravitational force exerted by the tidal bulge over the spherical domain $\mathcal{S}$. Hence for the thin atmospheric shell under study it is expressed as (e.g., Zahn, 1966; Auclair-Desrotour et al., 2019b):

$$\mathcal{T} = \frac{R_{\rm E}^2}{g}\int_{\mathcal{S}} \partial_\lambda U_{\rm T}\delta p_{\rm s} d\Omega, \tag{3.54}$$

where $d\Omega$ is the solid angle. Expanding both the pressure anomaly and the tidal pontential and picking up the semi-diurnal component ($l = m = 2$), we end up with the familiar expression of the quadrupolar torque in the thin layer approximation (e.g., Leconte et al., 2015; Auclair-Desrotour et al., 2019b):

$$\mathcal{T} = \sqrt{\frac{24\pi}{5}}\frac{M_\odot}{M_{\rm E}}\frac{R_{\rm E}^6}{a^3}\,{\rm Im}\{\delta p_{\rm s}\}, \tag{3.55}$$

where $M_\odot$ is the solar mass. Having dropped the modal and harmonic indices, we emphasize here that $\delta p_{\rm s}$ is the frequency-dependent semi-diurnal component of the surface pressure anomaly. Eq. (3.55) shows that the magnitude of the torque is fully determined by the magnitude of the complex quantity $\delta p_{\rm s}$, in analogy to the oceanic tides where we characterized the torque by the imaginary part of the Love number (see for

[10] For the solutions of the perturbed quantities, we adopt the exact equations laid down in Chapman and Lindzen (1969), which were developed in the adiabatic case. With our inclusion of radiative cooling, the solutions in the diabatic case are expected to be dependent on the frequency σ_0, as established in Auclair-Desrotour and Leconte (2018). We proceed as such cautiously, leaving the self-consistent treatment to the following stage of the work.

example Section 2.3.2). Furthermore, the action of the torque is fully dependent on the sign of the imaginary part of the pressure anomaly. Namely, when sign $(\mathrm{Im}\{\delta p_s\}) < 0$, the thermal torque is pushing the Earth in the direction of spin-orbit synchronization by depleting its rotational angular momentum budget, i.e., the thermal torque complements the oceanic tidal torque. In contrast, when sign $(\mathrm{Im}\{\delta p_s\}) > 0$, the thermal torque pushes the Earth away from synchronization by accelerating its spin rate, thus opposing the effect of solid-oceanic tides. Recalling the rotational stabilization scenario, we thus require a positive, and certainly large, surface pressure anomaly.

3.3 Thermal tide of a neutrally stratified atmosphere

We are interested in recovering an analytical expression of the frequency-dependent tidal torque in the limit of a neutrally stratified atmosphere (Section 3.2.1.1). Similar analytical expressions of the tidal perturbations, and consequently the torque, are only possible in few cases where assumptions are imposed on the atmospheric structure and the forcing. An example that is essential to our work is the solution provided in ALM19. The main assumption of the analytical model in ALM19 – along with the other assumptions we listed earlier – is the isothermal profile of the atmosphere, with which the authors managed to capture the essential features of the GCM-generated tidal spectrum. However, the Lamb resonance predicted analytically was characterized by two opposite peaks, mismatching the asymmetry of their GCM results (Figure 3.3, right panel). In dialogue with the latter, we present next our tidal model, specifically aiming at unravelling the asymmetry. Before embarking on the details of our model, and in dialogue with the analytical model in ALM19, we highlight our model's key ingredients.

3.3.1 Dissipative radiative transfer

In the dynamical model described hitherto, the thermal energy absorbed by the atmosphere is fully converted into the dynamics of tidal waves and thermal variations. However, in reality, thermal oscillations of a gas depend on its temperature and are associated with thermal losses. A thermally forced atmospheric layer thus releases heat into space, the ground, or into neighboring layers. This process of thermal cooling has been traditionally ignored in the case of diurnal and semi-diurnal tides on Earth since its signature on the redistribution of mass is at least an order of magnitude lower than

the other dynamical effects. Nevertheless, the significance of this mechanism was highlighted for atmospheres of planets near synchronization. Namely, the classical theory of non-dissipative, adiabatic tides predicts a singular response at synchronization, with the amplitude of pressure, density, and temperature perturbation diverging (This divergence can be observed in Figure 7 of Dobrovolskis and Ingersoll, 1980). For instance, the tidal response of Venus was studied by Correia and Laskar (2001) who characterized two possible regimes: a regime far from synchronization, where dissipative processes can be ignored; and a regime in the vicinity of synchronization, where the perturbations should annihilate themselves. This behavior was confirmed using the GCM simulations in Leconte et al. (2015).

In our case study of the Earth, although we are far from synchronization, a similar singular behavior of the response is expected at the Lamb resonance (Zahnle and Walker, 1987; Auclair-Desrotour et al., 2019b), unless we allow for dissipation to cap the peak. We thus introduce radiative losses, denoted by $J_{\rm rad}$, in the dynamics of atmospheric tides, particularly in the heat equation (Eq. 3.40). Building on the pioneering work of Lindzen and McKenzie (1967) on Newtonian cooling, and the work of Auclair-Desrotour et al. (2017a) and Auclair-Desrotour and Leconte (2018), thermal losses (heat per unit mass) are expressed as:

$$J_{\rm rad}(z,\delta T) = C_{\rm p}\sigma_0(z)\delta T \tag{3.56}$$

Thermal losses are here parameterized by the characteristic frequency σ_0, which we shall call the radiative frequency, indicative of the radiative cooling time. An evident caveat in this dissipative approximation is the linear dependence of $J_{\rm rad}$ on the temperature perturbation, which can be interpreted as an optically thin layer approximation (Auclair-Desrotour et al., 2017a). Indeed, this term corresponds to the behaviour of a gray body atmosphere where radiation escapes to space. However, the flux emitted by a single layer is naturally absorbed by the neighboring layers, inducing nonlinear thermal coupling. This is true specifically for optically thick atmospheres. However, accounting for such a complex mechanism would make the dynamical equations a hard beast to handle analytically. Newtonian cooling should thus be used with caution as a convenient approximation of thermal radiation, perhaps justified by matching with GCM numerical simulations run with more realistic descriptions of radiative transfer[11] (Leconte et al., 2015).

[11]Radiative transfer is computed consistently using the method of correlated-k distributions (e.g., Lacis and Oinas, 1991) both in Leconte et al. (2015) and in Auclair-Desrotour et al. (2019b), who used the LMD GCM (Hourdin et al., 2006) with similar physical setups.

The radiative frequency σ_0 can vary with the atmospheric altitude (Pollack and Young, 1975). However, following Lindzen and McKenzie (1967), we consider the limiting case where the radial profile of σ_0 is assumed to be uniform. An effective value computed by Leconte et al. (2015) with a GCM in the case of Venus is $\sigma_0 = 7.5 \times 10^{-7}$ s^{-1}. In our case, we allow σ_0 to be a free parameter. With the added thermal radiation term, the heat equation is re-written as:

$$\frac{C_\mathrm{p}}{\Gamma_1}\left(\partial_\mathrm{t}\delta T + \frac{1}{H}\frac{dT_0}{dx}V_r\right) = \frac{gH}{\rho_0}\left(\partial_\mathrm{t}\delta\rho + \frac{1}{H}\frac{d\rho_0}{dx}V_r\right) + J - J_\mathrm{rad}. \tag{3.57}$$

This slight modification is deceivingly simple, as it induces drastic variations in the vertical structure equation. Without going into the gory details of that procedure, we provide the final form of the vertical structure equation which finally reads as (Lindzen and McKenzie, 1967):

$$\frac{d^2y}{dx^2} + \frac{\sigma}{\sigma - i\sigma_0}\left\{\frac{1}{h}\frac{dH}{dx} + \frac{\kappa H}{h} - \frac{1}{4} - \frac{i\sigma_0}{2\sigma}\left[\frac{1}{H}\frac{dH}{dx} - \frac{1}{2} + \frac{1}{H}\frac{dH^2}{dx^2} - \frac{1}{H^2}\left(\frac{dH}{dx}\right)^2 + \frac{i\sigma_0}{\sigma - i\sigma_0}\right.\right.$$
$$\left.\left.\times\frac{1}{H}\frac{dH}{dx}\left(\frac{1}{2H}\frac{dH}{dx}\right)\right]\right\}y = \frac{\kappa J}{\Gamma_1 g h}\frac{\sigma}{\sigma - i\sigma_0}\exp\left\{-\frac{1}{2}\left[x - \int_0^x \frac{i\sigma_0}{H\sigma}\frac{dH}{dx}\frac{\sigma}{\sigma - i\sigma_0}dx\right]\right\}. \tag{3.58}$$

3.3.2 Thermal forcing profile

To solve the vertical structure equation in the form given by Eq. (3.58), it is necessary to define a vertical profile for the tidal heating power per unit mass J. As the atmosphere is optically thin in the visible, most of the Solar flux impinging on the Earth reaches the ground. The ground returns the absorbed energy to the atmosphere with a delay due to thermal inertia. Three exchange mechanisms are activated between the atmosphere and the surface. First, the major part of the absorbed Solar flux is re-emitted by the surface in the infrared, where part of it is absorbed by greenhouse gases filling the lowermost layers of the atmosphere, and the rest escapes towards space. Another part of the energy is transmitted to the atmosphere in the form of sensible heat, and due to the presence of water on Earth another part is given in the form of latent heat, both heat exchanges occurring in the planetary boundary layer near the surface (Pierrehumbert, 2010). Similar to Dobrovolskis and Ingersoll (1980) and following Lindzen et al. (1968)

and Auclair-Desrotour et al. (2019b), we adopt a tidal heating profile of the form:

$$J(x) = J_s e^{-b_J x}, \tag{3.59}$$

where J_s is the heat absorbed at the surface, and b_J is a dimensionless skin thickness that characterizes the decay of heating along the vertical coordinate. This functional form of J is consistent with the assumption that heat fluxes are absorbed near the planet's surface. Besides, it allows the distribution of heat per unit mass to vary between the Dirac distribution adopted by Dobrovolskis and Ingersoll (1980) where $b_J \to \infty$, and a uniform distribution where the whole air column is uniformly tidally forced in the limit $b_J = 0$. The decay is described by an exponential function to ease mathematical manipulations, noting that this choice allows us to preserve the form of the right-hand member of the wave equation (3.58).

The atmosphere is thus predominantly heated by the upward propagating radiative flux emitted by the surface in the infrared. To determine J_s, we invoke its dependence on the total propagating flux $\delta F_{\rm tot}$ by computing the energy budget over the air column. The net input of energy corresponds to the difference between the amount of flux absorbed by the column and associated with a local increase of thermal energy, and the amount that escapes into at the upper boundary into space. We quantify the fraction of energy actually transferred to the atmosphere and that is consequently available for tidal dynamics by α_A, where $0 \leq \alpha_A \leq 1$; the rest of the flux amounting to $1 - \alpha_A$ is radiated towards space. We thus have

$$\int_0^\infty J(x)\rho_0(x)H(x)dx = \alpha_A \delta F_{\rm tot} \ . \tag{3.60}$$

The background distributions of the pressure, density, and temperature in the neutrally stratified atmosphere are expressed as (Auclair-Desrotour, 2016)

$$p_0(x) = p_0(0)e^{-x}, \quad \rho_0(x) = \frac{p_0(0)}{gH(0)}e^{(\kappa-1)x}, \quad T_0(x) = \frac{gH(0)}{\mathcal{R}_s}e^{-\kappa x}, \tag{3.61}$$

while the vertical distribution of the pressure height scale follows

$$H(x) = H(0)e^{-\kappa x}. \tag{3.62}$$

These distributions allow us to write the heat absorbed at the surface as:

$$J_s = \frac{\alpha_A g(b_J + 1)}{p_s(0)}\delta F_{\rm tot}. \tag{3.63}$$

To completely define J_s, we still have to define the total flux F_{tot}. To do so, we establish the power flux budget for a small thermal perturbation at the planetary surface. We start with δF_{inc}, a variation of the effective incoming stellar flux – after the reflected component has been removed – absorbed at the surface. δF_{inc} generates a variation δT_s in the surface temperature T_s. This variation induces radiative emission with magnitude δF_{rad}. A fraction of the incident power, δQ_{gr}, is then transmitted to the ground by thermal conduction, and another fraction, δQ_{atm}, is transmitted to the atmosphere through turbulent thermal diffusion. Finally, as the atmosphere is heated surface thermal forcing, it undergoes radiative cooling, in a similar fashion to the surface. We denote the atmospheric flux impinging upon the surface by δF_{atm}. Under these definitions, δF_{tot} is expressed as

$$\delta F_{tot} = \delta F_{inc} - \delta Q_{gr}. \tag{3.64}$$

Having isolated these thermal mechanisms, the total power budget of the thermal perturbation at the surface interface is expressed as[12]:

$$\delta F_{inc} - \delta Q_{gr} = \delta Q_{atm} + \delta F_{rad} - \delta F_{atm}. \tag{3.65}$$

The surface radiative emission can be obtained by differentiating the Stefan-Boltzmann law as a function of the surface temperature assuming that the surface radiates as a black body. We thus obtain

$$\delta F_{rad} = 4\sigma_{SB} T_s^3 \delta T_s, \tag{3.66}$$

in the blackbody approximation, with σ_{SB} being the Stephan-Botlzmann constant. Without any serious loss of generality, and justified by the small magnitude of the atmospheric emission towards the surface, one can assume that δF_{atm} is also proportional to δT_s, and combine the two radiative terms δF_{rad} and δF_{atm} into a single term with an effective emissivity ϵ_R. This assumption can follow from: *i)* the fact that the bulk atmosphere responsible for the greenhouse effect is formed by the lowermost atmospheric layers where temperature oscillations are close to the surface temperature oscillations δT_s; *ii)* the fact that energy given to the atmosphere is a fraction of δF_{rad}, and the flux δF_{atm} is a fraction of this input energy, which implies it should have the same form of δF_{rad}, up to a scaling factor.

For our purposes, it suffices to compute the difference $\delta F_{inc} - \delta Q_{gr}$. To do so, we define the thermal exchanges δQ_{gr} and δQ_{atm} associated with the diffusive process by the gradient of temperature in the vicinity of the surface using the gradient-flux theory

[12] at this stage of the work, we ignore latent heat exchanges associated with changes of states.

(e.g., Garratt, 1994). Namely,

$$\delta Q_{\rm gr}(t) = k_{\rm gr}\frac{\partial T}{\partial z}\bigg|_{z=0^-}, \tag{3.67}$$

$$\delta Q_{\rm atm}(t) = -k_{\rm atm}\frac{\partial T}{\partial z}\bigg|_{z=0^+}. \tag{3.68}$$

In these definitions, $k_{\rm gr}$ and $k_{\rm atm}$ are, respectively, the thermal conductivities of the ground and the atmosphere at the interface. We further define the corresponding diffusivities as:

$$K_{\rm gr} = \frac{k_{\rm gr}}{\rho_0(0^-)C_{\rm gr}} \quad \text{and} \quad K_{\rm atm} = \frac{k_{\rm atm}}{\rho_0(0^+)C_{\rm p}}, \tag{3.69}$$

where $C_{\rm gr}$ is, in analogy to $C_{\rm p}$ in the atmosphere, the thermal capacity per unit mass of the ground. With these definitions, the power budget balance in Eq. (3.65) is re-written as:

$$\delta F_{\rm inc} - k_{\rm gr}\frac{\partial T}{\partial z}\bigg|_{z=0^-} = -k_{\rm atm}\frac{\partial T}{\partial z}\bigg|_{z=0^+} + 4\epsilon_{\rm R}\sigma_{\rm SB}T_{\rm s}^3\delta T_{\rm s}. \tag{3.70}$$

Temperature variations near the surface can be traced by the heat transport equations (e.g., Chapman and Lindzen, 1969)

$$\frac{\partial \delta T}{\partial t} = K_{\rm gr}\frac{\partial^2 \delta T}{\partial z^2} \quad \text{for } z < 0\,, \tag{3.71}$$

$$\frac{\partial \delta T}{\partial t} = K_{\rm atm}\frac{\partial^2 \delta T}{\partial z^2} \quad \text{for } z > 0\,. \tag{3.72}$$

which in the frequency domain read

$$i\sigma\delta T = K_{\rm gr}\frac{\partial^2 \delta T}{\partial z^2} \quad \text{for } z < 0\,, \tag{3.73}$$

$$i\sigma\delta T = K_{\rm atm}\frac{\partial^2 \delta T}{\partial z^2} \quad \text{for } z > 0\,. \tag{3.74}$$

These equations have solutions in the form:

$$\delta T(z) = \delta T_{\rm s}\exp\left\{(1+is)x/\delta^\sigma_{\rm gr}\right\} \quad \text{for} \quad z \le 0\,, \tag{3.75}$$

$$\delta T(z) = \delta T_{\rm s}\exp\left\{-(1+is)z/\delta^\sigma_{\rm atm}\right\} \quad \text{for} \quad z > 0\,, \tag{3.76}$$

where we use $s = \text{sign}(\sigma)$, and we denote by the pair $\delta^\sigma_{\rm gr}$ and $\delta^\sigma_{\rm atm}$ the skin thicknesses of heat transport by thermal diffusion in the ground and the atmosphere. We define them

as:

$$\delta^{\sigma}_{\rm gr} = \sqrt{\frac{2K_{\rm gr}}{|\sigma|}} \quad \text{and} \quad \delta^{\sigma}_{\rm atm} = \sqrt{\frac{2K_{\rm atm}}{|\sigma|}}\,. \tag{3.77}$$

The incident flux $\delta F_{\rm inc}$ and the temperature variation $\delta T_{\rm s}$ are essentially directly proportional. We denote this proportionality by the boundary layer transfer function $\mathcal{B}^{\sigma}_{\rm gr}$; namely:

$$\delta T_{\rm s} = \mathcal{B}^{\sigma}_{\rm gr}\delta F_{\rm inc}. \tag{3.78}$$

To obtain the explicit form of $\mathcal{B}^{\sigma}_{\rm gr}$, we substitute the solutions $\delta T(x)$ into the power balance equation (3.70). By straightforward manipulation we get:

$$\mathcal{B}^{\sigma}_{\rm gr} = \left\{\left(4\epsilon_{\rm R}\sigma_{\rm SB}T_{\rm s}^3\right)\left[1 + (1+si)\sqrt{\tau_{\rm bl}|\sigma|}\right]\right\}^{-1}, \tag{3.79}$$

which is identical to the form deduced in Auclair-Desrotour et al. (2017a). In this transfer function, we defined the timescale $\tau_{\rm bl}$ as:

$$\tau_{\rm bl} = \frac{1}{2}\left(\frac{I_{\rm gr} + I_{\rm atm}}{4\epsilon_{\rm R}\sigma_{\rm SB}T_{\rm s}^3}\right)^2, \tag{3.80}$$

where the functions $I_{\rm gr}$ and $I_{\rm atm}$ denote, respectively, the thermal inertia[13] of the ground and the atmospheric surface layer, specifically they are given as:

$$I_{\rm gr} = \rho_0(0^-)C_{\rm gr}\sqrt{K_{\rm gr}} \quad \text{and} \quad I_{\rm atm} = \rho_0(0^+)C_{\rm p}\sqrt{K_{\rm atm}}\,. \tag{3.81}$$

With these definitions, $\tau_{\rm bl}$ can be interpreted as a characteristic timescale of the surface thermal response. Namely, it is a diffusive timescale, which accounts for diffusion in the ground and in the atmospheric surface layer. It grows quadratically with the soil and atmospheric thermal inertias. We associate with $\tau_{\rm bl}$ the frequency $\sigma_{\rm bl} = \tau_{\rm bl}^{-1}$, a characteristic frequency that we use hereafter to parametrize the function $\mathcal{B}^{\sigma}_{\rm gr}$, and which reflects the thermal properties of the diffusive boundary layer. It will serve as the second free parameter of our tidal model, the first being the dissipative frequency σ_0. From Eq. (3.79), it is evident that $\sigma_{\rm bl}$ will play a significant role in the tidal response of the Earth. Namely, the ratio $\sigma/\sigma_{\rm bl}$ determines the angular delay of the ground temperature variations. As discussed in Auclair-Desrotour et al. (2017a), this frequency is used to explain the position of the diurnal peak observed in the surface temperature oscillations

[13]The term thermal inertia could be confusing at first glance, One can argue that this definition does not look identical to the usual expression thermal inertia in the literature, which is the square root of the product of the conductivity and the heat capacity per unit volume (e.g.m Hourdin et al., 1993). However, considering that the diffusivity is the conductivity divided by the heat capacity per unit volume, we recover the well-known definition of the thermal inertia.

being roughly three hours late with respect to the midday point. For our study of the global tidal response, the frequency ratio determines whether the ground response is synchronous with the thermal excitation (when $\sigma \ll \sigma_{\rm bl}$), meaning thermal inertias vanish, the soil and the surface layer cannot store energy, and the ground response is instantaneous; or if due to the combination of thermal inertias, the energy reservoir of the ground is huge, and the ground response lags the excitation, imposing another shift in the tidal bulge (when $\sigma \gtrsim \sigma_{\rm bl}$). This signature of $\sigma_{\rm bl}$ will be later reaped in our attempt to explain the Lamb resonance asymmetry. But we are getting ahead of ourselves, so without further ado, we finalize defining the thermal forcing profile.

With the definition of $\mathcal{B}^{\sigma}_{\rm gr}$, we re-write the temperature profile solution of Eq. (3.75) as:

$$\delta T(z) = \mathcal{B}^{\sigma}_{\rm gr} \exp\left\{(1+is)z/\delta_{\rm gr}\right\} \delta F_{\rm inc} \quad \text{for} \quad z \leq 0\,, \tag{3.82}$$

which upon derivation gives:

$$\left.\frac{\partial T}{\partial z}\right|_{z=0^-} = \frac{\mathcal{B}^{\sigma}_{\rm gr}(1+is)}{\delta_{\rm gr}} \delta F_{\rm inc}. \tag{3.83}$$

Substituting the latter in Eq. (3.67) we obtain:

$$\delta Q_{\rm gr} = \frac{k_{\rm gr}}{\sqrt{2K_{\rm gr}}} \sqrt{|\sigma|}\, \mathcal{B}^{\sigma}_{\rm gr} \delta F_{\rm inc}\,. \tag{3.84}$$

By virtue of the power budget balance in Eq. (3.70), we finally obtain for $\delta F_{\rm tot}$ (Eq. 3.64):

$$\delta F_{\rm tot} = \delta F_{\rm inc} \left[1 - \frac{k_{\rm gr}}{\sqrt{2K_{\rm gr}}} \sqrt{|\sigma|}\, \mathcal{B}^{\sigma}_{\rm gr}(1+si)\right]. \tag{3.85}$$

What remains for us to complete characterizing the thermal forcing profile is to explicitly define the incident flux $\delta F_{\rm inc}$. As we are considering the semi-diurnal forcing, we aim to extract the quadrupolar contribution from $\delta F_{\rm inc}$ (hereafter denoted by F for convenience). We start by expressing the day-night periodically varying flux F as:

$$F = \begin{cases} F_* \cos\Theta, & \text{for } 0 \leq \Theta \leq \pi/2 \\ 0, & \text{otherwise}\,, \end{cases} \tag{3.86}$$

where $F_* = L_*/4\pi a^2$, L_* being the stellar luminosity, a the star-planet distance, and Θ is the zenith angle. To obtain the quadrupolar component of the thermal forcing we first

expand F in Legendre Polynomials:

$$F(\Theta) = \sum_{l=0}^{\infty} F_l P_l(\cos\Theta), \tag{3.87}$$

where the expansion coefficients are given by

$$\begin{aligned} F_l &= \frac{2l+1}{2} \int_0^{\pi/2} F(\Theta) P_l(\cos\Theta) \sin\Theta d\Theta \,, \\ &= \frac{2l+1}{2} \int_0^{\pi/2} F_* P_l(\cos\Theta) \sin\Theta \cos\Theta d\Theta. \end{aligned} \tag{3.88}$$

Next, using the addition theorem, we write the Legendre Polynomials as series of spherical harmonics:

$$P_l(\cos\Theta) = \frac{4\pi}{2l+1} \sum_{m=-l}^{m=l} Y_{lm}(\theta,\lambda) Y^*_{lm}(\theta_S,\lambda_S) \,, \tag{3.89}$$

where the asterisk corresponds to complex conjugation and the coordinates $(\theta_S, \lambda_S) = [\pi/2, (\Omega - n_S)t]$ define the position of the Sub, n_S being its orbital mean motion. Thus we have:

$$F(\Theta) = \sum_{l=0}^{\infty} \sum_{m=-l}^{m=l} C_l F_l Y_{lm}(\theta,\lambda) Y^*_{lm}(\theta_S,\lambda_S) \,, \tag{3.90}$$

where we have defined $C_l = 4\pi/(2l+1)$. Using the definition of spherical harmonics

$$Y_{lm} = N_{lm} P_{lm} e^{im\lambda}, \tag{3.91}$$

with

$$N_{lm} = \sqrt{\frac{(2l+1)(l-m)!}{4\pi(l+m)!}} \,, \tag{3.92}$$

we re-write Eq. (3.90) as:

$$\begin{aligned}
F(\Theta) &= \sum_{l=0}^{\infty}\sum_{m=-l}^{m=l}\gamma_{lm}(\theta)\exp[im(\Lambda t+\lambda)] \\
&= \sum_{l=0}^{\infty}\sum_{m=-l}^{m=l}\gamma_{lm}(\theta)\cos[m(\nu t+\lambda)] + i\sum_{l=0}^{\infty}\sum_{m=-l}^{m=l}\gamma_{lm}(\theta)\sin[m(\nu t+\lambda)] \\
&= \sum_{l=0}^{\infty}\sum_{m=-l}^{m=l}\gamma_{lm}(\theta)\cos[m(\nu t+\lambda)] + i\sum_{l=0}^{\infty}\sum_{m=-l}^{m=-1}\gamma_{lm}(\theta)\sin[m(\nu t+\lambda)] \\
&+ i\sum_{l=0}^{\infty}\sum_{m=1}^{m=l}\gamma_{lm}(\theta)\sin[m(\nu t+\lambda)] \\
&= \sum_{l=0}^{\infty}\sum_{m=-l}^{m=l}\gamma_{lm}(\theta)\cos[m(\nu t+\lambda)] + i\sum_{l=1}^{\infty}\sum_{m=1}^{m=l}\sin[m(\nu t+\lambda)]\,[\gamma_{lm}(\theta)-\gamma_{l-m}(\theta)]\ ,
\end{aligned}$$

where we have defined $\gamma_{lm}(\theta) = C_l F_l N_{lm}^2 P_{lm}(\cos\theta)P_{lm}(0)$, and $\nu = \Omega - n_{\rm S}$. Next we note that

$$\gamma_{lm}(\theta) - \gamma_{l-m}(\theta) = C_l F_l\left[N_{lm}^2 P_{lm}(\cos\theta)P_{lm}(0) - N_{l-m}^2 P_{l-m}(\cos\theta)P_{l-m}(0)\right] = 0, \tag{3.93}$$

by virtue of the equality

$$P_{l-m} = (-1)^m\frac{(l-m)!}{(l+m)!}P_{lm}. \tag{3.94}$$

Thus $F(\Theta)$ is written as the real part of the thermal forcing function in the Fourier domain, $\tilde{F}(\Theta)$ which is defined as:

$$\tilde{F}(\Theta) = \sum_{l=0}^{\infty}\sum_{m=-l}^{m=l}\gamma_{lm}(\theta)e^{im(\nu+\lambda)}. \tag{3.95}$$

Finally we retrieve the quadrupolar component of the forcing in the form:

$$\tilde{F}_{22}(\theta) = \frac{15}{128}F_*\sin^2(\theta)e^{i(\sigma_{22}t+2\lambda)}. \tag{3.96}$$

Combined with Eq. (3.85), the latter equation allows us to express the heat absorbed at the surface $J_{\rm s}$ of Eq. (3.63) in its final form as:

$$J_{\rm s} = \frac{15}{128}F_*\frac{\alpha_{\rm A}g(b_{\rm J}+1)}{p_{\rm s}(0)}\left[1 - \frac{k_{\rm gr}}{\sqrt{2K_{\rm gr}}}\sqrt{|\sigma|}\mathcal{B}_{\rm gr}^{\sigma}(1+si)\right]. \tag{3.97}$$

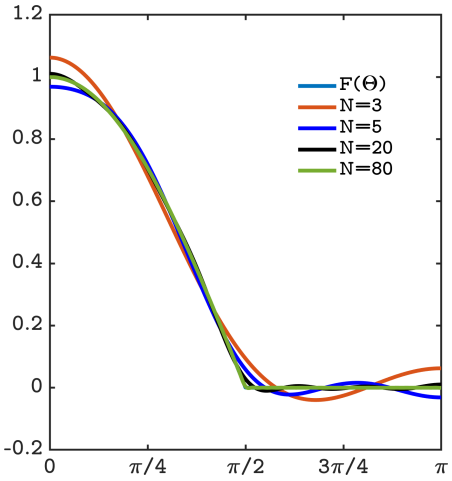

FIGURE 3.7: Convergence test of the harmonic decomposition of the thermal forcing function $F(\Theta)$ with amplitude $F_* = 1$.

3.3.3 Tidal response: the asymmetric Lamb resonance

Now we are fully geared to establish the tidal response. As elucidated in Section (3.2.1.1), we adopt the neutral stratification scenario, $N^2 = 0$, and we recall that

$$\kappa H = -\frac{dH}{dx}. \tag{3.98}$$

We impose this condition on the vertical structure equation Eq. (3.58), further substituting for J its definition of Eq. (3.59). It is then straightforward then to recast the vertical structure equation into a simpler one of the form:

$$\frac{d^2y}{dx^2} + \hat{k}^2_{x;n} y = \alpha e^{-\delta x}, \tag{3.99}$$

where we have defined the square of the radial wave-number as:

$$\hat{k}^2_{x;n} = \frac{1}{4}\frac{1}{\tilde{\sigma} - i}\left[-\tilde{\sigma} + \frac{\kappa^2}{\tilde{\sigma} - i} + i(1 + 2\kappa)\right], \tag{3.100}$$

or

$$\hat{k}_{x;n} = \pm\frac{1}{2(\tilde{\sigma}^2 + 1)}\left[\kappa\tilde{\sigma} + i(1 + \kappa + \tilde{\sigma}^2)\right]. \tag{3.101}$$

The non-dimensional function δ is defined as:

$$\delta = \frac{1}{2(\tilde{\sigma}^2 + 1)}\left[(1 + 2b_J)(\tilde{\sigma}^2 + 1) - \kappa + i\kappa\tilde{\sigma}\right], \tag{3.102}$$

while the forcing function α is:

$$\alpha = \frac{\kappa J_s}{\Gamma_1 g h} \frac{\tilde{\sigma}^2 + i\tilde{\sigma}}{\tilde{\sigma}^2 + 1}. \tag{3.103}$$

In these functions, we denote by $\tilde{\sigma}$ the non-dimensional frequency of dissipation. Namely, we have defined: $\tilde{\sigma} = \sigma/\sigma_0$. Furthermore, we denote by $\bar{\sigma}$ the non-dimensional parameter characterizing the response of the boundary layer. Namely, $\bar{\sigma} = \sqrt{|\sigma|/\sigma_{\rm bl}}$. We note that $\bar{\sigma}$ has not appeared explicitly yet in the preceding equations, but it is embedded in the definition of J_s. These two non-dimensional frequencies serve as the free parameters of our tidal model.

Before providing the solution to the vertical structure equation, we take a sneak peek at wave dynamics through the wavenumber variation. In Figure 3.8 we plot the surface of the $\hat{k}_{x;n}$ as a function of the normalized tidal frequency ω, and the dissipation frequency σ_0. For illustrative purposes, we do so for two different atmospheric structures: the neutrally stratified case that we are studying, and the stably stratified case in the isothermal limit. It is straightforward to produce the expression of the wavenumber in the latter case by imposing the condition $dH/dx = 0$ on the vertical structure equation. Without going through the full procedure, we provide the final form of the imaginary and real parts of the wavenumber in the isothermal case. They read as:

$$\mathrm{Im}\{\hat{k}^{\rm IS}_{x;n}\} = \frac{1}{\sqrt{2}} \left\{ \left[\frac{1}{16} + \frac{\kappa H \sigma^2}{h_n(\sigma^2 + \sigma_0^2)} \left(\frac{\kappa H}{h_n} - \frac{1}{2} \right) \right]^{\frac{1}{2}} + \frac{\kappa H \sigma^2}{h_n(\sigma^2 + \sigma_0^2)} - \frac{1}{4} \right\}^{\frac{1}{2}}, \tag{3.104}$$

$$\mathrm{Re}\{\hat{k}^{\rm IS}_{x;n}\} = \frac{1}{\sqrt{2}} \left\{ \left[\frac{1}{16} + \frac{\kappa H \sigma^2}{h_n(\sigma^2 + \sigma_0^2)} \left(\frac{\kappa H}{h_n} - \frac{1}{2} \right) \right]^{\frac{1}{2}} - \frac{\kappa H \sigma^2}{h_n(\sigma^2 + \sigma_0^2)} + \frac{1}{4} \right\}^{\frac{1}{2}}. \tag{3.105}$$

We recall here that the equivalent depth h_n is frequency dependent via Eq. (3.44). The imaginary part of the wavenumber is significant because it dictates the strength of the evanescent nature of the tidal waves, while the real part shows the strength of the propagative modes. In the neutrally stratified scenario, the buoyancy force, which serves as the restoring force of the gravity waves, vanishes. Thus we only expect non-propagating evanescent waves, as propagating gravity waves do not exist in convective layers. This is what we confirm in the surface plot of $\hat{k}_{x;n}$: $\mathrm{Im}\{\hat{k}_{x;n}\}$ maintains the same order of magnitude with a very slight window of variation as a function of the frequencies. In contrast, $\mathrm{Re}\{\hat{k}_{x;n}\}$ is orders of magnitude smaller, indicating the absence of propagating waves. In hindsight, this regime is preferable to better compute the

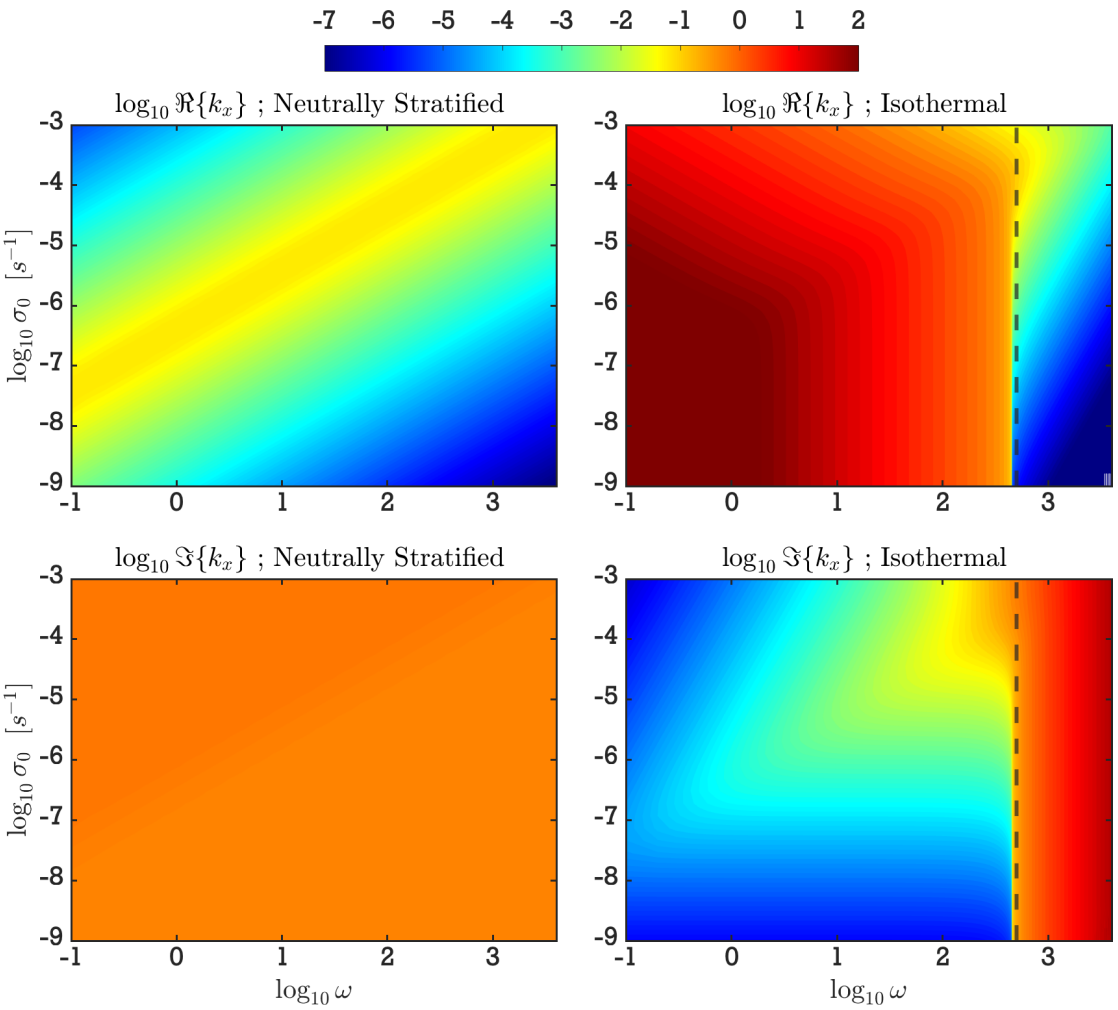

FIGURE 3.8: Surface maps of the logarithm of the imaginary and real parts of the radial wavenumbers $\hat{k}_{x;n}$ and $\hat{k}_x^{\mathrm{IS}}$. The former corresponds to the neutrally stratified case (panels on the left), while the latter corresponds to the isothermal case (panels on the right). The surfaces are plotted as a function of logarithms of the normalized tidal frequency $\omega = \sigma/(2n_{\mathrm{S}})$ and the dissipative frequency σ_0. The vertical line in the isothermal case marks the Lamb frequency given by Eq. (3.106). The plots indicate the strong evanescent nature of the tidal waves in the neutrally stratified atmosphere, and the existence of propagating and evanescent modes in the isothermal atmosphere, with a regime shift around the Lamb frequency.

tidal response. Gravity waves, at least in the adiabatic case, can involve oscillatory behavior that tend to annihilate the large-scale structure of the tidal response (see for e.g., Auclair-Desrotour, 2016)[14]. In contrast, the behavior is different in the isothermal case: $\mathrm{Im}\left\{\hat{k}_x^{\mathrm{IS}}\right\} \ll 1$ for a wide range of values of the frequencies (blue to green regions), indicating a weak evanescent regime. A regime-shift into evanescent modes is evident for very high σ, i.e., in the fast rotation limit, with the order of magnitude increase in $\mathrm{Im}\left\{\hat{k}_x^{\mathrm{IS}}\right\}$ (the red region). The position of this regime shift coincides with the Lamb

[14]It would be interesting to check if they would maintain this behavior when accounting for radiative cooling.

frequency, which represents the cut-off frequency of acoustic waves (Auclair-Desrotour et al., 2017a). This frequency is defined for every horizontal Hough mode n as (e.g., Chapman and Lindzen, 1969):

$$\sigma_n^{\mathrm{L}} = \frac{(\Lambda_n \Gamma_1 g H)^{1/2}}{R_{\mathrm{E}}}. \tag{3.106}$$

We mark with the vertical line the position of this frequency. It is expected that σ_0^{L} indicate the position of the tidal response resonance in the high frequency regime. The position is thus mainly dependent on the main gravity mode of the horizontal Hough modes, the surface temperature through H, and the planetary radius. The opposite regime shift is observed in $\mathrm{Re}\{\hat{k}_x^{\mathrm{IS}}\}$, indicating strong propagation before the Lamb resonance, and weak propagation after it. We now proceed to solve the vertical structure equation in the neutrally stratified limit. Eq. (3.99) admits the general solution

$$y(x) = A e^{i\hat{k}_{x;n}x} + B e^{-i\hat{k}_{x;n}x} + y_{\mathrm{p}}(x), \tag{3.107}$$

where we obtain the particular solution in the form:

$$y_{\mathrm{p}}(x) = \frac{\alpha}{\delta^2 + \hat{k}_{x;n}^2} e^{-\delta x}. \tag{3.108}$$

Applying the non-divergence boundary condition at the upper most layer of the atmosphere, we set $B = 0$ and choose the proper sign of the wavenumber accordingly, keeping only the evanescent waves under study. Noting that the imaginary part of $\hat{k}_{x;n}$ is always non-zero due to the included radiative cooling, contrary to the usual non-dissipative case Chapman and Lindzen (1969). As a consequence, one component of the general solution of the homogeneous equation tends to infinity at the limit $x \to \infty$, while the other component tends to zero. The second boundary condition is simply a wall condition at the ground, and it can be expressed as $V_r\big|_{x=0} = 0$. Thus from Eq. (3.51) we obtain the condition[15]:

$$\frac{dy(0)}{dx} + \left(\frac{H}{h} - \frac{1}{2}\right) y(0) = 0, \tag{3.109}$$

which gives us

$$A = \frac{\alpha}{\delta^2 + \hat{k}_{x;n}^2} \frac{\delta - H/h + 1/2}{i\hat{k}_{x;n} + H/h - 1/2}. \tag{3.110}$$

[15]The same comment of footnote 10 applies here.

Thus the general solution is thus given by:

$$y(x) = \frac{\alpha}{\delta^2 + \hat{k}_{x;n}^2} \left[\frac{\delta - H/h + 1/2}{i\hat{k}_{x;n} + H/h - 1/2} e^{i\hat{k}_{x;n}x} + e^{-\delta x} \right]. \tag{3.111}$$

As discussed earlier, to obtain the tidal torque, we compute the pressure anomaly at the surface δp_s, which is readily obtained from Eq. (3.50) using the general solution of Eq. (3.111). We thus have

$$\frac{\delta p_\mathrm{s}}{p_\mathrm{s}} = \frac{\Gamma_1}{\sigma} \frac{\alpha}{\delta^2 + \hat{k}_{x;n}^2} \frac{i\delta - \hat{k}_{x;n}}{i\hat{k}_{x;n} + H/h - 1/2}. \tag{3.112}$$

More precisely, the tidal torque is proportional to the imaginary part of δp_s. Obtaining the latter requires tedious but straightforward manipulations. In the process, we define another non-dimensional parameter, namely $\beta = \sigma_0^2/2\sigma_\mathrm{D}^2$, where the dynamical frequency $\sigma_\mathrm{D} = \sqrt{gH\Lambda}/R_\mathrm{E}$. Is is clear that β quantifies the relative importance of radiative cooling to the fluid "elasticity". On the other hand, σ_D is the typical frequency of long-wavelength compressibility waves, which are analogous to the long-wavelength surface gravity waves in the ocean, with the pressure height scale translating to the uniform oceanic thickness. We finally obtain:

$$\mathrm{Im}\left\{\frac{\delta p_\mathrm{s}}{p_\mathrm{s}}\right\} = \frac{2\alpha_\mathrm{A}\kappa g\Lambda\delta F_{22}\beta}{R_\mathrm{E}^2 p_\mathrm{s}(1 + 2\bar{\sigma} + 2\bar{\sigma}^2)\sigma_0^3} \frac{C_1\tilde{\sigma}^5 + C_2\tilde{\sigma}^4 + C_3\tilde{\sigma}^3 + C_4\tilde{\sigma}^2 + C_5\tilde{\sigma} + C_6}{D_1\tilde{\sigma}^8 + D_2\tilde{\sigma}^6 + D_3\tilde{\sigma}_4 + D_4\tilde{\sigma}^2 + D_5}, \tag{3.113}$$

where the numerator polynomial coefficients are given by:

$$\begin{aligned}
C_1 &= -2\,\mathrm{b_J}^2\,\beta\,F \\
C_2 &= -\mu_\mathrm{gr}\,\mathrm{b_J}^2\,\beta\,s\,\bar{\sigma}\;(\kappa + 2) \\
C_3 &= -\left(2\,\mathrm{b_J}^2\,\beta + 2\,\beta\,\kappa^2 - \mathrm{b_J}^2 - 4\,\mathrm{b_J}\,\beta\,\kappa\right)\,F \\
C_4 &= -\mu_\mathrm{gr}\,s\,\bar{\sigma}\,\left(2\,\mathrm{b_J}^2\,\beta + 2\,\beta\,\kappa^2 + \beta\,\kappa^3 - \mathrm{b_J}^2 - 4\,\mathrm{b_J}\,\beta\,\kappa - 2\,\mathrm{b_J}\,\beta\,\kappa^2 + \mathrm{b_J}^2\,\beta\,\kappa\right) \\
C_5 &= (\mathrm{b_J} - \kappa)^2\,F \\
C_6 &= \mu_\mathrm{gr}\,s\,\bar{\sigma}\,(\mathrm{b_J} - \kappa)^2,
\end{aligned}$$

with

$$F = 2\,\bar{\sigma} - \mu_\mathrm{gr}\,\bar{\sigma} - 2\,\mu_\mathrm{gr}\,\bar{\sigma}^2 + 2\,\bar{\sigma}^2 + 1, \tag{3.114}$$

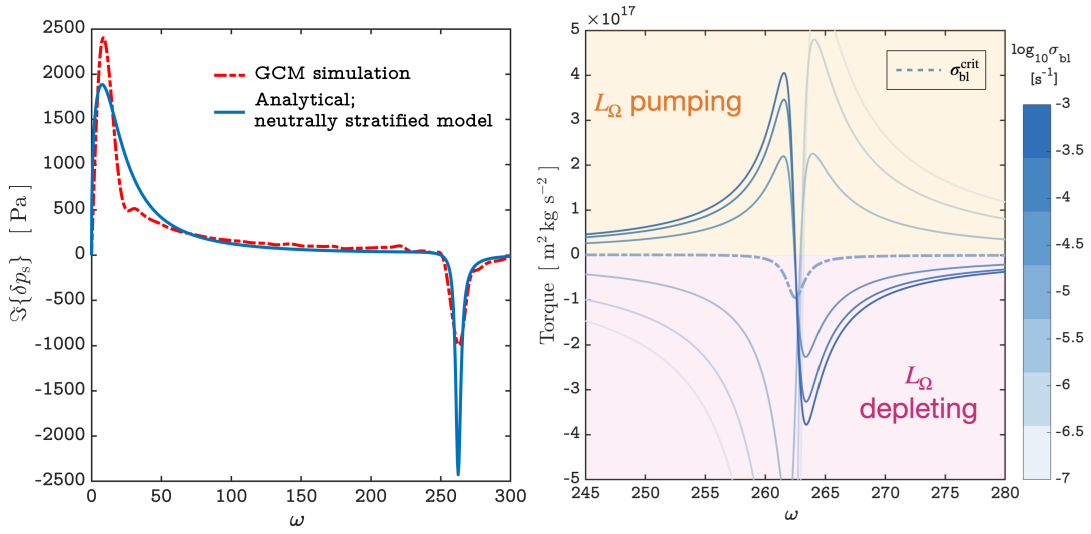

FIGURE 3.9: *Left:* Imaginary part of the quadrupolar component of the surface pressure anomaly as a function of the normalized forcing frequency $\omega = (\Omega - n_S)/n_S$. Plotted are the two curves corresponding to the spectrum of our analytical ab initio model in the neutrally stratification case (blue, given by Eq. (3.113)), and the spectrum obtained via the GCM simulations in Auclair-Desrotour et al. (2019b). To compare the two curves, we adopted the same reference case parameters of Auclair-Desrotour et al. (2019b), which correspond to a rocky Venus-like planet; more specifically, a dry Venus-sized planet with a surface of bare rocks, and a 10 bar atmosphere with the composition of the Earth's atmosphere, but irradiated by the same Solar flux as Venus. *Right:* We zoom over the vicinity of the Lamb resonance and plot the torque, which is directly proportional to the imaginary part of p_s (Eq. 3.55). We do so for different values of σ_{bl}, the effective frequency characterizing the thermal response of the ground. The values cover a range that goes from an instantaneous ground response (dark blue) to a delayed response (light blue).

and for the denominator we have:

$$
\begin{aligned}
D_1 &= 4\, b_J{}^2\, \beta^2,\\
D_2 &= b_J{}^2\, \beta^2\, \kappa^2 + 4\, b_J{}^2\, \beta^2\, \kappa + 8\, b_J{}^2\, \beta^2 - 4\, b_J{}^2\, \beta - 8\, b_J\, \beta^2\, \kappa + 4\, \beta^2\, \kappa^2,\\
D_3 &= b_J{}^2\, \beta^2\, \kappa^2 + 4\, b_J{}^2\, \beta^2\, \kappa + 4\, b_J{}^2\, \beta^2 - 2\, b_J{}^2\, \beta\, \kappa - 8\, b_J{}^2\, \beta + b_J{}^2 - 2\, b_J\, \beta^2\, \kappa^3 - 8\, b_J\, \beta^2\, \kappa^2\\
&\quad - 8\, b_J\, \beta^2\, \kappa + 8\, b_J\, \beta\, \kappa + \beta^2\, \kappa^4 + 4\, \beta^2\, \kappa^3 + 4\, \beta^2\, \kappa^2 - 4\, \beta\, \kappa^2,\\
D_4 &= 2\, b_J{}^2 - 4\, b_J{}^2\, \beta - 4\, \beta\, \kappa^2 - 2\, \beta\, \kappa^3 - 2\, b_J\, \kappa + \kappa^2 + 8\, b_J\, \beta\, \kappa + 4\, b_J\, \beta\, \kappa^2 - 2\, b_J{}^2\, \beta\, \kappa,\\
D_5 &= (b_J - \kappa)^2.
\end{aligned}
\tag{3.115}
$$

In the above expressions, we defined the dimensionless parameter μ_{gr} as

$$
\mu_{gr} = \frac{k_{gr}\sqrt{\sigma_{bl}}}{\epsilon_R \zeta_{gr}\sqrt{2K_{gr}}}. \tag{3.116}
$$

The results of this model are summarized in Figure 3.9. In the left panel we plot the frequency spectrum of the imaginary part of the pressure anomaly, accompanied with that generated by the GCM simulations in ALM19. The latter work recovered the tidal torque of a rocky planet with Venus-like orbital and structural parameters (also identical to those in Leconte et al., 2015); namely, a dry Venus-sized planet with a surface of bare rocks and a 10-bar Earth-like atmosphere, irradiated by the Solar flux irradiating Venus at its actual position. We thus use the same parameters listed there in our model, and we further tune our free parameters σ_0 and $\sigma_{\rm bl}$ to resemble the GCM-generated spectrum. As we noted earlier, the work of ALM19 is the only work, to-date, to have established the spectrum of the tidal torque in the high frequency regime, and thus the only work available to us to benchmark our model. In the right panel, we plot the tidal torque spectrum over a small frequency spectrum where we capture the Lamb resonance for different values of $\sigma_{\rm bl}$. Both panels allow the following observations:

- We capture with the neutrally stratified atmospheric model the inherent features of the spectrum obtained via sophisticated GCM simulations: *i)* the thermal peak near-synchronization with a comparable amplitude $\sim$ 2000 Pa; *ii)* the Lamb resonance in the high frequency regime; *iii)* the proper scaling of the spectrum that is almost linear near synchronization, and $\propto \sigma^{-1}$ in the high frequency regime. The success of obtaining an exact fit of the model to the GCM simulation in hindered by the complex interplay between the two free parameters, and the effect of the dissipative frequency. Increasing σ_0 would reduce the amplitude of the Lamb resonance, but also the amplitude of the thermal peak, and vice versa. Still, it is interesting, for now at least, to see all the spectral features captured in the model.

- Recalling that the Lamb resonance in the high frequency regime is essential for the rotational equilibrium hypothesis, we zoom over it in the panel on the right. The studied values of $\sigma_{\rm bl}$ correspond to a ground thermal response timescale that goes from instantaneous (dark blue) to very delayed (light blue) due to ground thermal inertia. As we discussed earlier, the Lamb resonance, as portrayed in ZW87 and BS16, required for the rotational equilibrium hypothesis features two peaks symmetric around the resonance frequency: a negative peak that complements the oceanic gravitational torque, thus depleting the Earth's angular momentum L_Ω, and a positive peak that opposes the gravitational tide and pumps L_Ω. This regime is observed via the dark blue curves.

With the introduction of the delayed thermal response of the ground (going from dark to light blue), the thermal tidal bulge is phase delayed such that the symmetry of the peaks is broken. The symmetry breaking is enhanced with decreasing $\sigma_{\rm bl}$ until a critical value $\sigma_{\rm bl}^{\rm crit}$ is reached, where the positive peak completely disappears. Beyond this critical value, the peaks reverse positions, with the positive peak becoming at the high frequency side of the resonance position, and are evidently characterized with smaller amplitudes than the negative peaks. The reason behind this transition lies in the variation of the position of the tidal bulge as we vary the thermal inertia of the ground via $\sigma_{\rm bl}$. This bulge lags the sub-stellar point by roughly 3 hours in the adiabatic tidal theory Chapman and Lindzen (1969), and more precisely by 2h26mn in the measurements shown in Figure 3.1. It is evident now that accounting for this bulge shift induces the Lamb asymmetry and has, most probably, significant effects on the Earth's rotational history.

We close this section by analyzing our model in the low frequency regime. The spectrum in this region features the near-synchronization thermal peak, and is often associated in the literature with a functional form that corresponds to the so-called Maxwell model (e.g., Efroimsky, 2012; Correia et al., 2014). This model describes the idealized behaviour of a forced oscillator composed of a string and a damper in series. It was shown in Auclair-Desrotour et al. (2019b) that this model does not match the numerical results of the GCM, though Leconte et al. (2015) obtained a good agreement, an issue worthy of further investigation. Due to the significance of the peak in the rotational stabilization of planets near synchronization, the quest for a simple model to describe this regime continues.

From our numerical exploration, it turns out that the low frequency regime is largely insensitive to variations in $\sigma_{\rm bl}$ and consequently $\bar{\sigma}$. Without any serious loss of generality, we study the limit of $\bar{\sigma} \rightarrow 0$, i.e. $\sigma_{\rm bl} \rightarrow \infty$. In this limit, Eq. (3.113) reduces to:

$$\mathrm{Im}\left\{\frac{\delta p_{\rm s}}{p_{\rm s}}\right\} = \frac{2\alpha_{\rm A}\kappa g \Lambda \delta F_{22}\beta}{R_{\rm E}^2 p_{\rm s}\sigma_0^3} \times \frac{C_1\tilde{\sigma}^5 + C_3\tilde{\sigma}^3 + C_5\tilde{\sigma}}{D_1\tilde{\sigma}^8 + D_2\tilde{\sigma}^6 + D_3\tilde{\sigma}^4 + D_4\tilde{\sigma}^2 + D_5}. \tag{3.117}$$

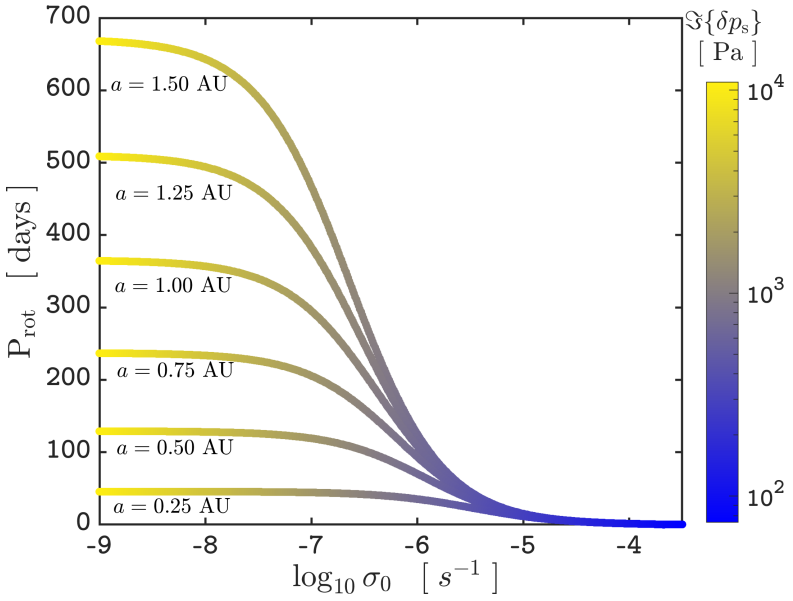

FIGURE 3.10: The position of the thermal peak near synchronization plotted in terms of the rotational period of the planet, as a function of the dissipation frequency σ_0, for different values of the planetary semi-major axis (Eq. 3.120). Color coding corresponds to the amplitude of the peak.

Taking the derivative we get:

$$\frac{d}{d\tilde{\sigma}} \mathrm{Im}\left\{\frac{\delta p_s}{p_s}\right\} = \frac{2\alpha_A \kappa g \Lambda \delta F_{22} \beta}{R_E^2 p_s \sigma_0^3} \times \left[\frac{5C_1\tilde{\sigma}^4 + 3C_3\tilde{\sigma}^2 + C_5}{D_1\tilde{\sigma}^8 + D_2\tilde{\sigma}^6 + D_3\tilde{\sigma}^4 + D_4\tilde{\sigma}^2 + D_5} - \frac{\left(C_1\tilde{\sigma}^5 + C_3\tilde{\sigma}^3 + C_5\tilde{\sigma}\right)\left(8D_1\tilde{\sigma}^7 + 6D_2\tilde{\sigma}^5 + 4D_3\tilde{\sigma}^3 + 2D_4\tilde{\sigma}\right)}{\left(D_1\tilde{\sigma}^8 + D_2\tilde{\sigma}^6 + D_3\tilde{\sigma}^4 + D_4\tilde{\sigma}^2 + D_5\right)^2} \right], \tag{3.118}$$

for which the roots satisfy:

$$\begin{aligned} 0 = {} & (-3C_1D_1)\,\tilde{\sigma}^{12} + (-C_1D_2 - 5C_3D_1)\,\tilde{\sigma}^{10} + (C_1D_3 - 3C_3D_2 - 7C_5D_1)\,\tilde{\sigma}^8 \\ & + (3C_1D_4 - C_3D_3 - 5C_5D_2)\,\tilde{\sigma}^6 + (5C_1D_5 + C_3D_4 - 3C_5D_3)\,\tilde{\sigma}^4 \\ & + (3C_3D_5 - C_5D_4)\,\tilde{\sigma}^2 + C_5D_5. \end{aligned} \tag{3.119}$$

As we are considering a planet rotating near synchronization with a strongly dissipative atmosphere, we take the lowest order terms in $\tilde{\sigma}$ to approximate the position of the

near-synchronization peak $\sigma_{\rm NSP}$ by the closed form solution:

$$\begin{aligned}\sigma_{\rm NSP} &= \sigma_0 \left(\frac{C_5 D_5}{C_5 D_4 - 3 C_3 D_5} \right)^{1/2} \\ &= \frac{\sigma_0 (b_{\rm J} - \kappa)}{\sqrt{(b_{\rm J} - \kappa)^2 \left[1 + 2\beta(1-\kappa)\right] - 2 b_{\rm J}^2}}.\end{aligned} \tag{3.120}$$

With $\sigma_{\rm NSP}$ defined also as semi-diurnal tidal frequency, we plot in Figure 3.10 the rotational period of the planet at which the thermal peak is encountered as a function of σ_0, for different values the planetary semi-major axis. First, we note the obvious, that with increasing σ_0 the thermal peak diminishes in amplitude. With increasing dissipation also, the position of the peak shifts towards lower rotational periods (higher spin rates), such that planets at different semi-major axes share the same peak. Allowing σ_0 to approach moderate values ($10^{-6} \sim 10^{-7}$ s^{-1}), a regime transition is encountered where the position of the peak shifts towards higher rotational periods and its amplitude grows to $\sim 10^3$ Pa. We note here that the inferred value of $\sigma_0 = 7.5 \times 10^{-7}$ via GCM simulations falls within this regime Leconte et al. (2015). Decreasing σ_0 further, the spectral position of the peak approaches synchronization.

3.4 Summary

In this chapter, we revisited the tempting hypothesis of the Earth encountering a rotational equilibrium in the geological past. The occurrence of this equilibrium is contingent upon the passage through an enhanced resonance in the thermal tide such that its associated torque is opposite in sign and comparable in magnitude to the gravitational counterpart in the mantle and the oceans. The opposing effects of the tidal bulges can then cancel out each other and the Earth would enter an eon of fixed length-of-day (LOD) associated with a zero tidal torque phase. The equilibrium was first studied by Zahnle and Walker (1987), then its stability against thermal fluctuations was tested more recently in Bartlett and Stevenson (2016). The occurrence of such a scenario has significant implications on paleooclimatic and ecosystem studies, with growing evidence on links between the evolving length-of-day and the evolution of Precambrian benthic life (e.g., Klatt et al., 2021).

Our motivation to revisit the hypothesis is based on an evident mismatch between certain geological proxies used to infer the past LOD, and the predicted LOD evolution

if the equilibrium scenario is surmised. After elucidating the possible reasons behind this mismatch, we proceeded to explore a single explanation: the thermal – also read Lamb – resonance either did not occur in the direction opposing the gravitational tide, or it did occur but with an amplitude that is insufficient to cancel the opposing torque. We pursued this scenario driven by the thermal tide spectrum established in Auclair-Desrotour et al. (2019b). The latter work is the first, and to-date the only work that managed to retrieve the planetary thermal tidal response using GCM simulations. The unfortunate news delivered from these GCM results to the equilibrium hypothesis is the absence of the resonant tidal peak required to accelerate the Earth's rotation. While further and more rigorous numerical exploration is required to predicate this surprising result, we attempted in this chapter to understand it from an analytical perspective.

Having convinced ourselves of the significant implications this hypothesis holds, we worked with the primitive equations of atmospheric dynamics. We developed a handy tidal model that allows for radiative cooling, but more importantly it accommodates the delayed thermal response of the ground. The two mechanisms entered our model parameterized by two effective parameters. The delayed response of the ground proved to be a possible suspect behind the asymmetry of the Lamb resonance observed in the GCM simulations. Our preliminary and fresh numerical implementation of the model suggests that the asymmetry is a robust feature when accounting, as one should, for diffusive mechanisms in the planetary boundary layer. The rotational equilibrium hypothesis of the Earth is thus jeopardized by this asymmetry, although we cannot make more definite quantitative claims at this stage of the work. We anticipate the model to be also useful for tidal evolution studies, especially in exo-planetary settings.

CHAPTER 4

CONCLUSIONS AND OUTLOOK

In this thesis work, we addressed a variety of geophysical phenomena that are germane to the long term dynamical evolution of the Earth-Moon system. The global picture is to enhance our understanding of and better retrieve the complex dynamical history of the system.

Focusing on the past evolution of the axial precession of the Earth, we provided a constrained contribution of the Cenozoic glacial cycles to the Earth's dynamical ellipticity. This constrained history will be used in the future long term numerical solutions for the orbital and rotational quantities of the Earth, entering through the time-dependent variation of the precession "constant" (Laskar et al., 2004, 2011a). Besides providing the evolution time-series, our model prediction of the surface loading effect precludes, when considered alone, the possibility of a past crossing of resonance with Jupiter and Saturn through the $s_6 - g_6 + g_5$ mode. However, along with surface loading, redistribution of mass within the Earth due to mantle convection also contributes to the evolution of the dynamical ellipticity, perhaps dominating its evolution over the long timescale. Such a contribution is also dependent on the viscosity profile. At present, different methods of recovering the past mantle flow yielded vastly different results, albeit using the same viscosity profile (e.g., Forte and Mitrovica, 1997; Morrow et al., 2012; Ghelichkhan et al., 2020). Moreover, the backward tidal evolution of the Earth's rotational velocity counteracts the effect of the dynamical ellipticity variation, driving the precession frequency away from this resonance. Thus a thorough and realistic study of the past evolution of the precession frequency and the occurrence of such a resonance requires a self consistent model that combines all three elements, leaving us with the need for more effort in this direction. Finally, while we focused on the symmetric second zonal harmonic of the geopotential, namely the c_{20} Stokes' coefficient, it is straightforward to extend our simulations to retrieve the other harmonics. The latter are required to compute a history of the Cenozoic true polar wander.

Next, we revisited the classic time-scale problem of the lunar origin. The problem was originally postulated in tidal models focused on bodily solid tides. However, it is well established now that this approach is obsolete, as the tidal response is dominated by oceanic tides which feature a completely differed dissipation spectrum. We thus addressed the following question: Can we develop a model based on the linear analytical theory of fluid tides, with a minimum number of free parameters, that can evade the time-scale problem? It turns out we can. In our constructed model, we coupled oceanic dissipation with solid Earth deformation, along with solid Earth dissipation when called for. The model also took into account, mimetically, the effect of continental drift and plate tectonic evolution. Our end result is, to our knowledge, the first modelled history of the Earth-Moon distance that fits both the present state of the system and the lunar formation age. Perhaps surprisingly, this modelled history was also in good agreement with the geological data, though we intentionally decided to be agnostic of the data when constructing the model.

While this result satisfactorily addresses the time-scale problem, we aim in the future to build on it and allow for other physical ingredients:

i) From a tidal perspective, we have only considered the predominant semi-diurnal luni-solar tidal constituents. However, it is straightforward to aim for a comprehensive tidal interplay by accounting for the other constituents (Williams and Boggs, 2016).

ii) From a modelling perspective, we argued for the spin rate of the Earth as the dominant regulator of tidal dissipation. However, as we have shown, the varying oceanic geometry also has its signature on the tidal spectrum. While we tried to take this effect into account by allowing for a hemispheric continental cap, we might still have undersampled the intricately varying continental configuration over geological timescales. Changing the oceanic domain on the sphere in the simple version we offered has already presented serious analytical and computational challenges in computing the tidal response. However, it is certainly worthy to develop a model of oceanic tides where the oceanic domain is not constrained to the hemisphere, but rather can be defined over any surface domain on the sphere. We have already taken steps in this direction and shall describe the theory in a forthcoming work. Such a model upgrade will allow us to actually follow the history of the continental formation and evolution smoothly, rather than switching between a hemispheric and a global oceanic configuration.

iii) Also from a modelling perspective, we have fixed the fitted free parameters over the Earth's lifetime. While this might be justified for the linear drag frequency as we argued in the main text, we are faced with growing evidence on the variation of oceanic volume with geologic time (e.g., Korenaga, 2013, 2018; Dong et al., 2021). It might thus be necessary to examine the sensitivity of the modelled history to uncertainties in the oceanic volume. We already know the effect of the volume on the spectrum: it will slightly vary the resonance amplitudes while shifting their spectral positions. That said, variations in water volume could be important during the relatively short time intervals spanned by resonant states. Another source of uncertainty emerges from the interplay between the possible presence of ice cap and oceanic tides. Ice caps accumulation and disintegration affect the water volume and increase the area of continental shelves. While their periodic effects can be averaged-out over the long tidal time-scale, severe glaciation episodes, such as those encountered in a snowball Earth scenario, may still leave their signature (Wunsch, 2016).

iv) From a dynamical perspective, we have adopted a reduced dynamical model where we focused on the polar component of the torque and its associated angular momentum exchange, all the while ignoring obliquity and eccentricity tides in the system. This may very well be justified as we are merely concerned with the time-scale problem. However, allowing for these components provides a critical opportunity of matching our backward integration predictions with forward integrations where more complex dynamical mechanisms are encountered (Touma and Wisdom, 1998). Such experiments can help us in our quest of constraining lunar formation scenarios and the resulting inclination problem. Namely, forward integrations that do not match the backward counterpart can help eliminate impact scenarios that produce the corresponding initial conditions. Furthermore, generalizing to triaxiality will allow us to test fundamental dynamical features of the system such as the vertical angular momentum constraint suggested by Tian and Wisdom (2020).

v) Also within the realm of dynamics, we shall next allow for lunar tides. Solid-body tidal dissipation within the Moon have also affected the evolution of the system. However, since the Moon is at present tidally locked into synchronous rotation, its semi-diurnal tide is characterized by zero frequency. The largest periodic tides on the moon are monthly, and they are associated with lunar eccentricity and obliquity (e.g., Williams and Boggs, 2015; Daher et al., 2021). Due to its

synchronous rotation, energy dissipation within the Moon should reduce its semi-major axis, opposing the dominant effect of terrestrial tides. As we argued in the main text, we ignored this effect because it is about 0.03% of the total tidal energy dissipation rate (e.g., Daher et al., 2021), and it gets significant only in the earliest times. However, we shall account for this effect if we plan to match our modelled history with post-impact predictions.

Furthermore, allowing for lunar tides will give us the opportunity to revisit lunar spin dynamics. A particular scenario of interest is the lunar spin axis Cassini state transition around 33 $R_{\rm E}$ (Peale and Cassen, 1978; Ward, 1975). This transition involves an amplified forced obliquity that enhances obliquity tides, feeding back into the tidal evolution. It furthermore plays an important role in the thermal history, and consequently the surface morphology of the Moon Wisdom (2006).

Though it seems compelling to expand our tidal evolution model to accommodate these elements, it will be difficult to decide what ingredient falls next in the hierarchy of contributions. Our initial hunch, supported by preliminary exploration, suggests that thermal tides are our runner up. This was the focus of Chapter 3. There we predicated that idealized models established earlier and utilized to suggest a fixed Precambrian day length should be abandoned. We attempted a cautious incursion on establishing a rudimentary model that provides the thermal tidal spectrum of a rocky planet. While we have not yet applied this model to the tidal evolution of the Earth, we successfully managed to benchmark it against the results of earlier GCM simulations. The key result of this model is that when we account for the thermal response of the ground, which lags the thermal forcing and shifts the thermal tidal bulge, the high-frequency Lamb resonance features an asymmetry. The latter is such that the peak of the tidal torque required for the rotational equilibrium of the Earth, which is present in idealized models, diminishes in our model and may even vanish completely. However, even if this thermal tidal peak, which opposes the effect of gravitational tides, is completely absent, its opposite peak is still present, and may be comparable in magnitude to Precambrian oceanic tides. It would then be necessary to account for thermal tides in the Earth's tidal evolution history. Finally, though this was our first foray into the problem, the analytical model we developed provides a physical description of multiple intervening players, and it can be easily implemented in other solar and extra-solar settings. A more rigorous attempt pertaining to the Earth's history, however, may very well require an armada of GCM simulations.

BIBLIOGRAPHY

Abe M., Mizutani H., Ooe M.: Influence of continental drift on the tidal evolution of the earth-moon system. In: Comparative Planetology, Geological Education, History of Geology: Proceedings of the 30th International Geological Congress, Beijing, China, 4-14 August 1996, VSP, vol **26**, pp 1–29 (1997)

Abramowitz M., Stegun I. A., Romer R. H.: Handbook of mathematical functions with formulas, graphs, and mathematical tables (1988)

Adhikari S., Ivins E. R., Larour E.: Issm-sesaw v1. 0: Mesh-based computation of gravitationally consistent sea-level and geodetic signatures caused by cryosphere and climate driven mass change. Geoscientific Model Development **9**(3), 1087–1109 (2016)

Adhikari S., Caron L., Steinberger B., Reager J. T., Kjeldsen K. K., Marzeion B., Larour E., Ivins E. R.: What drives 20th century polar motion? Earth and Planetary Science Letters **502**, 126–132 (2018)

Alcott L. J., Mills B. J., Poulton S. W.: Stepwise earth oxygenation is an inherent property of global biogeochemical cycling. Science **366**(6471), 1333–1337 (2019)

Amante C., Eakins B. W.: Etopo1 arc-minute global relief model: procedures, data sources and analysis. NOAA Technical Memorandum NESDIS NGDC-24 (2009)

Andrade E. N. D. C.: On the viscous flow in metals, and allied phenomena. Proceedings of the Royal Society of London Series A, Containing Papers of a Mathematical and Physical Character **84**(567), 1–12 (1910)

Antonov J., Levitus S., Boyer T.: Thermosteric sea level rise, 1955–2003. Geophysical Research Letters **32**(12) (2005)

Arbic B. K., Garrett C.: A coupled oscillator model of shelf and ocean tides. Continental Shelf Research **30**(6), 564–574 (2010)

Arbic B. K., Karsten R. H., Garrett C.: On tidal resonance in the global ocean and the back-effect of coastal tides upon open-ocean tides. Atmosphere-Ocean **47**(4), 239–266 (2009)

Arfken G. B., Weber H. J.: Mathematical methods for physicists (1999)

Argus D. F., Gross R. S.: An estimate of motion between the spin axis and the hotspots over the past century. Geophysical research letters **31**(6) (2004)

Argus D. F., Peltier W. R., Blewitt G., Kreemer C.: The viscosity of the top third of the lower mantle estimated using gps, grace, and relative sea level measurements of glacial isostatic adjustment. Journal of Geophysical Research: Solid Earth **126**(5), e2020JB021,537 (2021)

Arras P., Socrates A.: Thermal tides in fluid extrasolar planets. The Astrophysical Journal **714**(1), 1 (2010)

Artemieva I. M.: Global 1× 1 thermal model tc1 for the continental lithosphere: implications for lithosphere secular evolution. Tectonophysics **416**(1-4), 245–277 (2006)

Auclair-Desrotour P.: Dissipation des marées thermiques atmosphériques dans les super-terres. PhD thesis, Université Paris sciences et lettres (2016)

Auclair-Desrotour P., Leconte J.: Semidiurnal thermal tides in asynchronously rotating hot jupiters. Astronomy & Astrophysics **613**, A45 (2018)

Auclair-Desrotour P., Le Poncin-Lafitte C., Mathis S.: Impact of the frequency dependence of tidal q on the evolution of planetary systems. Astronomy & Astrophysics **561**, L7 (2014)

Auclair-Desrotour P., Mathis S., Le Poncin-Lafitte C.: Scaling laws to understand tidal dissipation in fluid planetary regions and stars i. rotation, stratification and thermal diffusivity. Astronomy & Astrophysics **581**, A118 (2015)

Auclair-Desrotour P., Laskar J., Mathis S.: Atmospheric tides in earth-like planets. Astronomy & Astrophysics **603**, A107 (2017a)

Auclair-Desrotour P., Laskar J., Mathis S., Correia A.: The rotation of planets hosting atmospheric tides: from venus to habitable super-earths. Astronomy & Astrophysics **603**, A108 (2017b)

Auclair-Desrotour P., Mathis S., Laskar J., Leconte J.: Oceanic tides from earth-like to ocean planets. Astronomy & Astrophysics **615**, A23 (2018)

Auclair-Desrotour P., Leconte J., Bolmont E., Mathis S.: Final spin states of eccentric ocean planets. Astronomy & Astrophysics **629**, A132 (2019a)

Auclair-Desrotour P., Leconte J., Mergny C.: Generic frequency dependence for the atmospheric tidal torque of terrestrial planets. Astronomy & Astrophysics **624**, A17 (2019b)

Austermann J., Mitrovica J. X., Latychev K., Milne G. A.: Barbados-based estimate of ice volume at last glacial maximum affected by subducted plate. Nature Geoscience **6**(7), 553–557 (2013)

de Azarevich V. L. L., Azarevich M. B.: Lunar recession encoded in tidal rhythmites: a selective overview with examples from argentina. Geo-Marine Letters **37**(4), 333–344 (2017)

Bailey I., Hole G. M., Foster G. L., Wilson P. A., Storey C. D., Trueman C. N., Raymo M. E.: An alternative suggestion for the pliocene onset of major northern hemisphere glaciation based on the geochemical provenance of north atlantic ocean ice-rafted debris. Quaternary Science Reviews **75**, 181–194 (2013)

Baldwin R. B.: A fundamental survey of the moon (1965)

Barboni M., Boehnke P., Keller B., Kohl I. E., Schoene B., Young E. D., McKeegan K. D.: Early formation of the moon 4.51 billion years ago. Science advances **3**(1), e1602,365 (2017)

Bart P. J.: Were west antarctic ice sheet grounding events in the ross sea a consequence of east antarctic ice sheet expansion during the middle miocene? Earth and Planetary Science Letters **216**(1-2), 93–107 (2003)

Bartek L., Sloan L. C., Anderson J., Ross M.: Evidence from the antarctic continental margin of late paleogene ice sheets: A manifestation of plate reorganization and synchronous changes in atmospheric circulation over the emerging southern ocean. Eocene-Oligocene climatic and biotic evolution Princeton Univ Press, Princeton, NJ , 131–159 (1992)

Bartlett B. C., Stevenson D. J.: Analysis of a precambrian resonance-stabilized day length. Geophysical Research Letters **43**(11), 5716–5724 (2016)

Bell Jr T.: Topographically generated internal waves in the open ocean. Journal of Geophysical Research **80**(3), 320–327 (1975)

Benz W., Slattery W., Cameron A.: The origin of the moon and the single-impact hypothesis i. Icarus **66**(3), 515–535 (1986)

Berger A.: Milankovitch theory and climate. Reviews of geophysics **26**(4), 624–657 (1988)

Best N., Havens R., LaGow H.: Pressure and temperature of the atmosphere to 120 km. Physical Review **71**(12), 915 (1947)

Bindeman I., Zakharov D., Palandri J., Greber N. D., Dauphas N., Retallack G., Hofmann A., Lackey J., Bekker A.: Rapid emergence of subaerial landmasses and onset of a modern hydrologic cycle 2.5 billion years ago. Nature **557**(7706), 545–548 (2018)

Bindoff N. L., Willebrand J., Artale V., Cazenave A., Gregory J. M., Gulev S., Hanawa K., Le Quere C., Levitus S., Nojiri Y., et al.: Observations: oceanic climate change and sea level. Cambridge University Press (2007)

Biot M. A.: Theory of deformation of a porous viscoelastic anisotropic solid. Journal of Applied physics **27**(5), 459–467 (1956)

Boas M. L.: Mathematical methods in the physical sciences. John Wiley & Sons (2006)

Bolmont E., Breton S. N., Tobie G., Dumoulin C., Mathis S., Grasset O.: Solid tidal friction in multi-layer planets: Application to earth, venus, a super earth and the trappist-1 planets-potential approximation of a multi-layer planet as a homogeneous body. Astronomy & Astrophysics **644**, A165 (2020)

Boué G., Laskar J.: Precession of a planet with a satellite. Icarus **185**(2), 312–330 (2006)

Boulila S., Galbrun B., Miller K. G., Pekar S. F., Browning J. V., Laskar J., Wright J. D.: On the origin of cenozoic and mesozoic "third-order" eustatic sequences. Earth-Science Reviews **109**(3-4), 94–112 (2011)

Boulila S., Laskar J., Haq B. U., Galbrun B., Hara N.: Long-term cyclicities in phanerozoic sea-level sedimentary record and their potential drivers. Global and Planetary Change **165**, 128–136 (2018)

Boyden J. A., Müller R. D., Gurnis M., Torsvik T. H., Clark J. A., Turner M., Ivey-Law H., Watson R. J., Cannon J. S.: Next-generation plate-tectonic reconstructions using GPlates. Cambridge University Press (2011)

Brosche P., Sündermann J.: Tidal friction and dynamics of the earth-moon system. Landolt-B6mstein (ed), Neue Serie, B **2**, 288–310 (1984)

Burša M., Groten E., Šíma Z.: Steady change in flattening of the earth: the precession constant and its long-term variation. The Astronomical Journal **135**(3), 1021 (2008)

Cambiotti G., Barletta V. R., Bordoni A., Sabadini R.: A comparative analysis of the solutions for a maxwell earth: the role of the advection and buoyancy force. Geophysical Journal International **176**(3), 995–1006 (2009)

Cambiotti G., Ricard Y., Sabadini R.: Ice age true polar wander in a compressible and non-hydrostatic earth. Geophysical Journal International **183**(3), 1248–1264 (2010)

Cameron A.: The origin of the moon and the single impact hypothesis v. Icarus **126**(1), 126–137 (1997)

Cameron A.: From interstellar gas to the earth-moon system. Meteoritics & Planetary Science **36**(1), 9–22 (2001)

Canup R. M.: Simulations of a late lunar-forming impact. Icarus **168**(2), 433–456 (2004)

Canup R. M., Asphaug E.: Origin of the moon in a giant impact near the end of the earth's formation. Nature **412**(6848), 708–712 (2001)

Canup R. M., Visscher C., Salmon J., Fegley Jr B.: Lunar volatile depletion due to incomplete accretion within an impact-generated disk. Nature geoscience **8**(12), 918–921 (2015)

Carter G. S., Merrifield M., Becker J. M., Katsumata K., Gregg M., Luther D., Levine M., Boyd T. J., Firing Y.: Energetics of m 2 barotropic-to-baroclinic tidal conversion at the hawaiian islands. Journal of Physical Oceanography **38**(10), 2205–2223 (2008)

Cartwright D. E.: Oceanic tides. Reports on Progress in Physics **40**(6), 665 (1977)

Castelnau O., Duval P., Montagnat M., Brenner R.: Elastoviscoplastic micromechanical modeling of the transient creep of ice. Journal of Geophysical Research (Solid Earth) **113**(B11):B11203 (2008)

Castillo-Rogez J. C., Efroimsky M., Lainey V.: The tidal history of Iapetus: Spin dynamics in the light of a refined dissipation model. Journal of Geophysical Research (Planets) **116**(E9):E09008 (2011)

Cazenave A., Llovel W.: Contemporary sea level rise. Annual review of marine science **2**(1), 145–173 (2010)

Chambat F., Ricard Y., Valette B.: Flattening of the earth: further from hydrostaticity than previously estimated. Geophysical Journal International **183**(2), 727–732 (2010)

Chao B., Yu Y., Chung C.: Variation of earth's oblateness j2 on interannual-to-decadal timescales. Journal of Geophysical Research: Solid Earth **125**(6), e2020JB019,421 (2020)

Chapman S., Lindzen R. S.: Atmospheric tides: thermal and gravitational, vol **15**. Springer Science & Business Media (1969)

Chen E. M. A., Nimmo F.: Tidal dissipation in the lunar magma ocean and its effect on the early evolution of the Earth-Moon system. Icarus **275**, 132–142 (2016)

Chen H., Leinenweber K., Prakapenka V., Prescher C., Meng Y., Bechtel H., Kunz M., Shim S.-H.: Possible h2o storage in the crystal structure of casio3 perovskite. Physics of the Earth and Planetary Interiors **299**, 106,412 (2020)

Cheng M., Eanes R., Shum C., Schutz B., Tapley B.: Temporal variations in low degree zonal harmonics from starlette orbit analysis. Geophysical Research Letters **16**(5), 393–396 (1989)

Cheng M., Tapley B. D., Ries J. C.: Deceleration in the earth's oblateness. Journal of Geophysical Research: Solid Earth **118**(2), 740–747 (2013)

Church J. A., White N. J., Konikow L. F., Domingues C. M., Cogley J. G., Rignot E., Gregory J. M., van den Broeke M. R., Monaghan A. J., Velicogna I.: Revisiting the earth's sea-level and energy budgets from 1961 to 2008. Geophysical Research Letters **38**(18) (2011)

Clark J. A., Farrell W. E., Peltier W. R.: Global changes in postglacial sea level: a numerical calculation. Quaternary research **9**(3), 265–287 (1978)

Cleveland W. S., Devlin S. J.: Locally weighted regression: an approach to regression analysis by local fitting. Journal of the American statistical association **83**(403), 596–610 (1988)

Condie K. C., Aster R. C.: Episodic zircon age spectra of orogenic granitoids: the supercontinent connection and continental growth. Precambrian Research **180**(3-4), 227–236 (2010)

Conrad C. P.: The solid earth's influence on sea level. Bulletin **125**(7-8), 1027–1052 (2013)

Cook C. P., Van De Flierdt T., Williams T., Hemming S. R., Iwai M., Kobayashi M., Jimenez-Espejo F. J., Escutia C., González J. J., Khim B.-K., et al.: Dynamic behaviour of the east antarctic ice sheet during pliocene warmth. Nature Geoscience **6**(9), 765–769 (2013)

Correia A., Laskar J.: The four final rotation states of venus. Nature **411**(6839), 767–770 (2001)

Correia A. C., Laskar J.: Different tidal torques on a planet with a dense atmosphere and consequences to the spin dynamics. Journal of Geophysical Research: Planets **108**(E11) (2003a)

Correia A. C., Laskar J.: Long-term evolution of the spin of venus: Ii. numerical simulations. Icarus **163**(1), 24–45 (2003b)

Correia A. C., Laskar J., de Surgy O. N.: Long-term evolution of the spin of venus: I. theory. Icarus **163**(1), 1–23 (2003)

Correia A. C., Boué G., Laskar J., Rodríguez A.: Deformation and tidal evolution of close-in planets and satellites using a maxwell viscoelastic rheology. Astronomy & Astrophysics **571**, A50 (2014)

Correia A. C. M., Laskar J. (2010) Tidal Evolution of Exoplanets. In: Exoplanets, Tucson, AZ: University of Arizona Press, pp 239–266, URL http://adsabs.harvard.edu/abs/2010exop.book..239C

Cowling T. G.: The non-radial oscillations of polytropic stars. Monthly Notices of the Royal Astronomical Society **101**, 367 (1941)

Cox C. M., Chao B. F.: Detection of a large-scale mass redistribution in the terrestrial system since 1998. Science **297**(5582), 831–833 (2002)

Coxall H. K., Wilson P. A., Pälike H., Lear C. H., Backman J.: Rapid stepwise onset of antarctic glaciation and deeper calcite compensation in the pacific ocean. Nature **433**(7021), 53–57 (2005)

Cramer B., Miller K., Barrett P., Wright J.: Late cretaceous–neogene trends in deep ocean temperature and continental ice volume: Reconciling records of benthic foraminiferal geochemistry (δ18o and mg/ca) with sea level history. Journal of Geophysical Research: Oceans **116**(C12) (2011)

Crease J.: Tables of the integral. $\int p_n^m(z)p_r^s(z)dz$ (1966)

Ćuk M., Stewart S. T.: Making the moon from a fast-spinning earth: A giant impact followed by resonant despinning. science **338**(6110), 1047–1052 (2012)

Ćuk M., Hamilton D. P., Lock S. J., Stewart S. T.: Tidal evolution of the Moon from a high-obliquity, high-angular-momentum Earth. Nature **539**(7629), 402–406 (2016)

Cummings W. D.: Evolving Theories on the Origin of the Moon. Springer (2019)

Cunha D., Correia A. C., Laskar J.: Spin evolution of earth-sized exoplanets, including atmospheric tides and core–mantle friction. International Journal of Astrobiology **14**(2), 233–254 (2015)

Daher H., Arbic B. K., Williams J. G., Ansong J. K., Boggs D. H., Müller M., Schindelegger M., Austermann J., Cornuelle B. D., Crawford E. B., et al.: Long-term earth-moon evolution with high-level orbit and ocean tide models. Journal of Geophysical Research: Planets **126**(12), e2021JE006,875 (2021)

Dahlen F., Smith M.: The influence of rotation on the free oscillations of the earth. Philosophical Transactions of the Royal Society of London Series A, Mathematical and Physical Sciences **279**(1292), 583–624 (1975)

Dalca A., Ferrier K., Mitrovica J., Perron J., Milne G., Creveling J.: On postglacial sea level—iii. incorporating sediment redistribution. Geophysical Journal International **194**(1), 45–60 (2013)

Daly R. A.: Pleistocene changes of level. American Journal of Science **10**(58), 281–313 (1925)

Daly R. A.: Origin of the moon and its topography. Proceedings of the American Philosophical Society **90**(2), 104–119 (1946)

Darwin G. H.: Xiii. on the precession of a viscous spheroid, and on the remote history of the earth. Philosophical Transactions of the Royal Society of London (170), 447–538 (1879)

De Vleeschouwer D., Vahlenkamp M., Crucifix M., Pälike H.: Alternating southern and northern hemisphere climate response to astronomical forcing during the past 35 my. Geology **45**(4), 375–378 (2017)

DeConto R. M., Pollard D.: Rapid cenozoic glaciation of antarctica induced by declining atmospheric co 2. Nature **421**(6920), 245–249 (2003)

Dehant V., Loutre M.-F., Berger A.: Potential impact of the northern hemisphere quaternary ice sheets on the frequencies of the astroclimatic orbital parameters. Journal of Geophysical Research: Atmospheres **95**(D6), 7573–7578 (1990)

Deland R.: The vertical structure of planetary-scale rossby waves. Quarterly Journal of the Royal Meteorological Society **96**(410), 756–757 (1970)

Denis C., Rybicki K., Schreider A., Tomecka-Suchoń S., Varga P.: Length of the day and evolution of the earth's core in the geological past. Astronomische Nachrichten **332**(1), 24–35 (2011)

Dhuime B., Hawkesworth C. J., Cawood P. A., Storey C. D.: A change in the geodynamics of continental growth 3 billion years ago. Science **335**(6074), 1334–1336 (2012)

Dickey J. O., Bender P., Faller J., Newhall X., Ricklefs R., Ries J., Shelus P., Veillet C., Whipple A., Wiant J., et al.: Lunar laser ranging: a continuing legacy of the apollo program. Science **265**(5171), 482–490 (1994)

Dickey J. O., Marcus S. L., de Viron O., Fukumori I.: Recent earth oblateness variations: Unraveling climate and postglacial rebound effects. Science **298**(5600), 1975–1977 (2002)

Dickman S.: Investigation of controversial polar motion features using homogeneous international latitude service data. Journal of Geophysical Research: Solid Earth **86**(B6), 4904–4912 (1981)

Dobrovolskis A. R., Ingersoll A. P.: Atmospheric tides and the rotation of venus i. tidal theory and the balance of torques. Icarus **41**(1), 1–17 (1980)

Dong J., Fischer R. A., Stixrude L. P., Lithgow-Bertelloni C. R.: Constraining the volume of earth's early oceans with a temperature-dependent mantle water storage capacity model. AGU Advances **2**(1), e2020AV000,323 (2021)

Dong S.-H., Lemus R.: The overlap integral of three associated legendre polynomials. Applied mathematics letters **15**(5), 541–546 (2002)

Doodson A. T. (1958) Oceanic tides. In: Advances in geophysics, vol **5**, Elsevier, pp 117–152

Douglas B. C.: Global sea level rise. Journal of Geophysical Research: Oceans **96**(C4), 6981–6992 (1991)

Douglas B. C.: Global sea rise: a redetermination. Surveys in Geophysics **18**(2), 279–292 (1997)

Downey B. G., Nimmo F., Matsuyama I.: The thermal-orbital evolution of the Earth-Moon system with a subsurface magma ocean and fossil figure. arXiv e-prints :arXiv:2209.00935 (2022)

Duan P., Huang C.: Intradecadal variations in length of day and their correspondence with geomagnetic jerks. Nature communications **11**(1), 1–8 (2020)

Duplessy J.-C., Labeyrie L., Waelbroeck C.: Constraints on the ocean oxygen isotopic enrichment between the last glacial maximum and the holocene: Paleoceanographic implications. Quaternary Science Reviews **21**(1-3), 315–330 (2002)

Dutton A., Carlson A. E., Long A., Milne G. A., Clark P. U., DeConto R., Horton B. P., Rahmstorf S., Raymo M. E.: Sea-level rise due to polar ice-sheet mass loss during past warm periods. science **349**(6244) (2015)

Dziewonski A. M., Anderson D. L.: Preliminary reference earth model. Physics of the earth and planetary interiors **25**(4), 297–356 (1981)

Efroimsky M.: Tidal dissipation compared to seismic dissipation: In small bodies, earths, and super-earths. The Astrophysical Journal **746**(2), 150 (2012)

Efroimsky M., Makarov V. V.: Tidal friction and tidal lagging. applicability limitations of a popular formula for the tidal torque. The Astrophysical Journal **764**(1), 26 (2013)

Efroimsky M., Williams J. G.: Tidal torques: a critical review of some techniques. Celestial Mechanics and Dynamical Astronomy **104**(3), 257–289 (2009)

Egbert G., Ray R.: Significant dissipation of tidal energy in the deep ocean inferred from satellite altimeter data. Nature **405**(6788), 775–778 (2000)

Egbert G. D., Ray R. D.: Semi-diurnal and diurnal tidal dissipation from TOPEX/Poseidon altimetry. Geophysical Research Letters **30**(17):1907 (2003)

Egbert G. D., Bennett A. F., Foreman M. G.: Topex/poseidon tides estimated using a global inverse model. Journal of Geophysical Research: Oceans **99**(C12), 24,821–24,852 (1994)

Egbert G. D., Ray R. D., Bills B. G.: Numerical modeling of the global semidiurnal tide in the present day and in the last glacial maximum. Journal of Geophysical Research: Oceans **109**(C3) (2004)

Eldrett J. S., Harding I. C., Wilson P. A., Butler E., Roberts A. P.: Continental ice in greenland during the eocene and oligocene. Nature **446**(7132), 176–179 (2007)

Emiliani C.: Temperatures of pacific bottom waters and polar superficial waters during the tertiary. Science **119**(3103), 853–855 (1954)

Emiliani C.: The temperature decrease of surface sea-water in high latitudes and of abyssal-hadal water in open oceanic basins during the past 75 million years. Deep Sea Research (1953) **8**(2), 144–147 (1961)

Eriksson K.: Tidal deposits from the archaean moodies group, barberton mountain land, south africa. Sedimentary Geology **18**(1-3), 257–281 (1977)

Eriksson K. A., Simpson E. L.: Quantifying the oldest tidal record: the 3.2 ga moodies group, barberton greenstone belt, south africa. Geology **28**(9), 831–834 (2000)

Eulenfeld T., Heubeck C.: Constraints on moon's orbit 3.2 billion years ago from tidal bundle data. arXiv preprint arXiv:220705464 (2022)

Fang J., Wu H., Fang Q., Shi M., Zhang S., Yang T., Li H., Cao L.: Cyclostratigraphy of the global stratotype section and point (GSSP) of the basal Guzhangian Stage of the Cambrian Period. Palaeogeography, Palaeoclimatology, Palaeoecology **540**, 109,530, URL https://www.sciencedirect.com/science/article/pii/S0031018219300057 (2020)

Farhat M., Auclair-Desrotour P., Boué G., Laskar J.: The resonant tidal evolution of the earth-moon distance. Astronomy & Astrophysics **665**, L1 (2022a)

Farhat M., Laskar J., Boué G.: Constraining the earth's dynamical ellipticity from ice age dynamics. Journal of Geophysical Research: Solid Earth **127**(5), e2021JB023,323 (2022b)

Farhat M. A., Touma J. R.: Laplace surface dynamics, revisited: satellites, exoplanets, and debris with distant, eccentric companions. Monthly Notices of the Royal Astronomical Society **507**(4), 6078–6093 (2021)

Farrell W.: Deformation of the earth by surface loads. Reviews of Geophysics **10**(3), 761–797 (1972)

Farrell W., Clark J. A.: On postglacial sea level. Geophysical Journal International **46**(3), 647–667 (1976)

Fienga A., Deram P., Di Ruscio A., Viswanathan V., Camargo J. I. B., Bernus L., Gastineau M., Laskar J.: INPOP21a planetary ephemerides. Notes Scientifiques et Techniques de l'Institut de Mécanique Céleste **110** (2021)

Findley W. N., Lai J. S., Onaran K., Christensen R. M.: Creep and Relaxation of Nonlinear Viscoelastic Materials With an Introduction to Linear Viscoelasticity. Journal of Applied Mechanics **44**(2), 364 (1977)

Fisher O.: On the physical cause of the ocean basins. Nature **25**(637), 243–244 (1882)

Forte A., Peltier W., Dziewonski A., Woodward R.: Dynamic surface topography: A new interpretation based upon mantle flow models derived from seismic tomography. Geophysical Research Letters **20**(3), 225–228 (1993)

Forte A., Moucha R., Rowley D., Quéré S., Mitrovica J., Simmons N., Grand S.: Recent tectonic plate decelerations driven by mantle convection. Geophysical research letters **36**(23) (2009)

Forte A. M., Mitrovica J. X.: A resonance in the earth's obliquity and precession overthe past 20 myr drivenbymantle convection. Nature **390**(6661), 676–680 (1997)

Fowler A., Ng F.: Glaciers and ice sheets in the climate system. Sliding, drainage and subgaciar geomorphology University of Limerick and University of Oxford Karthaus (2019)

Fox-Kemper B., Ferrari R., Pedlosky J.: On the Indeterminacy of Rotational and Divergent Eddy Fluxes. Journal of Physical Oceanography **33**, 478–483 (2003)

Fretwell P., Pritchard H. D., Vaughan D. G., Bamber J. L., Barrand N. E., Bell R., Bianchi C., Bingham R., Blankenship D. D., Casassa G., et al.: Bedmap2: improved ice bed, surface and thickness datasets for antarctica. The Cryosphere **7**(1), 375–393 (2013)

Galeotti S., DeConto R., Naish T., Stocchi P., Florindo F., Pagani M., Barrett P., Bohaty S. M., Lanci L., Pollard D., et al.: Antarctic ice sheet variability across the eocene-oligocene boundary climate transition. Science **352**(6281), 76–80 (2016)

Garratt J. R.: The atmospheric boundary layer. Earth-Science Reviews **37**(1-2), 89–134 (1994)

Garrett C., Munk W.: The age of the tide and the "q" of the oceans. Deep Sea Research and Oceanographic Abstracts **18**(5), 493–503 (1971)

Gasson E., DeConto R. M., Pollard D.: Modeling the oxygen isotope composition of the antarctic ice sheet and its significance to pliocene sea level. Geology **44**(10), 827–830 (2016a)

Gasson E., DeConto R. M., Pollard D., Levy R. H.: Dynamic antarctic ice sheet during the early to mid-miocene. Proceedings of the National Academy of Sciences **113**(13), 3459–3464 (2016b)

Gasson E. G., Keisling B. A.: The antarctic ice sheet. Oceanography **33**(2), 90–100 (2020)

Gent P. R., McWilliams J. C.: Consistent balanced models in bounded and periodic domains. Dynamics of Atmospheres and Oceans **7**(2), 67–93 (1983)

Gerkema T., Zimmerman J.: An introduction to internal waves. Lecture Notes, Royal NIOZ, Texel **207** (2008)

Gerstenkorn H.: Über gezeitenreibung beim zweikörperproblem. mit 4 textabbildungen. Zeitschrift fur Astrophysik **36**, 245 (1955)

Ghelichkhan S., Fuentes J. J., Hoggard M. J., Richards F. D., Mitrovica J.: The precession constant and its long-term variation. Icarus , 114,172 (2020)

Ghelichkhan S., Fuentes J. J., Hoggard M. J., Richards F. D., Mitrovica J. X.: The precession constant and its long-term variation. Icarus **358**, 114,172 (2021)

Gold T., Soter S.: Atmospheric tides and the resonant rotation of venus. Icarus **11**(3), 356–366 (1969)

Goldreich P.: History of the lunar orbit. Reviews of Geophysics **4**(4), 411–439 (1966)

Goldreich P., Soter S.: Q in the solar system. icarus **5**(1-6), 375–389 (1966)

Gotlib V. Y., Kagan B. A.: A reconstruction of the tides in the paleocean: results of a numerical simulation. Deutsche Hydrografische Zeitschrift **38**(2), 43–67 (1985)

Gradstein F. M., Ogg J. G., Schmitz M., Ogg G.: Geologic Time Scale 2020, vol **2**. Elsevier (2020)

Green J., Huber M., Waltham D., Buzan J., Wells M.: Explicitly modelled deep-time tidal dissipation and its implication for lunar history. Earth and Planetary Science Letters **461**, 46–53 (2017)

Green J. A. M., Huber M.: Tidal dissipation in the early eocene and implications for ocean mixing. Geophysical Research Letters **40**(11), 2707–2713 (2013)

Greene C. A., Gwyther D. E., Blankenship D. D.: Antarctic mapping tools for matlab. Computers & Geosciences **104**, 151–157 (2017)

Greff-Lefftz M.: Length of day variations due to mantle dynamics at geological timescale. Geophysical Journal International **187**(2), 595–612 (2011)

Griffiths S. D., Peltier W. R.: Modeling of polar ocean tides at the last glacial maximum: Amplification, sensitivity, and climatological implications. Journal of Climate **22**(11), 2905–2924 (2009)

Gross R. S.: The excitation of the chandler wobble. Geophysical Research Letters **27**(15), 2329–2332 (2000)

Gu P.-G., Peng D.-K., Yen C.-C.: Modeling the thermal bulge of a hot jupiter with the two-stream approximation. The Astrophysical Journal **887**(2), 228 (2019)

Gulick S. P., Shevenell A. E., Montelli A., Fernandez R., Smith C., Warny S., Bohaty S. M., Sjunneskog C., Leventer A., Frederick B., et al.: Initiation and long-term instability of the east antarctic ice sheet. Nature **552**(7684), 225–229 (2017)

Guo M., Korenaga J.: Argon constraints on the early growth of felsic continental crust. Science advances **6**(21), eaaz6234 (2020)

Gurnis M.: Ridge spreading, subduction, and sea level fluctuations. Science **250**(4983), 970–972 (1990)

Gurnis M., Turner M., Zahirovic S., DiCaprio L., Spasojevic S., Müller R. D., Boyden J., Seton M., Manea V. C., Bower D. J.: Plate tectonic reconstructions with continuously closing plates. Computers & Geosciences **38**(1), 35–42 (2012)

Guzewich S. D., Newman C., de la Torre Juárez M., Wilson R., Lemmon M., Smith M., Kahanpää H., Harri A.-M., et al.: Atmospheric tides in gale crater, mars. Icarus **268**, 37–49 (2016)

Halliday A., Rehkämper M., Lee D.-C., Yi W.: Early evolution of the earth and moon: new constraints from hf-w isotope geochemistry. Earth and Planetary Science Letters **142**(1-2), 75–89 (1996)

Hamano K., Abe Y., Genda H.: Emergence of two types of terrestrial planet on solidification of magma ocean. Nature **497**(7451), 607–610 (2013)

Han L., Huang R. X.: Using the Helmholtz Decomposition to Define the Indian Ocean Meridional Overturning Streamfunction. Journal of Physical Oceanography **50**(3), 679–694 (2020)

Hansen K. S.: Secular effects of oceanic tidal dissipation on the moon's orbit and the earth's rotation. Reviews of Geophysics **20**(3), 457–480 (1982)

Hartmann W. K.: Terrestrial and lunar flux of large meteorites in the last two billion years. Icarus **4**(2), 157–165 (1965)

Hauptvogel D., Pekar S., Pincay V.: Evidence for a heavily glaciated antarctica during the late oligocene "warming"(27.8–24.5 ma): Stable isotope records from odp site 690. Paleoceanography **32**(4), 384–396 (2017)

Hawkesworth C., Cawood P. A., Dhuime B.: The evolution of the continental crust and the onset of plate tectonics. Frontiers in earth science **8** (2020)

Hay C. C., Morrow E., Kopp R. E., Mitrovica J. X.: Estimating the sources of global sea level rise with data assimilation techniques. Proceedings of the National Academy of Sciences **110**(supplement_1), 3692–3699 (2013)

Hays J. D., Pitman W. C.: Lithospheric plate motion, sea level changes and climatic and ecological consequences. Nature **246**(5427), 18–22 (1973)

Heiskanen W. A.: Physical geodesy. Determination of the Geoid from Ground Anomalies **8**, 325–330 (1967)

Hertogen J., Janssens M.-J., Takahashi H., Palme H., Anders E.: Lunar basins and craters-evidence for systematic compositional changes of bombarding population. In: Lunar and Planetary Science Conference Proceedings, vol **8**, pp 17–45 (1977)

Herwartz D., Pack A., Friedrichs B., Bischoff A.: Identification of the giant impactor theia in lunar rocks. Science **344**(6188), 1146–1150 (2014)

Hide R., Birch N., Morrison L., Shea D., White A.: Atmospheric angular momentum fluctuations and changes in the length of the day. Nature **286**(5769), 114–117 (1980)

Hilgen F., Lourens L., Van Dam J., Beu A., Boyes A., Cooper R., Krijgsman W., Ogg J., Piller W., Wilson D. (2012) Chapter 29 - the neogene period. In: Gradstein F. M., Ogg J. G., Schmitz M. D., Ogg G. M. (eds) The Geologic Time Scale, Elsevier, Boston, pp 923–978

Hilgen F. J., Hinnov L. A., Abdul Aziz H., Abels H. A., Batenburg S., Bosmans J. H., de Boer B., Hüsing S. K., Kuiper K. F., Lourens L. J., et al.: Stratigraphic continuity and fragmentary sedimentation: the success of cyclostratigraphy as part of integrated stratigraphy. The Geological Society of London London (2015)

Hinnov L. A. (2018) Cyclostratigraphy and astrochronology in 2018. In: Stratigraphy & Timescales, vol **3**, Elsevier, pp 1–80

Hoang N. H., Mogavero F., Laskar J.: Chaotic diffusion of the fundamental frequencies in the solar system. Astronomy & Astrophysics **654**, A156 (2021)

Holgate S., Woodworth P.: Evidence for enhanced coastal sea level rise during the 1990s. Geophysical research letters **31**(7) (2004)

Holmberg E.: A suggested explanation of the present value of the velocity of rotation of the earth. Geophysical Journal International **6**, 325–330 (1952)

Holme R.: Length of Day Variations, Decadal, Springer Netherlands, Dordrecht, pp 469–470 (2007)

Hough S. S.: On the Application of Harmonic Analysis to the Dynamical Theory of the Tides. Part II: On the General Integration of Laplace's Dynamical Equations. Philosophical Transactions of the Royal Society of London Series A **191**, 139–185 (1898)

Hourdin F., Van P., Forget F., Talagrand O.: Meteorological variability and the annual surface pressure cycle on mars. Journal of the atmospheric sciences **50**(21), 11 (1993)

Hourdin F., Musat I., Bony S., Braconnot P., Codron F., Dufresne J.-L., Fairhead L., Filiberti M.-A., Friedlingstein P., Grandpeix J.-Y., et al.: The lmdz4 general circulation model: climate performance and sensitivity to parametrized physics with emphasis on tropical convection. Climate Dynamics **27**(7), 787–813 (2006)

Huang H., Gao Y., Jones M. M., Tao H., Carroll A. R., Ibarra D. E., Wu H., Wang C.: Astronomical forcing of middle permian terrestrial climate recorded in a large paleolake in northwestern china. Palaeogeography, Palaeoclimatology, Palaeoecology **550**, 109,735 (2020)

Huber B. T., MacLeod K. G., Watkins D. K., Coffin M. F.: The rise and fall of the cretaceous hot greenhouse climate. Global and Planetary Change **167**, 1–23 (2018)

Hut P.: Stability of tidal equilibrium. Astronomy and Astrophysics **92**, 167–170 (1980)

Hut P.: Tidal evolution in close binary systems. Astronomy and Astrophysics **99**, 126–140 (1981)

Ida S., Canup R. M., Stewart G. R.: Lunar accretion from an impact-generated disk. Nature **389**(6649), 353–357 (1997)

Imbrie J., Imbrie K. P.: Ice ages: solving the mystery. Harvard University Press (1986)

Ingersoll A. P., Dobrovolskis A. R.: Venus' rotation and atmospheric tides. Nature **275**(5675), 37–38 (1978)

Ishii M., Kimoto M.: Reevaluation of historical ocean heat content variations with time-varying xbt and mbt depth bias corrections. Journal of Oceanography **65**(3), 287–299 (2009)

Ivins E. R., Sammis C., Yoder C.: Deep mantle viscous structure with prior estimate and satellite constraint. Journal of Geophysical Research: Solid Earth **98**(B3), 4579–4609 (1993)

Jacchia L. G., Kopal Z.: Atmospheric oscillations and the temperature profile of the upper atmosphere. Journal of Atmospheric Sciences **9**(1), 13–23 (1952)

Jault D., Le Mouël J.: Circulation in the liquid core and coupling with the mantle. Advances in Space Research **13**(11), 221–233 (1993)

Jeffery G. B.: Ix. plane stress and plane strain in bipolar co-ordinates. Philosophical Transactions of the Royal Society of London Series A, Containing Papers of a Mathematical or Physical Character **221**(582-593), 265–293 (1921)

Jeffreys H.: The resonance theory of the origin of the moon (second paper). Monthly Notices of the Royal Astronomical Society **91**(1), 169–174 (1930)

Jevrejeva S., Moore J. C., Grinsted A., Woodworth P. L.: Recent global sea level acceleration started over 200 years ago? Geophysical Research Letters **35**(8) (2008)

Johnson B. W., Wing B. A.: Limited archaean continental emergence reflected in an early archaean 18 o-enriched ocean. Nature Geoscience **13**(3), 243–248 (2020)

Kagan B., Maslova N.: A stochastic model of the earth-moon tidal evolution accounting for cyclic variations of resonant properties of the ocean: An asymptotic solution. Earth, Moon, and Planets **66**(2), 173–188 (1994)

Kagan B. A.: Earth—moon tidal evolution: model results and observational evidence. Progress in Oceanography **40**(1-4), 109–124 (1997)

Kaser G., Cogley J., Dyurgerov M., Meier M., Ohmura A.: Mass balance of glaciers and ice caps: consensus estimates for 1961–2004. Geophysical Research Letters **33**(19) (2006)

Kaula W. M.: Tidal dissipation by solid friction and the resulting orbital evolution. Reviews of geophysics **2**(4), 661–685 (1964)

Kaula W. M.: An introduction to planetary physics. the terrestrial planets. An introduction to planetary physics The terrestrial planets (1969)

Kaula W. M.: Theory of satellite geodesy: applications of satellites to geodesy. Courier Corporation (2013)

van Keken P. E., Hacker B. R., Syracuse E. M., Abers G. A.: Subduction factory: 4. depth-dependent flux of h2o from subducting slabs worldwide. Journal of Geophysical Research: Solid Earth **116**(B1) (2011)

Kelvin L. o. k. a. W. T.: On the thermodynamic acceleration of the earth's rotation. Proceedings of the Royal Society of Edinburgh **11**, 396–405 (1882)

Kendall R. A., Mitrovica J. X., Milne G. A.: On post-glacial sea level–ii. numerical formulation and comparative results on spherically symmetric models. Geophysical Journal International **161**(3), 679–706 (2005)

Kim S.-T., O'Neil J. R.: Equilibrium and nonequilibrium oxygen isotope effects in synthetic carbonates. Geochimica et cosmochimica acta **61**(16), 3461–3475 (1997)

Kinoshita H.: Theory of the rotation of the rigid earth. Celestial mechanics **15**(3), 277–326 (1977)

Klatt J. M., Chennu A., Arbic B. K., Biddanda B., Dick G. J.: Possible link between earth's rotation rate and oxygenation. Nature Geoscience **14**(8), 564–570 (2021)

Kominz M. A., Browning J., Miller K., Sugarman P., Mizintseva S., Scotese C.: Late cretaceous to miocene sea-level estimates from the new jersey and delaware coastal plain coreholes: An error analysis. Basin Research **20**(2), 211–226 (2008)

Korenaga J.: Initiation and evolution of plate tectonics on earth: theories and observations. Annual review of earth and planetary sciences **41**(1), 117–151 (2013)

Korenaga J.: Crustal evolution and mantle dynamics through earth history. Philosophical Transactions of the Royal Society A: Mathematical, Physical and Engineering Sciences **376**(2132), 20170,408 (2018)

Krüger T.: Discovering the Ice Ages: international reception and consequences for a historical understanding of climate. Brill (2013)

Kump L. R., Barley M. E.: Increased subaerial volcanism and the rise of atmospheric oxygen 2.5 billion years ago. Nature **448**(7157), 1033–1036 (2007)

Kurokawa H., Foriel J., Laneuville M., Houser C., Usui T.: Subduction and atmospheric escape of earth's seawater constrained by hydrogen isotopes. Earth and Planetary Science Letters **497**, 149–160 (2018)

Lacis A. A., Oinas V.: A description of the correlated k distribution method for modeling nongray gaseous absorption, thermal emission, and multiple scattering in vertically inhomogeneous atmospheres. Journal of Geophysical Research: Atmospheres **96**(D5), 9027–9063 (1991)

Lamb H.: On atmospheric oscillations. Proceedings of the Royal Society of London Series A, Containing Papers of a Mathematical and Physical Character **84**(574), 551–572 (1911)

Lamb H.: Hydrodynamics dover publications. New York (1945)

Lambeck K.: The Earth's variable rotation: geophysical causes and consequences. Cambridge University Press (1980)

Lambeck K., Rouby H., Purcell A., Sun Y., Sambridge M.: Sea level and global ice volumes from the last glacial maximum to the holocene. Proceedings of the National Academy of Sciences **111**(43), 15,296–15,303 (2014)

Lambeck K., Purcell A., Zhao S.: The north american late wisconsin ice sheet and mantle viscosity from glacial rebound analyses. Quaternary Science Reviews **158**, 172–210 (2017)

Langebroek P. M., Paul A., Schulz M.: Simulating the sea level imprint on marine oxygen isotope records during the middle miocene using an ice sheet–climate model. Paleoceanography **25**(4) (2010)

Lantink M. L., Davies J. H. F. L., Ovtcharova M., Hilgen F. J.: Milankovitch cycles in banded iron formations constrain the earth–moon system 2.46 billion years ago. Proceedings of the National Academy of Sciences **119**(40), e2117146,119, URL https://www.pnas.org/doi/abs/10.1073/pnas.2117146119 (2022)

Laplace P.: Traite de mecanique celeste, five volumes. Paris: Chez JBM Duprat (1798)

Larsen H., Saunders A., Clift P., Beget J., Wei W., Spezzaferri S.: Seven million years of glaciation in greenland. Science **264**(5161), 952–955 (1994)

Laskar J.: Secular terms of classical planetary theories using the results of general theory. Astronomy and astrophysics **157**, 59–70 (1986)

Laskar J.: A numerical experiment on the chaotic behaviour of the solar system. Nature **338**(6212), 237 (1989)

Laskar J.: Large scale chaos and marginal stability in the solar system. Celestial Mechanics and Dynamical Astronomy **64**(1), 115–162 (1996)

Laskar J.: Note on the generalized hansen and laplace coefficients. Celestial Mechanics and Dynamical Astronomy **91**(3), 351–356 (2005)

Laskar J., Correia A. C.: The rotation of extra-solar planets. In: Extrasolar Planets: Today and Tomorrow, vol **321**, p 401 (2004)

Laskar J., Robutel P.: The chaotic obliquity of the planets. Nature **361**(6413), 608–612 (1993)

Laskar J., Joutel F., Boudin F.: Orbital, precessional, and insolation quantities for the earth from-20 myr to+ 10 myr. Astronomy and Astrophysics **270**, 522–533 (1993a)

Laskar J., Joutel F., Robutel P.: Stabilization of the earth's obliquity by the moon. Nature **361**(6413), 615–617 (1993b)

Laskar J., Robutel P., Joutel F., Gastineau M., Correia A., Levrard B.: A long-term numerical solution for the insolation quantities of the earth. Astronomy & Astrophysics **428**(1), 261–285 (2004)

Laskar J., Fienga A., Gastineau M., Manche H.: La2010: a new orbital solution for the long-term motion of the earth. Astronomy & Astrophysics **532**, A89 (2011a)

Laskar J., Gastineau M., Delisle J.-B., Farrés A., Fienga A.: Strong chaos induced by close encounters with ceres and vesta. Astronomy & Astrophysics **532**, L4 (2011b)

Lau H. C., Yang H.-Y., Tromp J., Mitrovica J. X., Latychev K., Al-Attar D.: A normal mode treatment of semi-diurnal body tides on an aspherical, rotating and anelastic earth. Geophysical Journal International **202**(2), 1392–1406 (2015)

Lau H. C., Faul U., Mitrovica J. X., Al-Attar D., Tromp J., Garapić G.: Anelasticity across seismic to tidal timescales: a self-consistent approach. Geophysical journal international , ggw401 (2016a)

Lau H. C., Mitrovica J. X., Austermann J., Crawford O., Al-Attar D., Latychev K.: Inferences of mantle viscosity based on ice age data sets: Radial structure. Journal of Geophysical Research: Solid Earth **121**(10), 6991–7012 (2016b)

Lear C. H., Elderfield H., Wilson P.: Cenozoic deep-sea temperatures and global ice volumes from mg/ca in benthic foraminiferal calcite. science **287**(5451), 269–272 (2000)

Lear C. H., Rosenthal Y., Wright J. D.: The closing of a seaway: ocean water masses and global climate change. Earth and Planetary Science Letters **210**(3-4), 425–436 (2003)

Leconte J., Wu H., Menou K., Murray N.: Asynchronous rotation of earth-mass planets in the habitable zone of lower-mass stars. Science **347**(6222), 632–635 (2015)

Lee D.-C., Halliday A. N., Snyder G. A., Taylor L. A.: Age and origin of the moon. Science **278**(5340), 1098–1103 (1997)

Lee U.: Tidal oscillations of rotating hot jupiters. Monthly Notices of the Royal Astronomical Society **494**(3), 3141–3155 (2020)

Lee U., Saio H.: Low-frequency nonradial oscillations in rotating stars. i. angular dependence. The Astrophysical Journal **491**(2), 839 (1997)

Legros H., Greff M., Tokieda T.: Physics inside the earth: deformation and rotation. LECTURE NOTES IN PHYSICS-NEW YORK THEN BERLIN- **682**, 23 (2005)

Levrard B., Laskar J.: Climate friction and the earth's obliquity. Geophysical Journal International **154**(3), 970–990 (2003)

Levy R., Harwood D., Florindo F., Sangiorgi F., Tripati R., Von Eynatten H., Gasson E., Kuhn G., Tripati A., DeConto R., et al.: Antarctic ice sheet sensitivity to atmospheric co2 variations in the early to mid-miocene. Proceedings of the National Academy of Sciences **113**(13), 3453–3458 (2016)

Levy R. H., Meyers S., Naish T., Golledge N., McKay R., Crampton J. S., DeConto R., De Santis L., Florindo F., Gasson E. G., et al.: Antarctic ice-sheet sensitivity to obliquity forcing enhanced through ocean connections. Nature Geoscience **12**(2), 132–137 (2019)

Liebrand D., de Bakker A. T., Beddow H. M., Wilson P. A., Bohaty S. M., Ruessink G., Pälike H., Batenburg S. J., Hilgen F. J., Hodell D. A., et al.: Evolution of the early antarctic ice ages. Proceedings of the National Academy of Sciences **114**(15), 3867–3872 (2017)

Lindzen R., Batten E., Kim J.-W.: Oscillations in atmospheres with tops. Monthly Weather Review **96**(3), 133–140 (1968)

Lindzen R. S., Blake D.: Lamb waves in the presence of realistic distributions of temperature and dissipation. Journal of Geophysical Research **77**(12), 2166–2176 (1972)

Lindzen R. S., McKenzie D. J.: Tidal theory with newtonian cooling. pure and applied geophysics **66**(1), 90–96 (1967)

Longuet-Higgins M. S.: The eigenfunctions of laplace's tidal equation over a sphere. Philosophical Transactions of the Royal Society of London Series A, Mathematical and Physical Sciences **262**(1132), 511–607 (1968)

Longuet-Higgins M. S., Pond G. S.: The free oscillations of fluid on a hemisphere bounded by meridians of longitude. Philosophical Transactions of the Royal Society of London Series A, Mathematical and Physical Sciences **266**(1174), 193–223 (1970)

Loomis B., Rachlin K., Luthcke S.: Improved earth oblateness rate reveals increased ice sheet losses and mass-driven sea level rise. Geophysical Research Letters **46**(12), 6910–6917 (2019)

Lourens L. J., Wehausen R., Brumsack H. J.: Geological constraints on tidal dissipation and dynamical ellipticity of the earth over the past three million years. Nature **409**(6823), 1029–1033 (2001)

Love A. E. H.: Some Problems of Geodynamics: Being an Essay to which the Adams Prize in the University of Cambridge was Adjudged in 1911, vol **911**. University Press (1911)

Lynch-Stieglitz J., Curry W. B., Slowey N.: A geostrophic transport estimate for the florida current from the oxygen isotope composition of benthic foraminifera. Paleoceanography **14**(3), 360–373 (1999)

MacDonald G. J.: Tidal friction. Reviews of Geophysics **2**(3), 467–541 (1964)

MacDonald G. J. (1966) Origin of the moon: dynamical considerations. In: The earth-moon system, Springer, pp 165–209

Margules M.: Air movements in a rotating sphäroid shell. sitzgsber. akad. wiss. wien, math.-nat. Cl Dept II a **101**, 597–626 (1892)

Mathews P., Lambert S.: Effect of mantle and ocean tides on the earth's rotation rate. Astronomy & Astrophysics **493**(1), 325–330 (2009)

Mathis S., Le Poncin-Lafitte C.: Tidal dynamics of extended bodies in planetary systems and multiple stars. Astronomy & Astrophysics **497**(3), 889–910 (2009)

Mathis S., Talon S., Pantillon F.-P., Zahn J.-P. (2008) Angular momentum transport in the sun's radiative zone by gravito-inertial waves. In: Helioseismology, Asteroseismology, and MHD Connections, Springer, pp 101–118

Matsuo K., Chao B. F., Otsubo T., Heki K.: Accelerated ice mass depletion revealed by low-degree gravity field from satellite laser ranging: Greenland, 1991–2011. Geophysical Research Letters **40**(17), 4662–4667 (2013)

Matsuyama I.: Tidal dissipation in the oceans of icy satellites. Icarus **242**, 11–18 (2014)

Matsuyama I., Mitrovica J., Daradich A., Gomez N.: The rotational stability of a triaxial ice-age earth. Journal of Geophysical Research: Solid Earth **115**(B5) (2010)

Matsuyama I., Trinh A., Keane J. T.: The Lunar Fossil Figure in a Cassini State. The Planetary Science Journal **2**(6):232 (2021)

Maurice M., Tosi N., Schwinger S., Breuer D., Kleine T.: A long-lived magma ocean on a young moon. Science advances **6**(28), eaba8949 (2020)

Mavromatis H., Alassar R.: A generalized formula for the integral of three associated legendre polynomials. Applied mathematics letters **12**(3), 101–105 (1999)

Melosh H.: New approaches to the moon's isotopic crisis. Philosophical Transactions of the Royal Society A: Mathematical, Physical and Engineering Sciences **372**(2024), 20130,168 (2014)

Merdith A. S., Williams S. E., Collins A. S., Tetley M. G., Mulder J. A., Blades M. L., Young A., Armistead S. E., Cannon J., Zahirovic S., et al.: Extending full-plate tectonic models into deep time: Linking the neoproterozoic and the phanerozoic. Earth-Science Reviews **214**, 103,477 (2021)

Meyers S. R., Malinverno A.: Proterozoic milankovitch cycles and the history of the solar system. Proceedings of the National Academy of Sciences **115**(25), 6363–6368 (2018)

Mignard F.: The evolution of the lunar orbit revisited. i. The Moon and the planets **20**(3), 301–315 (1979)

Mignard F.: The evolution of the lunar orbit revisited, ii. The Moon and the planets **23**(2), 185–201 (1980)

Mignard F.: Evolution of the martian satellites. Monthly Notices of the Royal Astronomical Society **194**(2), 365–379 (1981)

Miller K. G., Fairbanks R. G., Mountain G. S.: Tertiary oxygen isotope synthesis, sea level history, and continental margin erosion. Paleoceanography **2**(1), 1–19 (1987)

Miller K. G., Wright J. D., Browning J. V., Kulpecz A., Kominz M., Naish T. R., Cramer B. S., Rosenthal Y., Peltier W. R., Sosdian S.: High tide of the warm pliocene: Implications of global sea level for antarctic deglaciation. Geology **40**(5), 407–410 (2012)

Miller K. G., Browning J. V., Schmelz W. J., Kopp R. E., Mountain G. S., Wright J. D.: Cenozoic sea-level and cryospheric evolution from deep-sea geochemical and continental margin records. Science advances **6**(20), eaaz1346 (2020)

Milne G. A., Mitrovica J. X.: Postglacial sea-level change on a rotating earth. Geophysical Journal International **133**(1), 1–19 (1998)

Mitrovica J., Forte A.: Pleistocene glaciation and the earth's precession constant. Geophysical Journal International **121**(1), 21–32 (1995)

Mitrovica J., Forte A.: A new inference of mantle viscosity based upon joint inversion of convection and glacial isostatic adjustment data. Earth and Planetary Science Letters **225**(1-2), 177–189 (2004)

Mitrovica J., Forte A. M.: Radial profile of mantle viscosity: Results from the joint inversion of convection and postglacial rebound observables. Journal of Geophysical Research: Solid Earth **102**(B2), 2751–2769 (1997)

Mitrovica J., Peltier W.: Pleistocene deglaciation and the global gravity field. Journal of Geophysical Research: Solid Earth **94**(B10), 13,651–13,671 (1989)

Mitrovica J., Forte A., Pan R.: Glaciation-induced variations in the earth's precession frequency, obliquity and insolation over the last 2.6 ma. Geophysical Journal International **128**(2), 270–284 (1997)

Mitrovica J. X., Milne G. A.: On post-glacial sea level: I. general theory. Geophysical Journal International **154**(2), 253–267 (2003)

Mitrovica J. X., Peltier W. R.: On postglacial geoid subsidence over the equatorial oceans. Journal of Geophysical Research: Solid Earth **96**(B12), 20,053–20,071 (1991)

Mitrovica J. X., Wahr J.: Ice age earth rotation. Annual Review of Earth and Planetary Sciences **39**, 577–616 (2011)

Mitrovica J. X., Wahr J., Matsuyama I., Paulson A.: The rotational stability of an ice-age earth. Geophysical Journal International **161**(2), 491–506 (2005)

Mojzsis S. J., Arrhenius G., McKeegan K., Harrison T., Nutman A., Friend C.: Evidence for life on earth before 3,800 million years ago. Nature **384**(6604), 55–59 (1996)

Morrow E., Mitrovica J., Forte A., Glišović P., Huybers P.: An enigma in estimates of the earth's dynamic ellipticity. Geophysical Journal International **191**(3), 1129–1134 (2012)

Motoyama M., Tsunakawa H., Takahashi F.: Tidal resonance of eigenmode oscillation in the early earth's ocean and its acceleration effect on the moon's orbital evolution. Icarus **335**, 113,382 (2020)

Moucha R., Forte A. M., Mitrovica J. X., Rowley D. B., Quéré S., Simmons N. A., Grand S. P.: Dynamic topography and long-term sea-level variations: There is no such thing as a stable continental platform. Earth and Planetary Science Letters **271**(1-4), 101–108 (2008)

Muir J. M., Brodholt J. P.: Water distribution in the lower mantle: implications for hydrolytic weakening. Earth and Planetary Science Letters **484**, 363–369 (2018)

Müller M.: Synthesis of forced oscillations, part i: Tidal dynamics and the influence of the loading and self-attraction effect. Ocean Modelling **20**(3), 207–222 (2008)

Müller R. D., Seton M., Zahirovic S., Williams S. E., Matthews K. J., Wright N. M., Shephard G. E., Maloney K. T., Barnett-Moore N., Hosseinpour M., Bower D. J., Cannon J.: Ocean basin evolution and global-scale plate reorganization events since pangea breakup. Annual Review of Earth and Planetary Sciences **44**(1), 107–138 (2016)

Munk W.: Once again: once again—tidal friction. Progress in Oceanography **40**(1), 7–35 (1968)

Munk W. H., MacDonald G. J.: The rotation of the earth; a geophysical discussion. Cambridge [Eng] University Press (1960)

Murray C. D., Dermott S. F.: Solar system dynamics. Cambridge university press (1999)

Naish T., Powell R., Levy R., Wilson G., Scherer R., Talarico F., Krissek L., Niessen F., Pompilio M., Wilson T., et al.: Obliquity-paced pliocene west antarctic ice sheet oscillations. Nature **458**(7236), 322–328 (2009)

Naish T. R., Woolfe K. J., Barrett P. J., Wilson G. S., Atkins C., Bohaty S. M., Bücker C. J., Claps M., Davey F. J., Dunbar G. B., et al.: Orbitally induced oscillations in the east antarctic ice sheet at the oligocene/miocene boundary. Nature **413**(6857), 719–723 (2001)

Nakada M.: Polar wander caused by the quaternary glacial cycles and fluid love number. Earth and planetary science letters **200**(1-2), 159–166 (2002)

Nakada M., Okuno J., Lambeck K., Purcell A.: Viscosity structure of earth's mantle inferred from rotational variations due to gia process and recent melting events. Geophysical Journal International **202**(2), 976–992 (2015)

Nemchin A., Timms N., Pidgeon R., Geisler T., Reddy S., Meyer C.: Timing of crystallization of the lunar magma ocean constrained by the oldest zircon. Nature geoscience **2**(2), 133–136 (2009)

Neron de Surgy O., Laskar J.: On the long term evolution of the spin of the earth. Astronomy and Astrophysics **318**, 975–989 (1997)

NOAA N. O., Administration A., Force U. S. A.: US standard atmosphere, 1976, vol **76**. National Oceanic and Atmospheric Administration (1976)

North G. R., Pyle J. A., Zhang F.: Encyclopedia of atmospheric sciences, vol **1**. Elsevier (2014)

Ogilvie G. I.: Tidal dissipation in stars and giant planets. Annual Review of Astronomy and Astrophysics **52**, 171–210 (2014)

O'Neil J. R., Clayton R. N., Mayeda T. K.: Oxygen isotope fractionation in divalent metal carbonates. The Journal of Chemical Physics **51**(12), 5547–5558 (1969)

Ooe M.: Effects of configuration and bathymetry of the oceans on the tidal dissipation of the earth's rotation. Journal of Physics of the Earth **37**(5), 345–355 (1989)

Pahlevan K., Morbidelli A.: Collisionless encounters and the origin of the lunar inclination. Nature **527**(7579), 492–494 (2015)

Pälike H., Shackleton N. J.: Constraints on astronomical parameters from the geological record for the last 25 myr. Earth and Planetary Science Letters **182**(1), 1–14 (2000)

Pälike H., Norris R. D., Herrle J. O., Wilson P. A., Coxall H. K., Lear C. H., Shackleton N. J., Tripati A. K., Wade B. S.: The heartbeat of the oligocene climate system. science **314**(5807), 1894–1898 (2006)

Palmer T., Shutts G., Swinbank R.: Alleviation of a systematic westerly bias in general circulation and numerical weather prediction models through an orographic gravity wave drag parametrization. Quarterly Journal of the Royal Meteorological Society **112**(474), 1001–1039 (1986)

Payne J. L., McInerney D. J., Barovich K. M., Kirkland C. L., Pearson N. J., Hand M.: Strengths and limitations of zircon lu-hf and o isotopes in modelling crustal growth. Lithos **248**, 175–192 (2016)

Peale S.: Origin and evolution of the natural satellites. Annual Review of Astronomy and Astrophysics **37**(1), 533–602 (1999)

Peale S., Cassen P.: Contribution of tidal dissipation to lunar thermal history. Icarus **36**(2), 245–269 (1978)

Peck W. H., Valley J. W., Wilde S. A., Graham C. M.: Oxygen isotope ratios and rare earth elements in 3.3 to 4.4 ga zircons: Ion microprobe evidence for high δ18o continental crust and oceans in the early archean. Geochimica et Cosmochimica Acta **65**(22), 4215–4229 (2001)

Pekar S. F., DeConto R. M.: High-resolution ice-volume estimates for the early miocene: Evidence for a dynamic ice sheet in antarctica. Palaeogeography, Palaeoclimatology, Palaeoecology **231**(1-2), 101–109 (2006)

Pekeris C.: Atmospheric oscillations. Proceedings of the Royal Society of London Series A-Mathematical and Physical Sciences **158**(895), 650–671 (1937)

Peltier W.: The impulse response of a maxwell earth. Reviews of Geophysics **12**(4), 649–669 (1974)

Peltier W.: Constraint on deep mantle viscosity from lageos acceleration data. Nature **304**(5925), 434–436 (1983)

Peltier W.: The lageos constraint on deep mantle viscosity: results from a new normal mode method for the inversion of viscoelastic relaxation spectra. Journal of Geophysical Research: Solid Earth **90**(B11), 9411–9421 (1985)

Peltier W. (2015) 9.09 - the history of the earth's rotation: Impacts of deep earth physics and surface climate variability. In: Schubert G. (ed) Treatise on Geophysics (Second Edition), second edition edn, Elsevier, Oxford, pp 221–279

Peltier W., Jiang X.: The precession constant of the earth: Variations through the ice-age. Geophysical research letters **21**(21), 2299–2302 (1994)

Peltier W., Argus D., Drummond R.: Space geodesy constrains ice age terminal deglaciation: The global ice-6g_c (vm5a) model. Journal of Geophysical Research: Solid Earth **120**(1), 450–487 (2015)

Peltier W. R., Andrews J. T.: Glacial-isostatic adjustment—i. the forward problem. Geophysical Journal International **46**(3), 605–646 (1976)

Peltier W. R., Tushingham A.: Global sea level rise and the greenhouse effect: might they be connected? Science **244**(4906), 806–810 (1989)

Pendea I. F., Costopoulos A., Nielsen C., Chmura G. L.: A new shoreline displacement model for the last 7 ka from eastern james bay, canada. Quaternary Research **73**(3), 474–484 (2010)

Petit G., Luzum B. (2010) Iers conventions (2010). Tech. rep., Bureau International des Poids et mesures sevres (france)

Pico T., Creveling J., Mitrovica J.: Sea-level records from the us mid-atlantic constrain laurentide ice sheet extent during marine isotope stage 3. Nature communications **8**(1), 1–6 (2017)

Pierrehumbert R. T.: Principles of planetary climate. Cambridge University Press (2010)

Platzman G. W.: World ocean tides synthesized from normal modes. Science **220**(4597), 602–604 (1983)

Platzman G. W.: Normal modes of the world ocean. part iv: Synthesis of diurnal and semidiurnal tides. Journal of physical oceanography **14**(10), 1532–1550 (1984)

Poincaré H.: Sur l'équilibre d'une masse fluide animée d'un mouvement de rotation. Bulletin astronomique, Observatoire de Paris **2**(1), 109–118 (1885)

Poliakow E.: Numerical modelling of the paleotidal evolution of the earth-moon system. Proceedings of the International Astronomical Union **2004**(IAUC197), 445–452 (2004)

Pollack J. B., Young R.: Calculations of the radiative and dynamical state of the venus atmosphere. Journal of Atmospheric Sciences **32**(6), 1025–1037 (1975)

Pollard D., DeConto R. M.: Modelling west antarctic ice sheet growth and collapse through the past five million years. Nature **458**(7236), 329–332 (2009)

Pope E. C., Bird D. K., Rosing M. T.: Isotope composition and volume of earth's early oceans. Proceedings of the National Academy of Sciences **109**(12), 4371–4376 (2012)

Prat V., Lignières F., Ballot J.: Asymptotic theory of gravity modes in rotating stars-i. ray dynamics. Astronomy & Astrophysics **587**, A110 (2016)

Proudman J.: On the dynamical equations of the tides. Proceedings of the London Mathematical Society **2**(1), 1–20 (1920a)

Proudman J.: On the dynamical equations of the tides: Part iii.—oceans on a sphere. Proceedings of the London Mathematical Society **2**(1), 51–68 (1920b)

Pujol M., Marty B., Burgess R., Turner G., Philippot P.: Argon isotopic composition of archaean atmosphere probes early earth geodynamics. Nature **498**(7452), 87–90 (2013)

Ray R. D., Bills B. G., Chao B. F.: Lunar and solar torques on the oceanic tides. Journal of Geophysical Research: Solid Earth **104**(B8), 17,653–17,659 (1999)

Rayleigh L.: Xvii. on the vibrations of an atmosphere. The London, Edinburgh, and Dublin Philosophical Magazine and Journal of Science **29**(177), 173–180 (1890)

Raymo M. E., Mitrovica J., O'Leary M. J., DeConto R. M., Hearty P. J.: Departures from eustasy in pliocene sea-level records. Nature Geoscience **4**(5), 328–332 (2011)

Raymo M. E., Kozdon R., Evans D., Lisiecki L., Ford H. L.: The accuracy of mid-pliocene δ18o-based ice volume and sea level reconstructions. Earth-Science Reviews **177**, 291–302 (2018)

Regge T.: Symmetry properties of clebsch-gordon's coefficients. Il Nuovo Cimento (1955-1965) **10**(3), 544–545 (1958)

Renaud J. P., Henning W. G.: Increased tidal dissipation using advanced rheological models: Implications for io and tidally active exoplanets. The Astrophysical Journal **857**(2), 98 (2018)

Riley K. F., Hobson M. P., Bence S. J.: Mathematical methods for physics and engineering (1999)

Rocchi S., LeMasurier W. E., Di Vincenzo G.: Oligocene to holocene erosion and glacial history in marie byrd land, west antarctica, inferred from exhumation of the dorrel rock intrusive complex and from volcano morphologies. Geological Society of America Bulletin **118**(7-8), 991–1005 (2006)

Rose K. C., Ferraccioli F., Jamieson S. S., Bell R. E., Corr H., Creyts T. T., Braaten D., Jordan T. A., Fretwell P. T., Damaske D.: Early east antarctic ice sheet growth recorded in the landscape of the gamburtsev subglacial mountains. Earth and Planetary Science Letters **375**, 1–12 (2013)

Ross M., Schubert G.: Evolution of the lunar orbit with temperature-and frequency-dependent dissipation. Journal of Geophysical Research: Solid Earth **94**(B7), 9533–9544 (1989)

Roy K., Peltier W.: Grace era secular trends in earth rotation parameters: A global scale impact of the global warming process? Geophysical Research Letters **38**(10) (2011)

Roy K., Peltier W.: Space-geodetic and water level gauge constraints on continental uplift and tilting over north america: regional convergence of the ice-6g_c (vm5a/vm6) models. Geophysical Journal International **210**(2), 1115–1142 (2017)

Rubincam D. P.: Tidal friction in the earth–moon system and laplace planes: Darwin redux. Icarus **266**, 24–43 (2016)

Rufu R., Canup R. M.: Tidal evolution of the evection resonance/quasi-resonance and the angular momentum of the earth-moon system. Journal of Geophysical Research: Planets **125**(8), e2019JE006,312 (2020)

Sabadini R., Peltier W. R.: Pleistocene deglaciation and the Earth's rotation: implications for mantle viscosity. Geophysical Journal International **66**(3), 553–578 (1981)

Sabadini R., Yuen D. A., Boschi E.: Polar wandering and the forced responses of a rotating, multilayered, viscoelastic planet. Journal of Geophysical Research: Solid Earth **87**(B4), 2885–2903 (1982)

Sabadini R., Yuen D., Gasperini P.: The effects of transient rheology on the interpretation of lower mantle viscosity. Geophysical Research Letters **12**(6), 361–364 (1985)

Sabadini R., Vermeersen B., Cambiotti G.: Global dynamics of the Earth. Springer (2016)

Salmon J., Canup R. M.: Lunar accretion from a roche-interior fluid disk. The Astrophysical Journal **760**(1), 83 (2012)

Sanchez B. V.: Normal modes of the global oceans—a review. Marine Geodesy **31**(3), 181–212 (2008)

Schmidt O.: A theory of the earth's origin- four lectures: Moscow. Foreign Languages Publishing House (3), 139 (1958)

Scrutton C. (1978) Periodic growth features in fossil organisms and the length of the day and month. In: Tidal friction and the earth's rotation, Springer, pp 154–196

Shackleton N. J.: Paleotemperature history of the cenozoic and the initiation of antarctic glaciation: oxygen and carbon isotope analyses in dsdp sites 277,279, and 281. Initial Reports of Deep Sea Drilling Project **29**, 743–756 (1975)

Shackleton N. J., Backman J., Zimmerman H., Kent D. V., Hall M., Roberts D. G., Schnitker D., Baldauf J., Desprairies A., Homrighausen R., et al.: Oxygen isotope calibration of the onset of ice-rafting and history of glaciation in the north atlantic region. Nature **307**(5952), 620–623 (1984)

Shakun J. D., Corbett L. B., Bierman P. R., Underwood K., Rizzo D. M., Zimmerman S. R., Caffee M. W., Naish T., Golledge N. R., Hay C. C.: Minimal east antarctic ice sheet retreat onto land during the past eight million years. Nature **558**(7709), 284–287 (2018)

Shevenell A. E., Kennett J. P., Lea D. W.: Middle miocene ice sheet dynamics, deep-sea temperatures, and carbon cycling: A southern ocean perspective. Geochemistry, Geophysics, Geosystems **9**(2) (2008)

Siebert M. (1961) Atmospheric tides. In: Advances in geophysics, vol **7**, Elsevier, pp 105–187

Sinnesael M., De Vleeschouwer D., Zeeden C., Batenburg S. J., Da Silva A.-C., de Winter N. J., Dinarès-Turell J., Drury A. J., Gambacorta G., Hilgen F. J., et al.: The cyclostratigraphy intercomparison project (cip): consistency, merits and pitfalls. Earth-Science Reviews **199**, 102,965 (2019)

Slichter L. B.: Secular effects of tidal friction upon the earth's rotation. Journal of Geophysical Research **68**(14), 4281–4288 (1963)

Smylie D., Mansinha L.: The elasticity theory of dislocations in real earth models and changes in the rotation of the earth. Geophysical Journal International **23**(3), 329–354 (1971)

Sonett C., Chan M. A.: Neoproterozoic earth-moon dynamics: Rework of the 900 ma big cottonwood canyon tidal laminae. Geophysical Research Letters **25**(4), 539–542 (1998)

Sørensen A. L., Nielsen A. T., Thibault N., Zhao Z., Schovsbo N. H., Dahl T. W.: Astronomically forced climate change in the late cambrian. Earth and Planetary Science Letters **548**, 116,475 (2020)

Sorlien C. C., Luyendyk B. P., Wilson D. S., Decesari R. C., Bartek L. R., Diebold J. B.: Oligocene development of the west antarctic ice sheet recorded in eastern ross sea strata. Geology **35**(5), 467–470 (2007)

Sosdian S., Rosenthal Y.: Deep-sea temperature and ice volume changes across the pliocene-pleistocene climate transitions. Science **325**(5938), 306–310 (2009)

Spada G., Boschi L.: Using the post—widder formula to compute the earth's viscoelastic love numbers. Geophysical Journal International **166**(1), 309–321 (2006)

Spada G., Melini D.: Selen: a program for solving the "sea level equation"–manual version 1.2, december 2015, computational infrastructure for geodynamics (cig) (2015)

Spada G., Melini D.: Selen 4 (selen version 4.0): a fortran program for solving the gravitationally and topographically self-consistent sea-level equation in glacial isostatic adjustment modeling. Geoscientific Model Development **12**(12), 5055–5075 (2019)

Spada G., Stocchi P.: Selen: A fortran 90 program for solving the "sea-level equation". Computers & Geosciences **33**(4), 538–562 (2007)

Spada G., Yuen D. A., Sabadini R., Morin P. J., Gasperini P.: A computer-aided, algebraic approach to the post-glacial rebound problem. Math J **1**(2), 65–69 (1991)

Spada G., Sabadini R., Yuen D. A., Ricard Y.: Effects on post-glacial rebound from the hard rheology in the transition zone. Geophysical Journal International **109**(3), 683–700 (1992)

Spada G., Melini D., Galassi G., Colleoni F.: Modeling sea level changes and geodetic variations by glacial isostasy: the improved selen code. arXiv preprint arXiv:12125061 (2012)

Spencer Jones H.: The rotation of the earth, and the secular accelerations of the sun, moon and planets. Monthly Notices of the Royal Astronomical Society **99**, 541 (1939)

Stacey F. D., Davis P. M.: Physics of the Earth. Cambridge University Press (2008)

Stephenson F. R.: Historical eclipses and Earth's rotation. Cambridge University Press (2008)

Stephenson F. R., Morrison L. V., Smith F.: Long-term fluctuations in the earth's rotation: 700 bc to ad 1990. Philosophical Transactions of the Royal Society of London Series A: Physical and Engineering Sciences **351**(1695), 165–202 (1995)

Strauss W. A.: Partial differential equations: An introduction. John Wiley & Sons (2007)

Sun C., Xu W., Cawood P. A., Tang J., Zhao S., Li Y., Zhang X.: Crustal growth and reworking: A case study from the erguna massif, eastern central asian orogenic belt. Scientific reports **9**(1), 1–8 (2019)

Tanaka Y., Okuno J., Okubo S.: A new method for the computation of global viscoelastic post-seismic deformation in a realistic earth model (i)—vertical displacement and gravity variation. Geophysical Journal International **164**(2), 273–289 (2006)

Taylor G. I.: Waves and tides in the atmosphere. Proceedings of the Royal Society of London Series A, Containing Papers of a Mathematical and Physical Character **126**(800), 169–183 (1929)

Taylor G. I.: The resonance theory of semidiurnal atmospheric oscillations. Edward Stanford (1932)

Tegmark M.: An icosahedron-based method for pixelizing the celestial sphere. ApJL **470**, L81 (1996)

Tera F., Wasserburg G.: U-th-pb systematics in three apollo 14 basalts and the problem of initial pb in lunar rocks. Earth and Planetary Science Letters **14**(3), 281–304 (1972)

Tetley M. G., Williams S. E., Gurnis M., Flament N., Müller R. D.: Constraining absolute plate motions since the triassic. Journal of Geophysical Research: Solid Earth **124**(7), 7231–7258 (2019)

Thomson D. J.: Quadratic-inverse spectrum estimates: applications to palaeoclimatology. Philosophical Transactions of the Royal Society of London Series A: Physical and Engineering Sciences **332**(1627), 539–597 (1990)

Tian Z., Wisdom J.: Vertical angular momentum constraint on lunar formation and orbital history. Proceedings of the National Academy of Science **117**(27), 15,460–15,464 (2020)

Tian Z., Wisdom J., Elkins-Tanton L.: Coupled orbital-thermal evolution of the early earth-moon system with a fast-spinning earth. Icarus **281**, 90–102 (2017)

Tobie G., Mocquet A., Sotin C.: Tidal dissipation within large icy satellites: Applications to europa and titan. Icarus **177**(2), 534–549 (2005)

Tobie G., Grasset O., Dumoulin C., Mocquet A.: Tidal response of rocky and ice-rich exoplanets. Astronomy & Astrophysics **630**, A70 (2019)

Tort M., Dubos T.: Dynamically consistent shallow-atmosphere equations with a complete coriolis force. Quarterly Journal of the Royal Meteorological Society **140**(684), 2388–2392 (2014)

Touma J., Wisdom J.: Evolution of the earth-moon system. The Astronomical Journal **108**, 1943–1961 (1994a)

Touma J., Wisdom J.: Lie-poisson integrators for rigid body dynamics in the solar system. The Astronomical Journal **107**, 1189–1202 (1994b)

Touma J., Wisdom J.: Resonances in the early evolution of the earth-moon system. The Astronomical Journal **115**(4), 1653 (1998)

Touma J., Wisdom J.: Nonlinear core-mantle coupling. The Astronomical Journal **122**(2), 1030 (2001)

Touma J. R., Sridhar S.: The disruption of multiplanet systems through resonance with a binary orbit. Nature **524**(7566), 439–441 (2015)

Townsend J. P., Tsuchiya J., Bina C. R., Jacobsen S. D.: Water partitioning between bridgmanite and postperovskite in the lowermost mantle. Earth and Planetary Science Letters **454**, 20–27 (2016)

Tremaine S., Touma J., Namouni F.: Satellite dynamics on the laplace surface. The astronomical journal **137**(3), 3706 (2009)

Tripati A., Darby D.: Evidence for ephemeral middle eocene to early oligocene greenland glacial ice and pan-arctic sea ice. Nature communications **9**(1), 1–11 (2018)

Turcotte D., Kellogg L.: Implications of isotope data for the origin of the moon. In: Origin of the Moon, pp 311–329 (1986)

Tyler R.: Tidal dynamical considerations constrain the state of an ocean on enceladus. Icarus **211**(1), 770–779 (2011)

Tyler R. H.: Strong ocean tidal flow and heating on moons of the outer planets. Nature **456**(7223), 770–772 (2008)

Tyler R. H.: Heating of enceladus due to the dissipation of ocean tides. Icarus **348**, 113,821 (2020)

Tyler R. H.: On the tidal history and future of the earth–moon orbital system. The Planetary Science Journal **2**(2), 70 (2021)

Unno W., Osaki Y., Ando H., Saio H., Shibahashi H.: Nonradial oscillations of stars, ed. Unno, W, Osaki, Y, Ando, H, Saio, H, & Shibahashi, H **755** (1989)

Urey H. C.: Origin and history of the Moon. In Z. Kopal (Ed.), Physics and Astronomy of the Moon. Academic Press (1962)

Urey H. C.: The origin and evolution of the solar system. Space science , 123–168 (1963)

Vallis G. K.: Atmospheric and oceanic fluid dynamics. Cambridge University Press (2017)

Van Andel T. H.: New views on an old planet. Cambridge University Press (1994)

Varshalovich D. A., Moskalev A. N., Khersonskii V. K.: Quantum Theory of Angular Momentum. WORLD SCIENTIFIC (1988)

Vermeersen L. L. A., Sabadini R.: A new class of stratified viscoelastic models by analytical techniques. Geophysical Journal International **129**(3), 531–570 (1997a)

Vermeersen L. L. A., Sabadini R.: A new class of stratified viscoelastic models by analytical techniques. Geophysical Journal International **129**(3), 531–570 (1997b)

Viswanathan V., Rambaux N., Fienga A., Laskar J., Gastineau M.: Observational constraint on the radius and oblateness of the lunar core-mantle boundary. Geophysical Research Letters **46**(13), 7295–7303 (2019)

Volland H.: Solutions of laplace's tidal equation for complex frequencies. Journal of Atmospheric and Terrestrial Physics **36**(3), 445–459 (1974)

Wahr J. M.: The effects of the atmosphere and oceans on the earth's wobble and on the seasonal variations in the length of day—ii. results. Geophysical Journal International **74**(2), 451–487 (1983)

Walker J. C., Zahnle K. J.: Lunar nodal tide and distance to the moon during the precambrian. Nature **320**(6063), 600–602 (1986)

Wang H., Boyd J. P., Akmaev R. A.: On computation of hough functions. Geoscientific Model Development **9**(4), 1477–1488 (2016)

Ward W. R.: Past orientation of the lunar spin axis. Science **189**(4200), 377–379 (1975)

Ward W. R., Canup R. M.: Origin of the Moon's orbital inclination from resonant disk interactions. Nature **403**(6771), 741–743 (2000)

Ward W. R., Canup R. M., Rufu R.: Analytical model for the tidal evolution of the evection resonance and the timing of resonance escape. Journal of Geophysical Research: Planets **125**(6), e2019JE006,266 (2020)

Watterson I. G.: Decomposition of Global Ocean Currents Using a Simple Iterative Method. Journal of Atmospheric and Oceanic Technology **18**(4), 691 (2001)

Webb D.: On the age of the semi-diurnal tide. In: Deep Sea Research and Oceanographic Abstracts, Elsevier, vol **20**, pp 847–852 (1973)

Webb D.: Tides and tidal friction in a hemispherical ocean centred at the equator. Geophysical Journal International **61**(3), 573–600 (1980)

Webb D.: Tides and the evolution of the earth—moon system. Geophysical Journal International **70**(1), 261–271 (1982a)

Webb D. J.: The effect of polar wander on the tides of a hemispherical ocean. Geophysical Journal International **68**(3), 689–707 (1982b)

Weekes K., Wilkes M. V.: Atmospheric oscillations and the resonance theory. Proceedings of the Royal Society of London Series A Mathematical and Physical Sciences **192**(1028), 80–99 (1947)

Wells J. W., et al.: Coral growth and geochronometry. Nature **197**(4871), 948–950 (1963)

Westerhold T., Marwan N., Drury A. J., Liebrand D., Agnini C., Anagnostou E., Barnet J. S., Bohaty S. M., De Vleeschouwer D., Florindo F., et al.: An astronomically dated record of earth's climate and its predictability over the last 66 million years. Science **369**(6509), 1383–1387 (2020)

Whitehouse P. L.: Glacial isostatic adjustment modelling: historical perspectives, recent advances, and future directions. Earth surface dynamics **6**(2), 401–429 (2018)

Whitehouse P. L., Bentley M. J., Milne G. A., King M. A., Thomas I. D.: A new glacial isostatic adjustment model for antarctica: calibrated and tested using observations of relative sea-level change and present-day uplift rates. Geophysical Journal International **190**(3), 1464–1482 (2012)

Wilde S. A., Valley J. W., Peck W. H., Graham C. M.: Evidence from detrital zircons for the existence of continental crust and oceans on the earth 4.4 gyr ago. Nature **409**(6817), 175–178 (2001)

Williams G. E.: Tidal rhythmites: geochronometers for the ancient earth-moon system. Episodes Journal of International Geoscience **12**(3), 162–171 (1989)

Williams G. E.: Tidal rhythmites: key to the history of the earth's rotation and the lunar orbit. Journal of Physics of the Earth **38**(6), 475–491 (1990)

Williams G. E.: Precambrian length of day and the validity of tidal rhythmite paleotidal values. Geophysical Research Letters **24**(4), 421–424 (1997)

Williams G. E.: Geological constraints on the precambrian history of earth's rotation and the moon's orbit. Reviews of Geophysics **38**(1), 37–59 (2000)

Williams J. G., Boggs D. H.: Tides on the moon: Theory and determination of dissipation. Journal of Geophysical Research: Planets **120**(4), 689–724 (2015)

Williams J. G., Boggs D. H.: Secular tidal changes in lunar orbit and earth rotation. Celestial Mechanics and Dynamical Astronomy **126**(1), 89–129 (2016)

Winnick M. J., Caves J. K.: Oxygen isotope mass-balance constraints on pliocene sea level and east antarctic ice sheet stability. Geology **43**(10), 879–882 (2015)

Wisdom J.: Dynamics of the lunar spin axis. The Astronomical Journal **131**(3), 1864 (2006)

Wisdom J., Holman M.: Symplectic maps for the n-body problem-stability analysis. The Astronomical Journal **104**, 2022–2029 (1992)

Wisdom J., Tian Z.: Early evolution of the earth–moon system with a fast-spinning earth. Icarus **256**, 138–146 (2015)

Wisdom J., Dbouk R., Militzer B., Hubbard W. B., Nimmo F., Downey B. G., French R. G.: Loss of a satellite could explain saturn’s obliquity and young rings. Science **377**(6612), 1285–1289 (2022)

Wise D. U.: An origin of the moon by rotational fission during formation of the earth's core. Journal of Geophysical Research **68**(5), 1547–1554 (1963)

Wolf D.: Viscoelastodynamics of a stratified, compressible planet: incremental field equations and short-and long-time asymptotes. Geophysical Journal International **104**(2), 401–417 (1991)

Wood J. A.: Moon over mauna loa-a review of hypotheses of formation of earth's moon. Origin of the Moon , 17–55 (1986)

Wood R., Liu A. G., Bowyer F., Wilby P. R., Dunn F. S., Kenchington C. G., Cuthill J. F. H., Mitchell E. G., Penny A.: Integrated records of environmental change and evolution challenge the cambrian explosion. Nature ecology & evolution **3**(4), 528–538 (2019)

Wu P., Ni Z.: Some analytical solutions for the viscoelastic gravitational relaxation of a two-layer non-self-gravitating incompressible spherical earth. Geophysical Journal International **126**(2), 413–436 (1996)

Wu P., Peltier W.: Viscous gravitational relaxation. Geophysical Journal International **70**(2), 435–485 (1982)

Wunsch C.: The long-period tides. Reviews of Geophysics **5**(4), 447–475 (1967)

Wunsch C.: Tides of global ice-covered oceans. Icarus **274**, 122–130 (2016)

Yoder C., Williams J., Dickey J., Schutz B., Eanes R., Tapley B.: Secular variation of earth's gravitational harmonic j 2 coefficient from lageos and nontidal acceleration of earth rotation. Nature **303**(5920), 757–762 (1983)

Yoder C. F.: Astrometric and geodetic properties of Earth and the Solar System, vol **1**. Wiley Online Library (1995)

Yuen D. A., Peltier W.: Normal modes of the viscoelastic earth. Geophysical Journal International **69**(2), 495–526 (1982)

Zachos J., Pagani M., Sloan L., Thomas E., Billups K.: Trends, rhythms, and aberrations in global climate 65 ma to present. science **292**(5517), 686–693 (2001)

Zachos J. C., Dickens G. R., Zeebe R. E.: An early cenozoic perspective on greenhouse warming and carbon-cycle dynamics. Nature **451**(7176), 279–283 (2008)

Zahel W.: Mathematical modelling of global interaction between ocean tides and earth tides. Physics of the Earth and Planetary Interiors **21**(2-3), 202–217 (1980)

Zahn J.-P.: Les marées dans une étoile double serrée. In: Annales d'Astrophysique, vol **29**, p 313 (1966)

Zahnle K., Walker J. C.: A constant daylength during the precambrian era? Precambrian Research **37**(2), 95–105 (1987)

Zahnle K. J., Lupu R., Dobrovolskis A., Sleep N. H.: The tethered moon. Earth and Planetary Science Letters **427**, 74–82 (2015)

Zhang J., Dauphas N., Davis A. M., Leya I., Fedkin A.: The proto-earth as a significant source of lunar material. Nature Geoscience **5**(4), 251–255 (2012)

Zhang S., Wang X., Hammarlund E. U., Wang H., Costa M. M., Bjerrum C. J., Connelly J. N., Zhang B., Bian L., Canfield D. E.: Orbital forcing of climate 1.4 billion years ago. Proceedings of the National Academy of Sciences **112**(12), E1406–E1413 (2015)

Zharov V., Gambis D.: Atmospheric tides and rotation of the earth. Journal of Geodesy **70**(6), 321–326 (1996)

Zhong Y., Wu H., Fan J., Fang Q., Shi M., Zhang S., Yang T., Li H., Cao L.: Late Ordovician obliquity-forced glacio-eustasy recorded in the Yangtze Block, South China. Palaeogeography, Palaeoclimatology, Palaeoecology **540**, 109,520, URL https://www.sciencedirect.com/science/article/pii/S0031018219300240 (2020)

LIST OF FIGURES

LIST OF TABLES